AN EXPERIMENTAL AND NUMERICAL INVESTIGATION INTO REACTING VORTEX STRUCTURES ASSOCIATED WITH UNSTABLE COMBUSTION

Thesis by

Donald William Kendrick

In Partial Fulfillment of the Requirements

for the Degree of

Doctor of Philosophy

California Institute of Technology

Pasadena, California

1995

(Submitted October 28, 1994)

ACKNOWLEDGMENTS

The author wishes to thank the many individuals that inspired and aided in the completion of this manuscript and who made his stay at Caltech most enjoyable.

First, the author wishes to thank his family whose devotion and sacrifices have enabled the author to pursue studies beyond levels ever expected of him. Their support and council gave lift to a sometimes beleaguered mind.

Mar chraoibh is amhluidh bithidh e'n cois aimhne fàs a ta,
A bheir 'na h-aimsir toradh trom, gun duilleach chall no blàth.
Soirbhichidh leis gach ni d'an dean:ni h-amhluidh sin do bhi
Na daoine peacach; ach mar mholl air fhuadachadh le gaoith.

Salm 1r3

This program would not be possible without the endearing support of his thesis advisor, Professor Edward Zukoski, whose enthusiasm and suggestions have strengthened the academic zeal of the author. At no time was his door locked to the constant demands placed on him by the author or by his other students. Many helpful discussions were also made with other Caltech professors, most notably Professors Frank Marble, Fred Culick and Melany Hunt.

The author is also indebted to the help and encouragement from other students, past and present, at the institute. Such a rich international contingent made for a most stimulating research environment, even off hours at the pub. Dr. Thomas Zsak, a close friend, was invaluable in the completion of this research. Dr. Richard Chan, Dr. Jim

Sterling, Dr. Ian Waitz and Dr. Joe Yang also provided helpful suggestion and insight into the thesis work. In addition, Dr. Larry Hill provided much assistance in the high-speed camera work. UNIX and PC problems were handled most efficiently by Mr. Kevin Moore, Mr. Victor Burnley and Mr. Steve Palm. Technical assistance was also received from Mr. Windsor Lin.

Many of the staff members at GALCIT including Ms. Dorothy Eckerman, Mr. Alan Goody and Ms. Marionne Kirk provided much needed moral and technical support over the years.

Finally, the author wishes to thank his former professor, Professor Edward Hauptmann, of the Mechanical Engineering Department of the University of British Columbia for encouraging the author to pursue graduate studies at Caltech.

This work was funded by the Air Force Office of Scientific Research, Grant Number 89-0413, under the direction of Dr. Julian Tishkoff.

ABSTRACT

An experimental and numerical investigation into reacting vortex structures shed from a rearward facing step flameholder was performed to gain insight into the fundamental reasons why certain acoustic modes of the laboratory dump combustor were excited for a given set of flow parameters. Cases examined used premixed $CH_4 - air$ mixtures ($1.2 \leq \phi \leq 1.7$), various duct heights (2.54, 5.08 and 7.62 *cm*) and dump plane speeds (21, 30 and 35 *m/s*). The above parameters permitted observing instabilities having either one or both of the longitudinal acoustic modes present (188 or 234 *Hz*) in their respective pressure and velocity spectra.

Ignition of the vortex structures was found to be heavily dependent on geometry (i.e., duct height) and invariant to stoichiometric variations. This fact indicated the dominance of turbulent exchange processes over chemical effects for the pulsating flowfield. The coherent structures which typically convected at the local dump plane speed and exhibited high initial strain rates, were found to exhibit shorter burning times and more intense combustion for decreasing duct heights. Use of high-speed shadowgraph and chemiluminescent (CCD) imagery permitted a complete description of the typically nonuniform, reacting flowfield. Time-resolved vortex and floor temperature measurements as well as time-averaged floor heat flux measurements completed the quantitative description of the vortex structures.

Culick's technique of expanding the acoustic filed into orthogonal modes was employed to confirm mode selection theories and suggest the importance of the shape of the average burner distribution. A nonlinear heat release model was formulated whereby the vortices were characterized as gaussian envelopes convecting at the local dump plane

speed. The system of equations formulated was a set of two coupled oscillators with a nonlinear driving term. A final discussion was also undertaken to infer the geometrical implications into the mode selection process (what system acoustic mode was excited).

TABLE OF CONTENTS

LIST OF FIGURES

LIST OF TABLES

NOMENCLATURE

Variables:

a	*Sound speed*
A	*Floor area*
b, b_a	*Numerical model parameters*
c_i	*Numerical model parameter*
B	*Nondimensional fluctuating velocity:* $u'/\overline{u}$
C_p	*Specific heat at constant pressure*
d	*Duct height or Hydraulic diameter of duct*
d_g	*Gap height (0.64 mm)*
d_s	*Step height:* d-d_g
e	*Hemispherical emmissivity*
E_n	*Norm of mode shapes*
f	*Prescribed function for boundary conditions*
$\vec{F}$	*Source term in momentum equation*
h	*Convective heat transfer coefficient*
$\boldsymbol{h}$	*Nonlinear driving term in model*
i	*Vortex number*
j	*Time index*
k	*Coefficient of thermal conductivity*
k_n	*Wave number of mode n*
L	*Length of separation streamline*
m, m_a	*Numerical model parameters*
$\hat{n}$	*Unit normal vector*

Nu_d	*Nusselt number based on hydraulic diameter:* $Nu_d = \frac{hd}{k}$
Pr	*Prandtl number*
p	*Pressure*
$\boldsymbol{P}$	*Source term in energy equation*
q	*Rate of heat release per unit volume*
Q	*Spatially integrated rate of heat release*
$\dot{Q}_{floor}$	*Rate of heat flux to the floor*
R	*Universal gas constant*
$\boldsymbol{R}$	*Global Rayleigh Index*
Re_d	*Reynold's Number based on hydraulic diameter:* $\mathrm{Re} = \frac{\rho V_{dump} d}{\mu}$
S_l	*Laminar burning velocity*
$S_{p'-q'}$	*Cross-spectrum between pressure and heat release*
t	*Time*
$\boldsymbol{t}$	*Nondimensional time*
T	*Temperature*
T	*Period of oscillation*
T_g	*Hot gas temperature*
T_j	*Thermocouple junction temperature*
T_o	*Initial thermocouple temperature*
T_w	*Cool wall temperature*
T_{ad}	*Adiabatic flame temperature*
T_{mix}	*Mixture temperature at which chemical reactions begin*
u	*Velocity*
v_{v_i}	*Speed of vortex i*

V	*Chamber volume*
V_{dump}	*Average dump plane speed*
$\bar{x}$	*Spatial coordinate*
x_i	*Position of vortex i*
x_{rxn_i}	*Peak reaction location*
X_d	*Inner vortex core diameter*
X_w	*Outer vortex diameter*
X_t	*Length from dump plane to trailing edge of vortex*
X_l	*Length from dump plane to leading edge of vortex*

Greek Symbols:

$\dot{\varepsilon}$	*Vortex strain rate*
η_n	*Time-varying pressure amplitude of mode n*
ρ	*Density*
τ	*Thermocouple time constant*
τ_{d_i}	*Time delay from shedding to maximum in heat release*
τ_{id}	*Ignition delay*
τ_{max}	*Delay from injection of fresh charge to corresponding peak heat release*
τ_{mech}	*Mechanical delay (sub-delay of τ_{id})*
τ_{chem}	*Chemical delay (sub-delay of τ_{id})*
Ψ_n	*Mode shape of mode n*
μ	*Dynamic viscosity*
σ	*Stefan-Boltzman constant*
σ_a, σ_b	*Standard deviations of gaussian envelops used in model*

ϕ	*Mixture stoichiometry*
γ	*Ratio of specific heats*
$\eta_{Rayleigh}$	*Rayleigh efficiency*
$\theta_{p'-q'}$	*Phase difference between oscillatory pressure and heat release*
ω_n	*Frequency of mode n*
ϖ	*Average shedding frequency*
$\nu_{shedding}$	*Vortex shedding frequency*
λ	*Wavelength*

Notations:

$( )'$	*Fluctuating quantities*
$\bar{( )}$	*Averaged quantities*
$( )_{rms}$	*Root mean squared quantities*
$\langle \rangle$	*Ensemble-averaged quantities*
∇	*Gradient operator*
∇^2	*Laplacian operator*
$\frac{\partial}{\partial t}$	*Derivative with respect to variable t*

CHAPTER ONE
INTRODUCTION

1.1 INTRODUCTION TO PULSED COMBUSTION

Unsteady heat release within the confines of a reaction vessel is conducive to the excitation of system acoustic modes which may elevate oscillatory pressure magnitudes to unacceptable levels (combustion instabilities or pulsed combustion). These fluctuations, common to all propulsion systems, may attain sufficient amplitudes to cause excessive rates of heat transfer and/or vibrations, thereby undermining the system's integrity, reducing performance and/or causing failure (Culick, 1994).

Combustion driven oscillations were first observed in 1777 when Higgens placed a flame in a small, vertical tube and noticed it would "sing." Modern adaptations to this (Rijke Tube) yield predictable tones related to the longitudinal acoustic modes of the pipe excited and location of the flame within. Relative to conventional combustion systems, pulsed combustors have turbulent heat transfer rates and combustion intensities (volumetric energy release rate) far in excess of their steady, turbulent counterparts and reduced nitrogen oxide emissions by a factor of three. The general simplicity of many pulsed systems (self-aspirating) alleviates the need for air blowers and valves. Marked improvements in many industrial and chemical processes (pulverizing coal, for instance) are achieved through harnessing flow pulsations. Valveless L-Star combustors, fueled by either pulverized coal or natural gas are currently being developed for industrial and residential uses and are marked by a combustion chamber followed by an orifice. Such

genuine offshoots of combustion instabilities are generally undesired due to the inherent dangers they may invoke in systems not originally designed to withstand them.

Many high amplitude pressure oscillations have been observed in ramjet and turbofan systems with afterburners where flames are stabilized using flameholders (bluff bodies or sudden dumps). In such systems, periodic vortex shedding may occur due to the acoustic velocity fluctuations near the lip of the flameholder, resulting in periodic impingement of hot combusting gases on the combustor walls, thereby prematurely fatiguing engine components (see early design data for General Electric and Pratt & Whitney turbofan engines). Similar problems arise in solid and liquid propellant rockets where vortex shedding (primary feedback mechanism for continuation of the instability) arises from flow separation off baffles or other flow disturbances. Furthermore, longitudinal acoustic mode excitations which are more troublesome than their transverse counterparts ("screech instabilities") can interfere with the inlet shock system in ramjet engines causing performance losses and eventual failure.

Fuel and oxidizer supplies in liquid propellant rockets and fuel lines in industrial furnaces can also fluctuate due to unwanted pressure disturbances, resulting in growing pressure oscillations. The resulting oscillatory heat release, coupling to the system's acoustics, is typically thought to be primary feedback mechanism of such self-excited instabilities.

The multitude of pulsed systems used today (Helmholtz resonators, Schmidt and Rijke tubes), however, have a common underlying principal controlling their operation: the periodic addition of energy must be in phase with the oscillatory pressure oscillation or more precisely, the cyclic integral of oscillatory pressure and heat release must be positive.

Such a requirement, first formalized by Lord Rayleigh in 1878 and later adapted by Chu (Chu, 1965, 1956), is more commonly referred to as "Rayleigh's Criterion" and must be satisfied by all pulsed burners (Putnam and Faulkner, 1982). Despite the relative simplicity of the underlying principal, pulsed systems provide the researcher with a challenging environment: they are marked by highly complex, three-dimensional, transient and turbulent flowfields. Furthermore, nonlinear coupling and complex feedback associated with the interactions of the unsteady motions and combustion processes further complicates the issue. As such, considerable effort has been devoted to the understanding of combustion instabilities.

1.2 PREVIOUS WORK

After the initial discovery of unstable combustion in 1777, it was not until 1878 that Lord Rayleigh put forth his "Rayleigh's Criterion" explaining how energy may be added to the acoustic field. More intense research dwindled thereafter, and it was not until the nineteen-fifties that pulsed combustion received a revival of sort, however, some work was done earlier on Schmidt Tube propulsion devices of German V-1 bombs in Word War II (Sterling, 1987).

The observation that many propulsion chambers are cylindrical, permits the excitation of radial, transverse and/or longitudinal acoustic modes. High frequency oscillations or "screech" is associated with the excitation of transverse modes and was investigated by Rogers and Marble (Rogers and Marble, 1956). This instability was associated with asymmetric vortex shedding from V-shaped flameholders. Such self-excited instabilities have generally been controlled through the use of acoustic liners and

therefore pose less of a threat than their longitudinal, lower frequency or "rumble" counterparts (Hedge et al., 1986). Rogers and Marble did, however, provide insight into the roll vortices play in providing the necessary oscillatory heat release (feedback mechanism) to sustain the instabilities.

Investigations into longitudinal instabilities has been extensive. Davis (Davis, 1981) used high-speed cinematography to identify two modes of low frequency instabilities. The first mode showed the entire combustion zone underwent flow pulsations while in the second, periodic shedding of hot spots from the recirculation zone was observed. Heitor (Heitor et al., 1984) measured the frequency and strength of combustion induced oscillations for premixed $CH_4 - air$ mixtures stabilized behind baffles located along the axis of a closed-opened pipe. Smith and Zukoski (Smith and Zukoski, 1985) investigated instabilities in a dump combustor whereby large, vortical structures were periodically shed at one of the system's acoustic modes. The resulting unsteady combustion, later verified to be related to the impingement of the structures with the floor (Zsak, 1993; Sterling, 1987) was found to feed energy to the acoustic field, thereby continuing the pulsations. Earlier work (Keller et al., 1981), identified three modes of instabilities ("humming", "buzzing" and "chucking") and linked them to the action of recirculation zone vortices on the turbulent shear layer behind the step. The work revealed the importance of the fluid mechanics of the flame stabilization zone in the stability of the flowfield. Burning vortex structures which are capable of sustaining flow pulsations were investigated in other works (Kendrick et al., 1993; Bai et al., 1993; Zsak, 1993; Sterling and Zukoski, 1991; Zsak et al., 1991; Schadow et al., 1989; Sterling, 1987; Hedge et al., 1987; Poinsot et al., 1987; Hedge et al., 1986).

Longitudinal modes of the chamber can even be excited without combustion (Aaron, 1985) whereby the feedback mechanism for these "edgetone resonances" is due to the oscillatory forces resulting from vortex impingement.

Analytical work has also seen intense interest. A linear stability theory for liquid propellant rockets was developed by Crocco (Crocco and Cheng, 1956). Modeling employing kinetics of a stirred reactor was employed in some work (Yang, 1984; Ponizy and Wojcicki, 1984) while expansion of the system's acoustic modes into orthogonal modes was pioneered by Culick (Culick, 1992, 1976, 1975). His technique reduces the problem to a set of coupled oscillators for each of the modes present and allows for the implementation of many nonlinear effects (nonlinear gas dynamic effects, for instance). The method of characteristics was employed successfully by others (Tsujimoto and Machii, 1986; Ponizy and Wojcicki, 1984) to simulate more complex, pulsed burner geometries (Barr and Dwyer, 1991). Following the suggestions of F. E. Marble, one-dimensional acoustics have been used to predict system acoustic modes and eigenfrequencies (Zsak, 1993; Sterling, 1987; Smith, 1985) and by others (Crump et al., 1986) while more accurate one-dimensional modeling employing heat release distributions was also pursued (HA et al., 1992; Bhatia and Sirignano, 1991; Shyy and Udaykumar, 1990). Large Eddy Simulations or LES models were employed to capture the two-dimensional, hooked flame shapes observed in many unstable combustors (Menon and Jou, 1991, 1987) while vortex dynamics has also seen use (Najm and Ghoniem, 1993, 1991). The interaction between vortex structures, acoustic waves and chemical energy release was extensively studied by Kailasanath (Kailasanath et al., 1991) using a compressible, time-dependent, Flux-Corrected Transport Algorithm (Boris and Book, 1976).

Active control of combustion instabilities has logically seen much interest (Schadow et al., 1992; Menon, 1992; Fung, 1991; Poinsot et al., 1987) as well as investigations attempting to harness the improved heat transfer associated with flow pulsations (Arpaci et al., 1993; Eibeck et al., 1993; Dec et al., 1992; Dec and Keller, 1989; Park et al., 1982; Perry and Culick, 1974; Hanby, 1969).

1.3 OBJECTIVES OF THE PRESENT WORK

The objectives of the present work are as follows:

(1) Investigate the temporal and typically nonuniform development (ignition, convection and full combustion) of reacting vortex structures shed from a rearward facing step flameholder.

(2) Show how turbulent exchange mechanisms (fluid dynamics) tend to dominate their chemical counterparts in the ignition of the structures and, to a lesser extent, in the mode selection process (what combustor acoustic mode is excited).

(3) Investigate how vortices interact with the lower wall and detail how this impingement greatly enhances the turbulent mixing and eventual combustion of the structures.

(4) Use simple numerical techniques to reinforce conjectures about the mode selection process and detail the importance of the shape of the heat release profile.

(5) Infer from a rigorous analysis of three transitional cases (a sequence of runs exhibiting a distinct switch in vortex shedding frequencies - mode shift) how geometry also plays a fundamental roll in the mode selection process as it typically dictates when combustion occurs.

The typical diagnostic tools (pressure transducers, hot-wires, thermocouples, spark shadowgraph and instantaneous chemiluminescent imagery) are supplemented with two other techniques, essential in detailing the quasiperiodic flowfields seen here: high-speed shadowgraph and chemiluminescent imagery. These two nonintrusive techniques allow for a complete fluid dynamic and combustion description of the unstable flowfield which has typically been neglected in pulsed combustion work.

Chapter Two presents the experimental apparatus and diagnostic techniques that were used in the experiments. Chapter Three presents the bulk of the experimental results, detailing in particular the temporal growth characteristics of the convecting structures for runs of various flow speeds, fuel stoichiometries and geometries. It will be seen that prior structures influence, to some degree, the ignition times and times from when a vortex is shed to when one sees its corresponding peak rate of combustion. The interaction of the structures with the floor will also be examined through floor temperature and heat flux measurements. The creation of local "hot spots" (areas of intense temperature and heat flux) will be observed in areas near the vortex impingement location. The temporal growth rate of vortex temperatures will be investigated using fine-wire thermocouples, as well as the overall duct temperature distributions to outline the nonisentropic temperature fields existing within the duct.

Chapter Four will formulate theoretically and numerically why particular acoustic modes are excited relative to others for a given set of run parameters. The final chapter, Chapter Five, summarizes the findings of the investigation and presents concluding remarks about the nature of the observed instabilities.

CHAPTER TWO
DIAGNOSTICS

2.1 EXPERIMENTAL APPARATUS

The present experiments were carried out in a pulsed combustion facility more commonly referred to as a dump combustor whereby the flow issues or "dumps" over a rearward facing step flame holder into a larger chamber. The combustor was identical to that used by Zsak (Zsak, 1993) but differed somewhat from past Jet Propulsion Center (JPC) researchers (Sterling, 1987; Smith, 1985) in its adjustable floor and overall dimensions.

Figure 2.1 depicts the overall layout of the facility. Air and methane are brought together near the entrance of the plenum chamber after first being separately controlled by dome regulators and sonic nozzles enabling mixtures of any stoichiometry (ϕ) to be used. The two flows then mix and enter the axisymmetric plenum chamber either axially through a moveable, rotating, slotted device know as a siren (used to initiate instabilities for large duct heights (Zsak, 1993)) or tangentially further upstream. The flow is further mixed and straightened after passing through a series of flat and/or conical screens located within the plenum chamber. Consult *Figure 2.2*. The plenum smoothly contracts from a diameter of 15 *cm* to a rectangular inlet section measuring 2.54 *cm* high by 7.62 *cm* wide by 43 *cm* long. Near the end of the inlet section, the flow encounters a parabolic shaped lift which further restricts and accelerates the flow as it exhausts into the sudden expansion of the combustion chamber. This sudden expansion, commencing at the "dump plane," is more

commonly referred to as a flame holder since it serves to anchor flames having burning velocities much lower than the oncoming approach flow.

Measuring 83 *cm* long by 7.62 *cm* wide, the water cooled combustion chamber has seven floor and ten ceiling mounted access ports for pressure taps, thermocouples, heat gauges, etc. The adjustable combustor chamber height (2.54 to 15 *cm*) permitted creating vortices of varied sizes and allows the observer to investigate the geometric influence of the lower wall on the flow field. Optical access to the combustion chamber was achieved by replacing the 15 *cm* square, water cooled side panels with either 15 or 30 *cm* long Vycor glass windows. A spark igniter placed either on the floor or on the vertical "dump plane" wall served to initiate combustion. Once the combustion was started, the spark was removed and the recirculating hot products immediately downstream of the rearward facing step served to ignite subsequent cold gas mixtures. A variety of $CH_4 - air$ mixtures were investigated ranging in ϕ from 1.0 to 1.7 and in velocity (as measured directly over the step) from 21 to 35 *m/s*.

2.2 DATA ACQUISITION

Normal data acquisition was accomplished using a fully integrated hardware and software Computerscope ISC-67 system furnished by RC Electronics. The system consisted of a 16-channel A/D board, an external Instrument Interface and Scope Driver installed on a Zenith ZW-241-82 AT-compatible computer. Sixteen channels of data may be used at an aggregate sampling rate up to 1 *MHz*. Digital conversion is implemented with 12 bit accuracy over an input range of +/- 10 *volts*. A typical run acquiring 4 samples of data (pressure, velocity, intensity and a trigger signal) was typically sampled at 80 μs

(12.5 *KHz*) and for 0.655 *s*, thus allowing approximately 150 cycles of pressure or vortex shedding to be analyzed.

2.3 PRESSURE INSTRUMENTATION

Consistent with past JPC researchers (Zsak, 1993; Sterling, 1987; Smith, 1985), PCB model 106B piezoelectric pressure transducers were used to measure the oscillatory pressure within the combustion chamber. Mounted in small, water-cooled cavities along the upper wall to protect them from the high pressures and temperatures associated with combustion, the gauges had good signal to noise ratios and a sensitivity of 4410 *mV/atm*. The cavities were designed by Smith (Smith, 1985) such that their resonance frequency (5500 *Hz*) would be well above any acoustic frequency of the duct and that there would be no phase or magnitude adjustments for frequencies below 800 *Hz*. Typically one transducer was employed and it was located in the upper wall of the chamber, 12 *mm* downstream of the dump plane.

2.4 HOT-WIRE ANEMOMETRY

A constant temperature hot-wire anemometer (TSI model 1210-T1.5) placed either 3.2 or 6 *cm* upstream of the dump plane was employed to measure the flow velocity as the mixture issued into the combustion chamber. This velocity is referred to as V_{dump}. The circuitry was designed by Sobota (Sobota, 1987).

2.5 FINE-WIRE THERMOCOUPLES

Essential in understanding more of the structure and dynamics of premixed turbulent flames is the determination of accurate scalar fields as temperature. Both time-averaged and time-resolved thermocouple measurements were undertaken to examine more closely the ignition and quenching mechanisms on the reacting structures. The time-averaged measurements were done using uncoated, R-type, 25.4 μm diameter, thermocouples purchased from Omega while the time-resolved values were obtained using coated, S-type, 7.62 μm diameter, thermocouples manufactured by Tayco Engineering.

Recent advances in laser technology can conceivably provide nonintrusive and accurate measurements but are typically achieved at the expense of high costs and complex set-ups (Dec and Keller, 1990). Fine-wire thermocouples provide the cheap alternative but are not themselves without problems. Four problems typically plagued the thermocouple measurements: measurement bandwidths are typically limited to a few tens of *hertz* (due to the thermal inertia effects of the junction), they act as flow disturbances, they induce radiation errors and finally, may cause catalytic errors if made from highly reactive metals as platinum and if used in oxidizing environments characteristic of combustion flowfields (Miles and Gouldin, 1993). Use of some corrective techniques, however, will lessen some of the above problems.

Reducing the size of the thermocouple can minimize its influence as a dominant flowfield disturbance while knowledge of accurate, high-temperature metal properties - typically hard to find - can alleviate radiation effects. Furthermore, coating thermocouple junctions with an inert substance as silica (Fristrom and Westenberg, 1965) can reduce or even eliminate the catalytic effect which would tend to overestimate the measurement. It is

the thermal mass of the junction, however, that is the most critical obstacle in thermocouple use.

Compensated thermocouples (measurements corrected for thermal lag) to obtain temporally-resolved statistics in heated air flows (Talby et al., 1990; Hopkins et al., 1989) is considered well established (Miles and Gouldin, 1993). Similar techniques used in turbulent flames are suspect due to the variation in the thermocouple's time constant caused from local fluctuations in the flowfield's velocity, temperature and composition (Cambry, 1986; Nina and Pita, 1985). Examples of using compensated fine-wire thermocouples in studies of premixed turbulent flames include investigations of flame wrinkling (Yoshida and Tsuji, 1982, 1984) and heat transfer (Heitor et al., 1984; Chandran et al., 1984; Samuelson et al., 1984). The usual practice is to use one, global time constant which is valid for all fluid velocities, temperatures and compositions. Improvements to this practice have yielded instantaneous time constants where temperatures are measured simultaneously with velocities. Because these time constants are typically determined from heat transfer correlations which may be invalid under premixed flame conditions (Miles and Gouldin, 1993), these measurements are, too, not without error.

In the current experiments, a single mean time constant was chosen for the "time-resolved" measurements.

2.5.1 Theoretical Analysis of a Thermocouple

For a cylindrically modeled thermocouple junction immersed in a hot combustible gas surrounded by cooler walls, the energy balance is (Nina and Pita, 1985):

$$\frac{1}{4}c_p \pi d^2 \rho \, dx \frac{dT_j}{dt} = \pi d \, dx \, h\left(T_j - T_g\right) - \frac{1}{4}\pi d^2 k \frac{d^2 T_j}{dx^2} + \pi d \, dx e\sigma\left(T_j^4 - T_w^4\right) + \pi d \, dx q_{cat} \tag{2.1}$$

where c_p, d, ρ, k and e are the specific heat, diameter, density, thermal conductivity and emmissivity of the junction thermocouple, respectively. T_j, T_g, and T_w are the temperatures of the thermocouple's junction, hot gas (what is desired) and cold surrounding walls, respectively. Finally, h, σ, and q_{cat} are the forced convection coefficient, Stefan-Boltzman constant and rate of catalytic heating per unit area, respectively. The first term on the right hand side details the energy transfer due to forced convection between the hot gas and cooler thermocouple, the second term denotes axial conduction along the length of the wire due to uneven heating along the junction, the third term is the radiative exchange between the junction and cool walls and the fourth term is the heat source due to catalytic effects between the highly reactive platinum and flowfield constituents. Implicit in the above analysis is the absence of any radiative heat flux between the thermocouple and the hot gases which is typically valid for "clean" gases (Bradley and Mathews, 1968). In addition, the cool walls are assumed to be isothermal which is typically not the case.

The catalytic effect can be reduced or eliminated by coating the thermocouple with a non-catalytic substance such as silica (Miles and Gouldin, 1993; Yoshida, 1986) or beryllium and yttrium oxides (Chandran et al., 1984). For the measurements which used coated thermocouples, the coating was applied by simultaneously wafting the

thermocouple in a bunsen burner flame while spraying silicone oil into the flame (Fristrom and Westenberg, 1965). The coating was typically reapplied after each run to ensure its integrity and the longevity of the delicate junctions. Consult *Figure 2.3* for a comparison of one coated and one uncoated, 7.62 μm diameter, S-type thermocouples placed 5.08 and 10.16 *cm* downstream of the dump plane, respectively. The top trace is the pressure, the middle one is the coated thermocouple while the bottom trace is the uncoated one. Even though the trace of the coated thermocouple is slightly smoother due to its increased thermal inertia, it is still capable of tracking the cyclic temperature fluctuations when compared to the pressure signal.

Choice of such small diameter thermocouples was also done to substantially reduce conduction errors which could also undermine the measurements. With the above problems addressed and assuming the cool wall temperature is much smaller than the junction temperature, $T_w^4 << T_j^4$, one may write (Miles and Gouldin, 1993):

$$T_g = \left(1 + \tau \frac{d}{dt}\right) T_j + \tau \left(\frac{4e\sigma}{\rho c_p d}\right) T_j^4 \tag{2.2}$$

where the thermocouple time constant, τ, is given by:

$$\tau = \frac{\rho c_p d}{4h} \tag{2.3}$$

The first term in equation (2.2) represents the correction due to a constant thermal time lag while the second is the correction due to radiation. The problem now reduces to determining τ and the other high temperature platinum properties. The coefficient of

specific heat, c_p, was found to obey a linear fit in the temperature range $600 < T_g < 2000$ K (Touloukian, 1967). Values of hemispherical emmissivity for platinum can be found in the literature (Bradley and Entwistle, 1966; Davisson and Weeks, 1924) but another approach is to use empirical fits based on electromagnetic theory (Davisson and Weeks, 1924). The latter was the approach used here. The catalytic coating is fairly transparent to high temperature, short wavelength radiation so no correction to e was made (Bradley and Mathews, 1968).

The final and most important parameter sought is the thermocouple time constant. Much effort has been done in this area (Petit et al., 1982; Yule et al., 1978; Odidi, 1974) and new techniques are still being tried (Miles and Gouldin, 1993). The general practice is to heat the thermocouple up to some temperature T_o and to watch its decay on an oscilloscope. It should be noted that $\tau = \tau(t)$ due to the dependence of the convective coefficient on temperature and flow velocity. The time constant for the present thermocouples (7.62 μm diameter) was found by applying a 2 Hz amplified rectangular wave form to the thermocouple and recording the temperature decay on RC Electronics during the downgoing edge of the pulse (consult *Figure 2.4*). Accuracy was improved by sampling at 100 KHz and over several dump plane speeds, $21 \le V_{dump} \le 35 m/s$, and initial temperatures, $400 \le T_o \le 2000 K$. A sample decay curve and results for a V_{dump} of 30 m/s are found in *Figures 2.5* and *2.6*, respectively. Since a single, global time constant was desired, all results were averaged yielding an average time constant of 0.44 ms. The conversion of the raw signal to the final gas temperature-time trace was therefore straightforward: the voltage trace was first smoothed (*Figure 2.7*) to ensure accurate evaluation of its derivatives, then processed by a program to perform the operation of equation (2.2).

Figure 2.8 shows a sample signal before and after application of equation (2.2) and shows the small error (phase and amplitude) made in using no compensation for this small sized thermocouple.

2.6 SINGLE-SHOT INTENSIFIED CAMERA IMAGES AND SHADOWGRAPHS

An instantaneous description of the fluid dynamics and combustion occurring within the duct is provided by the simultaneous use of a spark shadowgraph system and Charge Injection Device (CID) camera.

Time-resolved chemiluminescence measurements were acquired from a General Electric TN2505A solid-state CID camera (*Figure 2.9*) which divides the flow into an array of 360 by 240 pixels of 8 bit resolution. Consult *Figure 2.10* for the spectral response of the camera. No interference filters were used so that all broad band radiation was captured including the primary emission bands for $CH_4 - air$ mixtures (Bulewicz, 1967): C_2 (516.5 *nm*), CH (431.5 *nm*) and OH (306.4 *nm*). Based on past combustion research (Samaniego et al., 1993, 1991; Barr and Keller, 1991; Tang et al, 1991), local heat release rates were derived from chemiluminescence measurements of spontaneous radicals within the flame. The physical basis for this linear relationship between heat release and broad band radiation is that the chemiluminescence of the flame is proportional to the rate of production of excited molecules (Sterling, 1991). For a fixed stoichiometry, the linearity has been proven satisfactory for both laminar and turbulent flames (Hurle et al., 1968; Diederichsen and Gould, 1965; Clark and Bittker, 1954).

A Poynting Products PC-170 programmable frame grabber board with Silicon Video software is used in conjunction with the CID camera to interface it with the Zenith AT computer. The typical mode of operation is to take a snapshot of the reacting flowfield at an exposure time of 15 - 60 μs after a prescribed delay from the positive-going zero-crossing of the pressure signal measured near the dump plane. The delay circuit was designed by Zsak (Zsak, 1993). The intensified images were stored in binary format and were thereafter processed and displayed using the software package PV-WAVE.

Fluid dynamic features of the reacting flowfield were captured using a standard Z-configuration shadowgraph arrangement with a Polaroid camera and 2 μs spark-gap light source. Two 30 *cm* diameter parabolic mirrors were employed to capture the 30 *cm* duct length representing the observed combustion extent. Use of both the CID camera and shadowgraph arrangement simultaneously was achieved by inserting a 60% transmittive/40% reflective beam splitter into the optical system to allow visualization by both techniques. Consult *Figure 2.11*. A typical run entailed taking a shadowgraph image at a certain instant in the pressure cycle then waiting approximately 15 μs (so the light from the spark would not interfere with the CID image) before taking a CID image. The images were sufficiently sharp to discern the important flowfield features. The technique provided the author with a typically undocumented resource which revealed the instantaneous fluid dynamic and combustion processes in the flow.

2.7 FLOOR THERMOCOUPLES

R and J-type coaxial thermocouples manufactured by Medtherm Corporation were flush mounted with the water-cooled floor to assess the vortex/floor interaction. The 0.8

mm diameter thermocouples were spaced at 5.08 *cm* increments in access ports along the centerline for the floor as shown in *Figure 2.12*. The two R-type thermocouples were placed near the vortex impingement location while the remaining J-types took up the other positions. The junction between the two dissimilar metals was formed by smoothly scribing the surface with a razor blade under a microscope. A cold junction bath and high signal to noise amplifiers completed the measurement system. See *Figure 2.13* for a sketch of a typical thermocouple.

2.8 FLOOR HEAT FLUX GAUGES

To more fully quantify the vortex/floor interaction, time-averaged floor heat flux measurements were undertaken using Rdf Micro-Foil Heat Flux Sensors (models 20453-1 and 27036-1). A separate stainless steel floor was machined so that the gauges could be directly adhered to the floor to minimize thermal losses. The gauges utilize a polyimide film (Dupont Kapton) thus rendering them extremely thin and inexpensive. The gauges were glued directly to the floor using a highly thermally conductive and high temperature epoxy known as Omegabond 200. *Figure 2.14* depicts their placement along the centerline of the floor.

2.9 HIGH-SPEED SHADOWGRAPHS

The same Z-configuration shadowgraph system that was used for the CID/Shadowgraph images was employed to film high-speed movies of the reacting vortices. Such cinematography would allow any cycle-to-cycle variations to be captured

which would have been impossible with the techniques discussed previously. The high-speed camera was a Hycam, 16 *mm* rotating prism unit framing at around 5100 pictures per second. By placing timing and event markers on the film, the images were accurately related to their pressure, velocity or photomultiplier traces. For the time-resolved thermocouple measurements, for instance, a high-speed movie was taken simultaneously with the acquisition of the temperature data. After approximately 12 *m* of film had passed (the approximate time for the film speed to remain relatively constant), a triggering signal was sent to start the data acquisition system and to the film itself. Timing blips were also imprinted on the film at 1000 *Hz* to determine its speed throughout the data acquisition time. *Figure 2.15* shows a photograph of the Hycam camera. The exposure time of each image is the inverse of the framing rate, thus rendering them less sharp than their single-shot counterparts.

2.10 HIGH-SPEED CCD IMAGERY

The knowledge that the present reacting flowfield is highly aperiodic due to competing acoustic frequencies hints that more quantitative high-speed filming techniques are warranted. The single-shot CID images are satisfactory for instantaneous measurements or for characterization of a repeatable cycle, but fail if the flow is highly nonuniform and noncyclic. To capture the temporally developing ignition and combustion on the reacting structures, a high-speed Charged Coupled Device (CCD) imaging system was employed from the Kodak Company. The Ektapro Image Intensifier System consisted of an intensified imager, a controller and the Ektapro processor (TR1006). The Intensified Imager was a standard Ektapro Imager modified by the addition of an image intensifier assembly. The controller was used to control the gate and gain functions of the

Intensified Imager. Consult *Figure 2.16* for a diagram of the two-stage intensifier. The photocathode is formed by a thin layer of photoemissive material on the inside surface of the first-stage intensifier tube. The lens focuses the image on the photocathode which emits an electron each time a photon strikes its surface. The electrons from the photocathode are drawn through and multiplied by the micro channel plate (MCP). The electrons leaving the MCP excite a phosphor screen recreating the image that was on the photocathode. A standard Nikon lens was used in all experiments and gating was set to 15 μs to sufficiently freeze the flow. Gain was set so as not to saturate the intensifier and all runs having different gain setting were corrected for by normalizing their average images by their respective power output values. Two channels of data (pressure and velocity) were superimposed on each image.

The camera had a framing capacity from 30 to 6000 images per second, gate limits from 10 μs to 5 *ms* and an input spectral sensitivity from 440 to 700 *nm* (Consult *Figure 2.17*). Framing rates greater than 1000 *Hz* relied on "split framing" the 239 by 192 pixels (8 bits per pixel) array into smaller vertical chunks. Framing at 2000 *Hz*, for instance, is accomplished by reducing the vertical resolution in half such that a 239 by 96 array is only available. The long aspect ratio of the duct made this technique acceptable.

A typical run entailed starting the facility, setting the Ektapo system in the trigger mode, engaging the trigger and then storing the images in the Ektapro processor at either 3000 (7.62 *cm* duct), 4000 (5.08 *cm* duct) or 6000 (2.54 *cm* duct) *Hz*. After the run, 500 to 1200 images (depending on memory space) were downloaded to a 33 *MHz* - 486 Micro Q PC computer via an AT-GPIB board. The images were then processed using in-house software as PV-WAVE. *Figure 2.18* depicts the complete layout of the system.

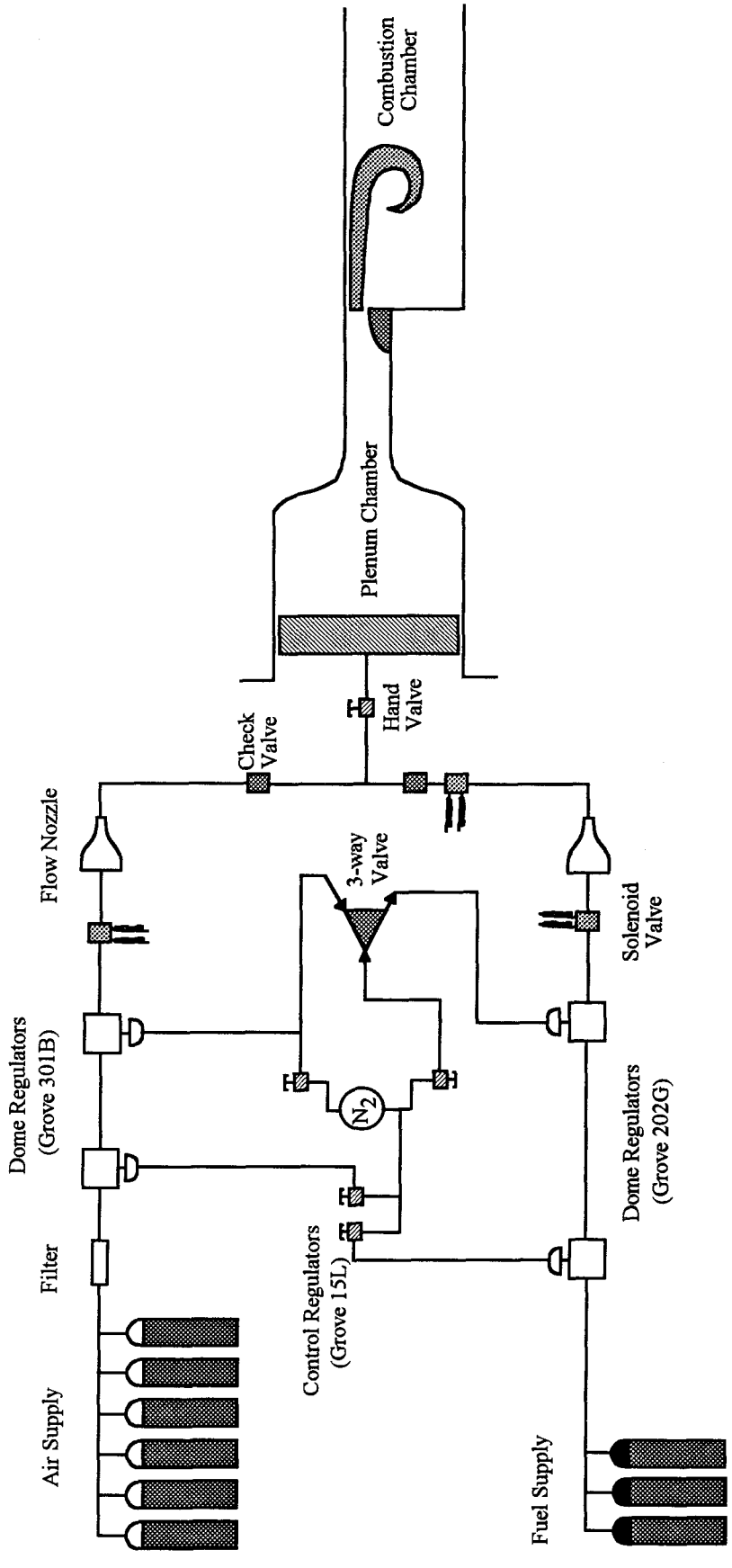

Figure 2.1: Overall view of laboratory dump combustor facility.

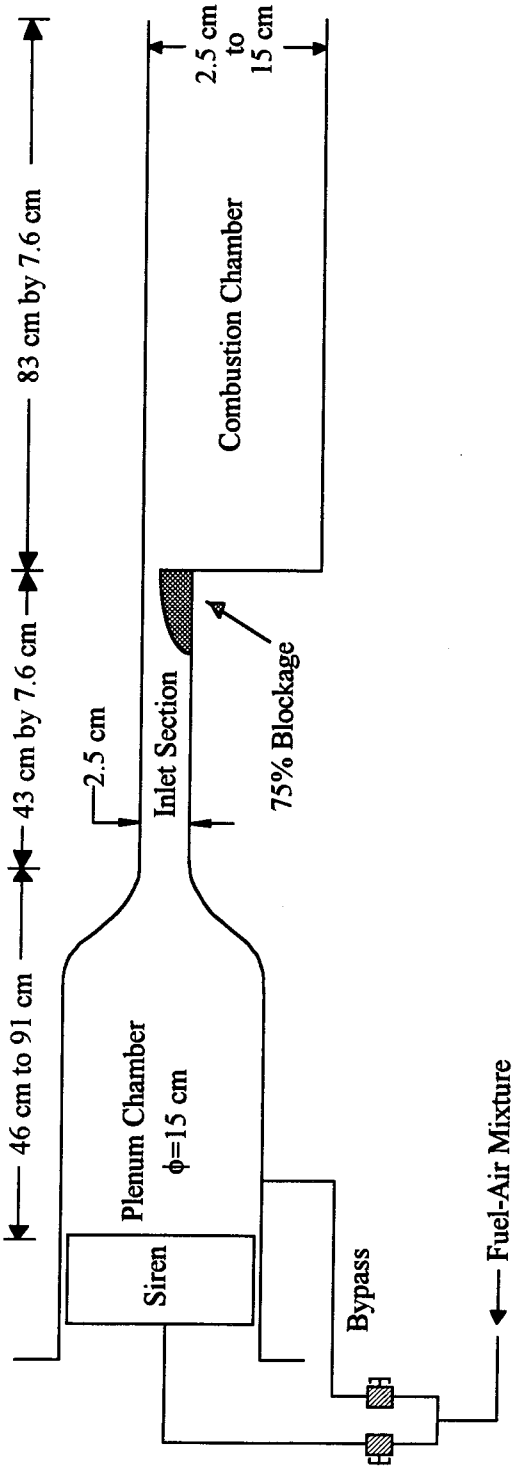

Figure 2.2: Diagram of experimental apparatus.

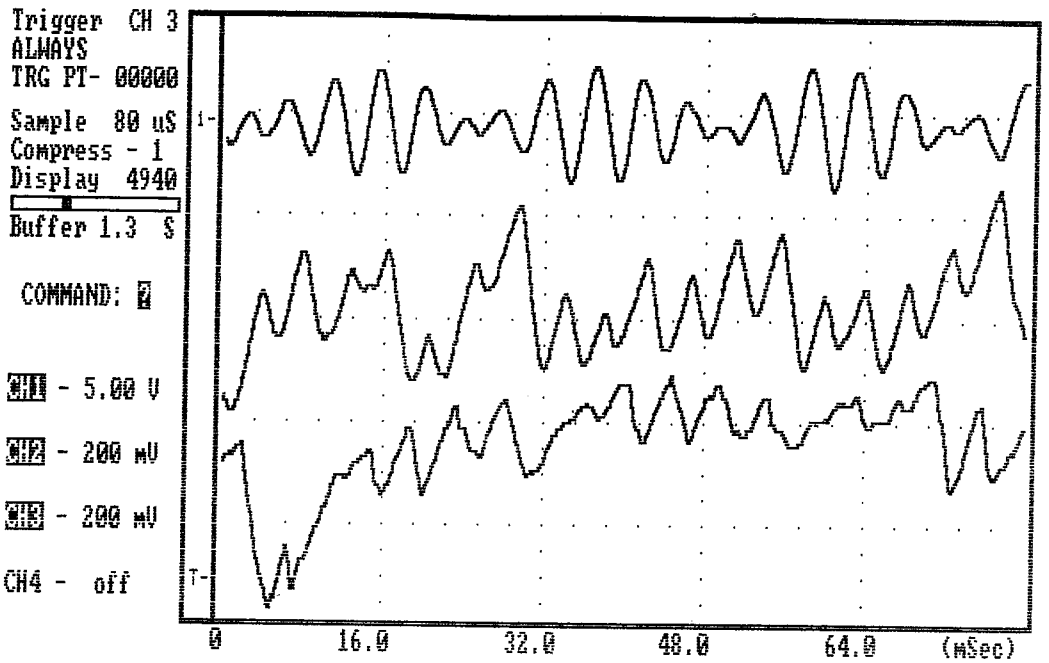

Figure 2.3: Coated (middle curve) and uncoated (bottom curve) temperature traces together with pressure signal (top curve).

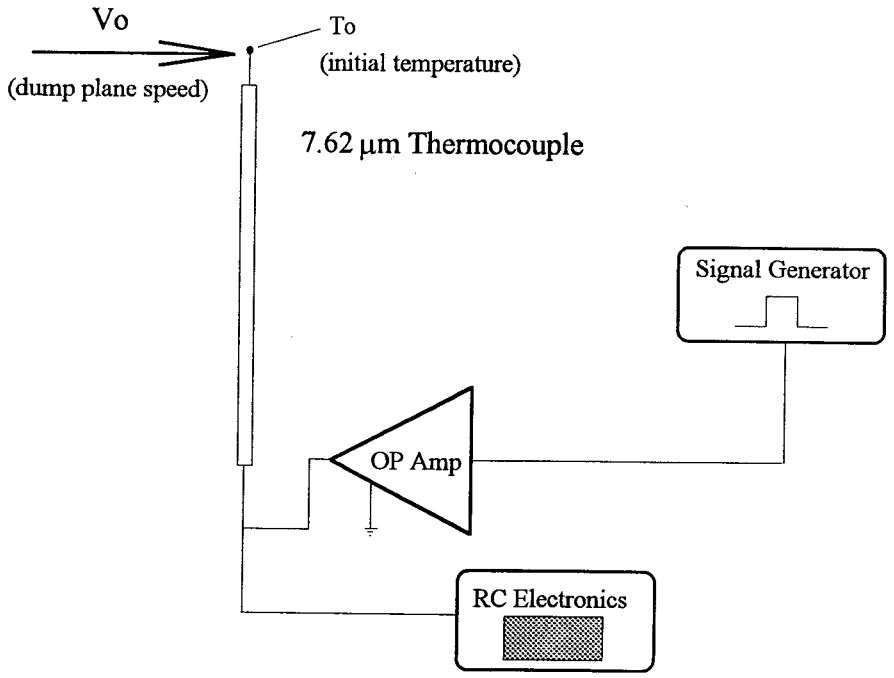

Figure 2.4: Circuit to determine thermocouple time constants.

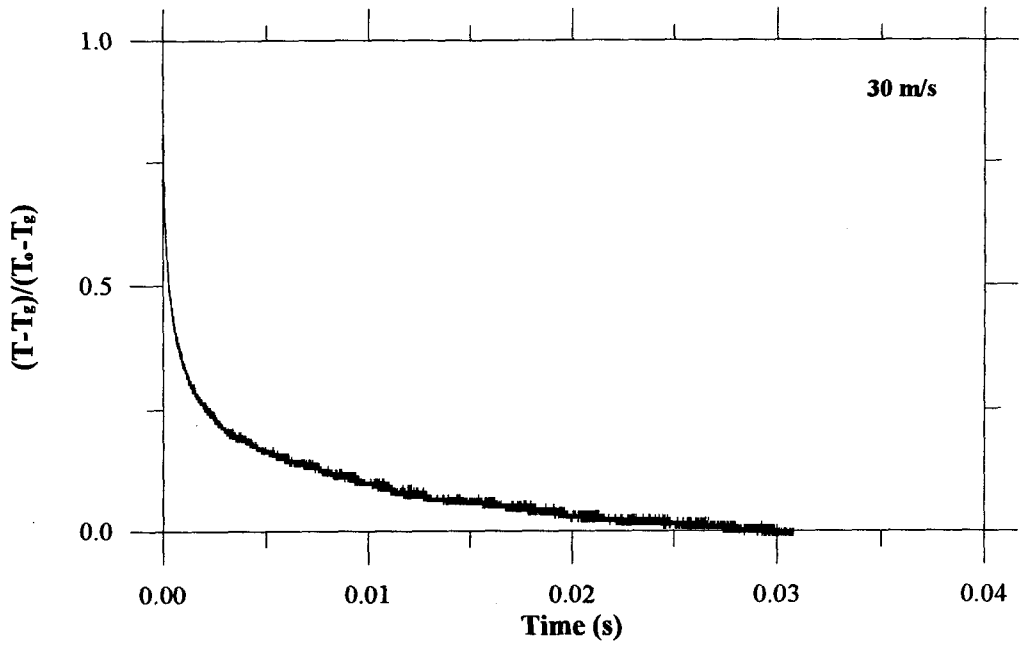

Figure 2.5: Sample decay curve after heating 7.62 μm thermocouple to temperature T_o in surrounding air at temperature T_g.

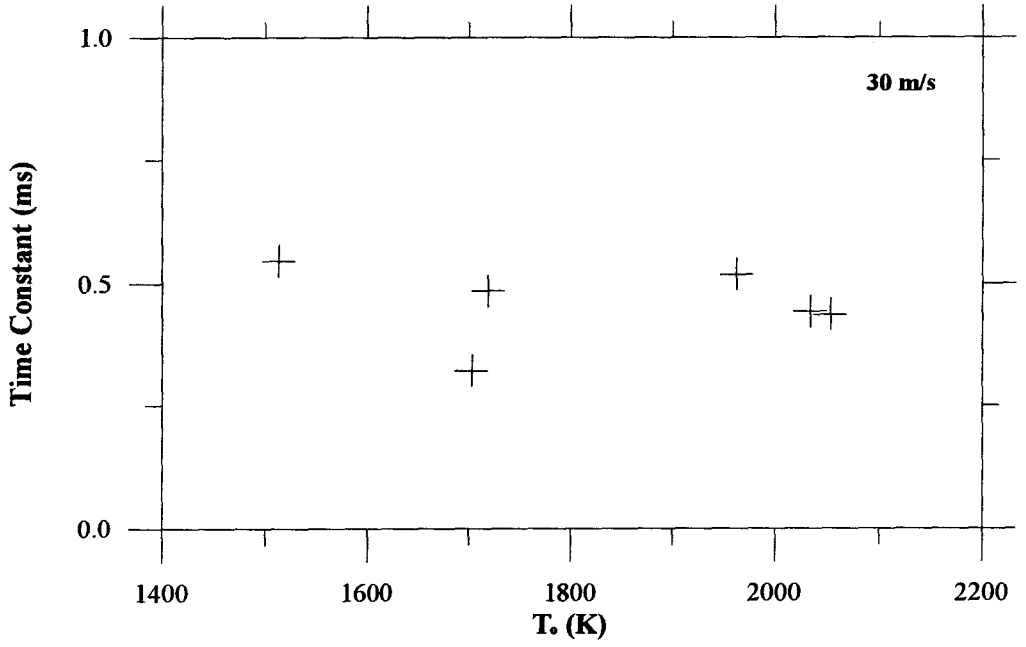

Figure 2.6: Time constant results for a variety of initial temperatures, T_o, at a V_{dump} of 30 m/s.

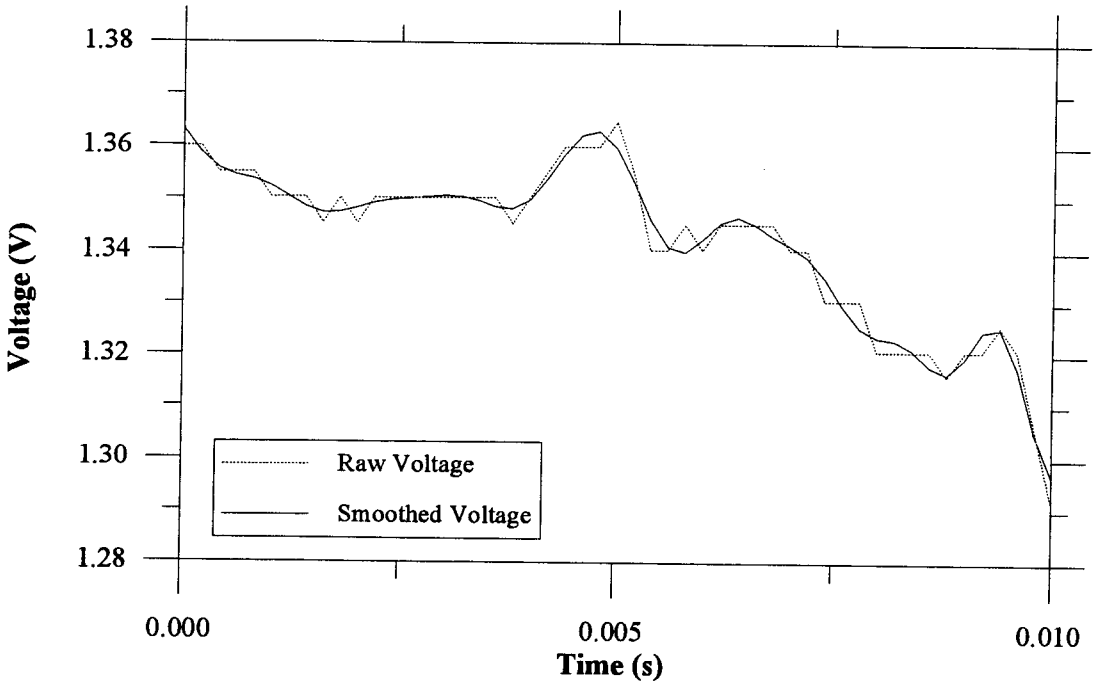

Figure 2.7: Raw and smoothed temperature trace (0-1000 Hz bandwidth).

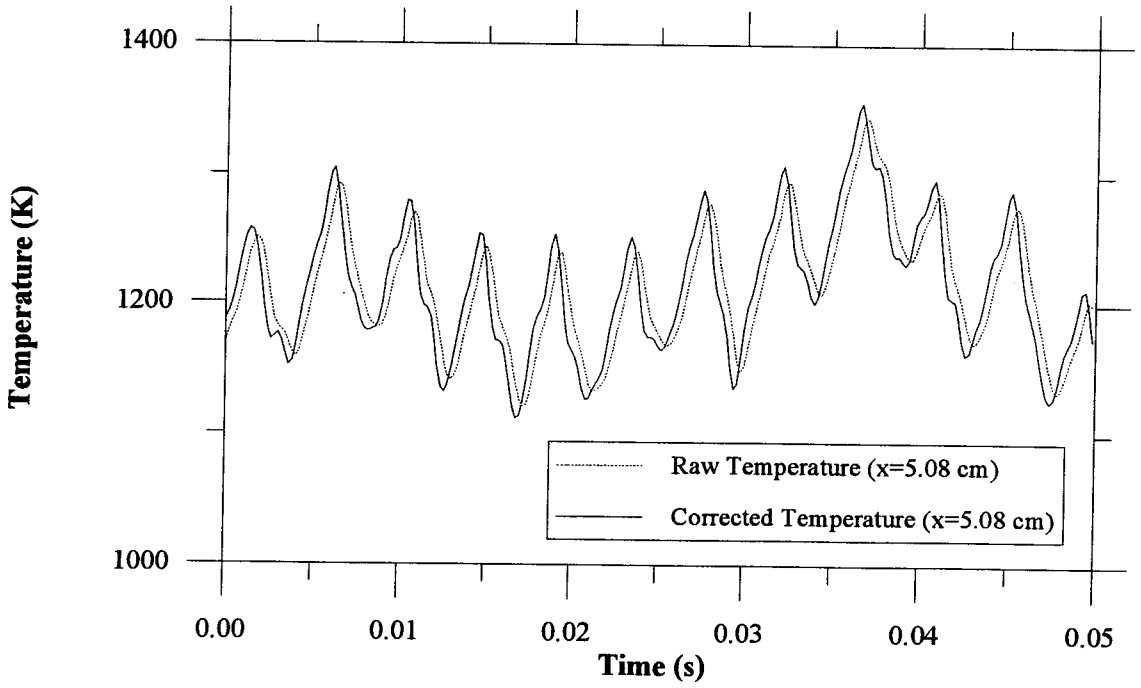

Figure 2.8: Raw and corrected (radiation and thermal lag) temperature traces.

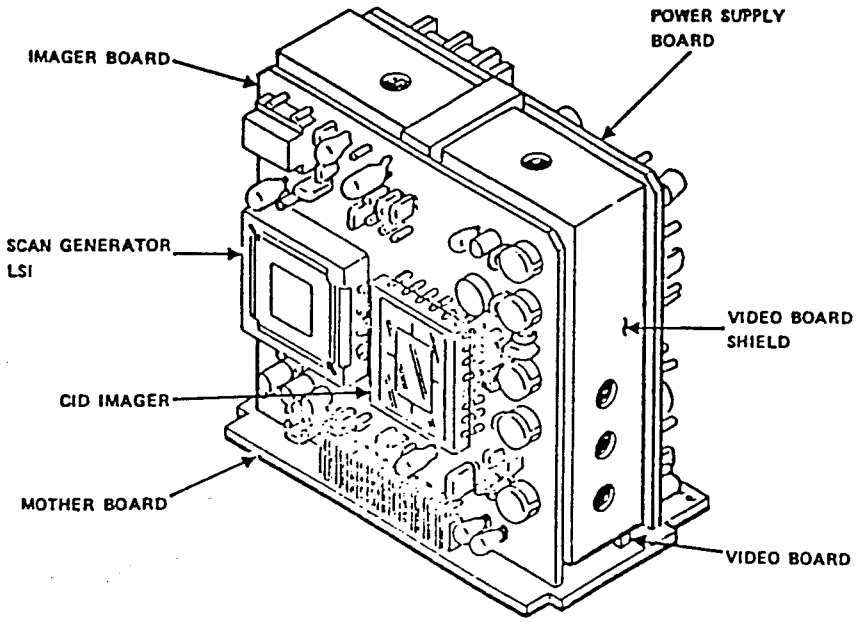

Figure 2.9: Diagram of CID camera from General Electric Company.

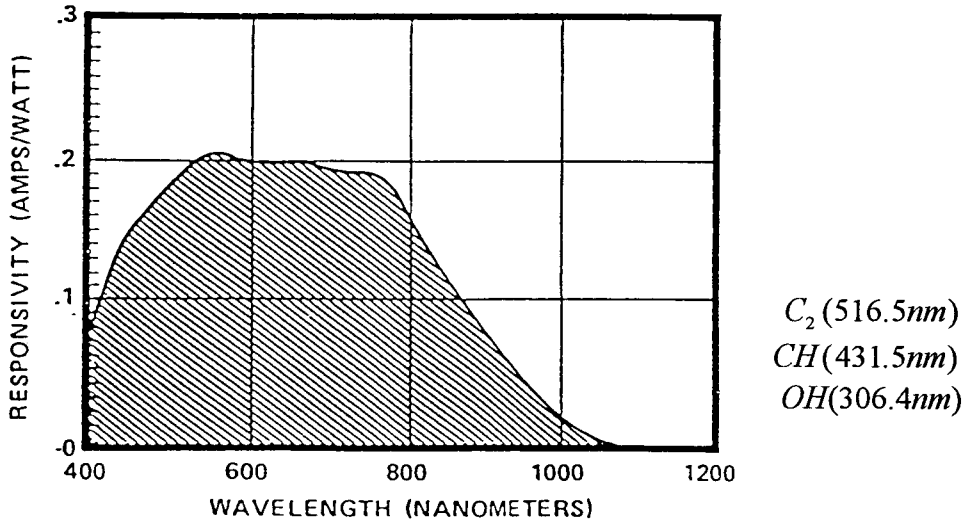

Figure 2.10: Spectral response of CID camera.

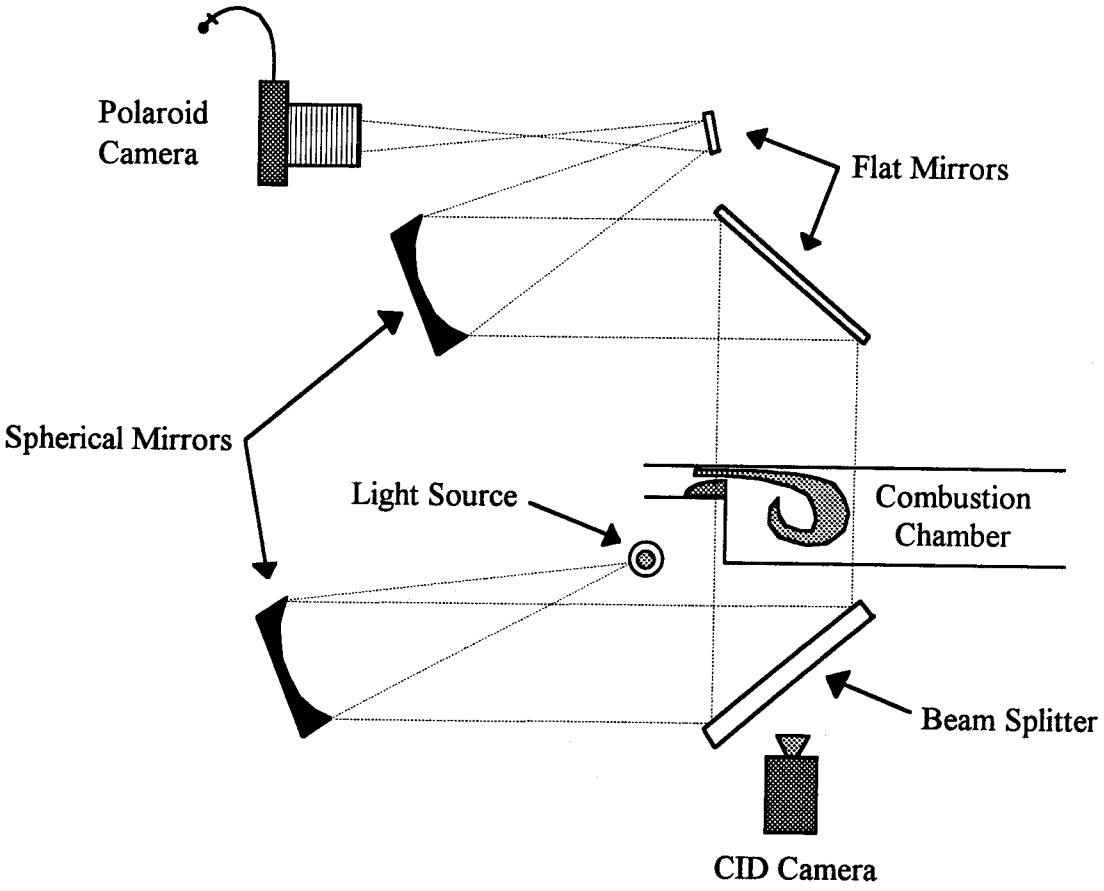

Figure 2.11: Optical arrangement for flow visualization.

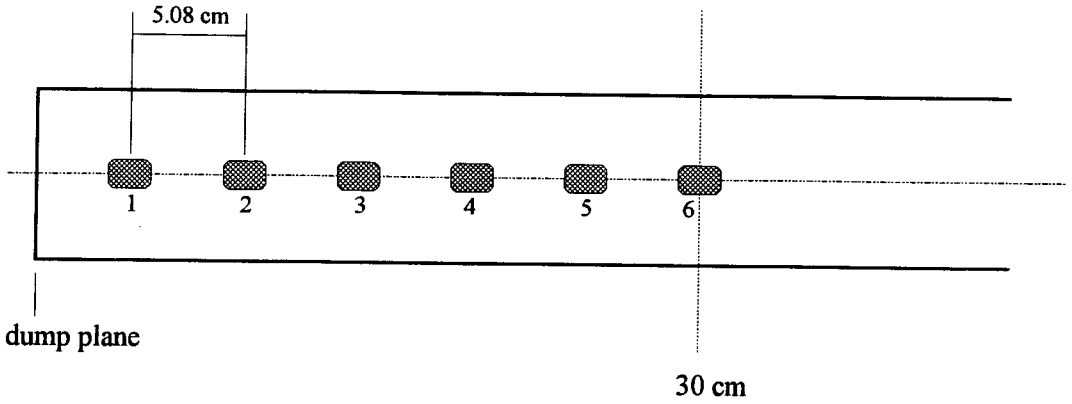

Figure 2.12: Placement of the Medtherm coaxial thermocouples.

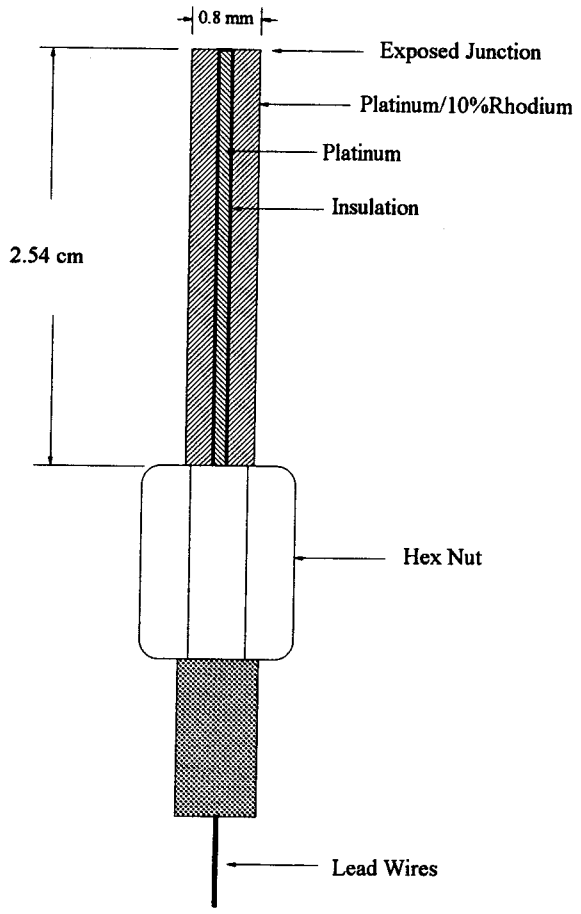

Figure 2.13: Diagram of a coaxial thermocouple.

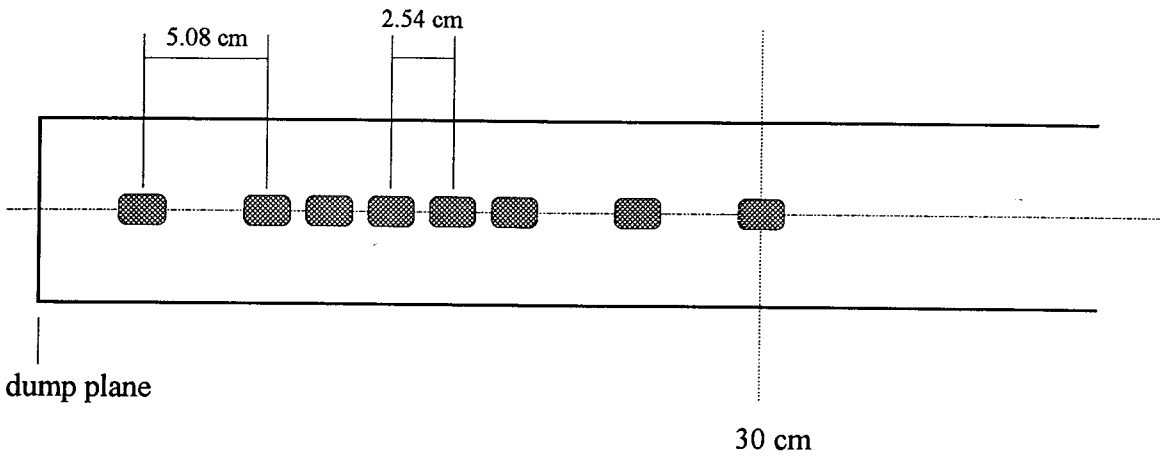

Figure 2.14: Placement of heat flux gauges.

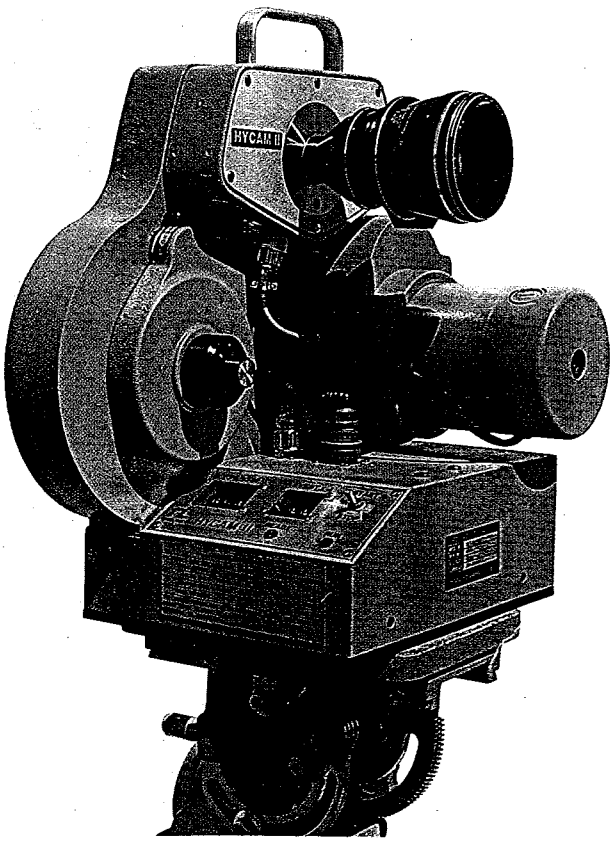

Figure 2.15: Diagram of Hycam Camera.

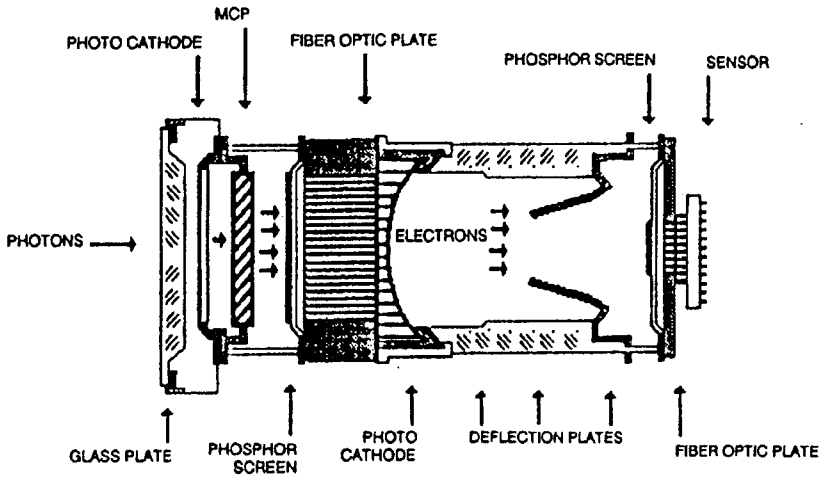

Figure 2.16: Diagram of two-stage Image Intensifier.

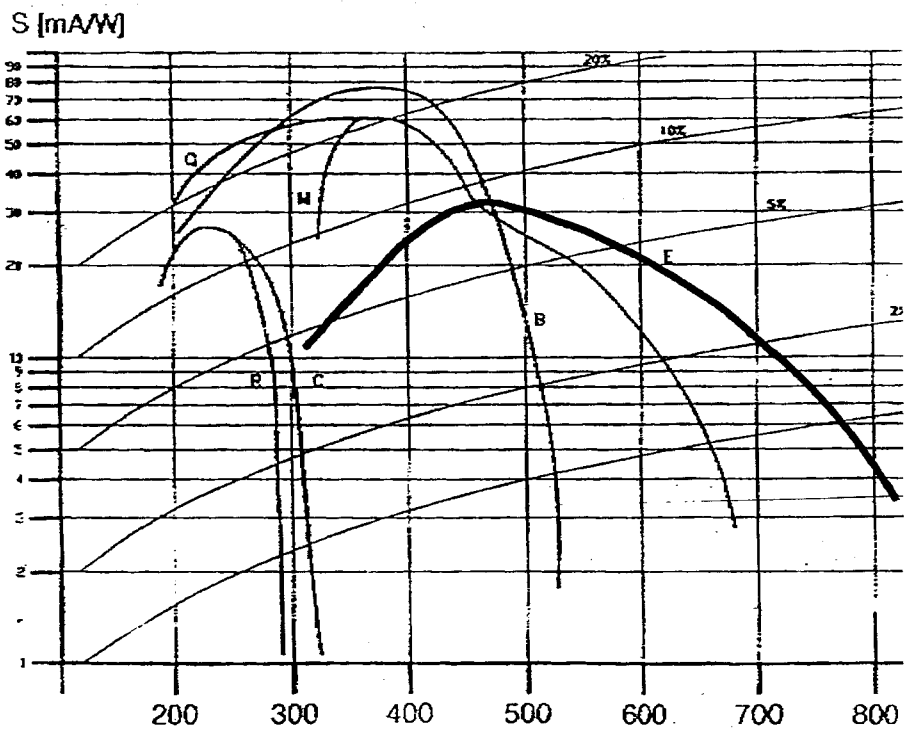

C_2 (516.5*nm*) CH(431.5*nm*) OH(306.4*nm*)

Figure 2.17: Spectral response of the CCD Kodak Camera (see ***curve E****).*

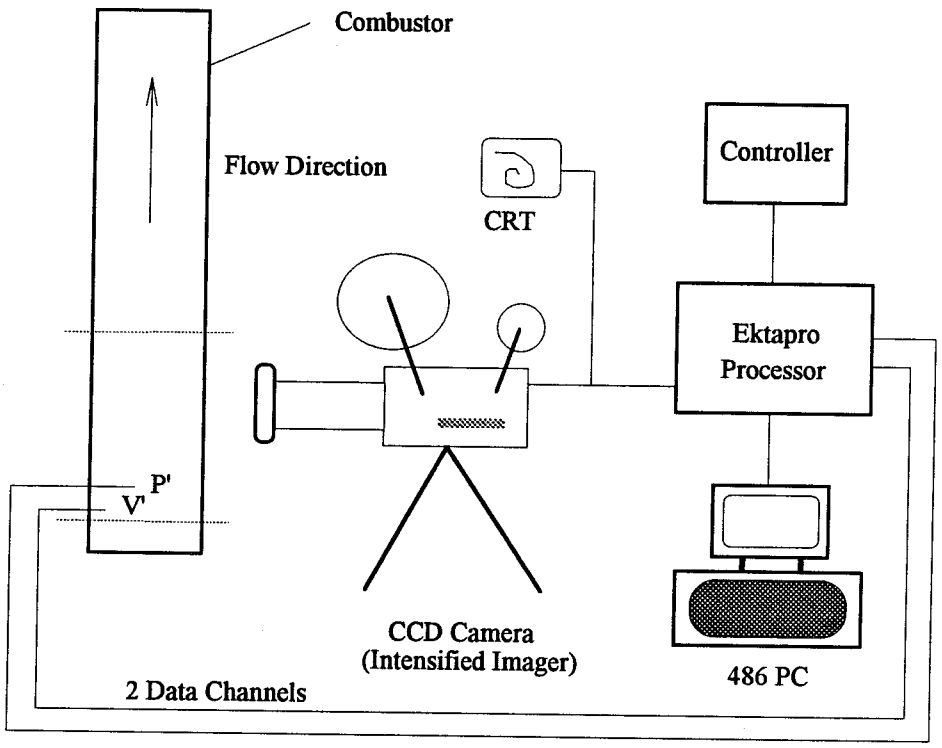

Figure 2.18: Layout of the high-speed Kodak CCD system.

CHAPTER THREE
EXPERIMENTAL RESULTS

This chapter presents the results of experiments conducted in the laboratory dump combustor for a variety of dump plane speeds (V_{dump}), stoichiometries (ϕ) and geometries (duct height, d) using premixed methane and air as the working fluid. The chapter begins with a description of how the flow is transformed from a stable burning shear layer (stable combustion) to one dominated by reacting vortex structures shed from the lip of the rearward facing step (unstable or pulsed combustion). The results will show that such a phenomena results from the coupling between the acoustic and heat release fields, first introduced by Lord Rayleigh (Rayleigh, 1945) and later adapted by Chu (Chu, 1956, 1965). The analysis will then focus on the dynamics of one case before venturing to extract more quantitative flowfield data such as floor temperature and heat flux values, duct and vortex temperatures, and specifically, how these "drivers of instabilities" (Schadow et al., 1989; Smith, 1985) ignite and burn as they convect down the duct.

3.1 GENERAL FLOWFIELD DESCRIPTION

3.1.1 Stable/Unstable Flowfield Description

Under a unique selection of dump plane speeds, duct heights and stoichiometries (Sterling, 1987), conditions exists whereby oscillatory pressure amplitudes within the chamber grow to extraordinary levels (Keller and Westbrook, 1986; Sterling, 1987). Such pressure growth which characterizes all unstable combustors can attain values ten times greater than their stable counterparts (consult Section 3.4). Besides augmenting cyclic pressure levels, the flowfield which was once characterized by a turbulent, burning shear layer, is transformed into one dominated by reacting vortex structures shed from acoustic velocity fluctuations at the step (Zsak, 1993). *Figures 3.1* and *3.2* are shadowgraph images depicting the stable and unstable regimes, respectively. Fast Fourier Transforms (FFTs) and inspection of the resulting pressure, velocity and intensity traces, reveal many important features of the unstable flow: (1) the traces have frequency components clustering near longitudinal acoustic modes of the facility (Zsak, 1993), (2) vortices are shed at either one or all of the dominant frequencies in the pressure spectra, (3) oscillatory pressure values can approach 15% of the mean (taken to be atmospheric) while velocity fluctuations can even reach 100% of the dump plane speed and finally, (4) each vortex is typically associated with a corresponding chemiluminescent spike. For simplicity, the vortex shedding frequency, $\nu_{shedding}$, will be associated with its closest acoustic counterpart (natural frequency) based on prior acoustic modeling (Zsak, 1993; Sterling, 1987). For the present work, 188 *Hz* and 234 *Hz* will be the generic shedding frequencies, despite the fact temperature variations and nonuniformities invoke departures from these values (Laverdant et al., 1986).

3.1.2 Analysis of One Unstable Cycle: 7.62 cm duct, $V_{dump} = 30 m/s$, $\phi = 1.4$

3.1.2.1 General Data Trends

Figure 3.3 depicts the oscillating amplitudes of the velocity (v'), pressure (p') and heat release (q') traces for one case exhibiting distinct flow oscillations. Pressure and velocity data were acquired 1.27 *cm* downstream and 3.2 *cm* upstream of the dump plane, respectively. The heat release trace was compiled from high-speed CCD camera work (discussed later) integrated over the 30 *cm* of duct length viewed by the camera. The 239 by 64, 8 bit per pixel array comprising an image was converted to actual *wattage* units by normalizing the images by their predicted power output (35 *kW*) and assuming a linear relation between chemiluminescence and heat release for a fixed ϕ (Hurle et al., 1968; Dierderichsen and Gould, 1965; Clark and Bittker, 1954). Typically there is a rough one-to-one correspondence between the peaks of all three traces though a more careful inspection of the trace reveals the phasing of the heat pulse can precede (point 1), coincide (point 2) or even lag (point 3) the pressure maximum (consult the numbers above the pressure trace in *Figure 3.3*). The apparent beating of both the pressure and velocity traces is seen on examination of their resulting FFTs (*Figures 3.4a* and *3.4b*) and is due to the excitation of multiple acoustic modes. Such competition between modes results in an interesting collection of dynamical behavior, leading to noticeable cycle-to-cycle variations and warranting the need for high-speed CCD cinematography which is typically absent in pulsed combustion work (Samaniego, 1993; Zsak, 1993; Schadow et al., 1989).

Previous numerical work (Zsak, 1993; Sterling, 1987) was employed to calculate the pressure and velocity mode shapes for the 7.62 *cm* duct height. The results for the three most dominant modes appear in *Figures 3.5a* and 3.5*b* ($x = 0$ denotes the dump plane). For all the cases examined herein, only the two lowest modes, "188" and "234" *Hz*,

appear important. What is interesting is that the three modes predicted by the model represent the first, second and third harmonics of the entire combustor if it modeled as a simple, closed-opened pipe. Their corresponding mode shapes, therefore, each have one, two and three nodes, respectively, on examination of *Figure 3.5a.*

Understanding the shedding, ignition and full combustion of a typical structure is paramount in unraveling the dynamics of the present flowfield. As such, a sequence of time-resolved shadowgraph and CCD images will be presented to outline both the fluid dynamics and combustion occurring.

3.1.2.2 High-Speed Shadowgraph Sequence

The single-shot shadowgraph system used by past JPC researchers (Zsak, 1993) was replaced with a high-speed shadowgraph technique employing a Hycam camera. A complete sequence of images for the present run is illustrated in *Figure 3.6.* As with all shadowgraph movies discussed here, the framing rate was set to 5100 frames per second, enabling approximately 22 images per cycle (every 16 degrees) to be captured for this run of period 4.3 *ms* (230 *Hz*). The sequence depicts approximately one and a half cycles of oscillation to reveal the events prior to shedding and after impingement of the structure with the floor. Shedding typically occurs near a minimum in the velocity trace ($V'_{\min}$) though many exceptions to this rule occur, especially in the present, quasiperiodic case with two competing frequencies. As a result, vortices may even be shed as early as a pressure maximum (nearly one quarter of a cycle earlier). With the above precautions addressed, it will be henceforth assumed that the structures are shed at $V'_{\min}$. The shadowgraph images depict second derivatives of density with distance and therefore depicts strong temperature gradients within the duct (Liepmann and Roshko, 1957).

The data show that there are typically more than one structure in the chamber at any one time. Their spacing is as expected based on an assumed convection speed of 21 *m/s* (dump plane speed; to be verified later) and period of 4.3 *ms*: 9 *cm*. *Image d* denotes the approximate time of shedding, coincident with a velocity minimum and near a zero crossing in pressure (consult *Figure 3.3*). The once pinched off 6.35 *mm* gap opening into the duct, allows a fresh, cold charge to enter, whereafter it forms a distinct bump (*images f-j*). This bump later (*image l*) forms into a distinct and highly regular coherent structure (Schadow et al., 1989) whereby the cold gas has spiraled into itself as evidenced by the curling of its tail, engulfing the core with perhaps hot combustion products. This spiraling ability of the vortex will be seen to be an important ignition mechanism. As the earlier structure burns fully (*image q*), the new structure opens up somewhat and begins to exhibit many fine-scale structures within its core and tail. Such fine scale regions, indicative of intense turbulent exchange, are typically associated with the initiation of combustion as will be seen later and as noted by others (Zsak, 1993). As the earlier structure burns (*image q-s*), it appears to be only modestly influenced by the cooler, lower wall. The newly shed structure continues opening up, exhibiting more fine-scale structures with time. As will be seen, the structure is typically burning by this time (8 *cm* downstream of the step). As the pressure drops, signifying the end of the combustion of the oldest structure, the newest structure burns more and as another V'_{min} is encountered (*image aa*), the process repeats. From the time of shedding to the when the vortex burns fully (~ 14 *cm* downstream), it has spent from 1.5 to 2 complete cycles of pressure within the duct.

3.1.2.3 High-Speed CCD Sequence

The above shadowgraph sequence was useful in characterizing the fluid dynamical aspects of the flow, but said little about ignition and combustion. This was accomplished

through the use of a high-speed intensified imaging system from Kodak as described in Chapter Two.

Chemiluminescence imaging of pulsating flows has seen wide use though it is typically limited to single-shot or time-averaged images (Samaniego, 1993, 1991; Zsak, 1993; Tang et al., 1991; Barr and Keller, 1991). A sequence or "average" cycle is typically built from a collection of single images taken from numerous, yet repeatable runs by phase-locking the images to a specific instant in the pressure cycle. Such techniques are accurate when single-mode, repeatable cycles are excited, but fail when quasiperiodic limit cycles (as in the present case) are encountered. High-speed CCD imagery provides the researcher with a typically unused, yet powerful tool to clearly delineate the more complex flowfield associated with multiply excited modes.

A complete cycle of chemiluminescence images appears in *Figure 3.7a* and *3.7b* while *Figure 3.7c* shows where they are located with respect to their data traces. The framing rate was 3000 images per second and gating was set to 15 μs to sufficiently freeze the flow. No interference filters were used. Each image was corrected for noise and processed and colourized using the software package PV-WAVE. The colour bar denotes the intensity levels: 0, no combustion while 255 denotes saturation of the intensifier (the gain was adjusted to avoid this).

From the sequence, there is a clear delay (ignition delay) from the instant of injecting the cold charge to the first occurrence of chemiluminescence (ignition). This is interesting since although the shadowgraph images clearly showed a visible structure from the moment of injection into the chamber, no combustion is associated with it until more downstream locations are reached. For this cycle, ignition commences along the leading

edge - coinciding with the tail of the previous structure - and then proceeds along the circumference, continuing interior to zones of higher vorticity as evidence from the finer scale, turbulent fluctuations within the structure's core (Ghoniem, 1991). It is interesting to see combustion commences as two lobes, separating the stream of cold gas. It should be emphasized that although interfacial regions separating the cold and hot gases (a shear layer region) are burning at this time (see image f115, for instance), the bulk of the structure comprising the cold stream does not burn fully till much (~2 *ms*) later (consult image f124). By image f126, the vortex has impacted the cool floor (~ 450 *K*) and its quenching effect inhibits any further burning development. Hot products are seen to feed into the recirculation zone, serving to ignite later structures. Burning appears to start around 6-7 *cm* from the step and terminate some 11 *cm* downstream, forming a rather compact burning zone. It is interesting to see that burning typically commences in the shear layer-like region of the *outer* circumference of the vortex where evidence of much fine-scale structures is present. A more exact technique at comparing simultaneously taken shadowgraph and intensified images was undertaken using a combination of a CID and single-shot shadowgraph cameras and will be described next.

3.1.2.4 Single-Shot Shadowgraph/CID images

Figures 3.8 and *3.9* depict two sets of shadowgraph (exposure time 2 μs) and CID images (gated at 15 μs) taken 15 μs (1.5 degrees in the pressure cycle) apart. The CID images were processed identically as the CCD ones and were taken a short time after the shadowgraphs so as not to be contaminated with the very intense spark source comprising the shadowgraph system. The tic marks on all the images represent 2.54 *cm* intervals. Examining *Figure 3.8*, the two structures have been in the duct for 2.4 *ms* and 6.48 *ms* measured from the minimum in the velocity trace. Clearly apparent is the ignition delay: no combustion is associated with the most recently shed vortex even though it is clearly

present in the shadowgraph image. Obviously, insufficient time has elapsed before the hot product have started to ignite this fresh charge. The intricate structuring associated with the tail and core regions of the oldest vortex seen in the shadowgraph image, clearly exhibit intense burning as previously speculated.

Figure 3.9 reveals two similar structures but later on in their development relative to the previous figure. The most recent vortex which has spent some 4.08 *ms* in the duct, is seen to exhibit burning within its core due perhaps to the ability of the cold tail to trap product originally within the recirculation zone. Another burning zone is located near its leading edge due, perhaps, to its close proximity to the still burning tail of the earlier structure. Again, fine scale structures seen in the shadowgraph images are good indicators of intense combustion activity. Examination of many CID and CCD images reveals ignition proceeds in either of two forms: (1) along the vortex's outer circumference or, (2) within its core. Consult *Figure 3.10*. Mechanism (1) typically prevails.

3.1.2.5 Vortex Growth and Strain Parameters

The growth and ignition of the structures was further investigated by monitoring their various dimensions with time. Consulting *Figure 3.11*, they are: (1) X_d: inner core diameter, (2) X_w: outer vortex diameter, (3) X_t: distance from dump plane to trailing edge and (4) X_l: distance from dump plane to leading edge. All dimension were nondimensionalized by the duct height, *d*. *Figure 3.12a* and *3.12b* depict the result for both X_t and X_l, respectively. Error bars denote *rms* error for 10 ensembles (10 vortex structure examined). The dimensions were acquired by projecting the images as large as possible against a viewing screen to reduce errors. A linear fit of the data is included as well as a dashed line depicting the growth rate assuming a convection velocity equaling the average dump plane speed (21 *m/s*).

The initially slow vortices are seen to accelerate once ignition commences due perhaps to the volumetric increase accompanying combustion. The structures travel slightly above the dump plane speed overall and the respective best fit slopes of both X_t and X_l lines are 26 and 27 *m/s*, respectively. The combustion's influence on X_w is clearly seen in *Figure 3.13* where a sudden jump in its growth rate is experience, coincident again with ignition. A darker line has been included to emphasize this point.

Spurred by investigations of the influences of flames with vortices (Driscoll et al., 1994; Kobayashi and Kitano, 1993; Roberts et al., 1993, 1992; Rutland and Ferziger, 1991; Ghoniem, 1991) and the knowledge of strain's influence in the correct modeling of pulsed systems (Barr and Keller, 1991), vortex strain was examined by two methods. The first method based the strain on the inner core diameter as this clearly dictates how tightly wound the structures are. As such, the strain rate, $\dot{\varepsilon}$, is expressed as:

$$\dot{\varepsilon} = \frac{\dot{X}_d}{X_d}.$$

A more appropriate technique would be to base the strain on the relative length of the separation streamline of length L (see *Figure 3.11*) separating the hot product and cold reactants. This would yield the following:

$$\dot{\varepsilon} = \frac{\dot{L} - \frac{1}{2}V_{dump}}{L - \frac{1}{2}V_{dump}t}.$$

The quantity $\frac{1}{2}V_{dump}t$ (average distance traveled by a particle in the cold gas shear layer) was subtracted from L to represent the relative stretching of the separation streamline. Both techniques yielded similar trends as shown in *Figures 3.14a* and *3.14b*. Included on the plots is the laminar extinction limit taken from Law (Law et al., 1986) which represent the maximum strain rate for combustion at the given stoichiometry . The extreme straining experienced early on in the structure's growth could be a plausible mechanical delay, τ_{mech}, to suppress ignition, helping to explain the discrepancy between the shadowgraph and intensified images seen earlier. Strain rates appear to subside to acceptable levels, as far as burning is concerned, approximately 2.3-2.8 *ms* after shedding.

The observation that ignition typically commences along the outer circumference as opposed to the inner core circumference can be partially explained by plotting the strain rates based on both X_d and X_w simultaneously (*Figure 3.15*). For almost the entire time of measurement, the strain rate based on the outer dimension is considerably lower than its inner counterpart. Hence it appears this less strained interface has, at least, a greater likelihood of sustaining earlier combustion based solely on straining grounds.

3.1.2.6 Ignition Delays and Delays to Maximum Heat Release

Pulsed combustion work has typically stressed the importance of the timing of the heat release and ignition processes as it is ultimately their correspondence with the pressure field that dictates if an instability is produced and to what extent (Keller et al., 1990; Barr et al., 1990; Keller et al., 1989; Keller and Westbrook, 1986; Rayleigh, 1945). Hence, determining ignition times and times from when a structure is shed to when it burns fully are paramount in understanding the underlying instability (Barr et al., 1990).

It is typically assumed that the ignition delay time, τ_{id}, which will be defined here as the time from when a vortex is shed to the first occurrence of chemiluminescence, is composed of three sub-delays: (1) $\tau_{species}$: the time to mix the cold fuel with cold oxidizer, (2) τ_{mech}: the time to physically mix the cold mixture with hot products of combustion (assume to be at their adiabatic flame temperature) to some temperature T_{mix} at which noticeable reactions take place and (3) τ_{chem}: a chemical or kinetic time for the reactions to take place assuming the unburned charge has attained temperature T_{mix}. The total ignition delay has been shown to be roughly equal to the sum of all three sub-delays and will be the practice taken here (Keller et al., 1989). Because premixed conditions prevail, $\tau_{species}$ will be identically equal to zero. Hence τ_{mech} and τ_{chem} should be the important parameters in the present work. Ignition delays have strong dependencies on initial mixture temperatures, T_{mix}, and consequently ϕ. *Figures 3.16* and *3.17* stress these points. *Figure 3.16* presents shock tube ignition delays taken from Grillo (Grillo and Slack, 1976) and was compiled using a conventional shock tube whereby the reflected shock wave heated the mixture to some elevated temperature ($\sim T_{mix}$). After the passage of this reflected shock, the hot mixture was timed till the observance of either chemiluminescence or a pressure rise. Because of these specific conditions which are clearly different from the present arrangement, these results should only be used as a guide. The temperature dependency is expected since reaction rates are exponential functions of temperatures (Kuo, 1986). *Figure 3.17* represents numerical work from a HCT code (Lund, 1978) assuming the mixture has been heated to T_{mix} ($\sim 1650\ K$) and the reactions take place in a well stirred reactor (Westbrook et al., 1988). Strictly speaking, these results represent τ_{chem} since in both cases, the unburned charge has already been heated to T_{mix}.

Figures 3.18a and *3.18b* depict the ignition delay data measured from a pressure maximum (slightly before a velocity minimum) to the first observation of

chemiluminescence as evidenced from the CCD images. The results are plotted versus the chamber pressure existing just prior to shedding and during the full burning of the structure itself. This was done to investigate if prior chamber pressures (pressure near instant of shedding which characterized amount of hot recirculating products - *Figure 3.18a*) influenced ignition delays. In addition, ignition delays were plotted versus their corresponding pressure (during combustion of the vortex itself) to also infer any trend. The times were measured from a pressure maximum instead of velocity minimum due to the smoother pressure signal (which made programming easier) and knowledge that the severe beating of the pressure signal made shedding locations irregular (i.e. not at a V'_{min}). These actions and the irregularity of the shedding location no doubt contribute to the observed scatter and tend to artificially increase all measurement *equally* (assuming constant phasing between the velocity and pressure signals) by approximately 1 *ms*. However, what is desired is to see if there are any trends with the prevailing conditions. Included on the plots are ignition delay data taken from Grillo (Grillo and Slack, 1976) at an initial (1300 *K*), intermediate (1400 *K*) and average (1488 *K* - see Section 3.6) recirculation zone temperatures. A single error bar has been included to depict an average error with each measurement. Apparent from the plots is a weak inverse trend with pressure existing near the time of shedding and an opposite trend existing for pressures at the time of full combustion of the structure. Typically, the larger the chamber pressure, the greater the associated combustion activity (see *Figure 3.3*) which would tend to augment the amount of residual hot products available for later structures thereby reducing ignition times. Ignition times also appear longer for structures exhibiting greater pressures as they burn fully and could indicate they initially contained more fuel which would tend to take a longer time to heat and consequently ignite. Delays to when one sees peak burning of the associated structures appear in *Figures 3.19a* and *3.19b* and follow similar, yet more decisive, trends than their ignition counterparts.

3.1.2.7 Comparison of Ignition Delay for Three Cases

Ignition delays for the following three cases in Table 3.1 were recorded to show the general invariance of τ_{id} with ϕ for the present flowfield.

Table 3.1: *Ignition Delay Cases.*

Duct Height (*cm*)	$V_{dump}\ (m/s)$	ϕ
5.08	30	1.2
5.08	30	1.4
5.08	30	1.6

Figure 3.20 depicts the results as well as the τ_{chem} predictions based on Barr's work (Barr et al., 1990). The ignition delay data was acquired in a slightly different manner than before to alleviate the problems associated with the determination of the exact instant of shedding (It will be shown later that the 5.08 *cm* duct cases exhibit repeatable shedding near $V'_{\min}$). Using the average vortex speed (see next section) and axial location of combustion occurring closest to the dump plane (found from averaged images of each case compiled from approximately 60 cycles of pressure), an ignition delay was formed. The invariance with ϕ can be accurately explained by the combined effects of τ_{chem} and τ_{mech} occurring simultaneously. As ϕ increases, thus increasing τ_{chem}, the chamber pressure is seen to increase almost 4 times (see Section 3.4), thereby accelerating the turbulent exchange process and consequently lowering τ_{mech}. It should be reiterated that the above results should be treated separately from the time delay for full combustion of the vortex which typically occurs some 3-4 *ms* later. "Full" combustion is typically a more complex phenomena involving the action of the floor and is responsible for the observed heat peaks seen in *Figure 3.3.*

3.1.3 Comparison of Several Unstable Cases

3.1.3.1 Geometric Influences on the Flowfield

One of the most dominant effects on the flowfield was shown to be geometry (Zsak, 1993). The most efficient way of illustrating this point is by presenting average images for three cases having identical V_{dump} and ϕ for each of the duct heights: 2.54, 5.08 and 7.62 *cm* (*Figure 3.21*). The average images were compiled from approximately 60 cycles of pressure and represent results for a V_{dump} of 21 *m/s* and a ϕ of 1.4. The upstream shift in the burning region with decreasing chamber height should come as no surprise. Evidently, the floor retards the lengthy development of the structure in contrast to the 7.62 *cm* duct and provides a more rapid and vigorous mixing environment which lengthens the burning region. Examination of the Hycam shadowgraph movies for this smallest duct height clearly details the fine-scale, turbulent mixing at work which typically starts closer to the step for the smaller duct. As such, ignition commences further upstream, providing a more abundant supply of hot combustion products in this region. There is typically only one vortex at a time in the chamber. The 5.08 *cm* duct typically parallels its 7.62 *cm* counterpart while revealing some characteristics of the smallest duct. With the smallest duct height, high-speed CCD images reveal structures typically ignite from contact with a continuously reacting shear layer attached to the step. To complement these average images, partial sequences of CCD images for the 5.08 and 2.54 *cm* duct heights, 21 m/s, $\phi = 1.4$ are presented in *Figures 3.22* and *3.23a*, respectively. What is increasing apparent with lower duct heights is the influence of the lower wall in the distortion of the vortex structures which tends to augment the mixing of the hot and still (typically) unreacted main charge of gas within. This geometric influence accelerates tremendously the full combustion process as speculated by others (Zask, 1993) and typically dictates the location of peak combustion (combustion typically occurs a short

time after impingement with the smaller chambers). Also apparent is that, except for the 7.62 *cm* case which was seen to be only modestly influenced by the floor, impingement precedes the axial location of peak combustion. For the 2.54 *cm* case, for instance, structures typically impinge approximately 4-5 *cm* downstream of the step (see *Figure 3.28* - to be discussed) but are seen to have their peak burning location approximately 6 *cm* further downstream (see *Figure 3.21*). This discrepancy reinforces the notion of the importance of the floor in the acceleration of the combustion process for structures in smaller ducts. The 7.62 *cm* cases, conversely, must typically rely on the entrainment of hot product due to the structure's own vorticity and diffusive capabilities since typically full combustion coincides more closely with impingement.

Figures 3.23b and *3.23c* show simultaneous shadowgraph (top photo) and CID (bottom image) images for two sets of vortices in the 2.54 *cm* duct (21 m/s, $\phi = 1.4$): one early on in its development and another during complete combustion of its charge. Tic marks are spaced 2.54 *cm* apart. As with the 7.62 *cm* images, fine scale structures reflect burning regions. The top set of images reveal initial burning in the core and near the leading edge. The oldest structure's tail is still burning and is seen to cling to the upper wall. The lower set of images (*Figure 3.23c*) reflect the intense and more uniform burning experienced for smaller duct heights. An interesting feature is the upstream propagation of combustion activity beyond the lip of the step which helps to ignite subsequent mixtures.

3.1.3.2 Vortex Growth Rate Parameters

Frequency or mode shifts (changes in $\nu_{shedding}$) were found to have only a minimal effect on the two growth rate parameters X_t and X_l (see *Figures 3.24* and *3.25*). Error bars show *rms* errors calculated from five ensembles (five vortices were examined). For a dump plane speed of 30 *m/s* (*Figure 3.24a* and *3.24b*), X_t speeds are initially lower than

the average dump plane speed curve (dotted line), but around 1 *ms* appear to accelerate and travel at roughly 30 *m/s*. The best fit curves for both the 234 and 188 *Hz* cases over the entire interval are, respectively, 27.7 and 26.7 *m/s*. The X_l based growth rates tend to travel much more closely to the average dump plane speed in agreement with 7.62 *cm* results discussed earlier. As combustion proceeds, acceleration of both X_l fronts is seen and is reflected in their overall best fit slopes: 31.4 (234 *Hz*) and 32.9 (188 *Hz*) *m/s*.

For a dump plane speed of 35 *m/s* (*Figures 3.25a* and *3.25b*), similar results are found except that both X_t dimensions slow down considerably *2.5 ms* after shedding. The structures are typically impacting the floor at this time which would tend to retard the development of the rear fronts. It was found that almost all of the 188 *Hz* parameters grew slightly faster than their 234 *Hz* counterparts. As will be shown, oscillatory pressure values increase almost five times during a mode transition from 188 to 234 *Hz* which would tend to accelerate the growth of all vortex dimensions.

Geometric influences were found to exert the most striking influence on the growth rate parameters. This should come as no surprise since it was found decreasing the duct height highly distorted the vortex structures and lengthened the burning zone. *Figures 3.26a* and *3.26b* depict the results for X_t and X_l, respectively, for two duct heights: 2.54 and 5.08 *cm*. The extreme pressures within the smaller duct (2-3 times larger than in the 5.08 *cm* duct) obviously accelerate the two front speeds over their larger duct counterparts. With increasing pressures comes more cycle-to-cycle variations as evidence from the high-speed camera work and is reflected in larger overall error bars for the 2.54 *cm* parameters. As expected, the smaller duct with its greater pressures and geometric influences on structures, accelerates the growth rate of the inner core diameter (*Figure 3.27a*), X_d, and consequently its corresponding strain rate (*Figure 3.27b*).

3.1.3.3 Vortex Impingement Location

Geometric influences were found to alter impingement locations as expected (*Figure 3.28*). The figure presents results for a variety of speeds and stoichiometries for the three duct heights investigated plotted as the impingement distance, I, (measured from the dump plane) versus the step height, d_s. The step height is the duct height, d, minus the gap height (0.64 *cm*). More disparities are seen for the smallest duct height due to the extreme chamber pressure causing more pronounced variations between cases. Typical error bars have been included. The results are compared to the expected impingement location of a turbulent, nonreacting shear layer (spreading half angle of 7 degrees) and turbulent, reacting shear layer and are seen to grow at much smaller rates. Unstable values are much lower as expected due to the large X_w growth rate which generally dictates when the structures impact the wall for a fixed geometry. The growth rate can be approximated as:

$$I/d_s = 1.83.$$

3.2 DRIVING AND DAMPING OF INSTABILITIES: RAYLEIGH'S CRITERION

3.2.1 Formulation

A thorough investigation of pulsed combustion cannot be achieved without addressing the chemical-acoustic interactions that inevitably occur. As shown by others (Samaniego, 1993; Sterling, 1991, 1987; Yu et al.,1991; Keller et al., 1989; Schadow et al., 1989; Culick, 1987; Poinsot et al.,1987; Lord Rayleigh, 1945), it is this interaction between the pressure and the heat release which typically sustains the instabilities. Hence

studying the energy exchange process between p' and q' is paramount in unraveling the problems associated with pulsed systems such as why ramjets "unstart" (Oran, 1988), the general stability of pulsed systems (Shyy and Udaykumar, 1990) and strategies for controlling combustion instabilities (Menon and Jou, 1991). To elucidate this point, the mathematical formulation of the above statement which is known as Rayleigh's Criterion will be presented.

Following the analysis of Sterling (Sterling, 1991), the inviscid, nonconducting conservation equations are linearized into mean and fluctuating components. First-order terms of the momentum equation are multiplied by u'(fluctuating part of the velocity), while the first-order terms of the energy equation are multiplied by $p'/\gamma\,\overline{p}$ where $\overline{p}$ and p' are the mean and fluctuating components of the pressure, respectively and γ is the ratio of specific heats. The resulting two equations are then added yielding:

$$\frac{D}{Dt}\left(\frac{p'^2}{2\gamma\,\overline{p}}+\frac{\overline{\rho}\,u'^2}{2}\right)=\frac{\gamma-1}{\gamma\,\overline{p}}p'q'-\frac{u'p'}{\gamma\,\overline{p}}\frac{\partial\overline{p}}{\partial x}-\frac{\partial}{\partial x}(u'p')-\left(\rho'u'\overline{u}+\overline{\rho}\,u'^2+\frac{p'^2}{\overline{p}}\right)\frac{\partial\overline{u}}{\partial x},$$

where:

$$\begin{aligned}
p(pressure) &= \overline{p}+p' \\
u(velocity) &= \overline{u}+u' \\
q(heat) &= \overline{q}+q' \\
\rho(density) &= \overline{\rho}+\rho'.
\end{aligned}$$

After integrating the equation over the combustor's volume, the left-hand side represents the total change in energy of the acoustic field while the right side reflects how this energy exchange may be accomplished. The first term on the right-hand side is the

Rayleigh Term and shows that energy may be exchanged through the coupling of the pressure with the heat release. The second and third terms are typically neglected due to the assumed orthogonality between p' and u'. The remaining term on the right-hand side is the mean flow gradient term which can assume large values near abrupt area changes and/or where heat is released (Sterling, 1991).

3.2.2 Mechanisms for Energy Addition/Dissipation

The importance of the Rayleigh term in dictating how much energy can be potentially exchanged with the acoustic field can be demonstrated by an order of magnitude analysis for a typical run: 5.08 *cm* duct, $V_{dump} = 30m/s$, $\phi = 1.4$. The total burner output for this case, assuming products are brought back to room temperature, is about 50 *kW* (*STANJAN*, 1985). Using previous acoustic work (Zsak, 1993; Sterling, 1987; Smith, 1985) to determine the pressure and velocity mode shapes, integrating the left-hand side of the above equation over the combustor's volume yielded an available acoustic energy of 0.42 J (78 *W* based on its $\nu_{shedding}$ of 188 *Hz*). The majority of this energy can be found in the plenum chamber where the mode shapes take on large values.

The potential contribution of the Rayleigh term using average values for p' and q' and assuming both are in phase, is 285 *W*. (It was observed that the instantaneous Rayleigh Indexes can even approach 800 *W* for this case). Other acoustic sources of energy addition/dissipation include contributions due to the mean flow gradient, nonideal reflections at the ends of the apparatus, dissipation in the boundary layers and each can be approximated as less than a *watt* (Sterling, 1991). A final contribution typically ignored in the literature deals with the energy gained or lost by walls since they are basically plates in a gas undergoing acoustic resonance which according to Swift (Swift, 1988), modify the

standing wave vibrating along a direction parallel to them. This results in two important effects: (1) a heat flux near the plate's surface along the direction of the vibration and (2) the generation or absorption of power near the surface of the plate. These two effects, produced by the coupling between sound waves and solid boundaries, are the rudiments for all thermoacoustic engines. Using his analysis, the potential energy loss due to this mechanism is estimated at 6 *W*.

A summary of the above mechanisms is presented in Table 3.2 where values have been normalized by the acoustic energy/cycle and clearly shows the importance of the Rayleigh term in dictating how much energy may be exchanged with the acoustic field.

Table 3.2: *Energy Exchange Mechanisms Normalized by Available Acoustic Energy/Cycle.*

Acoustic Energy for 1 cycle	Rayleigh Mechanism	Acoustic Floor Work	End Loses	Boundary Layer Losses
1.0	3.64	0.08	0.013	0.0014

3.2.3 Analysis of Time-Varying and Two-Dimensional Rayleigh's Criterion

The following section deals with an analysis of the temporally varying and two dimension Rayleigh Indexes for the 11 cases listed below in Table 3.3.

Table 3.3: *Rayleigh's Criterion Cases Investigated.*

Case No.	Duct Height (*cm*)	V_{dump} (*m/s*)	ϕ	$\nu_{shedding}$ (*Hz*)	$\eta_{Rayleigh}$ (%)
1	2.54	21	1.6	188	0.990
2	5.08	21	1.4	234	0.061
3	5.08	30	1.2	234	0.060
4	5.08	30	1.4	188 w/ 234	0.082
5	5.08	30	1.6	188	0.115
6	5.08	35	1.2	234	0.085
7	5.08	35	1.4	188	0.209
8	5.08	35	1.6	188	0.496
9	7.62	21	1.2	234	0.140
10	7.62	21	1.4	234	0.190
11	7.62	21	1.6	188/234	0.180

The mathematical formulation of Rayleigh's Criterion, first formalized by Chu (Chu, 1956, 1965) and adopted by others (Shyy and Udaykumar, 1990; Samaniego et al., 1993; Menon and Jou, 1991; Barr and Dwyer, 1991) reads as follows:

$$\mathbf{R} = \frac{\gamma - 1}{\gamma \bar{p}} \int_V dV \int_t^{t+\tau} p'(\vec{x},t) q'(\vec{x},t) dt,$$

where the first integration is over the volume and the second is over time. The above index can be broken into time or spatial varying indices by dropping the integration in either time or space, respectively. Hence $\mathbf{R}$[1] represents the energy added/subtracted to/from the acoustic field per cycle due to the coupling between the oscillatory heat and pressure signals. An alternate form developed by Culick (Culick, 1987) and utilized by others (Sterling, 1991; Hedge et al., 1987) reads:

[1] The units of the Total Rayleigh Index are Joules.

$$\mathbf{R} = \mathbf{C}\left|S_{p'-q'}\right|\cos\left(\theta_{p'-q'}(\nu)\right)$$

where:

$\mathbf{C}$ = *constant*
$S_{p'-q'}$ = *cross spectrum between p' and q'*
$\theta_{p'-q'}$ = *phase difference between p' and q' at frequency* ν.

The above representation is based on expanding p' into normal acoustic modes (Culick, 1976, 1990, 1991).

Figures 3.29 through *3.39* depict the results for the 11 cases. The middle image is the average burner distribution and was calculated by averaging all CCD images for a particular run. Typically, this amounted to approximately 60 cycles of pressure. The contour levels denote intensity values ranging from 0 (cold) to 255 (hot) and are proportional to burner output power for a fixed ϕ (Hurle et al., 1968; Diederichsen and Gould, 1965; Clark and Bittker, 1954). The top contour plot is the two-dimensional Rayleigh Index found by temporally integrating the instantaneous index $\mathbf{R}(x,y,t)$. Dotted contours represent damping regions while solid contours are driving regions and are labeled in units of $Joules/m^2$. The two-dimensional intensity plots were converted to *watts* as discussed before (Section 3.1) while the pressure was taken to be constant spatially due to the compactness of the burning zone relative to the acoustic wavelength and the small transverse dimension (Hedge et al., 1987; Samaniego et al., 1993). Each instantaneous CCD image is first subtracted pixel by pixel from the corresponding average image and then multiplied by the instantaneous pressure values. The entire process was then integrated over time, resulting in the two-dimensional images. The values above each

upper plot denote the Global Rayleigh Index (in *Joules*), found by integrating $\mathbf{R}(x,y,t)$ both in time and space. The lower figure is merely $\mathbf{R}(t)$ or the time varying index integrated over space. Included for completeness are the corresponding pressure and heat release traces. Similar results have been obtained experimentally (Samaniego et al., 1993; Sterling, 1991; Hedge et al., 1987) and numerically (Kailaisanath, 1991; Menon and Jou, 1991) but experimental results typically rely on building a sequence of images (to get $q'(x,x,t)$ values) from a collection of single images taken at different phases in the pressure cycle, thus rendering an "averaged" cycle. As it will be seen, such a technique is valid only if there are minimum cycle-to-cycle variations but the present work is characterized by much temporal variations which would have gone unnoticed using cycle averaging techniques.

A quick examination of the results reveals the two-dimensional Rayleigh Indices vary considerably from case to case, are two-dimensional and characterized by alternating driving and damping regions. The above pattern of zones can be simply explained by first assuming the pressure to be represented as:

$$p(t) = P\cos(2\pi\nu t),$$

where ν is the frequency of the oscillations. Furthermore, the heat release may be modeled as a convecting pulse, moving at the dump plane speed as verified by Hycam work (Samaniego, 1993):

$$q'(x,y,t) = Q\cos\left(2\pi(x-ut)/\lambda\right).$$

Hence the spatial Rayleigh Index would read:

$$\mathbf{R}(x) = \frac{\gamma - 1}{\gamma \bar{p}} \int p'q'dt \equiv \frac{\gamma - 1}{\gamma \bar{p}} PQ\cos(2\pi \nu x/\lambda),$$

where:

$$\nu = \nu_{shedding}$$
$$\lambda = V_{dump}/\nu.$$

Hence the Rayleigh Index would indeed be sinusoidal as reflected in the plots. To take an example (*Figure 3.31*), 5.08 *cm.* duct, $V_{dump} = 30\ m/s$, $\phi = 1.2$ and $\nu_{shedding} = 234\ Hz$, the analysis would yield:

$$\lambda = 30/234 = 0.13\ m,$$

which corresponds closely to the approximate wavelength of $\mathbf{R}(\bar{x})$ on inspection of *Figure 3.31*. Another interesting feature is found by examining the total, spatially integrated Rayleigh Index $\mathbf{R}(t)$ (bottom curve) where it seen that tremendous cycle-to-cycle variations do exist which have typically gone unnoticed with past researchers (Sterling, 1987, 1991). All cases experience driving of the instability as reflected in their positive global indices. The long term motion in a limit cycle, however, dictates that the net energy exchange must be zero so this surplus energy from acoustic sources is inevitably lost by one of the aforementioned mechanisms. The most likely source of dissipation, however, is heat lost to the walls (to be discussed) since this can account for 2000-3000 *watts* just along the 30 *cm* of duct floor examined, far in excess of the surplus acoustic energy calculated.

The double-peaked nature which typically characterizes all the $\mathbf{R}(t)$ curves reflects the existence of strong, stable pulsations and results when both expansion and compression waves are in phase with the minimum and maximum of the energy release profiles, respectively (Barr and Dwyer, 1991). The net result is that both p' and q' curves have close phase relationships as can be verified from the plots.

3.2.4. 2.54 cm Duct Height Results

The 2.54 *cm* duct height case (*Figure 3.29*) is marked by a long driving region extending from the dump plane to approximately 20 *cm* downstream. The remainder of the duct exhibits damping and is reminiscent of prior 2.54 *cm* work (Sterling, 1987, 1991). P' and q' oscillations are typically in phase yielding strong driving of this 188 *Hz* mode $(\mathbf{R} = 68\ Joules)$.

3.2.5. 7.62 cm Duct Height Results

Figures 3.37 through *3.39* depict the results for this duct height. The interesting thing to note is the shortening of the driving region's "tail," the narrowing of the damping region closest to the dump plane and the emergence of another damping region near the downstream end of the duct as ϕ increases from 1.2 to 1.6. In addition, the driving region seems to correspond with the peak burning location as shown by comparison of the driving region with the average burner distribution (middle figures). Again, all three cases experience driving as indicated by their positive Global Rayliegh Indexes and double-peaked $\mathbf{R}(t)$ curves. The observed transverse variation in $\mathbf{R}(x,y)$relative to the 2.54 *cm* case, reflects the higher complexity of the flowfield and hints at a more two-dimensional flow.

3.2.6 5.08 cm Duct Height Results

Figures 3.30 through *3.36* reveal interesting trends develop as mode changes occur. For the $V_{dump} = 30\ m/s$ cases (*Figure 3.31* through *3.33*), the 234 *Hz* case (*Figure 3.31)* is marked by damping near the dump plane, a central driving region then a final damping region (there is a very small driving region near the dump plane, not shown, however). As the 188 *Hz* mode is engaged, however, a large driving region near the dump plane develops and occupies nearly half of the duct length, replacing a prior damping region. As with the higher $\nu_{shedding}$ cases, a damping region occupies the more downstream region of the duct. Another interesting feature is the peak in the driving region gradually moves upstream with increasing ϕ. Like the 7.62 *cm* cases, there is a high degree of transverse variation in $\mathbf{R}(x,y)$. Driving-damping interfaces are marked by convex surfaces pointing towards the damping zone, reminiscent of their respective average images. Because the $\mathbf{R}(\bar{x})$ wavelength λ equals $V_{dump}/\nu_{shedding}$, λ will increase with decreasing $\nu_{shedding}$ and explains the smaller number of driving-damping zones with the leaner run ($\nu_{shedding}$= 234 *Hz*).

The $V_{dump} = 35\ m/s$ transitional cases (*Figures 3.34-3.36*) are marked by an even more complicated pattern of driving and damping regions. The 234 *Hz* case is again marked by a damping, driving, then damping regions but also exhibits a slight driving region near the dump plane. As ϕ increases and the 188 *Hz* mode is introduced, it appears this more upstream damping region which was surrounded by two smaller driving regions gives way to a larger region of driving extending approximately two thirds of the duct's length from the dump plane. Also apparent in the two richer figures (*Figure 3.35* and *3.36)* is the pinching of the driving zone near the upper wall at each ends.

To summarize, the 234 *Hz* mode is typically driven by a central driving region with two outer damping regions, while the 188 *Hz* cases are characterized by a more simpler driving-damping arrangement. Furthermore, the higher shedding cases generally have a more compact (smaller) driving zone which could explain why theses instabilities are much weaker than their 188 *Hz* counterparts.

3.2.7 Temporal Evolution of R(x,y,t)

It is interesting to see the temporal evolution of the Rayleigh Index to investigate if the driving-damping regions remain fixed both in time and space. *Figures 3.40a, b,* and *c* depict the results for Case 6. The left-hand images represent instantaneous Rayleigh Indexes $\mathbf{R}(x,y,t)$ while the right-hand images are their instantaneous chemiluminescent images artificially colourized as described before. Contours have been left unlabelled for clarity. The framing rate of the camera was set at 4000 *Hz* so that the time between images is 250 μs ($\nabla t/T = 250\mu s/5.3ms = 0.047$). The three pages represent just over one complete pressure cycle beginning with the cycle denoted with a "*" in *Figure 3.34.* Clearly, regions of driving and damping are changing continuously and exhibit much two dimensionality. Interestingly, the newly shed vortex on the first page (*Figure 3.40a*) begins as a driving region for the first five images but suddenly switches to a damping region in the final image. It maintains its status as a damping region for the following six images, but during the third image on *Figure 3.40c,* it switches again to a driving region with a corresponding reversal in the once driving region to its right.

3.2.8 Rayleigh Efficiency

A more efficient way of interpreting the Global Rayliegh Index is by defining the Rayleigh Efficiency $\eta_{Rayleigh}$ (Keller and Westbrook, 1986; Barr and Dwyer, 1991):

$$\eta_{Rayleigh} = \frac{R}{C_p \overline{P}\overline{\dot{Q}}} \int_0^1 p'\dot{Q}'dt = \frac{\gamma - 1}{\gamma \overline{P}\overline{\dot{Q}}} \int_0^1 p'\dot{Q}'dt$$

where the bar represents cyclic averages, the primes are deviations from these averages, the time has been normalized by the period of oscillations and the rate of heat release appearing has been integrated over volume. Conditions which induce the largest $\eta_{Rayleigh}$ are characterized by the strongest pulsations and represent the optimal design conditions for pulse burners (Barr and Dwyer, 1991). The last column in Table 3.3 depicts the Rayleigh Efficiency and shows that for the 5.08 *cm* duct, the mode transition from 234 *Hz* to 188 *Hz* induces larger $\eta_{Rayleigh}$ and hence explains why much larger p' oscillations are experienced (discussed later). This larger p' oscillation consequently causes greater vortical impact along the floor, enhances mixing and facilitates larger q' values (discussed later). Also seen is the large increases in efficiency with the smallest duct height, again reflected in larger p' and q' values as will be shown later.

3.3 FLOOR TEMPERATURE MEASUREMENTS

Past work has shown how the combustor's floor is essential in the reignition process since the interaction between the vortex and the floor greatly augments overall turbulence values and thereby enhances the mixing between hot and cold gases (Zsak,

1993). Furthermore, the low temperature of the floor can in some instances cause local extinction of combustion in the structures and may also reduce the amount of hot product entering the recirculation zone. It is instructive, therefore, to investigate the floor's temperature distribution to qualitatively assess its influence on the flowfield.

The coaxial thermocouples discussed in Chapter Two were spaced 5.08 *cm* apart along the centerline of the floor (see *Figure 2.12*) between the dump plane (x=0) and 30 *cm* downstream which represented the downstream limit of combustion activity. The low response time of the gauges (1-10 μs as quoted by the manufacturer) provided excellent temporal resolution if needed. The following cases were analyzed:

Table 3.4: *Floor Temperature Cases (Coax. Thermocouples).*

Duct Height (*cm*)	V_{dump} (*m/s*)	ϕ	$\nu_{shedding}$ (*Hz*)
2.54	21, 30	1.6	188
5.08	21	1.6	188
5.08	30	1.2, 1.4, 1.6	234, 234, 188
5.08	35	1.2, 1.4, 1.6	234, 234, 188
7.62	21	1.4, 1.6	234/188
7.62	30	1.4, 1.6	234/188
7.62	35	1.4, 1.6	234/188

3.3.1 General Temperature Trends

Figure 3.41 depicts all six temperature-time traces for one case, 7.62 *cm* duct, V_{dump}=21 *m/s* and ϕ=1.4. There appears to be a slight augmentation in some traces with time, indicative of the heating effect of the vortices, but no evidence of any cyclic

temperature variations. The floor, it appears, is influenced minimally by the vortices and therefore must provide a considerable cooling and quenching effect on the flowfield.

3.3.2 Unsteady/Steady Comparison

Figure 3.42 depicts the considerable temperature augmentation at all measurements locations when the flow is oscillating than when it is stable. The stable runs were gathered by suppressing the instabilities through the addition of steel wool in the plenum chamber. Also evident is the formation of a "hot spot" near the vortex impingement point (x=15 *cm*) which could severely undermined the integrity of chamber walls incapable of withstanding such intense side effects of combustion instabilities (Culick, 1988). It will be shown later that these "hot spots" cause intense heating (Section 3.4) which can even melt the walls of some combustion chambers.

3.3.3 Velocity Effects

Figures 3.42a and *3.42b* depict the velocity effects for six, 7.62 *cm* duct cases at two stoichiometries (1.4 and 1.6). As shown in the plots, increasing the dump plane speed causes overall augmentation in temperatures at each measurement station due perhaps to the greater impact velocity of the structures with the floor. It will be shown later (Section 3.4) that increases in impact velocity (vortex velocity at the point of impact with the floor) are responsible for sizeable variations in floor heat transfer. It should be remarked that all measurements were acquired 20 *s* after initiation of the instability. Plots showing comparisons of temperature data were typically acquired 20 *s* after start-up unless otherwise stated.

3.3.4 Geometric Effects

Figures 3.43a and *3.43b* depict the geometric effects (duct height variation) are restricted to areas immediately downstream of the dump plane (x=5.08 *cm*). This should come as no surprise since decreasing the duct height causes impingement locations to shift upstream. The maximum temperatures still seems to congregate near the central region of the chamber and is due, no doubt, to the intense combustion activity located here. The coarse spacing of the gauges did not permit a more precise determination of the temperature in this region, however.

3.3.5 Frequency Effects

Figure 3.44 reveals results from two, 5.08 *cm*, 35 *m/s* cases, undergoing a mode change from 234 (ϕ=1.4) to 188 *Hz* (ϕ=1.6). Included for comparison is the shear layer distribution for the leaner run. Again, all data was obtained 20 *s* after start-up. The interesting observation is that the richer run has higher overall temperatures than its leaner counterpart except near the most downstream locations. Furthermore, the leaner run has a more constant profile near the downstream end of the duct. It appears, therefore, that $\nu_{shedding}$ changes provide the most pronounced effect on the floor's temperature distribution. To investigate this further, temperature profiles for a series of runs measured after various times (10-30 *s*) were compiled for transitional cases (234 -188 *Hz* shedding) at two dump plane speeds (30 and 35 *m/s*). Consult *Figures 3.45* and *3.46*. What is remarkable is the similarity of all profiles under constant $\nu_{shedding}$ (234 *Hz*), irrespective of V_{dump}. As the 188 *Hz* mode is engaged by increasing ϕ to 1.6, the profiles change dramatically: the last three measurements stations decline at a much faster rate than their leaner counterparts who in some instance remain fairly constant. Hence it is seen that

$\nu_{shedding}$ has the most noticeable effect on disrupting the once seemingly invariant floor temperature distribution. The next section will show how such effects correspond to noticeable floor heat flux variations.

3.4 FLOOR HEAT FLUX MEASUREMENTS

The floor temperature distributions show peculiarities arise as the shedding frequency changes. Furthermore, they reflect the profound effect that flow oscillations and impingement play in the creation of local "hot spots" and overall temperature augmentation. To elucidate if such discrepancies reflect corresponding heat flux variations, measurements were done for most of the floor temperature cases examined previously. Due to the long response time of the heat flux gauges (20 *ms*), time-averaged values were only obtained. *Figure 2.14* depicts their placement along the centerline of the floor. No gauges were placed after the 30 *cm* point as this typically represented the end of the combustion activity on examination of CCD images. Gauges were concentrated near the vortex impingement region. The present work will reveal that improvements over steady heat flux values can be expected, the appearance of "hot spots" or locations of intense floor heat transfer and interesting trends develop as the shedding frequency changes.

The observation that the present flowfield incorporates both flow oscillations and reattachment (due to the vortices shed from the step) provides the author with an unique and typically undocumented flowfield. Much effort has been devoted towards heat transfer in separated flows from either abrupt expansions (Cho and Goldstein, 1994; Scherer et al., 1993; Scherer and Wittig, 1991; Sparrow et al., 1987; Vogel and Eaton, 1985; Habib and McEligot, 1982) or flow blockages (Liou et al., 1993; Aragaki et al., 1991; Sparrow et

al., 1987; Žukauskas, 1982; Koram and Sparrow, 1978) and from pulsating flows (Arpaci et al., 1993; Kim et al., 1993; Dec at al., 1992; Dec and Keller, 1989; Cho and Hyun, 1990; Perry and Culick, 1974; Hanby, 1969). To the author's knowledge, however, research combining the effects of both mechanisms on heat transfer is scarce or absent entirely.

It will be shown that the characteristics of separated flow heat transfer are seen in the present investigations: relatively low values in the recirculation or separations bubble, a maximum near the flow reattachment point due to high shear stresses manifested from larger turbulent velocity fluctuations (Scherer and Wittig, 1991; Vogel and Eaton, 1985; Miyashita et al., 1980) and a gradual decay downstream of impingement as the flow assumes its fully developed profile. Recent numerical attention has been undertaken (Cho and Goldstein, 1994) to predict the highly complex flow patterns near the impingement region as this location is principally responsible for the high heat fluxes values associated with separated flows over conventional flowfields.

Experiments dealing with oscillating flow in pulsed combustor tailpipes have shown improvements (Dec and Keller, 1989; Perry and Culick, 1974; Hanby, 1969) or reductions (Alhaddad and Coulman, 1982; Park et al., 1982) relative to their steady turbulent values but such discrepancies are typically due to a lack of systematic variation of the governing flow variables or the knowledge that improvements or reductions can be predicted depending on the measurement location (Kim et al., 1993), the magnitude of the pulsations (Park et al., 1982; Hanby, 1969) or frequency of oscillations (Cho and Hyun, 1990). Accurate attempts at solving the nonsteady heat transfer problem have largely relied on extending the results from turbulent duct flow analysis (Colburn Analogy) to the Quasi-Steady limits (Hanby, 1969) which assumes the flow to remain steady at the

instantaneous velocity, requiring pulsations of low frequency and amplitude (Dec and Keller, 1989). Such restrictions are typically violated in conventional pulse burners (excessive pressure induce flow reversals) so such comparisons should be viewed with discretion. Furthermore, the Quasi-Steady theory makes use of the Reynold's Analogy, coupling the momentum and energy equations, which has come into disrepute in recent work (Dec and Keller, 1990). As a result, researchers have been forced to develop their own heat flux correlations (Arpaci et al., 1993).

3.4.1. Axial Floor Heat Flux Distribution

3.4.1.1 2.54 cm Duct Results

Table 3.5 depicts the four cases examined while *Figures 3.47a-d* shows their corresponding axial heat flux distributions.

***Table 3.5:** 2.54 cm Duct Cases (Floor Heat Flux).*

Case	V_{dump} (m/s)	ϕ	$\nu_{shedding}$ (Hz)
1	21	1.6	188
2	30	1.5	188
3	30	1.6	188
4	30	1.7	188

For all the above cases, an overall lowering in $\dot{Q}_{floor}(x)$ is seen with increasing axial distance. Peak values for all profiles are found at the first station (5.08 *cm*) and coincide as expected with the approximate vortex impingement location since this region exhibits high shear stresses (Cho and Hyun, 1990; Žukauskas, 1982) and consequently large convective transport properties (Kim et al., 1993). The coarse spacing of the gauges

for this duct height prevented exact determination of $\dot{Q}_{floor}(x)$ at impingement (around 5 *cm* downstream of the step) and therefore precludes any information about the heat flux within the recirculation bubble. The observation of a second peak in the profiles near the 12 *cm* location is evidence of increased turbulent activity and is probably due to combustion occurring nearby and its associated augmentation in turbulence (Driscoll et al., 1994) and gas temperatures. Hence there are two heat flux maxima: one associated with impingement of the structures and another associated with the more downstream location of peak combustion. Examination of CCD images confirm this conjecture. The trend of lower heat flux values with downstream distance, reminiscent of turbulent pipe flow (Kreith and Bohn, 1986; Scherer and Wittig, 1991), is consistent with separated flow results which reflect diminishing enhancements over steady flow values as the blockage ratio (open area for flow devided by pipe diameter) decreases (Koram and Sparrow, 1978). Examination of the total heat flux over the 30 *cm* of duct length investigated (*Figure 3.48*) reveals that the increases in $\dot{Q}_{floor}$ with increasing ϕ accompany sizeable pressure increases which is typical in oscillating flows with flow reversals (Hanby, 1969). It will be see that such pressure increases are the primary mechanism for increasing $\dot{Q}_{floor}$ through its inevitable effect in augmenting near wall turbulence levels despite the associated ϕ increases which would tend to lower bulk temperatures and hence $\dot{Q}_{floor}$. This is further evidence of how the macroscopic turbulent processes dominate the chemical effects in the present flowfield.

3.4.1.2 7.62 cm Duct Results

A more thorough examination of axial heat flux was undertaken for this duct height. Table 3.6 depicts the cases analyzed while *Figure 3.49a-e* shows their profiles.

Table 3.6: *7.62 cm Duct Cases (Floor Heat Flux).*

Case	V_{dump} (*m/s*)	ϕ	$\nu_{shedding}$ (*Hz*)
1	21	1.4	234/188
2	21	1.5	234/188
3	21	1.6	234/188
4	30	1.4	234/188
5	35	1.4	234/188

For a constant V_{dump}, stoichiometric effects have relatively little influence on the shape of the distributions but typically invoke slight increases in the heat flux due to corresponding pressure increases (Consult *Figure 3.50* for the 21 *m/s* results). Included on the plot are the expected results from the Quasi-Steady Theory which will be discussed later. Due to the relatively small chamber pressures involved relative to the 2.54 *cm* cases, $\left|P'_{2.54cm}/P'_{7.62cm}\right| \approx 5$, only marginal, linear increases in $\dot{Q}_{floor}$ with pressure were found.

An interesting trend is the gradual shifting of the peak in the distribution as the flow velocity is increased and is probably due to the downstream shift in the impingement location and/or peak burning location. Due to the similarity of all profiles, a description of only one case, V_{dump}=21 m/s, ϕ=1.4, will be made (*Figure 3.51*). Included in the plot is the corresponding floor temperature measurements and vortex impingement location. Error bars denote the *rms* fluctuations about the ensemble mean, $\langle T \rangle_{rms}$ or $\langle \dot{Q} \rangle_{rms}$, while the lower most plot denotes the nondimensional, *rms* of the fluctuating temperature or T'_{rms}. The lack of correspondence between the temperature and heat flux peaks should not be alarming as the thermocouple spacing was coarse (5.08 *cm*). What should be apparent, however, is the general similarity of both the temperature and heat flux profiles. As with all separated flow downstream of a rearward facing step (Scherer and Wittig, 1991; Vogel and Eaton, 1985; Koram and Sparrow, 1978), relatively low heat flow values are found in

the recirculation zone, a maximum near the flow reattachment or here, vortex impingement point, and values typical for attached boundary layers further downstream. For steady, nonreacting and reattaching flow, reattachment is around six to eight step height (d_s) downstream of separation (Scherer et al., 1993; Scherer and Wittig, 1991; Drewry, 1978) while steady, reacting results show reattachment is approximately 3.5 step heights downstream (Gabruk and Roe, 1994). Both results are, of course, greater than observed here (see Section 3.1) due to the transverse growth of the vortex structures. The relatively low heat flux values immediately downstream of the step is due to the presence of the homogenous recirculating zone (Zukoski, 1956) which separates the high turbulence levels associated with the detached shear layer and the wall, constituting a source of resistance to the heat transfer. Note the relatively small T'_{rms} values.

As proven by Sparrow (Sparrow et al., 1987) and observed by others (Cho and Goldstein, 1994; Scherer et al., 1993; Aragaki et al., 1991) heat flux maxima typically occur slightly upstream of the reattachment point due to the presence of higher streamwise and transverse velocities (Sparrow et al., 1987) creating larger turbulence levels here (Vogel and Eaton, 1985). This appears consistent with the T'_{rms} values in this region. The gradual dropping in $\dot{Q}_{floor}$ after impingement is generally attributed to the redevelopment of the flow and the gradual thickening of the boundary layer (Koram and Sparrow, 1978). It is interesting to see that $\dot{Q}_{floor}$ does not continue steadily declining with further downstream locations and is probably due to the gradual augmentation of v' (fluctuating part of velocity) as the velocity antinode (located near the end of the duct) is approached (Hanby, 1969). Again, the gradual augmentation of T'_{rms} at downstream locations confirms this conjecture.

3.4.1.3 5.08 cm Duct Results

The heat flux profiles for this duct height are similar to their 7.62 *cm* counterparts so little will be said about them. Consult *Figures 3.52a-d.* Also shown are summaries for two cases, $V_{dump} = 30\,m/s$ and $\phi = 1.4, 1.6$, showing both floor temperatures and heat flux data (*Figure 3.53* and *3.54*). Again, errors bars represent *rms* fluctuations about the ensemble mean (5 ensembles). The similarity of all profiles should be apparent as well as the location of the impingement point seems to precede the heat flux maximum unlike its 7.62 *cm* counterpart. This could be due to the shortness of the recirculation zone (Sparrow et al., 1987) or merely the coarse spacing of the gauges.

3.4.2 Pipe Flow Correlations and Quasi-Steady Analysis

Future heat flux comparisons will be made with respect to turbulent pipe flow analysis and Quasi-Steady Theory. Analysis of turbulent heat transfer in pipes is typically achieved using the Colburn Correlation based on the Reynold's Analogy (Kreith and Bohn, 1986) which relates heat transfer to the friction coefficient. It states:

$$\overline{Nu}_d = 0.027 \mathrm{Re}_d^{0.8} \mathrm{Pr}^{0.3} \left(\frac{\mu_b}{\mu_s} \right)^{0.14},$$

where:

$\overline{Nu}_d$ = *average Nusselt Number* $= \dfrac{hd}{k}$

d = *Hydraulic diameter*

Pr = *Prandtl Number*

μ_b = *dynamic viscosity at bulk fluid temperature*

μ_s = *dynamic viscosity at wall temperature.*

All properties are taken at the bulk "b" fluid temperature except μ_s. The fractional viscosity term is added (Seider and Tate, 1936) to correct for large transverse temperature variations.

More accurate attempts at solving the unsteady heat transfer problem have largely relied on extending the foregoing analysis to Quasi-Steady limits (Arpaci et al., 1993; Dec and Keller, 1989; Hanby, 1969). Its limitations and shortcomings have already been addressed but it is still the only available theory. Basically, the flow is assumed to have the following form:

$$u = \overline{u}\left(1 + B\cos\left(\frac{2\pi t}{\mathrm{T}}\right)\right) \quad ,$$

where:

$$B = u'/\overline{u}.$$

Applying the Quasi-Steady Analysis to the above relation yields the following:

$$\overline{Nu}_d = 0.027\,\mathrm{Re}_d^{0.8}\,\mathrm{Pr}^{0.3}\left(\frac{\mu_b}{\mu_s}\right)^{0.14} \times \int_0^1 \left(\left|1 + B\cos(2\pi t)\right|\right)^{0.8} dt,$$

where the time has been nondimensionalized by the period of oscillations, T. Care must be taken in evaluating the diffusion parameters as there are typically large axial temperature variations.

To compare the forgoing results with the Quasi-Steady Theory, heat flux values from all three duct heights ($V_{dump} = 30\,m/s$ and $\phi = 1.6$) are plotted on one graph together with their corresponding Quasi-Steady results (*Figure 3.55*). Three lines are

shown since each reflects a different duct height and consequently hydraulic diameter. Also included are values representing stable, turbulent flow found by adding steel wool in the plenum chamber to dampen the flow oscillations. The theory predicts no initial heat transfer enhancement (actually a slight reduction) over steady values (Cho and Hyun, 1990; Park et al., 1982; Hanby, 1969) until flow reversals occur: i.e. $B > 1$. After this point, a linear increase with pressure is expected. It should be noted that values for u' were calculated from p' using linear acoustic theory (Dec and Keller, 1989). The data reflects this expected linear growth with pressure, though as typically found (Arpaci et al., 1993; Dec and Keller, 1989), experimental values are much higher than those predicted from theory. This apparent mismatch is typically due to the assumption of constant gas properties in the acoustic equations relating p' to u' (thereby effecting u') and neglecting the higher turbulence values associated with combustion and impingement which would tend to elevate $\dot{Q}_{floor}$. Ignoring such effects contributes to the theory's shortcomings and are the probable reason for the discrepancy observed in *Figure 3.50* (7.62 *cm* duct, 21 *m/s*) between the Quasi-Steady predictions and experimental findings. Here, it is seen that the Quasi-Steady Theory predicts an opposite trend for $\dot{Q}_{floor}$ than what is observed. The theory obviously assumes that one is in the no enhancement region of the curve (see *Figure 3.55*).

3.4.3 Heat Flux Variations during Mode Changes

This section will reveal peculiar trends in $\dot{Q}_{floor}$ develop as the vortex shedding frequency gradually shifts from 234 to 188 *Hz*. The analysis will focus entirely on the 5.08 *cm* duct cases as this configuration is the only geometry which permits mode shifts from subtle changes in the flow parameters (see *Figure 4.1*). Comparisons will be made with

turbulent pipe flow, Quasi-Steady and shear layer data. The transitional cases shown in Table 3.7 will be examined:

Table 3.7: *Heat Flux Cases (Transitions).*

Case	V_{dump} (m/s)	$\phi_{234-188Hz}$	$\Delta\dot{Q}_{floor}$ (W)
1	21	1.4	300
2	25	1.4	400
3	30	1.4	500
4	35	1.4	900

The second column indicates the dump plane speed at which the transition from 234 to 188 *Hz* occurs while the third column is the approximate rich limit for a 234 *Hz* instability. Mixtures richer than this have increasing 188 *Hz* components in their respective pressure and velocity FFTs.

Figures 3.56-3.59 depict the total floor heat transfer values for each of the above cases. Included on the plots are the values predicted from turbulent pipe flow correlations. Also included on the two highest dump speed cases are the corresponding steady, turbulent shear layer data. Dotted lines separate areas of 234 and 188 *Hz* shedding and bound regions where shedding frequencies can have components of both modes. A typical sequence of pressure FFTs as this mode shift occurs is seen in *Figure 3.60* and shows how energy is being exchanged between the two competing frequencies.

The graphs reveal that as a mode change occurs through increases in ϕ, $\dot{Q}_{floor}$ linearly increases with introduction of the 188 *Hz* mode. Furthermore, the rate of $\dot{Q}_{floor}$ growth appears to increase with increasing dump plane speed. These results seem

reassuring since the aforementioned Rayleigh Efficiencies show a similarly greater growth rate with ϕ for larger V_{dump} (see 30 *m/s* cases, Table 3.3). Plots depicting the two highest dump plane speeds (30 and 35 *m/s*) reveal this augmentation subsides somewhat as the rich flammability limit is reached whereafter the instability stops due to extinction. What is remarkable is that for the two transitional Cases 3 and 4, a constant $\dot{Q}_{floor}$ is observed for a constant $\nu_{shedding}$ of 234 *Hz*. The combustor's inability to maintain the 234 *Hz* instability for the two lowest speed cases for stoichiometries below 1.4 prevented seeing similar trends (the flow went stable). It is interesting to see the pressure's response during these mode changes. *Figure 3.61* and *3.62* depict the results for Cases 3 and 4. As expected, sizeable pressure increases accompany both V_{dump} transitions which is the probable cause for the heat flux trends. The results, however, are contrary to predictions from turbulent pipe flow as shown by the gradual lowering in $\dot{Q}_{floor}$ over the identical ϕ range. Furthermore, the Quasi-Steady Theory (*Figure 3.63*) predicts a similar trend of lowering $\dot{Q}_{floor}$ with increasing ϕ for all the transitional V_{dump} cases except for 35 m/s case whose pressure magnitudes must place it in the augmentation region of the Quasi-Steady curve (Hanby, 1969: consult *Figure 3.55*). Even though the pressure is increasing through all the transitions, it is apparently insufficient as far as the theory is concerned. It should be remembered, however, that the Quasi-Steady analysis has severe limitations like the failure to incorporate heat transfer augmentation due to flow separation (Vogel and Eaton, 1985; Scherer and Wittig, 1991) which itself can be considerable. Proof that the observed pressure increases must indeed generate sufficient turbulence activity to invoke such heat flux enhancements can be found by plotting the vortex impact velocity (velocity just prior to contact with the wall; based on X_w - see Section 3.1) as a mode change occurs (*Figures 3.64a* and *3.64b*). This data was compiled from high-speed movies and represents averages from 10 vortices. Error bars have been included and represent *rms* fluctuations about the mean and reflect the high disorder at all stoichiometries. Although

the 234 to 188 *Hz* transition occurred at a lower ϕ (problems with the dump combustor caused some varied results over time), a sizeable jump in impact speed is seen as the 188 *Hz* mode is introduced. More importantly, larger *rms* floor temperature fluctuations are experienced with the richer run at almost all axial locations (*Figure 3.65*). Hence the heat flux augmentations are indeed caused by the higher turbulence levels generated along the floor (Vogel and Eaton, 1985). The last column of Table 3.7 indicates the approximate magnitude of these increases. The resulting $\dot{Q}_{floor}$ increases caused from increases in p' should not be surprising as it was shown in Section 3.2 that sizeable increases in Rayleigh Efficiency ($\eta_{Rayleigh}$) were observed as the 188 *Hz* mode was engaged thereby causing the observed pressure increases and hence augmentations turbulent exchange mechanisms.

A final note concerns the stable heat flux values. All unstable V_{dump} cases reflect sizeable increases in heat flux over their steady values. The benefits of pulsed burners is clearly seen. Also apparent in *Figure 3.58* is the heat flux associated with stable turbulent pipe flow calculations is lower than the separated flow (experimental) results which themselves are much lower than pulsating values (compare data at $\phi = 1.4$). It should seem obvious, therefore, that pulsed systems incorporating both mechanism (pulsations and separated flows) would be advantageous. *Figure 3.66a* and *3.66b* summarize the shear layer results for two dump plane speeds (30 and 35 *m/s*, respectively) and reveal they too are influenced by the increases in near wall turbulence levels (note the increases in pressure with ϕ).

3.4.4 Correlating the Heat Flux Data

The inherent complexities associated with pulsating flows has resulted in a rather sparse treatment of correlating its heat transfer data. The failure of the Quasi-Steady to

provide satisfactory results, principally due to its neglect of pulsating frequency and other flowfield features (separation) on heat transfer, has lead some researchers to develop their own heat flux correlations (Arpaci et al., 1993; Dec and Keller, 1989). Further complicating the issue is the knowledge that many pulsed systems incorporate reattaching flows which has itself seen intense research due to its own complexities (Liou et al., 1993; Scherer et al., 1993; Scherer and Wittig, 1991). The following discussion will show how a satisfactory correlation exists for the present heat transfer data which draws insight from both flow pulsation and separated flow work.

Figure 3.67 summarizes the heat flux data presented as Nusselt numbers, $\overline{Nu}_d$, versus their corresponding Reynolds Number, Re_d. The heat flux values were integrated over the 30 *cm* of duct length investigated. The $\dot{Q}_{floor}$ values were converted to $\overline{Nu}_d$ by forming an equivalent convection heat transfer coefficient, *h*, from $\dot{Q}_{floor}$ as follows:

$$h = \frac{\dot{Q}_{floor}}{A\,\Delta T},$$

where A denotes the floor area and ΔT is the temperature difference found by subtracting an average floor temperature (410 K - consult Section 3.3) from an average bulk temperature in the duct. Apparent from the plot is the increase in $\overline{Nu}_d$ with Re_d, the grouping of data into regions of constant duct height and the ordering of data according to V_{dump}. Hence it may be written: $\overline{Nu}_d = fn\left(\mathrm{Re}_d, V_{dump}, d\right)$. As a result, the following nondimensional groups were chosen for the correlation:

$$\mathrm{Re}_d, \quad \left(\frac{\varpi d}{V_{dump}}\right), \quad \left(\frac{d_g}{d}\right),$$

where:

$$\varpi = average\ shedding\ frequency = 211\ Hz$$
$$d = hydraulic\ diameter\ of\ the\ duct$$
$$d_g = gap\ height\ (6.4\ mm).$$

An average shedding frequency was chosen since data on only two pulsation frequencies was obtained. The three nondimensional groups reveal that the present flowfield incorporates turbulent pipe flow $\left(\mathrm{Re}_d\right)$ (Kreith and Bohn, 1986), flow pulsation $\left(\frac{\varpi d}{V_{dump}}\right)$ (Arpaci et al., 1993) and separated flow $\left(\frac{d_g}{d}\right)$ (Koram and Sparrow, 1978) mechanisms. The following correlation gave the best fit to the experimental data:

$$\overline{Nu}_d = 0.028\,\mathrm{Re}_d^{\,0.75}\left(\frac{\varpi d}{V_{dump}}\right)^{0.68}\left(\frac{d_g}{d}\right)^{1.23}.$$

Consult *Figure 3.68*. The correlation is remarkably good considering the complexity of the flowfield. It should be noted that the above correlation gave satisfactory results for the present combustor but should be used with discretion for other pulsed systems. Hence it is seen that the convective heat transfer coefficient varies as follows:

$$h \propto d^{-0.8} V_{dump}^{\ 0.07}.$$

The correlation predicts a strong dependence on duct height and a somewhat weaker dependence on dump plane speed.

3.5 DUCT TEMPERATURE MEASUREMENTS

The aim of this section will be twofold. The first part will describe time averaged temperature mappings for two duct height configurations to differentiate the geometrical effects on the temperature field. In the second section, time resolved temperature profiles of the reacting structures themselves will be presented to assess how combustion quantitatively develops within the structures as they convect down the duct.

3.5.1 Average Duct Temperature Distributions

Prior work has revealed ignition mechanisms, burning development and average burning distributions show marked variations from case to case. The way in which the wall affects the average burner profiles, for instance, clearly alters with differing duct heights. Hence it is possible that such scalar fields as temperature to be equally modified due to the differing flow conditions as geometry, $\nu_{shedding}$, etc. Partial mappings of the temperature fields will be presented for the following two cases:

Table 3.8: *Cases for Temperature Mappings.*

Case No.	Duct Height (cm)	V_{dump} (m/s)	ϕ	$\nu_{shedding}$ (Hz)
1	2.54	21	1.3	188
2	7.62	21	1.3	188/234

The measurements were made with 25.4 μm, R-type, uncoated junction thermocouples not corrected for radiation errors (It will be shown later that this will induce only around 10 K error in the measurements so exclusion of these corrections is

acceptable). The time constants for these thermocouples (approximately 2 *ms*) were insufficient to obtain time-resolved measurements. The thermocouples were inserted into the floor at access ports spaced 5.08 *cm* apart and at varying heights. Measurements closer to the dump plane were accomplished by fastening a thermocouple into the rearward facing step itself.

3.5.1.1 Case 1: 2.54 cm Duct Measurements

Figure 3.69 details the measurement locations (dark dots) for Case 1. Temperatures in the vortex impingement and recirculation zones, essential in understanding the ignition process, were ensured with these measurement locations. Note the dimensions in the figures are given in *centimeters.* From examining the average CCD images for the same duct height, it was deemed unnecessary to probe for temperatures further downstream as CCD images revealed a fairly uniform heat distribution in this region.

Figure 3.70 shows the vertical temperature profile 50.8 *mm* downstream from the step. Included also is the lone measurement located 14 *mm* downstream and 9.5 *mm* above the floor, deep in the heart of the recirculation zone. The vertical profiles were joined by a spline fit (tension factor 2.0). Error bars representing the standard deviation, σ, of the measurements were included and were calculated from over two hundred cycles of shed vortices. Since the measurements were time-averaged, the σ values could loosely represent attenuated T'_{rms} values. Examination of the plot reveals the highest temperature (1842.2 *K*) to be located within the recirculation zone itself, probably due to the upstream propagation of the flame over the step. The σ of this measurement (24.3 *K*) characterizes the relative uniformity of the temperature within this reignition region. The quenching effect due to the water cooled wall is clearly demonstrated by the dramatic lowering in

temperature as the floor is approached (Floor data was unfortunately unavailable for this case, but will be presented for the next one). Taking an approximate value of 440 K for the floor temperature (consult *Figure 3.43a*), one can see there is a tremendous ∇T near the floor and reflects the large $\dot{Q}_{floor}$ values discussed earlier and as found by others (Dec and Keller, 1990). The quenching effect of the upper wall is also evident, but is of lesser magnitude relative to the lower floor. The interesting note is the peaking of the curve around 8 *mm* from the floor, indicative of the lower route the hot products take as they enter the recirculation zone. The σ for the three lowest readings is around 32 K while the value for the highest measurement location $(y = 19.1\,mm)$ is 60 K, indicative of the larger temperature fluctuations associated with the upper regions of the structures as they pass the measurement location. The lower measurement location $(y = 3.2\ mm)$, well within the vortex impingement location and hence surrounded by a relatively homogenous area of hot products, is conversely marked with a lower σ (37.0 K).

Figure 3.71 reveals the results 101.6 *mm* from the dump plane. The most striking feature is the uniformity in temperature with the highest three measurement locations, confirmed by the corresponding average CCD image for a nearly identical case (*Figure 3.21*: $\phi = 1.4$, $V_{dump} = 21\,m/s$). The quenching effect of the lower wall is evident but is of smaller degree than at the $x = 50.8\,mm$ station due to the slightly smaller ∇T here. Furthermore, this slightly smaller ∇T is reflected in a lower $\dot{Q}_{floor}$ at the identical location. The uppermost temperature values appear to exhibit the greatest increase with downstream distance, increasing 267 K over the 50.8 *mm* length measured. The second greatest temperature increase is at the second highest measurement station $(y = 12.7\,mm)$. Although the vortex impingement location is near the 50.8 *mm* axial location, complete or more intense burning is not seen till more downstream locations are encountered. The highest temperature associated with the $y = 19.1\,mm$ location is also

evident by the average CCD image (*Figure 3.21*) which also reveals maximal burning in the same area.

3.5.1.2 Case 2: 7.62 cm Duct Measurements

Due to the larger duct height and the more two-dimensional nature of the heat release distribution (*Figure 3.21*), a more rigorous mapping of the temperature field was undertaken. *Figure 3.72* shows the measurement locations for this case, appearing again as dots. As with the 2.54 *cm* duct height, the measurements were concentrated near the impingement (approx. 15.24 *cm* downstream) and lower duct regions. Included are the floor temperature values discussed earlier (Section 3.3) for a nearly identical case: $\phi = 1.4$.

Figure 3.73 details the vertical temperature profile 50.8 *mm* downstream of the dump plane. Again, the quenching effect of the lower wall is evident by the sharp ∇T near the floor. The close location of T_{max} (1821.7 *K*) to the floor (15 *mm*), indicates that like the 2.54 *cm* case, the path of hot product issuing into the recirculation zone is along the lower region of the duct. Unlike the previous case which revealed a more compact burning distribution and consequently more uniform temperature profile at this station, this larger duct height yielded a more two-dimensional flow as indicated from the temperature profiles and average CCD image (*Figure 3.21*).

As expected from the average CCD image, moving downstream into the more intense burning zone elevated all temperatures (*Figures 3.74, 3.75* and *3.76*). Values at $x = 101.6\,mm$ (*Figure 3.74*) revealed a fairly uniform temperature profile, averaging 1801.5 *K* throughout the near 35 *mm* in vertical distance measured. The highest gas temperature (1739 *K*) nearest to the floor occurs at this station and seems to fix the highest wall ∇T and consequently the largest $\dot{Q}_{floor}$ (*Figure 3.51*) which corresponds

closely to the vortex impingement location some 2 *cm* downstream (the lack of access holes along the floor did not permit a closer inspection of the reattachment region). As speculated by others (Lalwani et al., 1979), the impingement process may periodically thin the thermal boundary layer, thus encouraging a greater exchange of hot and cold gases, thus augmenting $\dot{Q}_{floor}$ in this region.

The two other middle stations ($x = 152.5\,mm, 203.2\,mm$) revealed similar profiles with a gradual lowering in ∇T near the wall. The final station (*Figure 3.77*, $x = 254\,mm$) revealed a more gentler ∇T near the wall, resulting in the lowest $\dot{Q}_{floor}$. It appears, therefore, that the temperature profiles follow closely the trends expected from the average image (*Figure 3.21*) in that the central regions are marked by more uniform profiles, while the ends portray a more transverse varying profile accompanied lower $\dot{Q}_{floor}$ values.

Moving downstream along the highest measurement plateau ($y = 38.1\,mm$), one sees a tremendous temperature increase beginning at 1646 K and peaking to 1944 K, indicative of a more concentrated burning region relative to its 2.54 *cm* counterpart. The second highest level ($y = 25.4\,mm$) is marked with only a slight temperature increase (1734 K to 1865 K) and peaks to 1892 K ($x = 203.2\,mm$), leveling to 1858 K ($x = 254\,mm$). This horizontal line cuts directly throughout the burning region and reflects therefore the relative uniform temperature in this region.

The measurements plateau at $y = 3.2\,mm$ shows the widest variation in average temperature, ranging from 1739 K at $x = 101.6\,mm$ to a scant 748.2 K at $x = 254\,mm$ and in σ. The reattaching structures cause widespread velocity fluctuations, resulting in the

vigorous mixing of hot and cold gases and hence large variations in temperature with these measurement stations (Dec and Keller, 1990).

Figure 3.78 depicts the temperature variation moving into the recirculation zone a distance 15.88 *mm* above the floor. Included also is the measurement taken 14 *mm* downstream of the dump plane and 60.33 *mm* above the floor. The horizontal profile reveals a tremendous temperature increase as one moves further into the recirculation zone. The temperature begins at a modest 1236 *K* and increases monotomically to 1433, 1633 and finally to 1799 *K* at only 38.1 *mm* from the cooled dump plane wall. Also evident is the overall lower recirculation zone temperature than that found in the more compact 2.54 *cm* configuration: compare 1842 *K* (2.54 *cm* duct) with an average value of 1488 *K* for the 7.62 *cm* recirculation zone temperature.

3.5.2 Time-Resolved Vortex Temperature Measurements

The following section will outline the first known temporally resolved temperature measurements for a nonsteady, reacting flow using initially uncompensated, fine-wire, junction thermocouples. In particular, the temperature profiles of the reacting structures themselves will be investigated as the vortices convects down the duct. The following three cases will be investigated:

Table 3.9: *Time-Resolved Temperature Cases.*

Case No.	Duct Height (*cm*)	V_{dump} (*m/s*)	ϕ	T_{ad} (*K*)	$\nu_{shedding}$ (*Hz*)
1	7.62	21	1.4	1983	188/234
2	5.08	30	1.4	1983	234
3	5.08	30	1.6	1832	188

The small time constant associated with these thermocouples (0.44 *ms*) provided only minimal phase and magnitude errors in temperature if neglected. Nevertheless, the measurements were corrected for accuracy.

Case 1 will investigate the temperature evolution of structures having minimal influence with the floor while the remaining cases will assess the geometric and frequency effects on the temporal evolution of the temperature.

Figures 3.79 and *3.80* detail the thermocouple arrangement for the 7.62 and 5.08 *cm* duct configuration, respectively. The thermocouples were arranged in a descending order to capture the core of the structures as they convected down the duct. This would facilitate an accurate evaluation of the temperature through a horizontal slice of the vortex. The thermocouples used were 7.62 μm in diameter, Pt-Pt/10%Rh (S-type), coated with silica to reduce catalytic effects (Gaydon and Wolfhard, 1970). Their extremely low time constants (0.44 *ms*), provided excellent temporal resolution for this harsh flow environment. A high-speed Hycam camera operated at around 5100 frames per second (as discussed previously) was operated simultaneously with the collection of temperature data so that the measurements of temperature and pressure could be accurately related to their corresponding shadowgraph images using a series of timing

blips and event markers on the film. After collection of the temperature data, the measurements were corrected for radiation errors and non-zero time constants.

3.5.2.1 Case 1: 7.62 cm Duct, 21m/s, ϕ=1.4

3.5.2.1.1 General Temperature Trends

Figure 3.81 details a sample of all seven temperature traces together with their corresponding pressure signal (lowest curve). The ability of the thermocouples to capture the pertinent temperature fluctuations associated with the passage of the coherent structures is clearly evident and supported by their respective FFTs which have identical peaks in comparison with the pressure spectra. The frequency resolution of the traces is retained until the third location ($x = 15.24cm$), after which the vortex impinges or reattaches with the lower floor and yields measurements having little or no cyclic variations. The observation that the first three measurement stations are nearly identical except phase shifted reflects the initial cyclic variations of heat is due to the bulk convection of hot and cold gas pockets carried by the vortex itself (Keller et al., 1989). The temperature fluctuations superimposed on these traces can be typically attributed to the rapid convection of hot and cold gas initiated by the combustion process (Keller et al., 1989, 1990) once the vortex had impacted the floor. The latter stations (4-7) relay information about the hot products and how they are influenced by the floor.

To further illustrate the relationship between the pressure and temperature traces as typically done for turbulent flames (Tanaka and Yanagi, 1983; Yoshida and Tsuji, 1982; Hammer, 1994), the cross-correlation between the two fluctuating variables p' and T' was done for each measurement station (*Figure 3.82*). The correlation appears to increase slightly from Stations 1 to 3, then sharply drops with Station 6 due to the breakup of the

structure. The modest increase in correlation with stations 2 and 3 relative to 1 could be due to the delayed nature in which the temperature profile sets up in the vortex and is further demonstrated by their more smoother traces.

3.5.2.1.2 Average Temperature Variation at each Measurement Station

Figure 3.83 depicts the average temperatures associated with each of the seven measurement stations together with their corresponding *rms* fluctuations about the mean. A quick glance at the plot reveals that the highest degree of fluctuations are associated with the first three measurement stations and the largest coincides closely with the impingement point ($x = 15.24\ cm$). The *rms* fluctuations for these three stations are relatively large and measure, respectively, 61.2, 68.9 and 78.7 K, and should come as no surprise since the action of the impinging structures induces large velocity gradients thereby increasing temperature fluctuations (Dec and Keller, 1990). Furthermore, the large fluctuations associated with the first two stations reflect the large thermal gradients within the structure itself. The peak temperature is associated with the fifth station ($x = 20.32\ cm$) and measures 1678 K, some 300 K short of the adiabatic flame temperature for this ϕ. The quenching effect of the walls is clearly seen as the profile drops some 50 K between stations 5 and 7 and is further indicated by a lowering in their respective *rms* fluctuations which drops to around 33 K. A subtle note is the jump in the slope of the curve as the second station is passed, indicative of the delayed nature in which combustion is initiated in the structure. Also, the temperature continues to rise after the vortex impacts the floor suggesting the onset of peak combustion is enhanced by the floors presence as speculated by others (Zsak, 1993; Sterling, 1987; Smith, 1985). The rate of reaction or energy release in such turbulent and oscillating flows is generally controlled by the rate of turbulent mixing, rather that the chemical reaction rates (Heitor et al., 1984; Bray, 1980). As such, the floor's presence is fundamental in this intensification

of turbulence activity. Furthermore, as the combustion process initiates, it too contributes to the augmentation of turbulence activity since it increases local velocity fluctuations within the flame zones as it squirts hot products upstream and downstream (Crauford et al., 1985). The net effect is a continued rise in temperature after impingement as hot products come in contact with the downstream thermocouples.

3.5.2.1.3 Time-Resolved Temperature Traces

Figure 3.84 depicts the cross-sectional temperature profiles of five structures as they pass the first measurement station. The axial distance refers to the instant the structure contacts the thermocouple divided by the total time it is in contact with the gauge. Assuming the vortex convects at a constant speed as verified by high-speed Hycam work, this nondimensional time can be taken as a "distance" so that the temperature curve actually represents a temperature profile through the vortex itself. As shown, the structure has an offset, parabolic profile whose nose has a slightly elevated temperature relative to the upstream or "tail" end with the core exhibiting the highest temperature (1250 *K*) due to the entrainment of hot products into it from the recirculation zone. Such asymmetric temperature profiles within vortices shed from a heated cylinder have also been found by others (Mi and Antonia, 1994) and agree quite well to theoretical predictions for a diffusing line vortex (Carslaw and Jaeger, 1959). The disparity between the hottest (core) and coldest (tail) regions is around 50 *K*. The similarity of all profiles reflects the initial uniformity of the structures' temperature distributions from cycle to cycle. It is worth noting that the thermal gradients existing within the structure is another way (in addition to the floor) for the propagation of combustion through the vortex. The preferential acceleration of the lighter gases (products) in the structure's core towards the cooler, surrounding gases due to the imposed pressure gradient, increases the shear velocity between the hot and cold gases and intensifies the turbulent exchange (Heitor et al., 1984;

Spalding, 1982). Similar arguments have been applied in studies of premixed turbulent flames to show that a source of turbulent kinetic energy can be manifested from the interaction between pressure and density gradients (Libby and Bray, 1981; Bray et al., 1981; Masuya and Libby, 1981). This mechanism is probably of lesser importance when compared to the floor's action, however.

Unfortunately this technique fails in predicting accurate temperature profiles as the structure convects downstream since one is comparing temperatures at different instances in time. As the structure gets to the second station, for instance, its size has grown to approximately 3-4 *cm* so the time difference from when the "nose" temperature was taken to when the "tail" or end measurement was taken is around 1.5-2 *ms*, close to the period of the temperature oscillations themselves (4.3 *ms*). As such, three regions of the reacting structures will be monitored to accurately determined their temperature-time histories: "nose", "core" and "tail." Consult the diagram below.

Sketch 3.1

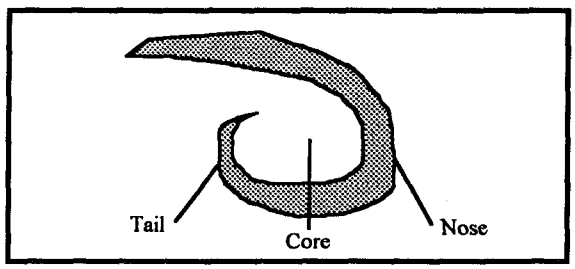

Figures 3.85, 3.86 and *3.87* depict the results for the tail, core and nose regions, respectively. The averaged curve (darker line on plots) together with its error bars representing *rms* fluctuations about the mean, is superimposed on the five cycles examined. Between Stations 1 and 3 ($5.08 \leq x \leq 15.25\,mm$), the structure exhibits a fairly uniform temperature increase with downstream distance measuring approximately 19.1

K/cm (core region data only). As the third and fourth stations are passed, this growth rate increases sharply to around 61.4 *K/cm* and coincides with the vortex impingement point and largest observed $\dot{Q}_{floor}$. As the cooling and quenching effects of the lower wall are felt, a reduction in the rate of temperature growth is experienced despite a continued rise in T_{tail}, T_{core} and T_{nose}. It is here (Station 5) where all three regions experience their peak temperatures. Again, it is worth noting the increase in temperature in all three regions of the vortex after impingement and is due to the increase in turbulence activity on impact with the floor that accelerates combustion.

Heat flux to the floor reduces any more temperature increases as seen by lower temperature values for each successive measurement station (-5.1 *K/cm*). Furthermore, the floor tends to dampen any nonuniformities between cycles as evidence by the general lowering in rms fluctuations of T_{tail}, T_{core} and T_{nose} (see *Figure 3.85*, for instance). It is this quenching and cooling effect of the floor which generally inhibits NO_x formation - typically in low amounts in pulsed burners (Corliss et al., 1984) - since it shortens the residence time of hot products at elevated temperatures (Keller and Hongo, 1990; Edelman et al., 1979).

As expected, the core attains the highest overall temperature at Station 5 due to the entrainment of hot products though the nose too exhibits extreme temperatures which are typically exceeding their core counterparts. The close agreement between the three measurements (core, tail and nose) near the latter stations reflects the relative uniformity in temperature throughout the structure due to the floor's stabilizing effect.

3.5.2.2 Case 2: 5.08 cm Duct, 30m/s, ϕ=1.4

3.5.2.2.1 General Temperature Trends

Figure 3.88 gives a sample of the temperature-time traces for this case and they appear similar to the previous one except that their cyclic nature disappears at only the second station. This should come as no surprise since the structures typically impact the floor at this location ($x = 10.16\,cm$) which would promote a more irregular temperature curve at more upstream locations relative to Case 1.

3.5.2.2.2 Average Temperature Variation

Figure 3.89 depicts the average temperature recorded at each station for this case, together with their *rms* fluctuations about the mean, all normalized by the largest temperature encountered. As with Case 1, Station 2 represents the location where a more rapid increase in T is experienced (although very slightly) and where the highest degree of fluctuations, as indicated by its *rms* fluctuation, is seen which seems consistent since this location is close to the impingement point. The downstream lengthening of the burning region is also evident as the average temperature decreases only after the sixth station, 5.08 *cm* later than Case 1 and at a slower rate. Obviously, the quenching effect of the lower wall has less of an effect in this more compact duct configuration. In addition, the higher amplitude oscillations associated with this duct are reflected in greater *rms* fluctuations at each measurement location. A final note is that despite the greater pressure oscillations associated with this case, there is a fairly smooth, linear increase in average temperature with each successive station, indicative of the more uniform combustion development present.

3.5.2.2.3 Time-Resolved Temperature Traces

Figure 3.90, 3.91, and *3.92* depict the average temperature traces from 5 vortices for T_{tail}, T_{core} and T_{nose}, respectively. The most striking feature is the apparent linearity in temperature increase for all three regions up to station 5 and the more gentler decline thereafter. Unlike the average plot, however, all three regions experience their maximum variances at the Station 1 rather than 2. Structures typically reattach between these two stations so they are expected to exhibit much cycle-to-cycle variation. It is interesting to note that Stations 4 and 6 are marked with the smallest *rms* fluctuations and reinforces earlier statements of the stabilizing effect of the floor. Station 5, however, reflects a large nonuniformity between structures and is probably due to the rapid mixing of hot and cold gases just after impingement. On comparison with Case 1 (nearly identical ϕ), it is seen that the last three stations exhibit slightly greater temperatures and is probably due to the greater compactness of the burning zone (i.e.: smaller reaction vessel).

3.5.2.3 Case 3: 5.08 cm Duct, 30m/s, ϕ=1.6

3.5.2.3.1 General Temperature Trends

Unlike Case 2, cyclic temperature variations seem to persist well past the second station despite an increase in p'_{rms} from approximately 2000 to 4000 *Pa* (*Figure 3.93*). After the second station, however, this apparent pattern disappears and the traces become reminiscent of Case 2's.

3.5.2.3.2 Average Temperature Variation

Previous results have show that accompanying ϕ increases are appreciable p'_{rms} increases (*Figure 3.61*) and this is reflected in somewhat larger *rms* fluctuations at each measurement station except Station 3 due to the higher fine-scale velocity fluctuations

accompanying these pressure increases (*Figure 3.94*). This nonuniformity persists long after the structures impinge on the floor (Stations 5, 6 and 7) where *rms* values take on an average value of 46 K.

3.5.2.3.3 Time-Resolved Temperature Traces

Figures 3.95, *3.96*, and *3.97* depict the average tail, core and nose profiles computed again from five cycles of vortices. Between Stations 1 and 2, there is an interesting trend developing: all three regions, there is a distinct jump in T_{tail}, T_{core} and T_{nose} after the second measurement point, indicative of the delayed nature in which combustion develops in this lower $\nu_{shedding}$ case which is surprising since CCD images and τ_d measurements revealed only little variation in ignition delay between this case ($\phi = 1.6$, $\nu_{shedding}$=188 *Hz*) and Case 2 ($\phi = 1.4$, $\nu_{shedding}$=234 *Hz*). It is postulated that this subtle mechanism could be due to an initial chemical effect due to the increase in stoichiometry which would lower overall temperatures. More will be said on this in Chapter Four.

After the second station, however, all three vortex regions experience relatively linear increases and peak at Station 5, one station earlier than Case 2 and reflects its shorter, more compact burning zone (consult its average CCD image from *Figure 4.25c*). After Station 5, there is a greater rate of temperature decline with all three curves when compared to Case 2, resulting from the larger $\dot{Q}_{floor}$ values at impingement for this higher ϕ run discussed earlier (Compare *Figure 3.53* with *Figure 3.54*). The results are reminiscent of the average floor temperature plots discussed in Section 3.3. When both Case 2 and 3's T_{core} are plotted on the same graph (*Figure 3.98*), it is interesting to see the richer run (Case 3) exhibits typically higher overall temperatures than its leaner counterpart at each axial location. Obviously the higher pressures associated with this run induce greater velocity fluctuations and hence better burning (as discussed previously),

thus driving up T_{core} and $\dot{Q}_{floor}$. It should be noted that the initial delay in temperature growth experienced for the richer run is short term and fluid mechanical effects must thereafter dominate to reduce opposing chemical effects.

3.5.2.4 Overall Comparison of Vortex and Floor Temperatures with $\dot{Q}_{floor}$

Figures 3.99, 3.100 and *3.101* depict summaries for $\dot{Q}_{floor}$, T_{core} and T_{floor} for Cases 1, 2 and 3, respectively. Included on the plots is the approximate vortex impingement location appearing as a dotted line averaged from over 20 cycles, accurate to within 0.5 *cm*. Bars representing *rms* fluctuations have been omitted for clarity.

In conventional steady, forced convection theory, the difference between the T_{core} and T_{floor} curves represents the driving ∇T for the heat flux to the floor. It can be seen that although this reflects the upstream and downstream $\dot{Q}_{floor}(x)$ trends, discrepancies arise in the impingement region, suggesting a more complicated heat transfer mechanism at work here. According to separated flow theory, however, heat transfer will increase linearly along the separation region (region extending from the dump plane to the reattachment point) and reach a maximum at the impingement location (Žukauskas et al., 1982; Habib and McEligot, 1982). This maximum results from the high velocity fluctuations accompanied by high turbulent shear stresses reaching peak values at the reattachment point. The present results follow this expected trend within the resolution of the gauge spacing.

Although T_{core} continues to increase after reattachment with an accompanying drop in T_{floor} thus increasing ∇T, $\dot{Q}_{floor}(x)$ does not increase since the intense turbulent activity associated with the reattachment point is gradually subsiding. Consequently, $\dot{Q}_{floor}(x)$ values approach expected results for turbulent flat plate theory as a more fully developed

flow is attained (Kreith and Bohn, 1986; $\check{Z}$ukauskas et al., 1982; Koram and Sparrow, 1978): 43, 56 and 52 kW / m^2 for Cases 1, 2 and 3, respectively).

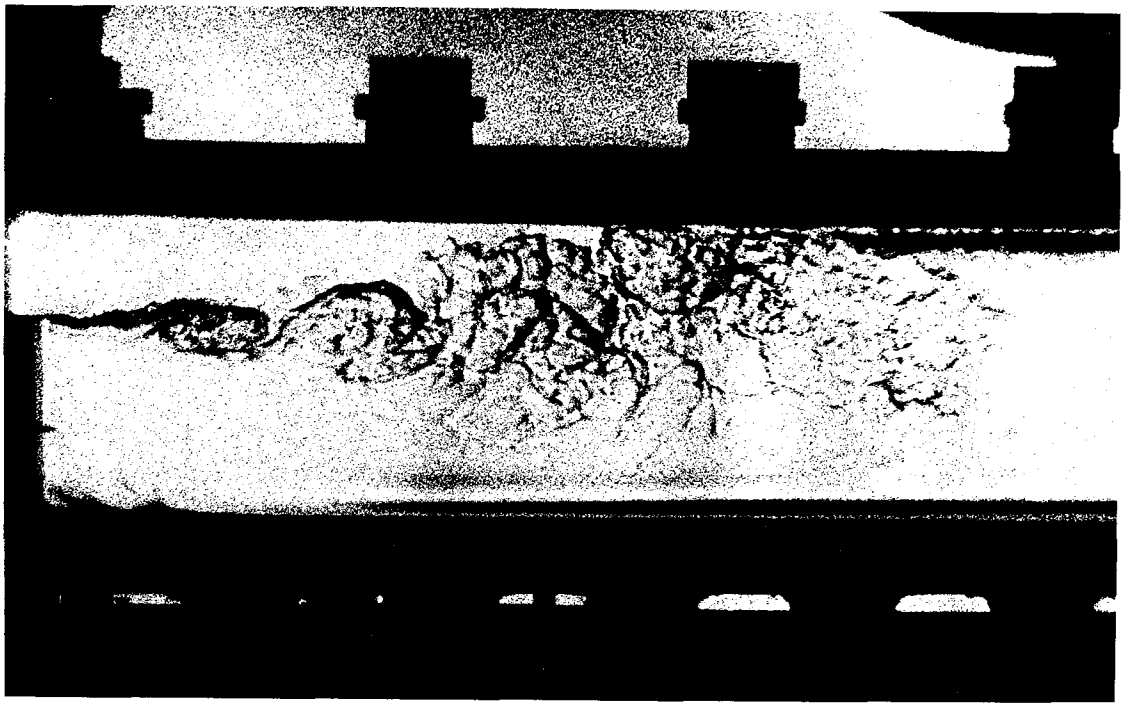

Figure 3.1: Flowfield undergoing stable combustion.

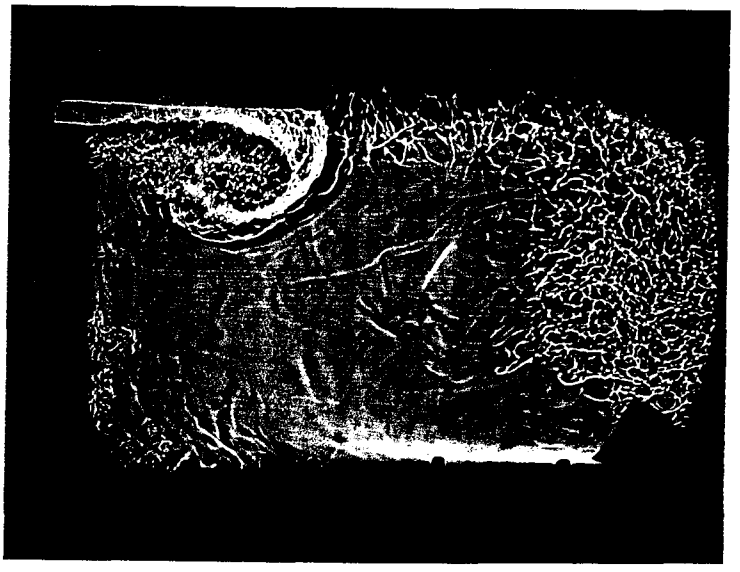

Figure 3.2: Flowfield undergoing unstable combustion.

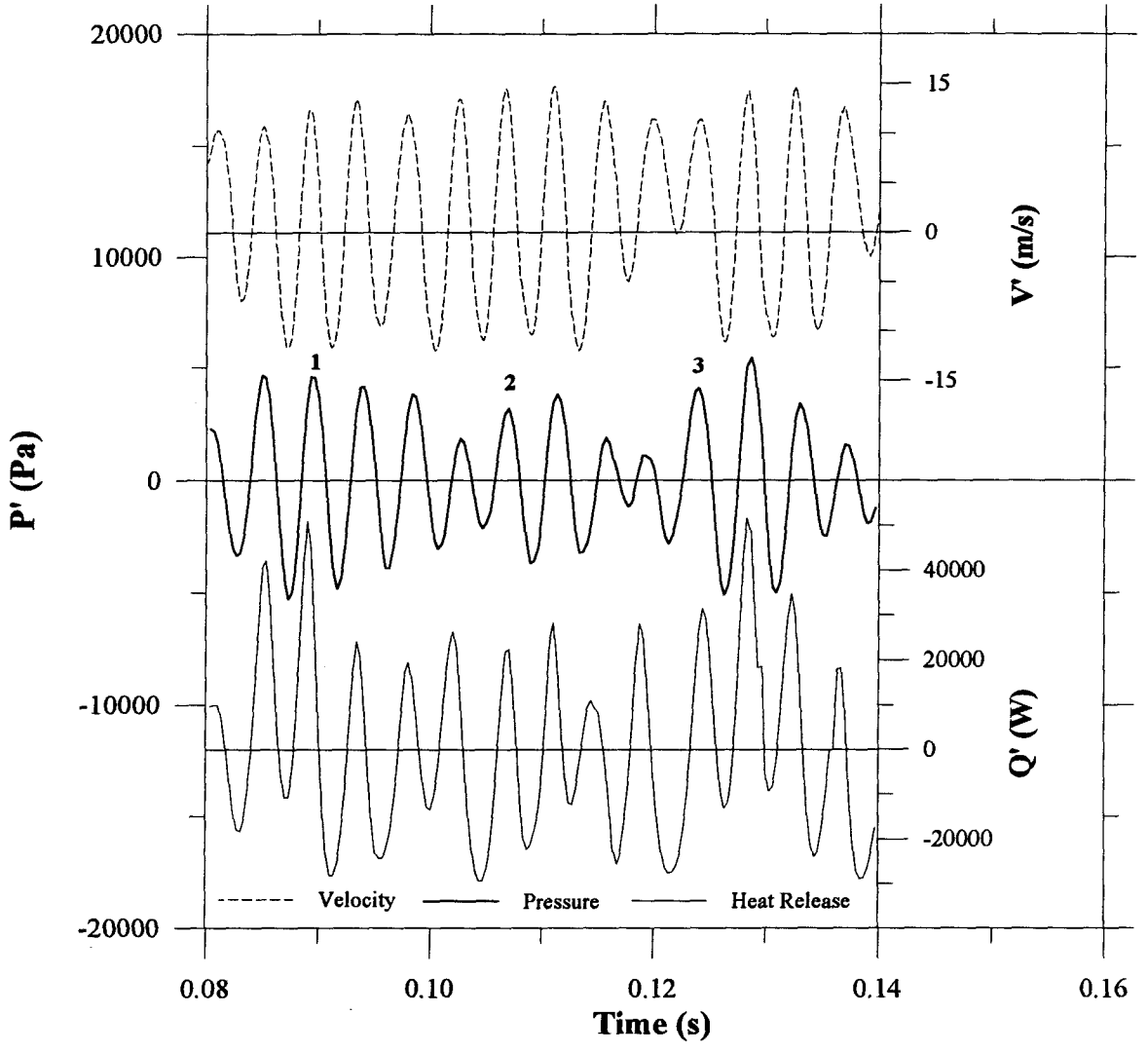

Figure 3.3: Summary of velocity, pressure and heat release traces: 7.62 cm duct, V_{dump}=21 m/s, ϕ=1.4.

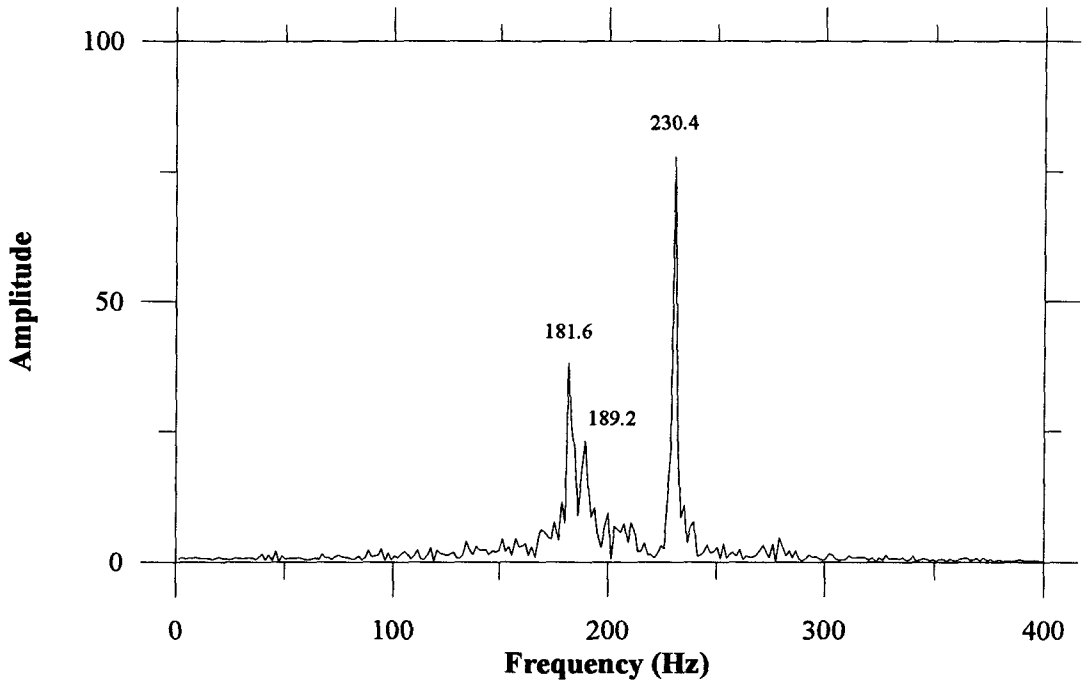

Figure 3.4a: Pressure FFT for 7.62 cm duct, V_{dump}=21 m/s, ϕ=1.4.

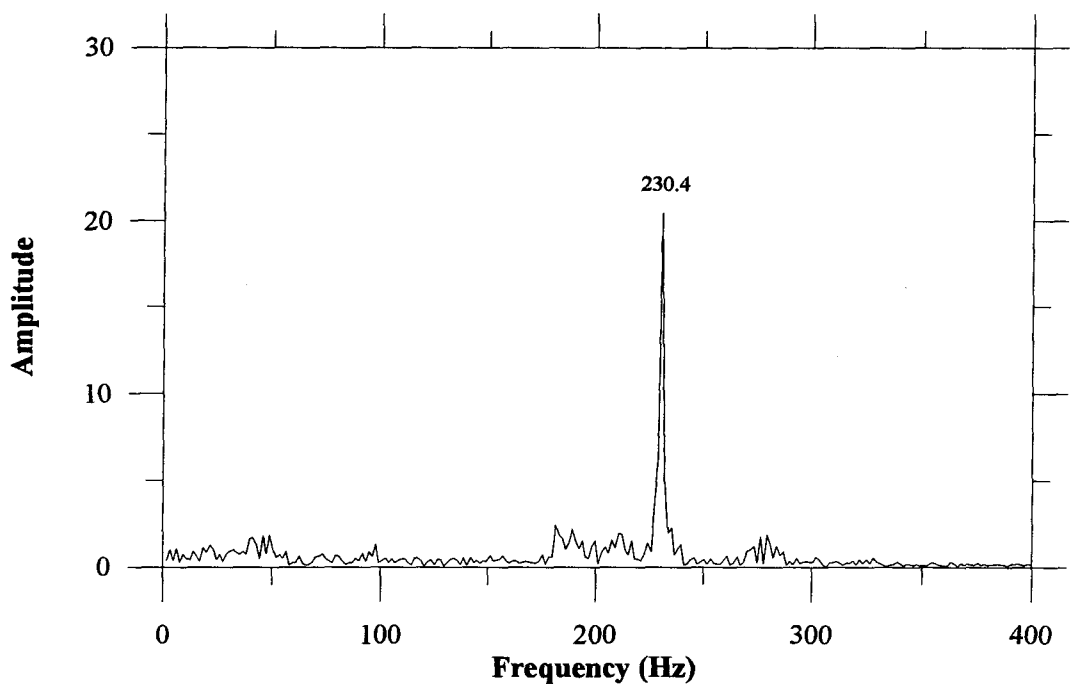

Figure 3.4b: Velocity FFT for 7.62 cm duct, V_{dump}=21 m/s, ϕ=1.4.

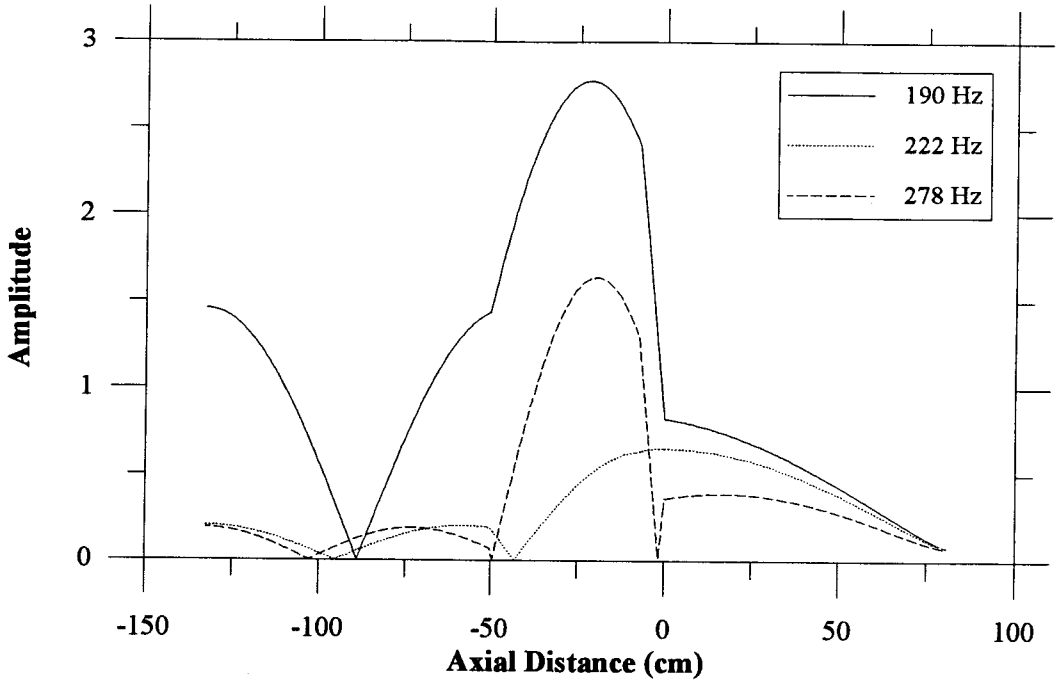

Figure 3.5a: Pressure mode shapes for 7.62 cm duct.

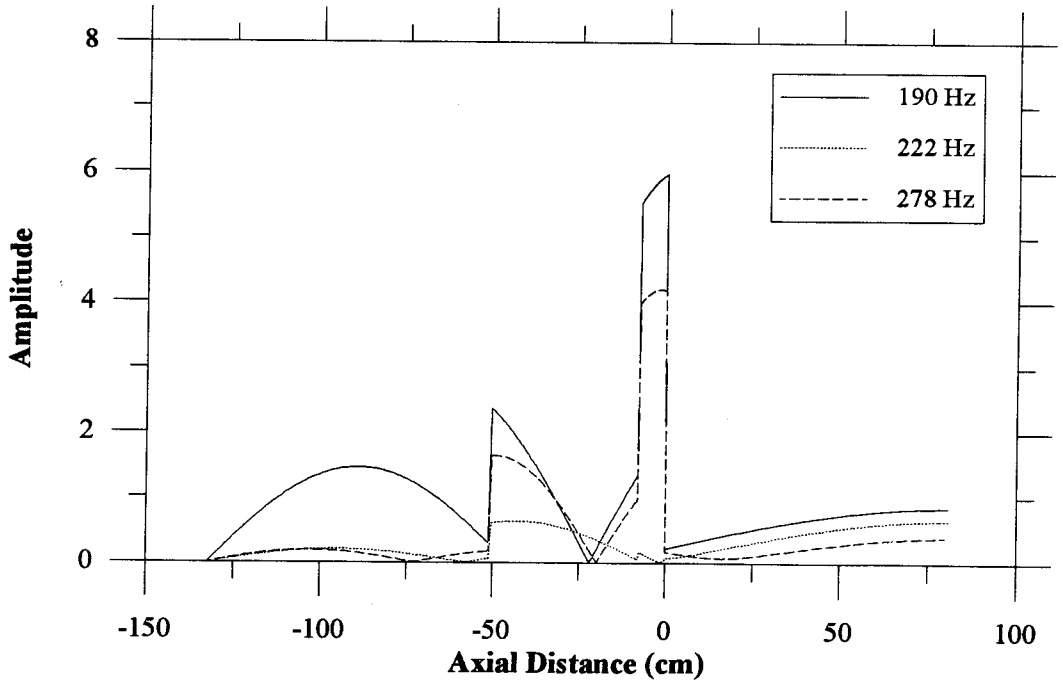

Figure 3.5b: Velocity mode shapes for 7.62 cm duct.

(*a*) -48 degrees

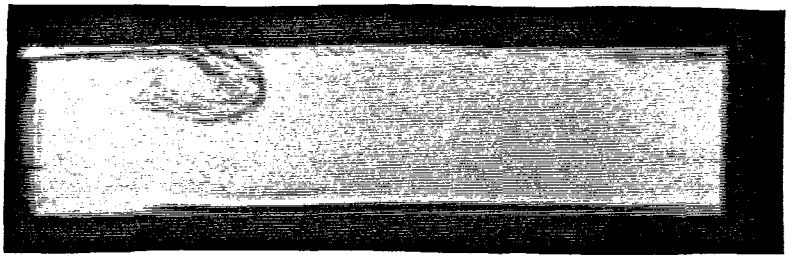

(*b*) -32 degrees

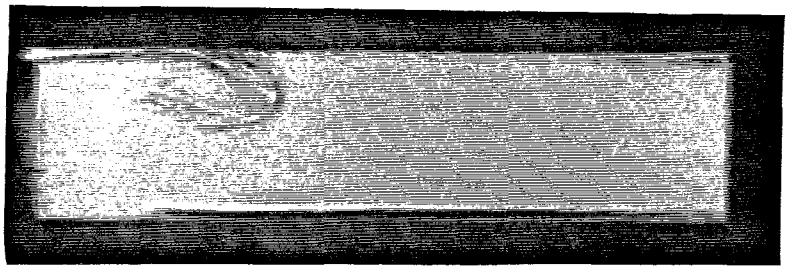

(*c*) -16 degrees

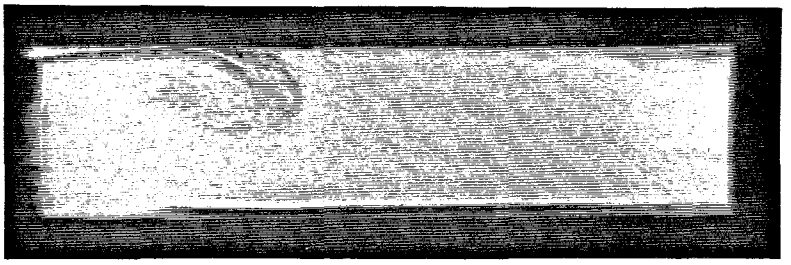

(*d*) 0 degrees

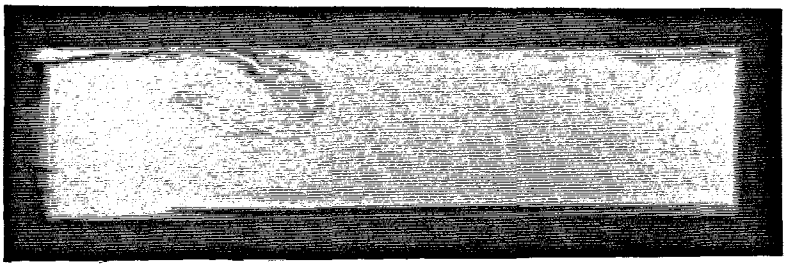

(*e*) 16 degrees

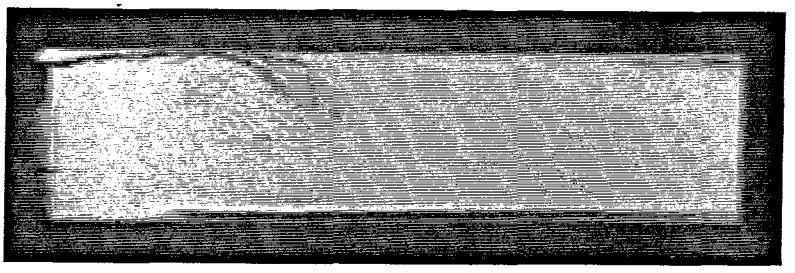

Figure 3.6a-e: Sequence of high-speed shadowgraphs for 7.62 cm duct, V_{dump}=21 m/s, ϕ=1.4.

(*f*) 32 degrees

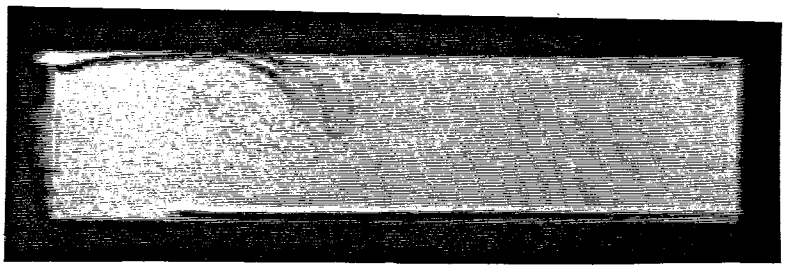

(*g*) 48 degrees

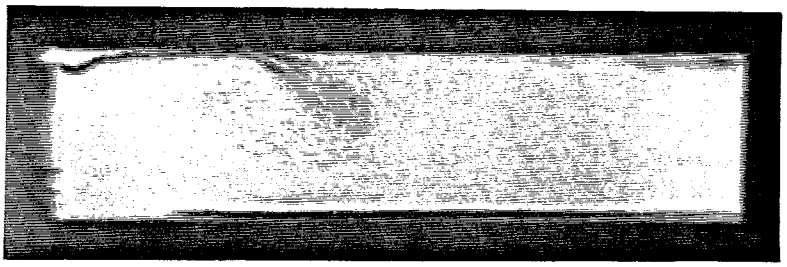

(*h*) 64 degrees

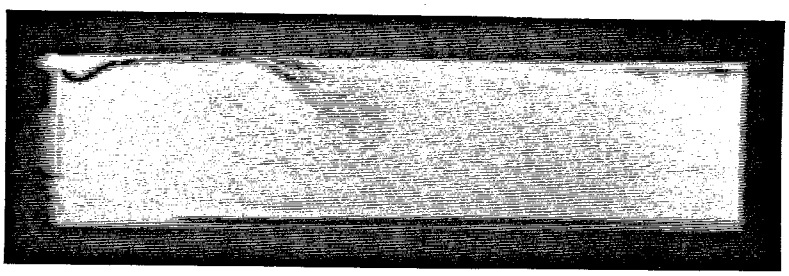

(*i*) 80 degrees

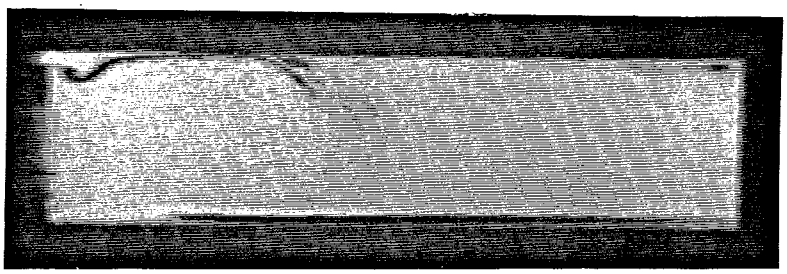

(*j*) 96 degrees

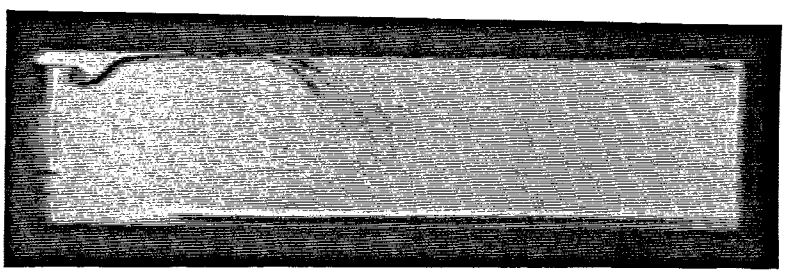

Figure 3.6f-j: Sequence of high-speed shadowgraphs for 7.62 cm duct, V_{dump}=21 m/s, ϕ=1.4.

(*k*) 112 degrees

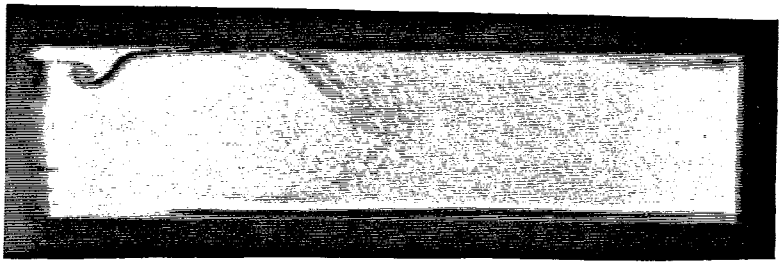

(*l*) 128 degrees

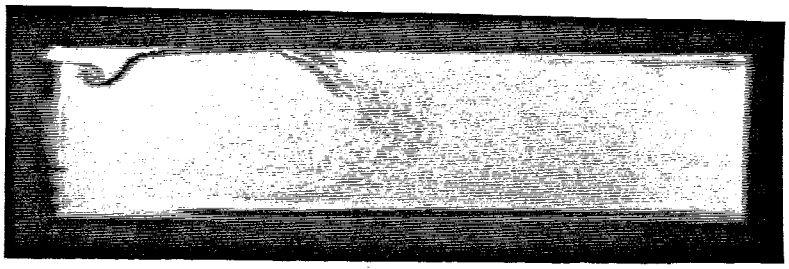

(*m*) 144 degrees

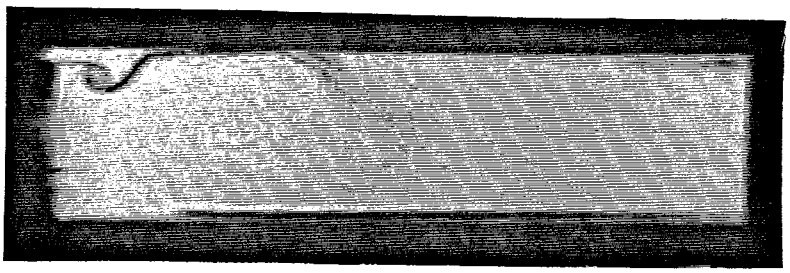

(*n*) 160 degrees

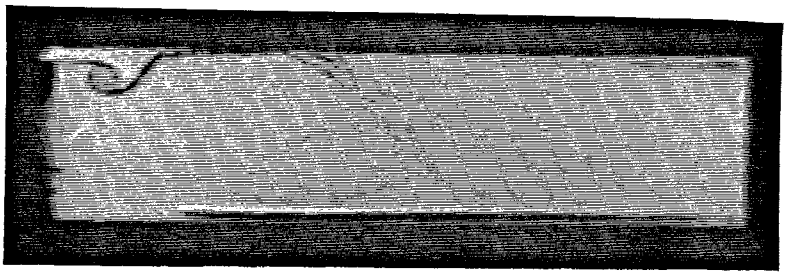

(*o*) 176 degrees

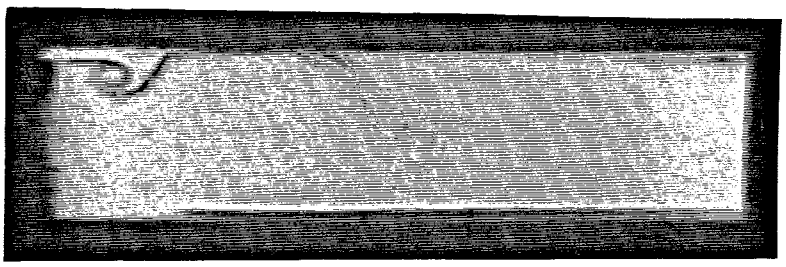

Figure 3.6k-o: Sequence of high-speed shadowgraphs for 7.62 cm duct, V_{dump}=21 m/s, ϕ=1.4.

(*p*) 192 degrees

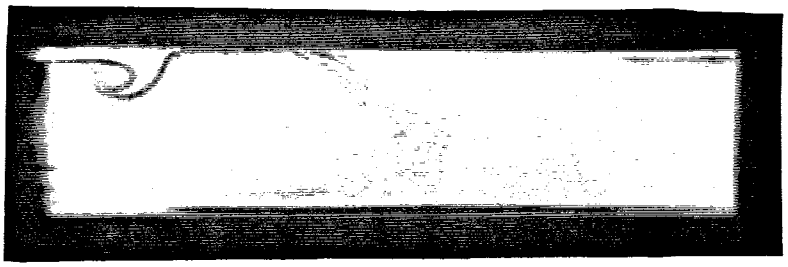

(*q*) 208 degrees

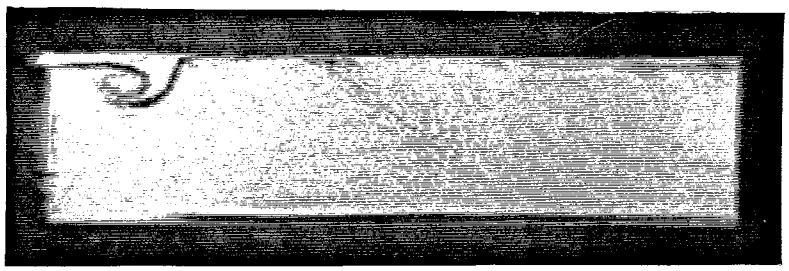

(*r*) 224 degrees

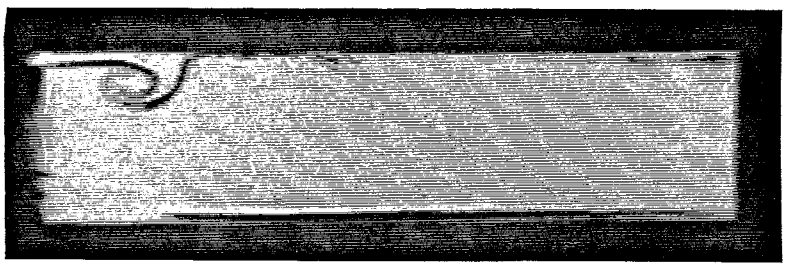

(*s*) 240 degrees

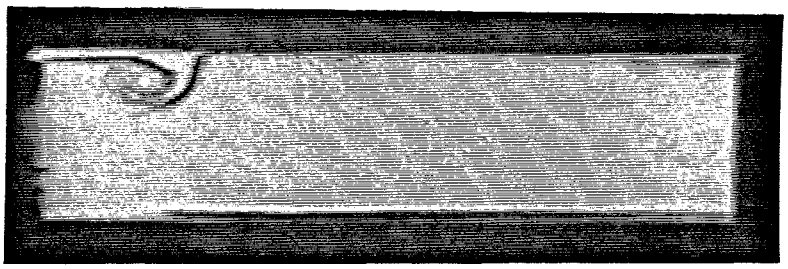

(*t*) 256 degrees

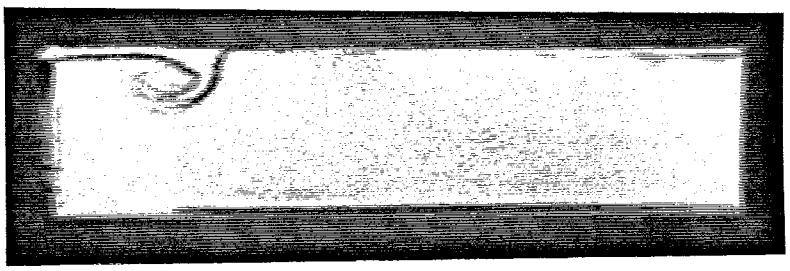

Figure 3.6p-t: Sequence of high-speed shadowgraphs for 7.62 cm duct, V_{dump}=21 m/s, ϕ=1.4.

(*u*) 272 degrees

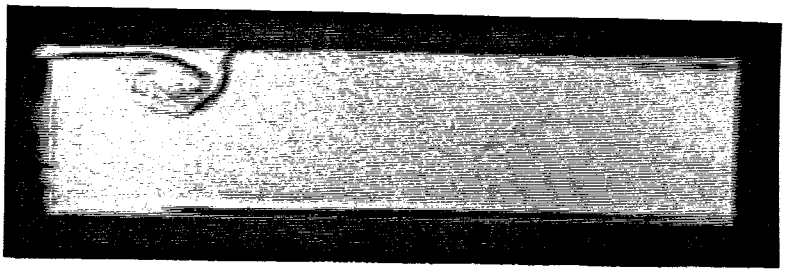

(*v*) 288 degrees

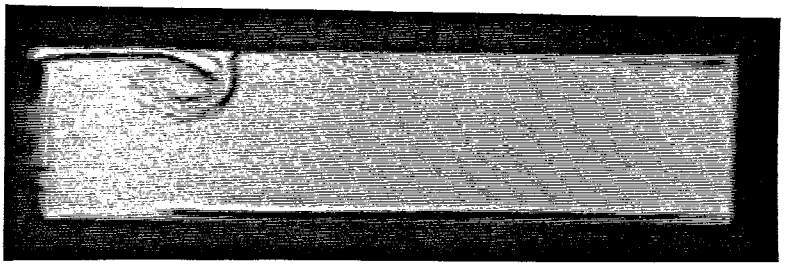

(*w*) 304 degrees

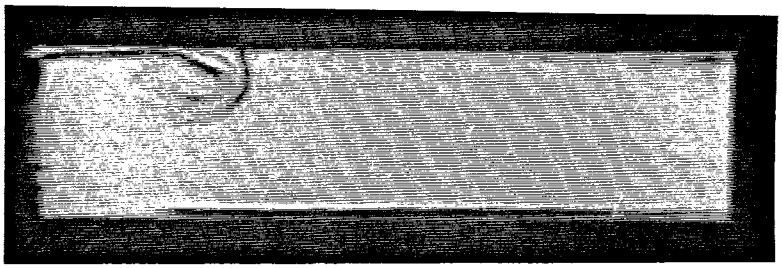

(*x*) 320 degrees

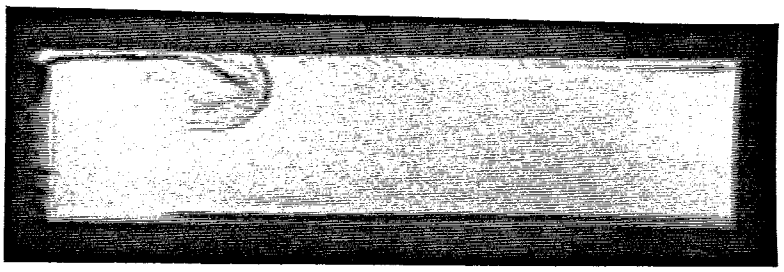

(*y*) 336 degrees

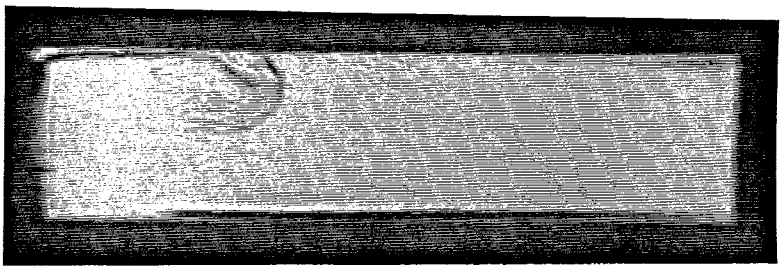

Figure 3.6u-y: Sequence of high-speed shadowgraphs for 7.62 cm duct, V_{dump}=21 m/s, ϕ=1.4.

(*z*) 352 degrees

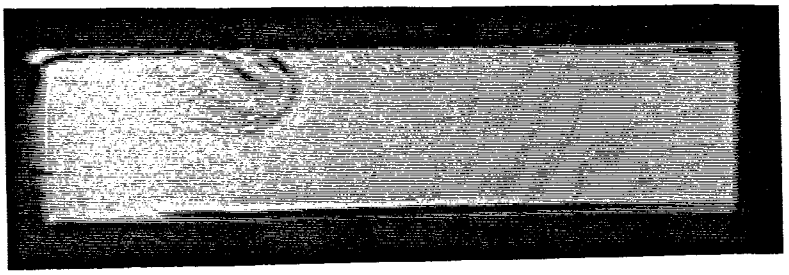

(*aa*) 368 degrees

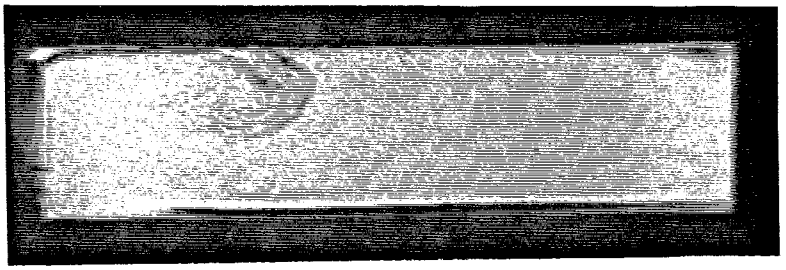

(*bb*) 384 degrees

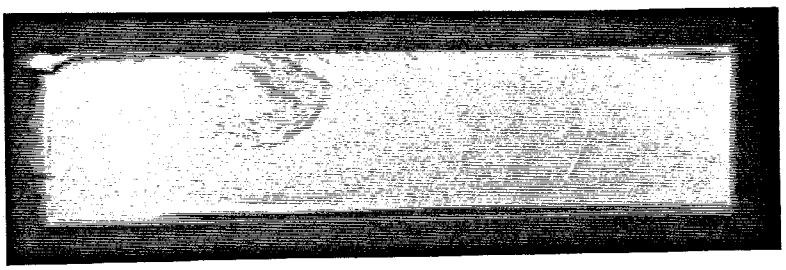

cc) 390 degrees

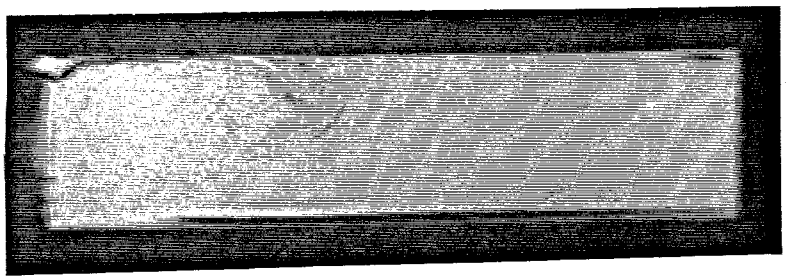

(*dd*) 406 degrees

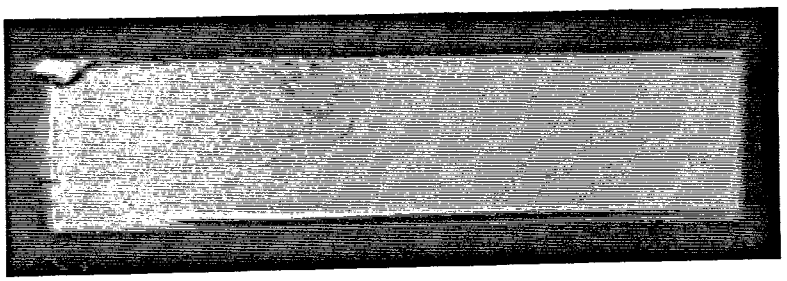

Figure 3.6z-dd: Sequence of high-speed shadowgraphs for 7.62 cm duct, V_{dump}=21 m/s, ϕ=1.4.

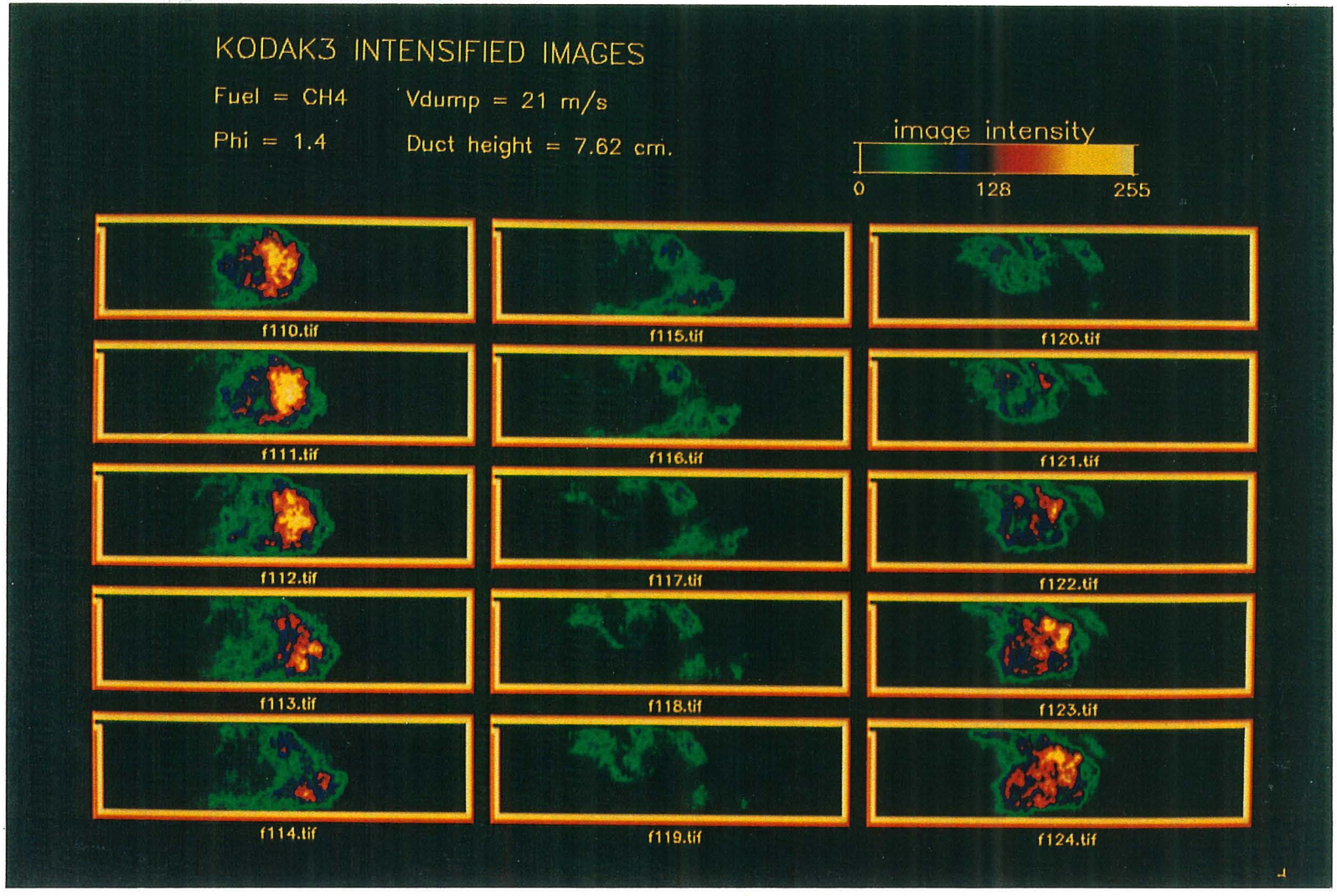

Figure 3.7a: Sequence of high-speed CCD images for 7.62 cm duct, 21 m/s, $\phi = 1.4$.

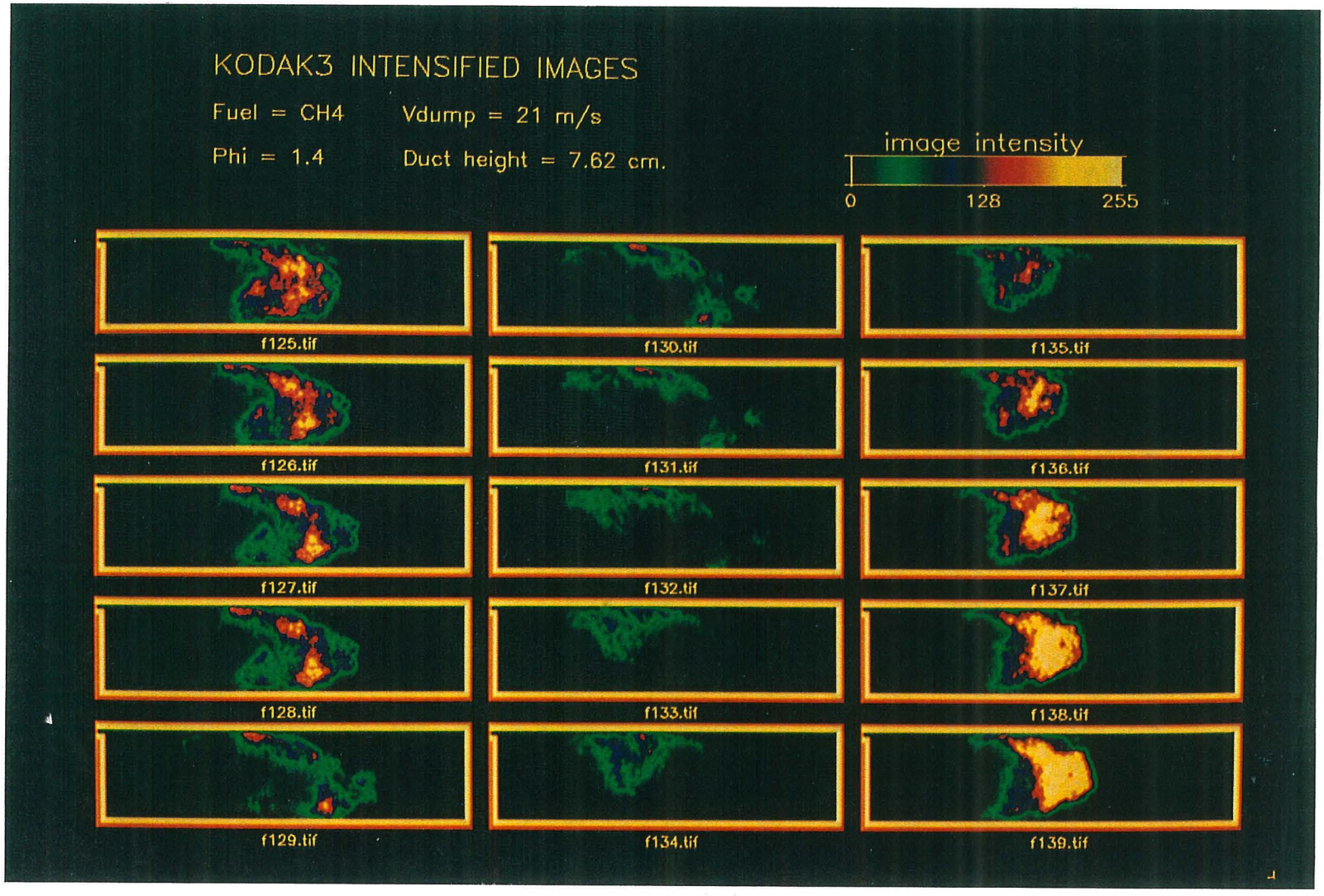

Figure 3.7b: Sequence of high-speed CCD images for 7.62 cm duct, 21 m/s, $\phi = 1.4$.

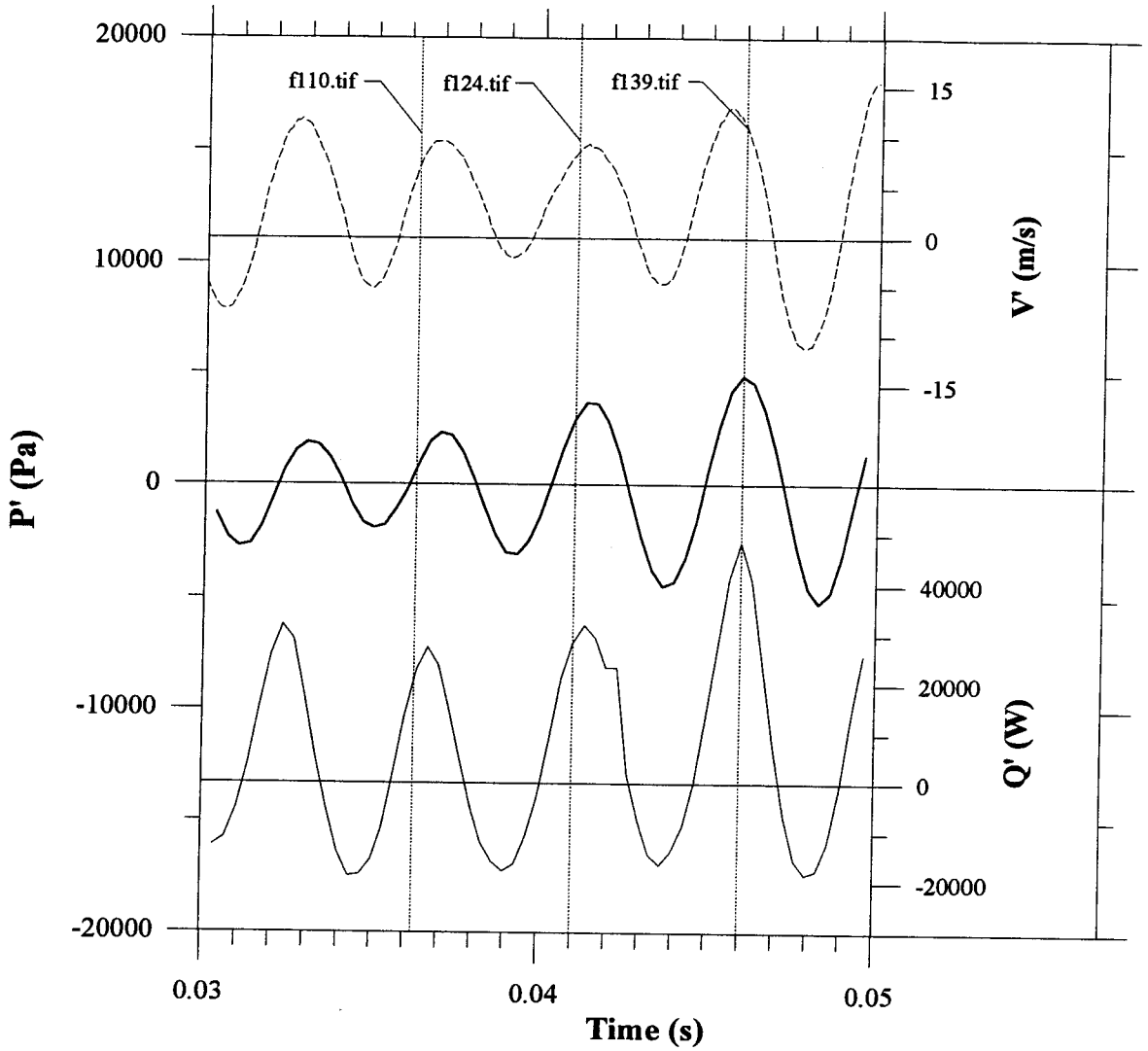

Figure 3.7c: Location of images on pressure trace.

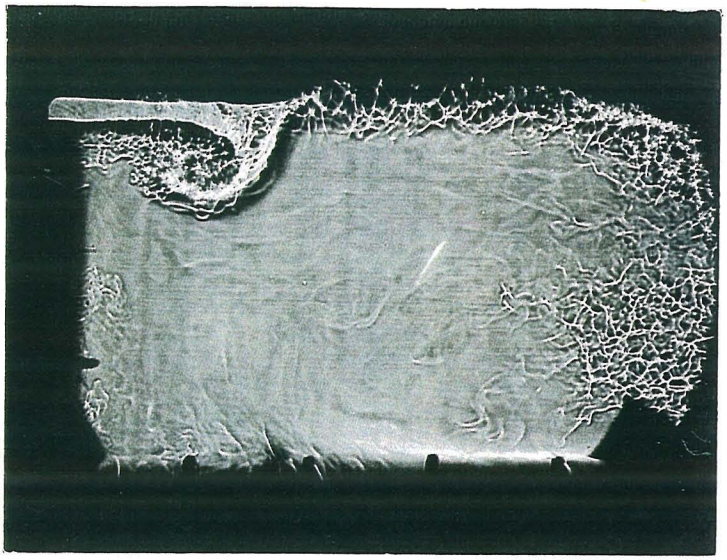

(*a*)

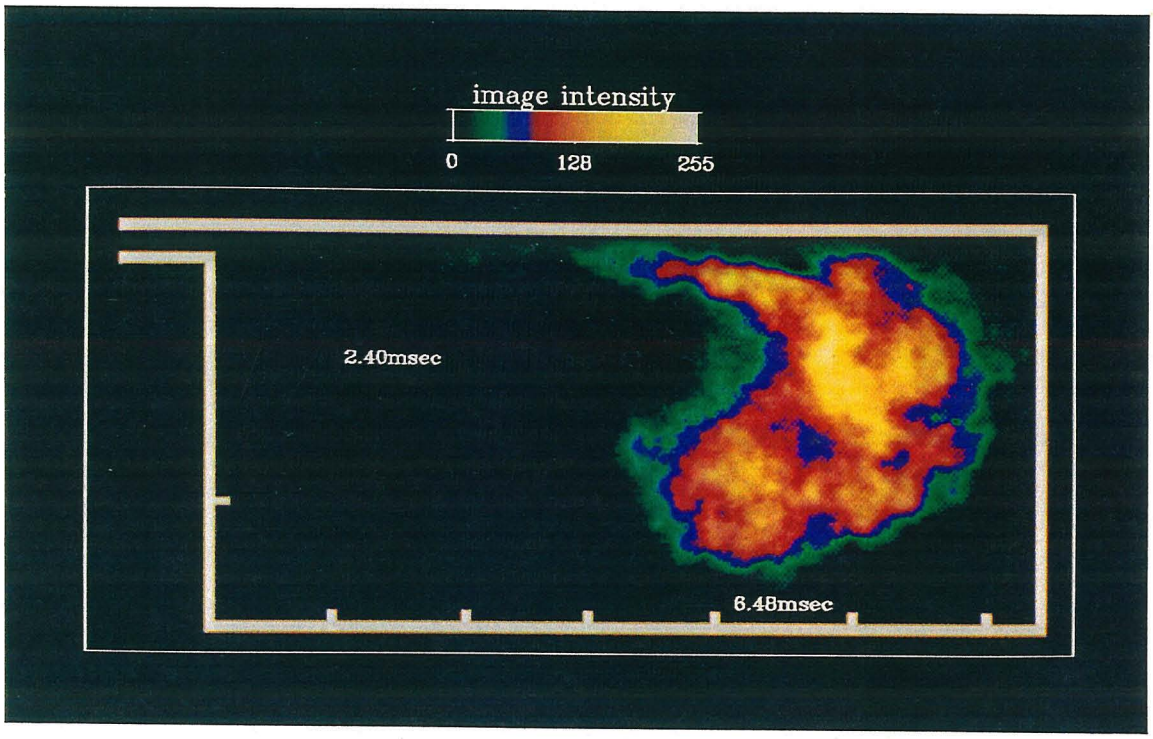

(*b*)

Figure 3.8: Simultaneous (a) shadowgraph and (b) chemiluminescence images at 203° in pressure cycle for 7.62 cm duct, V_{dump}=21 m/s, ϕ=1.4.

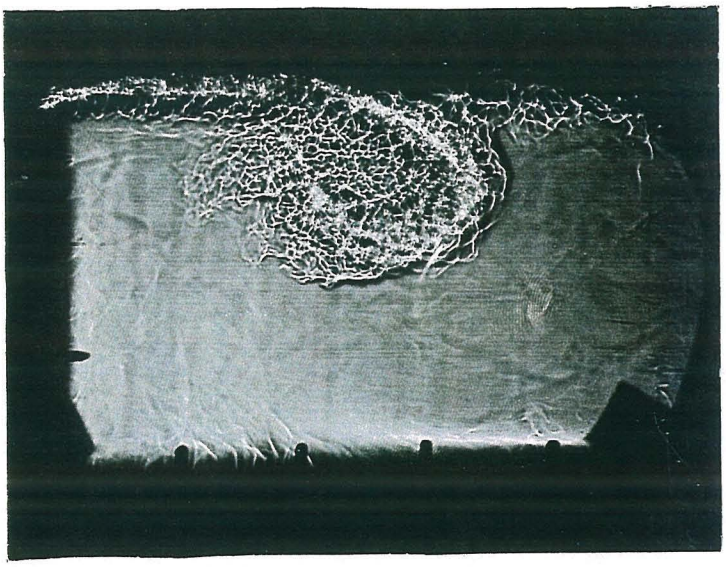

(*a*)

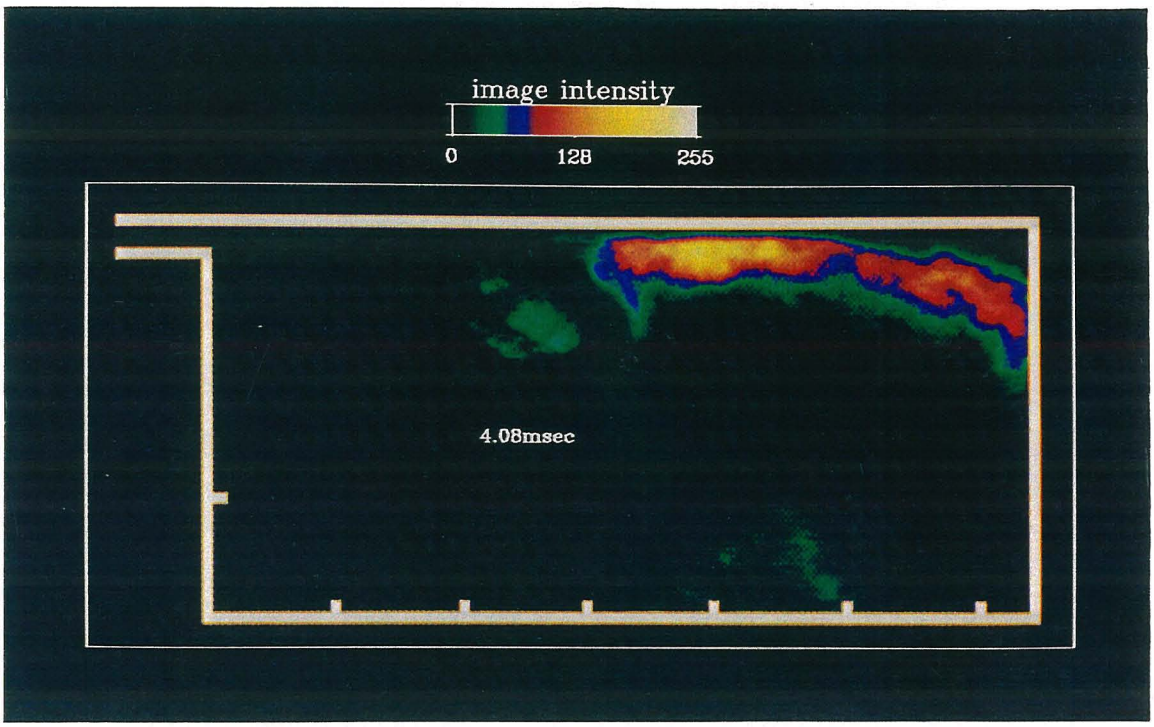

(*b*)

Figure 3.9: Simultaneous (a) shadowgraph and (b) chemiluminescence images at 345° in pressure cycle for 7.62 cm duct, V_{dump}=21 m/s, ϕ=1.4.

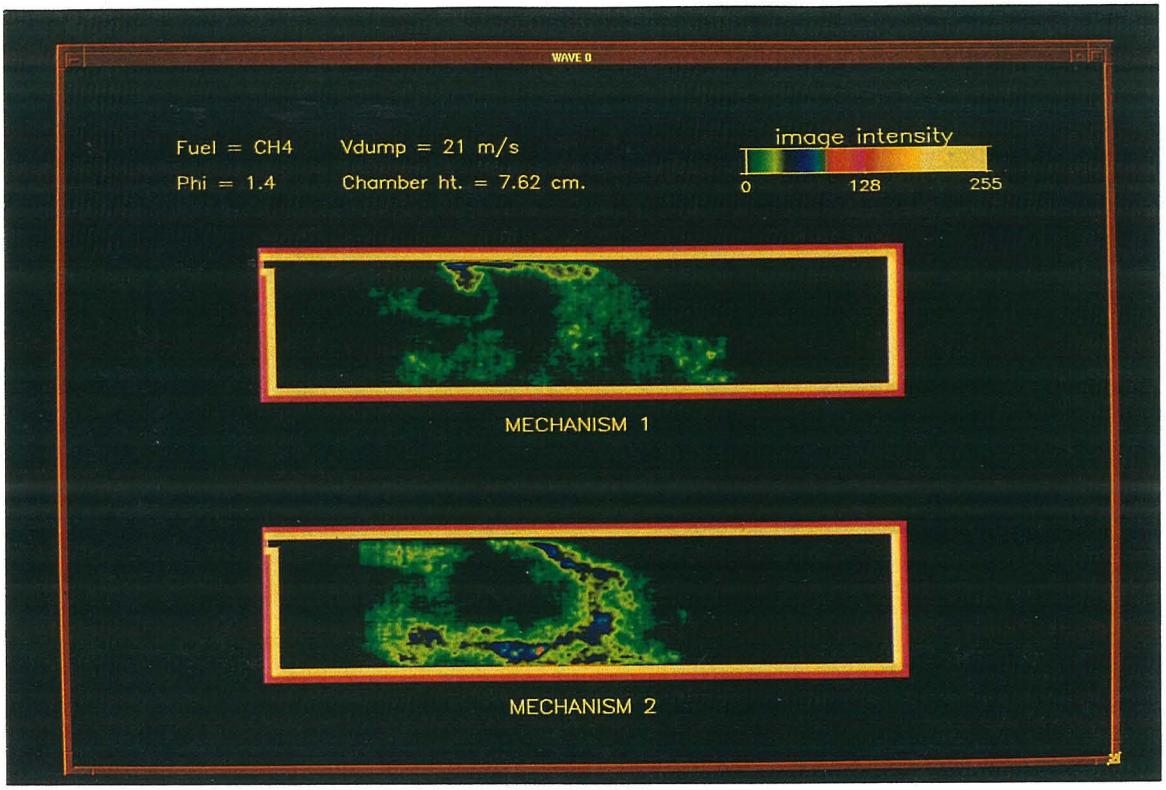

Figure 3.10: Two ignition mechanisms for 7.62 cm duct, V_{dump}=21 m/s, ϕ=1.4 instability.

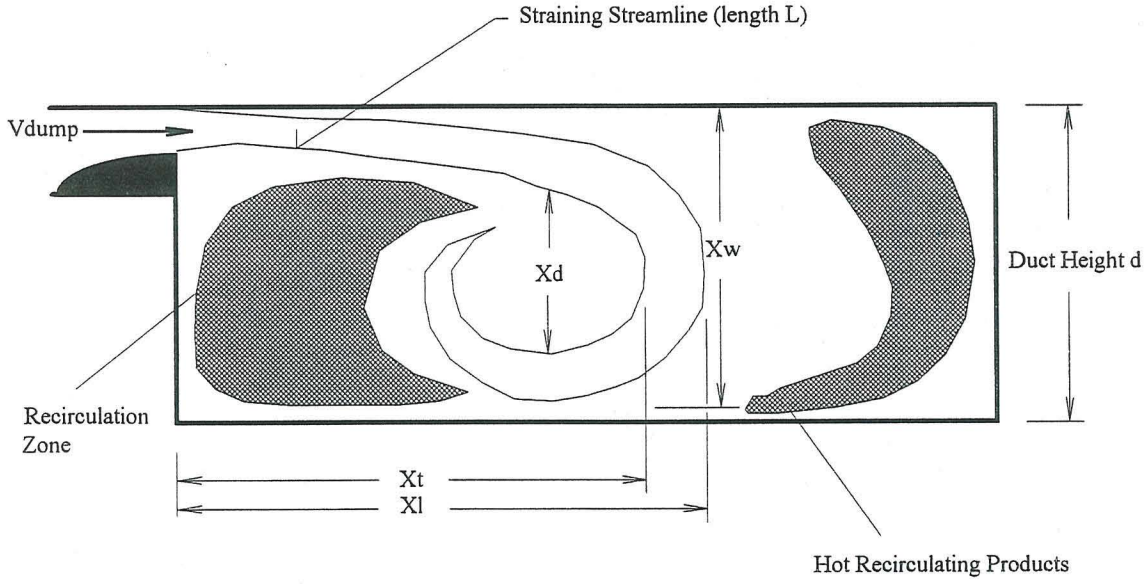

Figure 3.11: Sample structure in chamber with annotations.

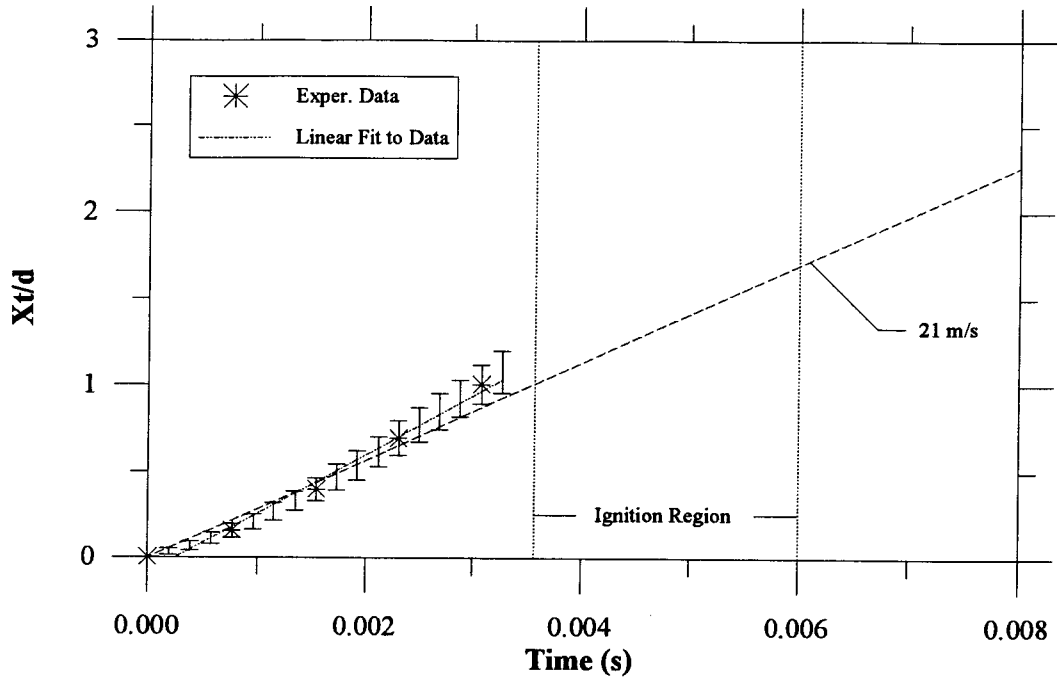

Figure 3.12a: X_t variation with time: 7.62 cm duct, V_{dump}=21 m/s, ϕ=1.4.

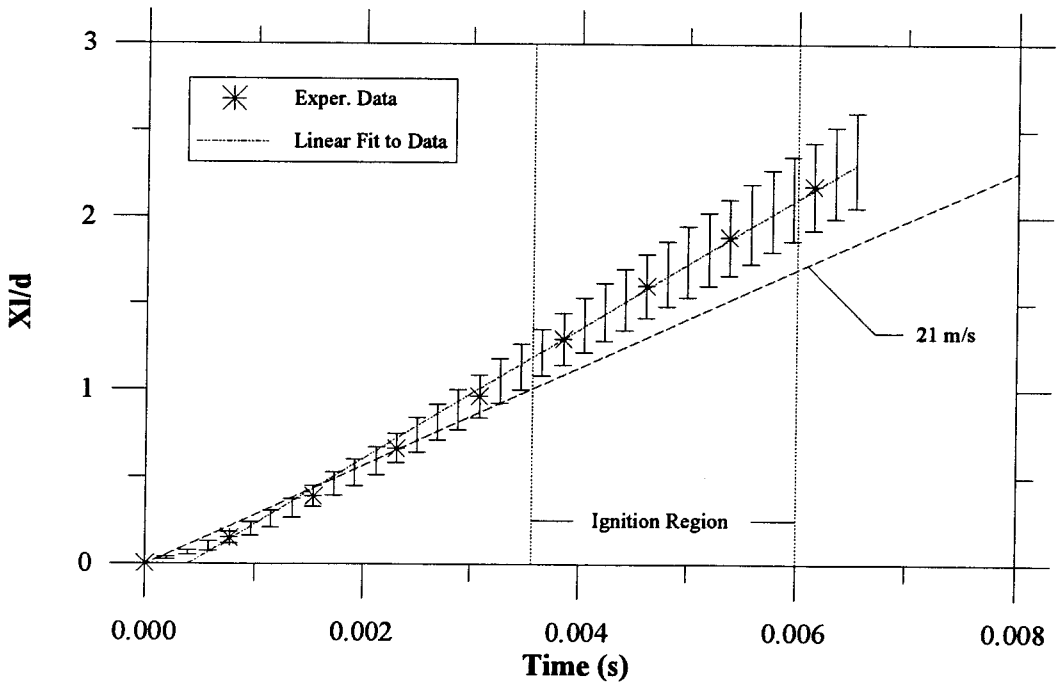

Figure 3.12b: X_l variation with time: 7.62 cm duct, V_{dump}=21 m/s, ϕ=1.4.

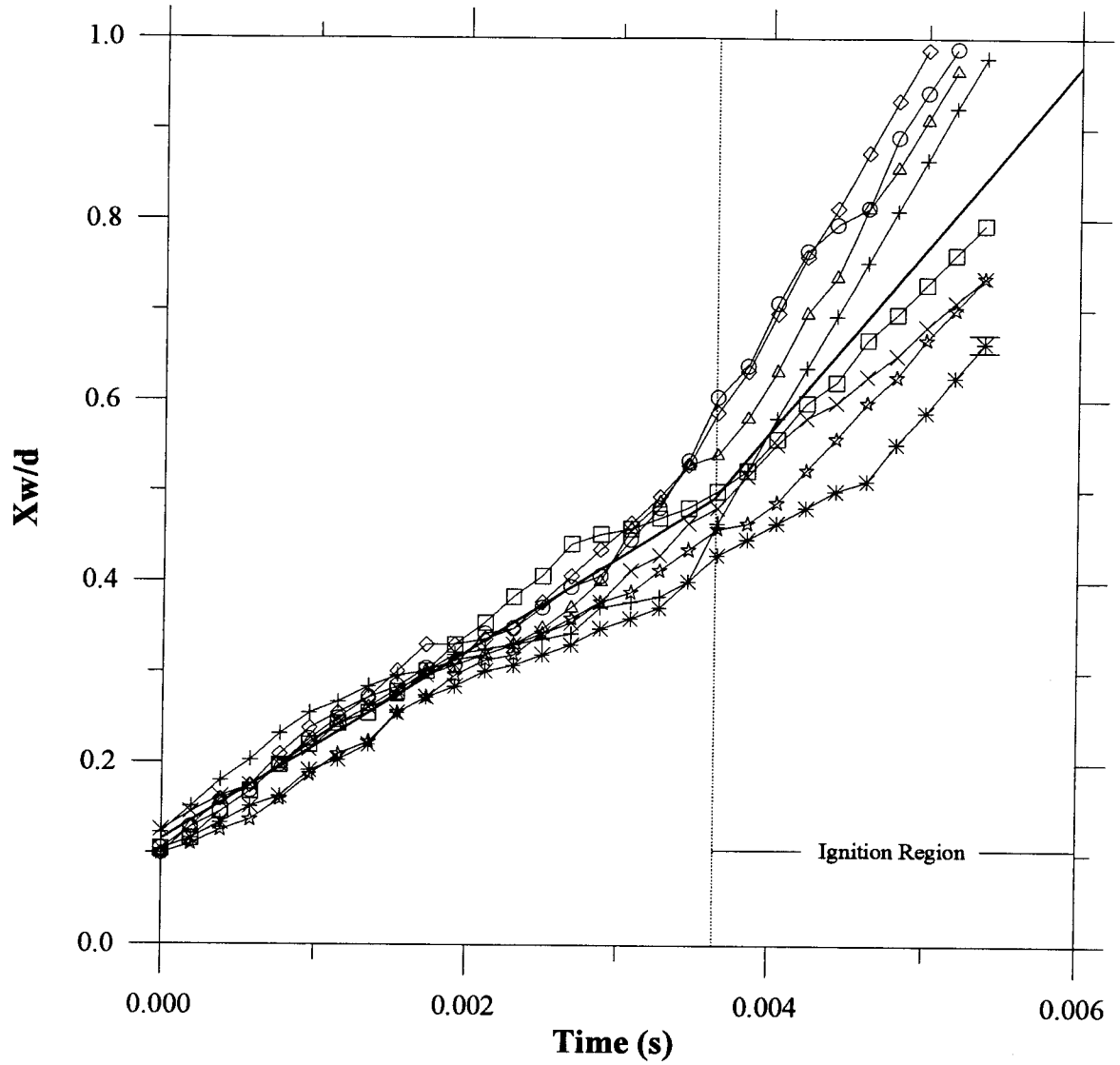

Figure 3.13: X_w versus time: 7.62 cm duct, V_{dump}=21 m/s, ϕ=1.4.

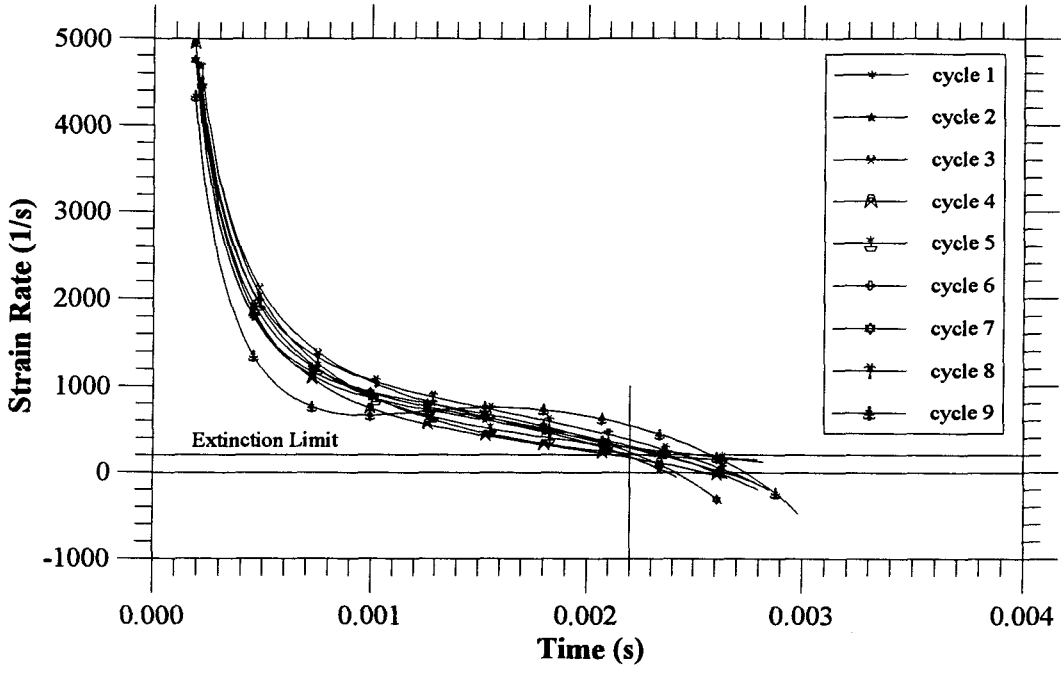

Figure 3.14a: Strain rate based on X_d: 7.62 cm duct, V_{dump}=21 m/s, ϕ=1.4.

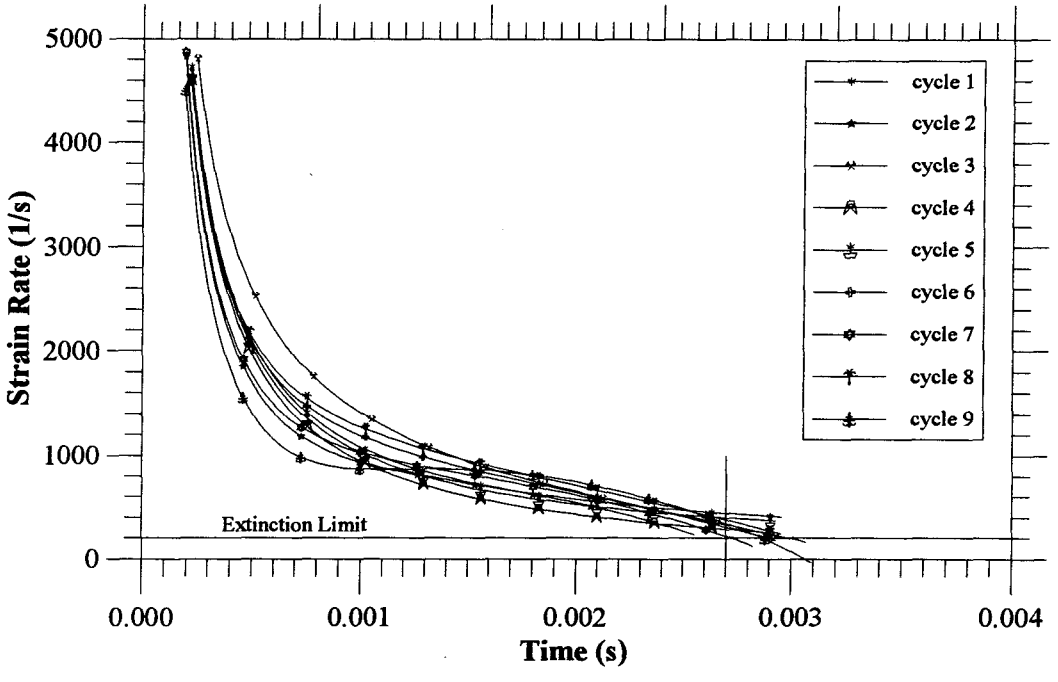

Figure 3.14b: Stain rate based on $\left(L-\frac{1}{2}V_{dump}\,t\right)$: 7.62 cm duct, V_{dump}=21 m/s, ϕ=1.4.

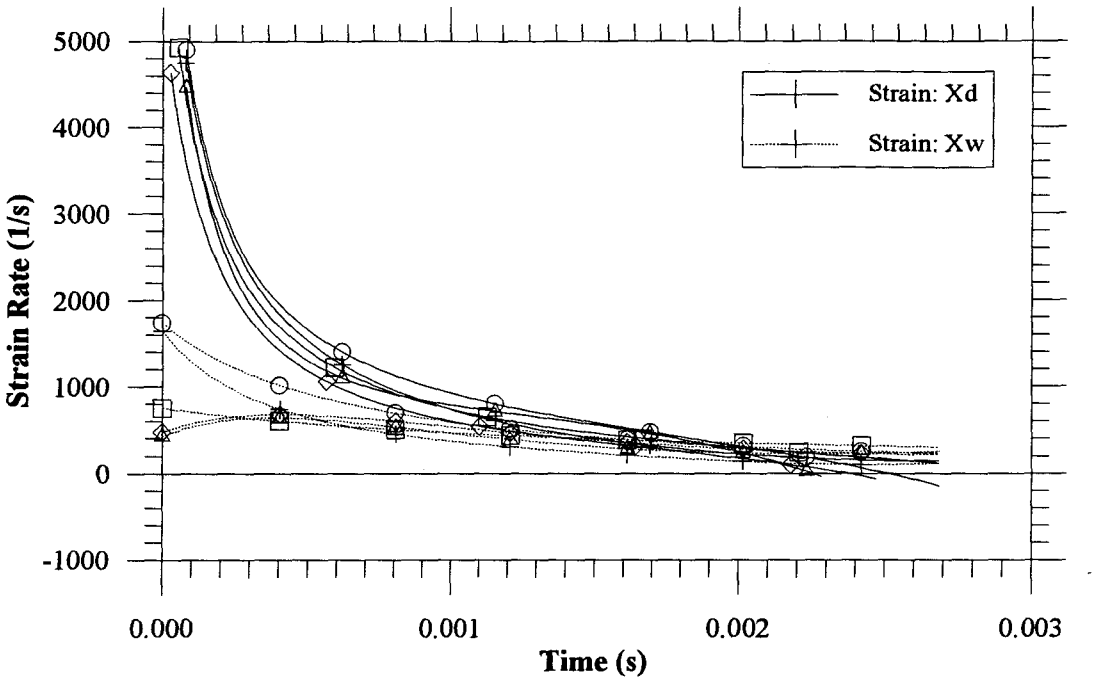

Figure 3.15: Comparison of inner (X_d) and outer (X_w) strain rate values: 7.62 cm duct, V_{dump}=21 m/s, ϕ=1.4.

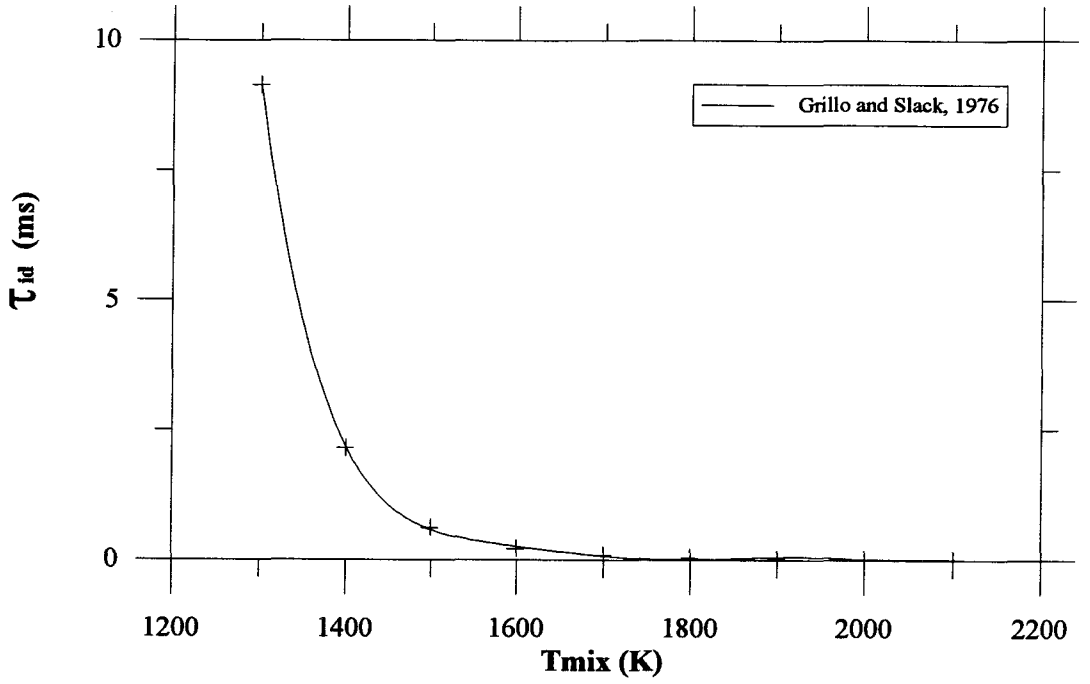

Figure 3.16: Ignition delay versus initial mixture temperature, T_{mix}.

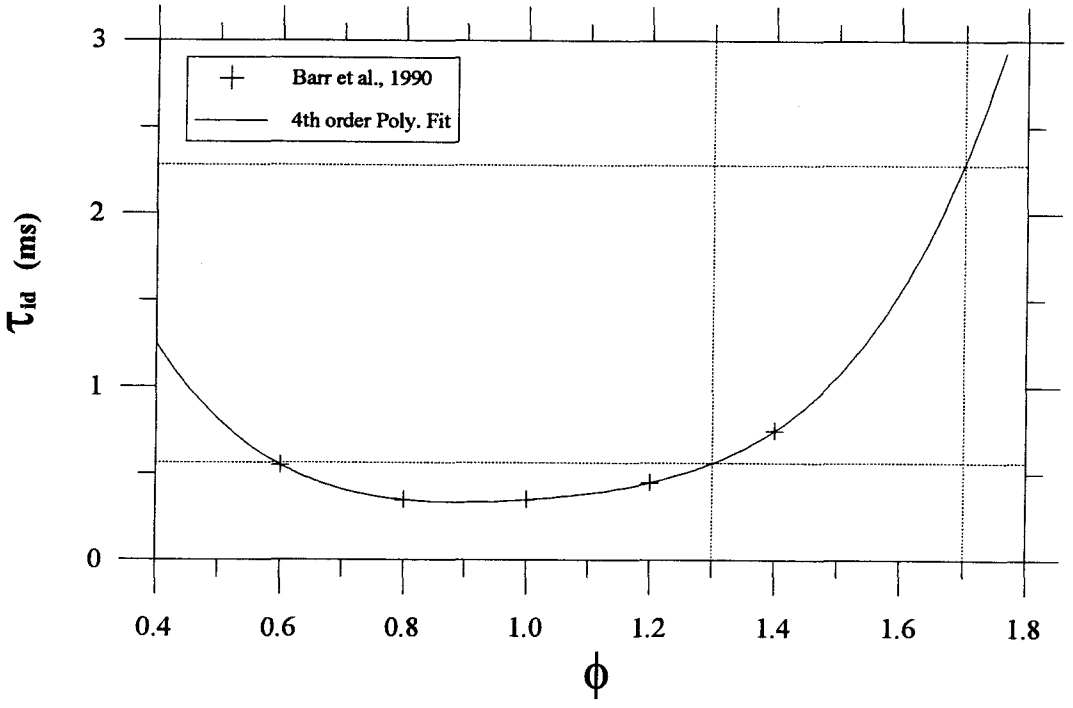

Figure 3.17: Ignition delay plotted versus ϕ assuming heated reactants.

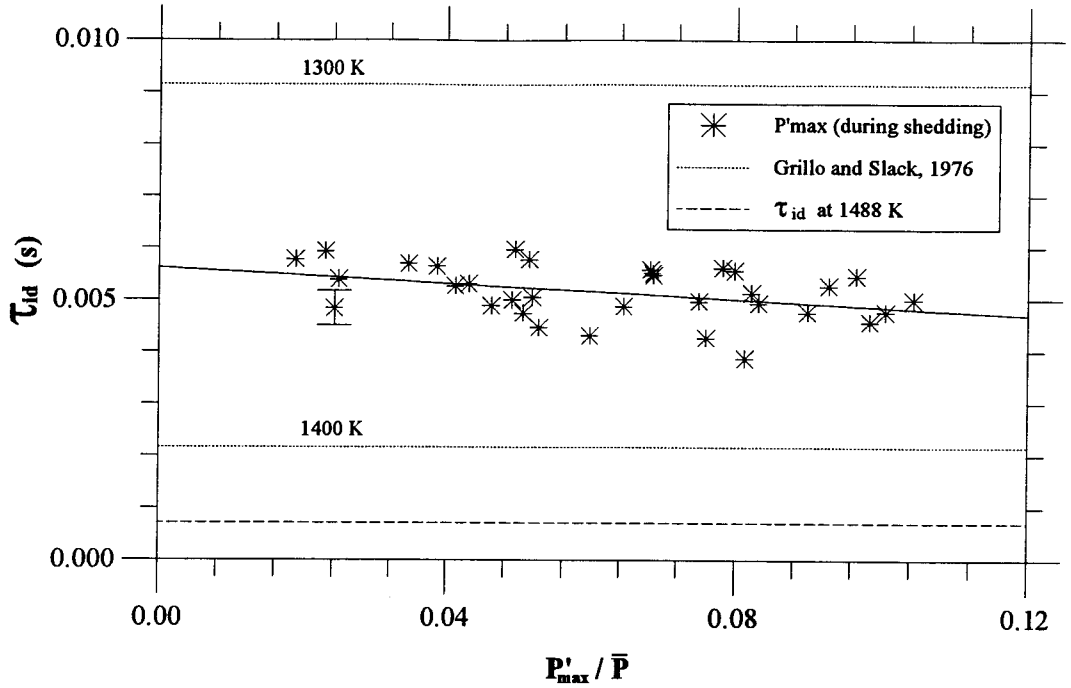

Figure 3.18a: Ignition delay plotted versus P'_{max} during shedding.

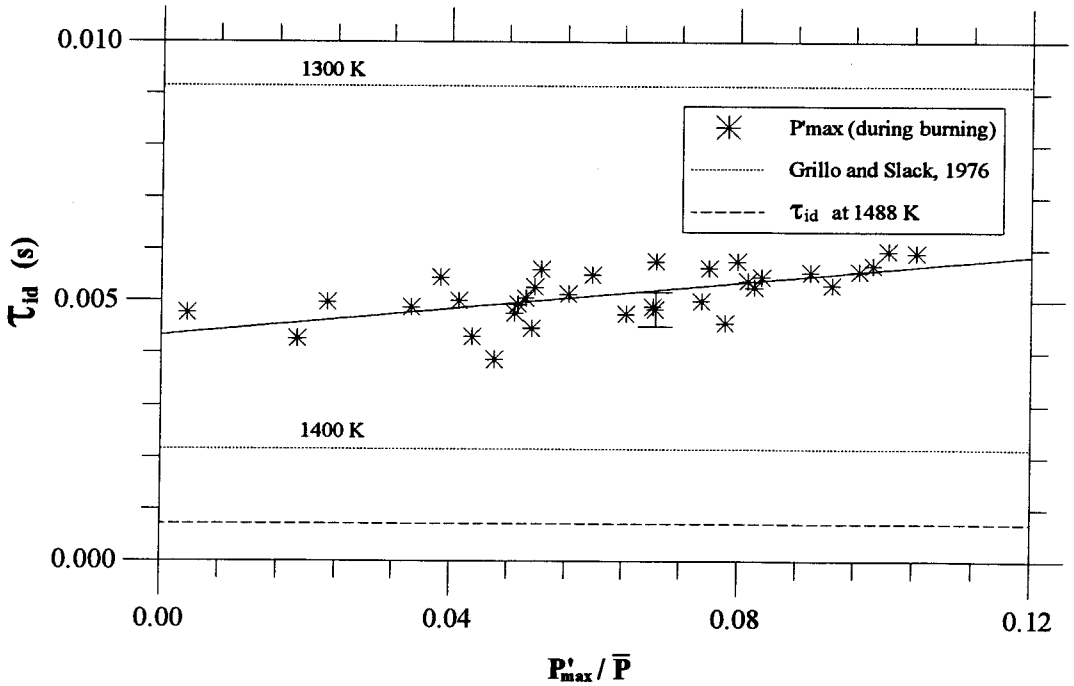

Figure 3.18b: Ignition delay plotted versus P'_{max} during burning.

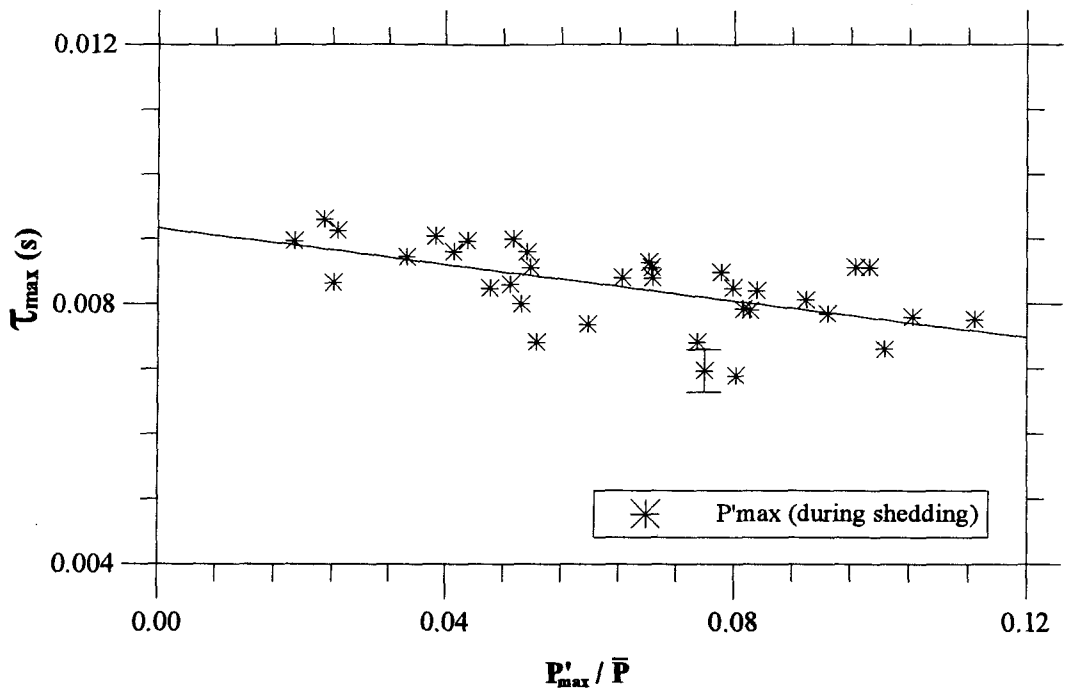

Figure 3.19a: Delay to I_{max} plotted versus P'_{max} during shedding.

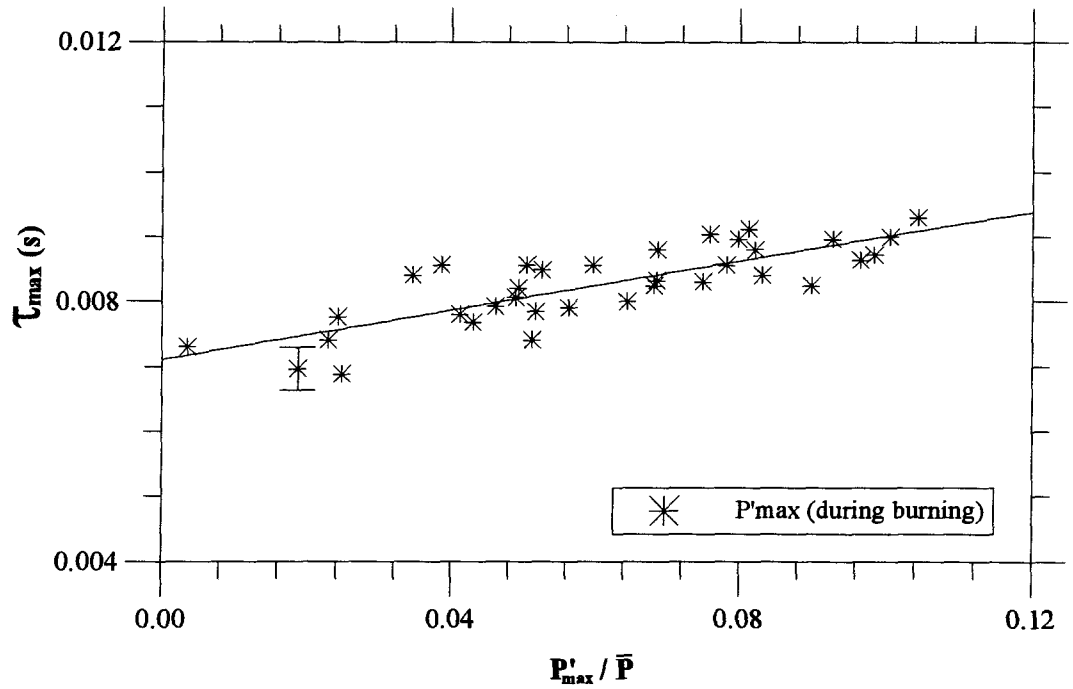

Figure 3.19b: Delay to I_{max} plotted versus P'_{max} during burning.

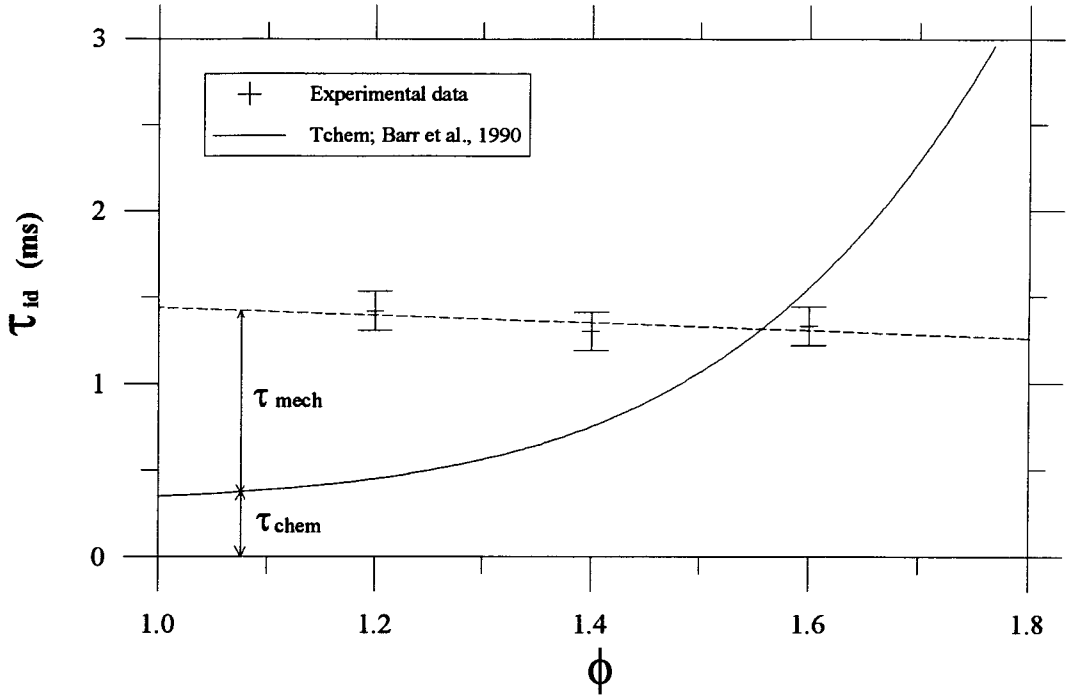

Figure 3.20: Ignition delay versus ϕ: 5.08 cm duct, $V_{dump} = 30\ m/s$.

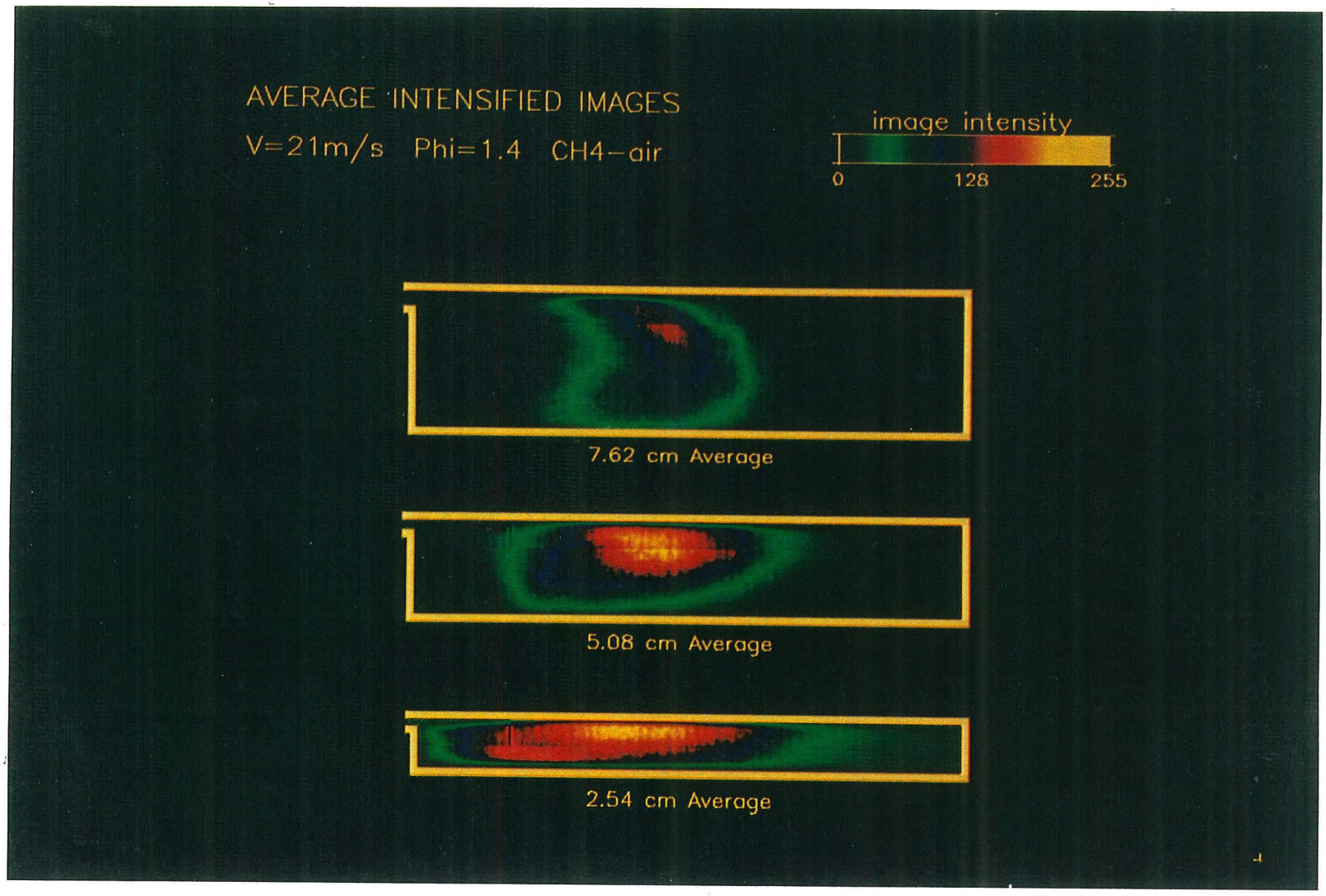

Figure 3.21: CCD averaged images: 21 m/s, $\phi = 1.4$; 7.62, 5.08 and 2.54 cm ducts.

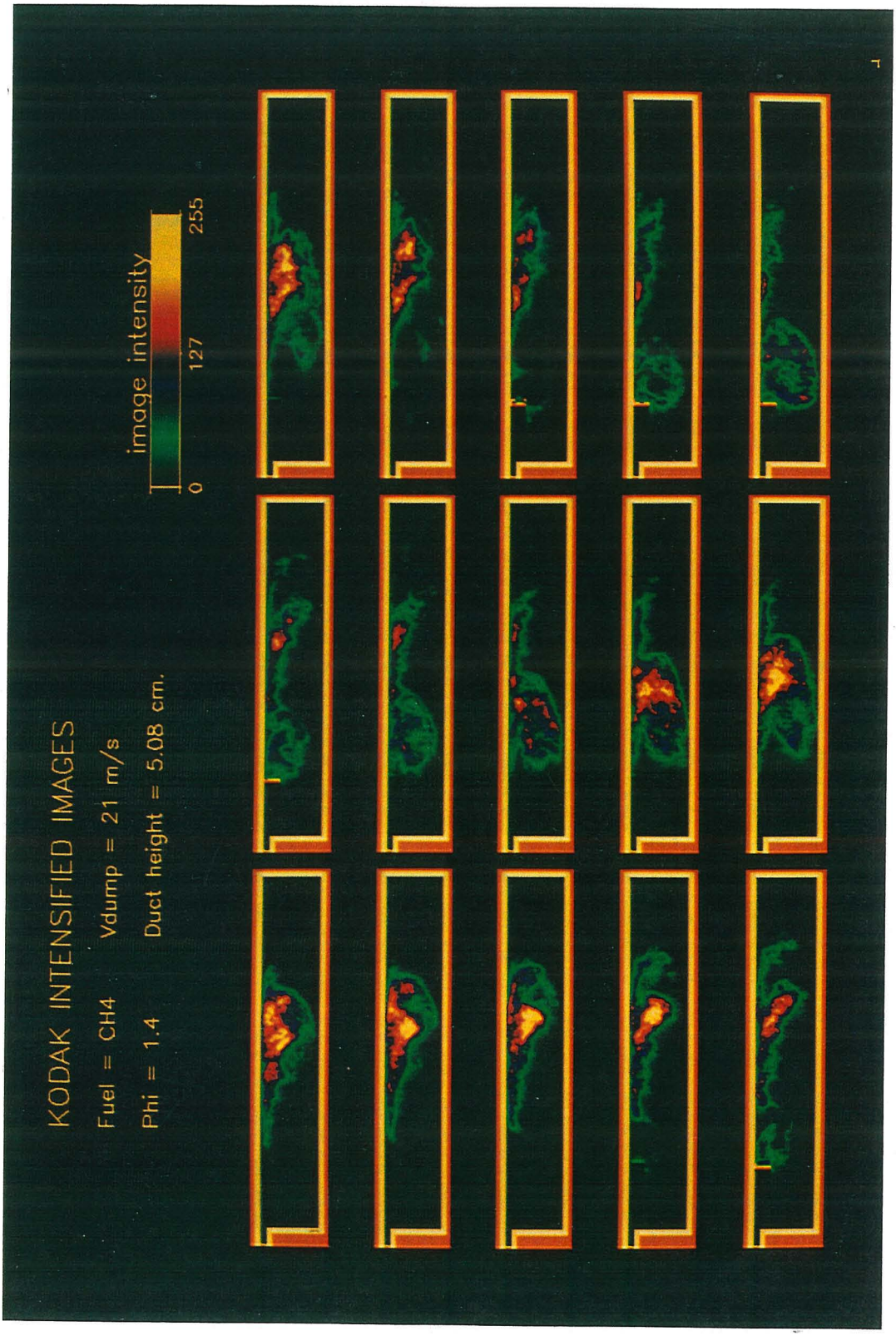

Figure 3.22: Partial CCD sequence: 5.08 cm duct, 21 m/s, $\phi = 1.4$.

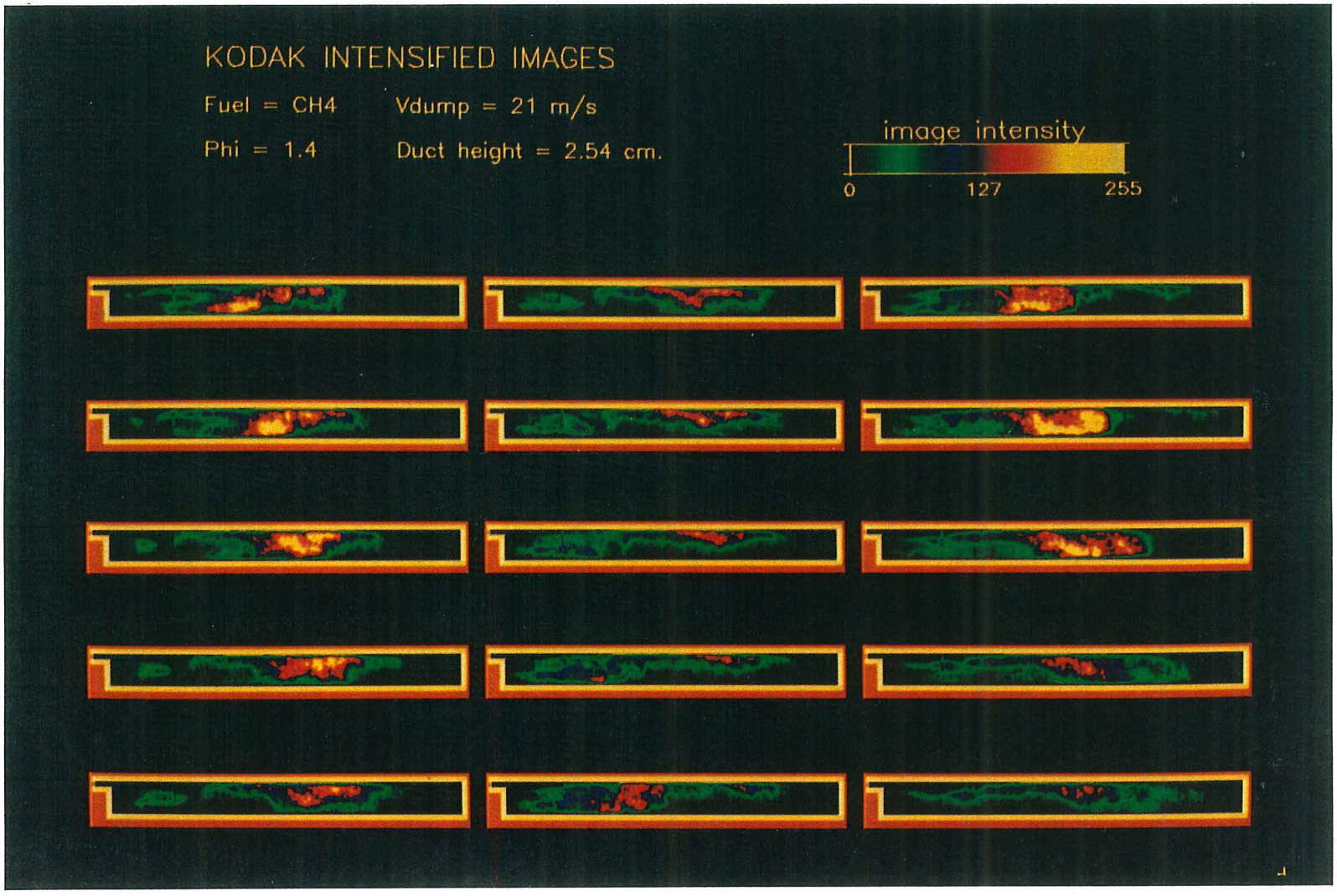

Figure 3.23a: Partial CCD sequence: 2.54 cm duct, 21 m/s, $\phi = 1.4$.

(b)

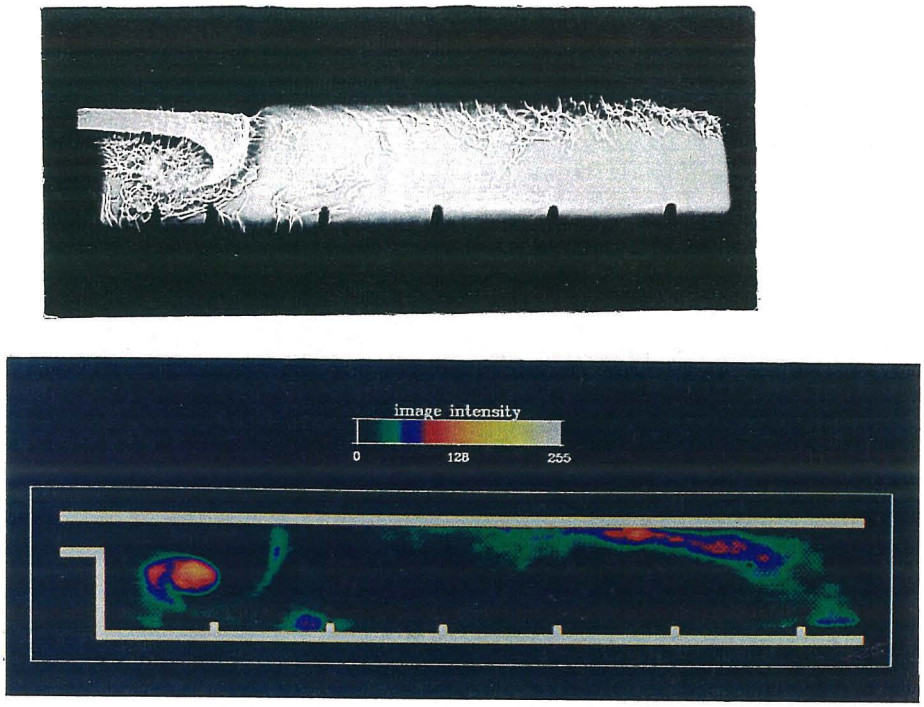

(c)

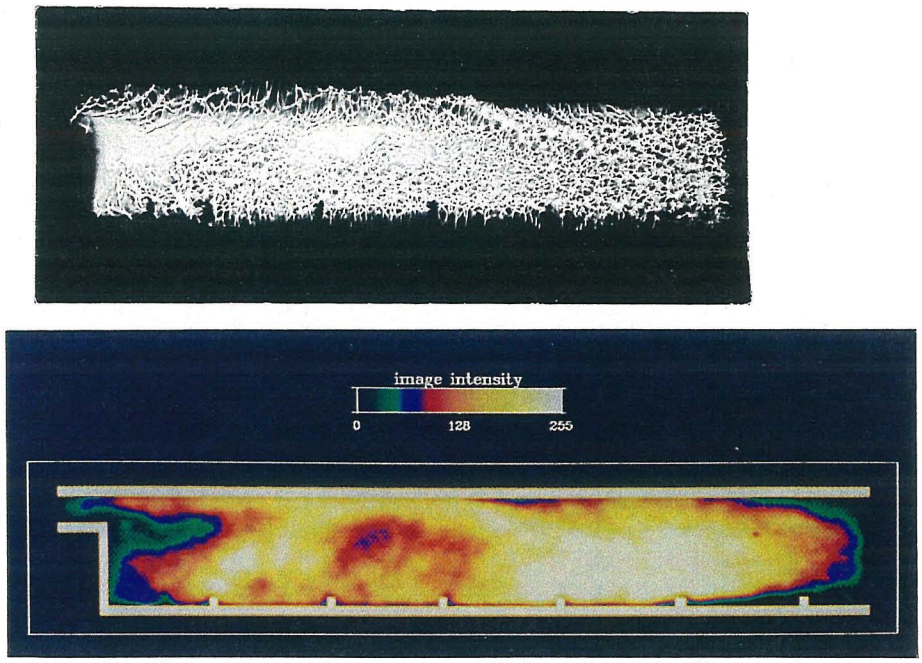

Figure 3.23: (b) Simultaneous shadowgraph (top) and chemiluminescence (bottom) images 81° and (c) 142° in pressure cycle; 2.54 cm duct.

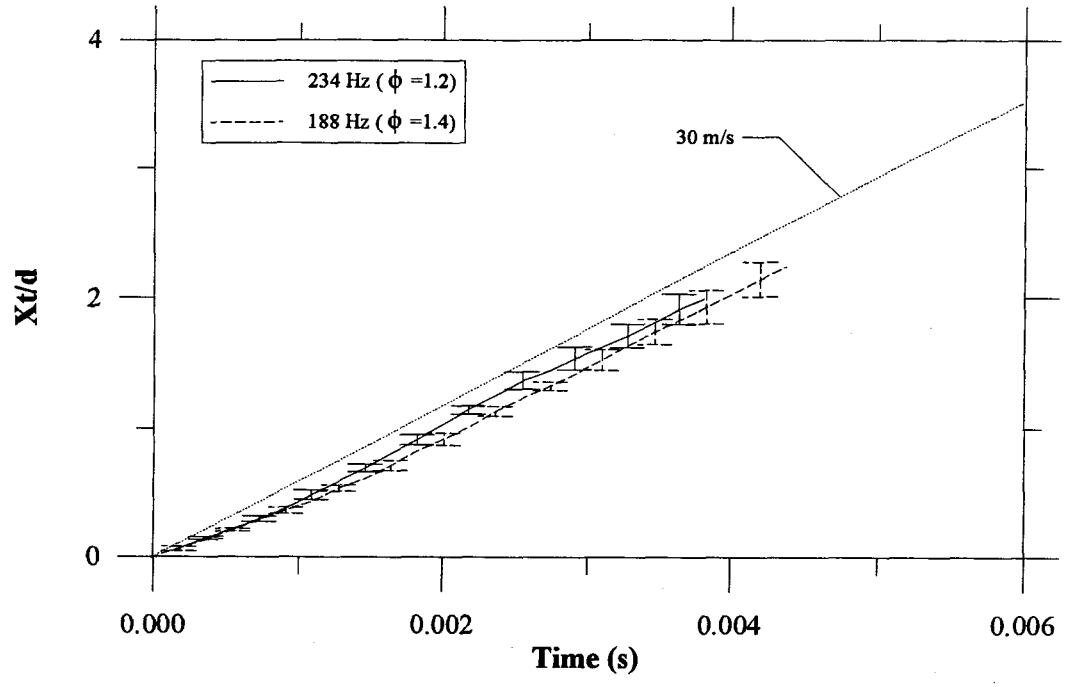

Figure 3.24a: X_t variation with time for two $\nu_{shedding}$: 5.08 cm duct, $V_{dump} = 30 m/s$.

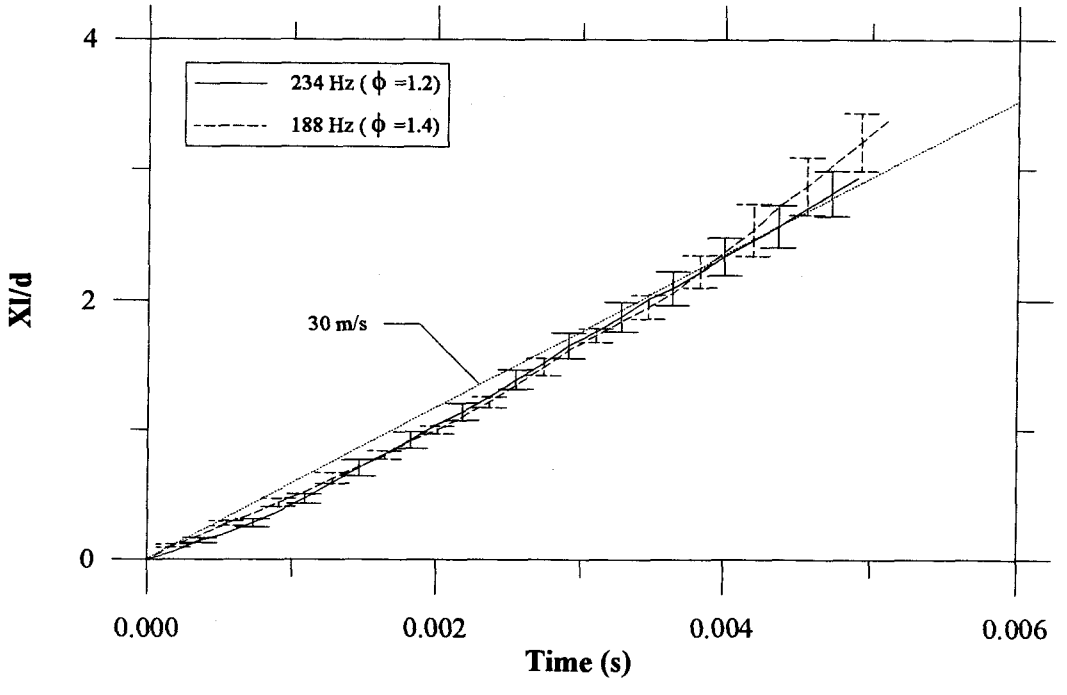

Figure 3.24b: X_l variation with time for two $\nu_{shedding}$: 5.08 cm duct, $V_{dump} = 30 m/s$.

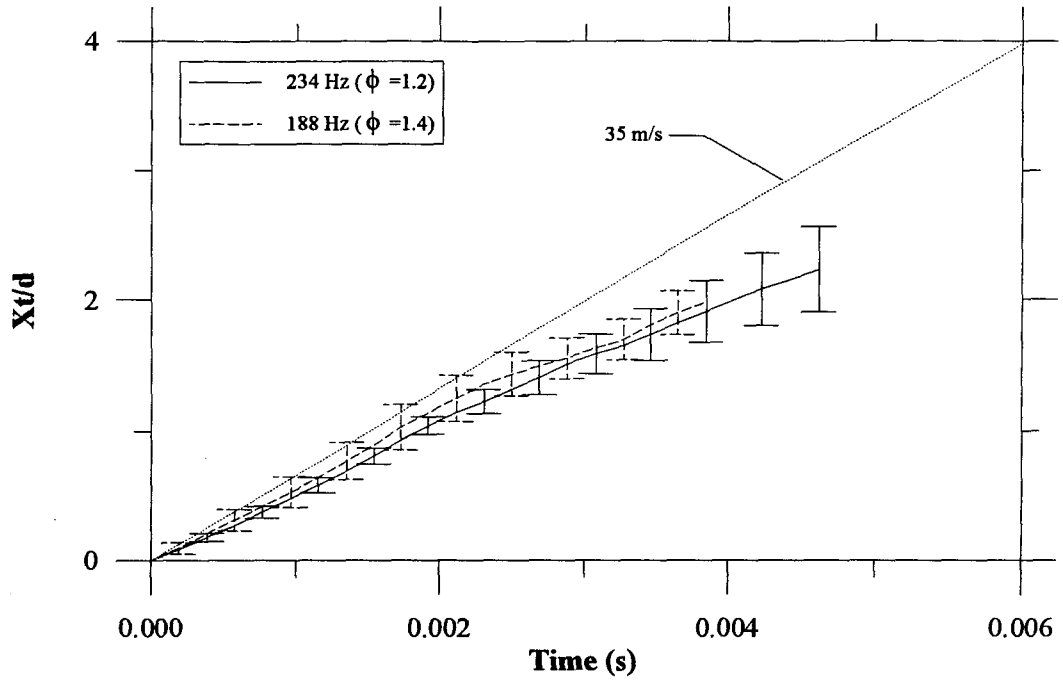

Figure 3.25a: X_t variation with time for two $\nu_{shedding}$: 5.08 cm duct, $V_{dump} = 35 m/s$.

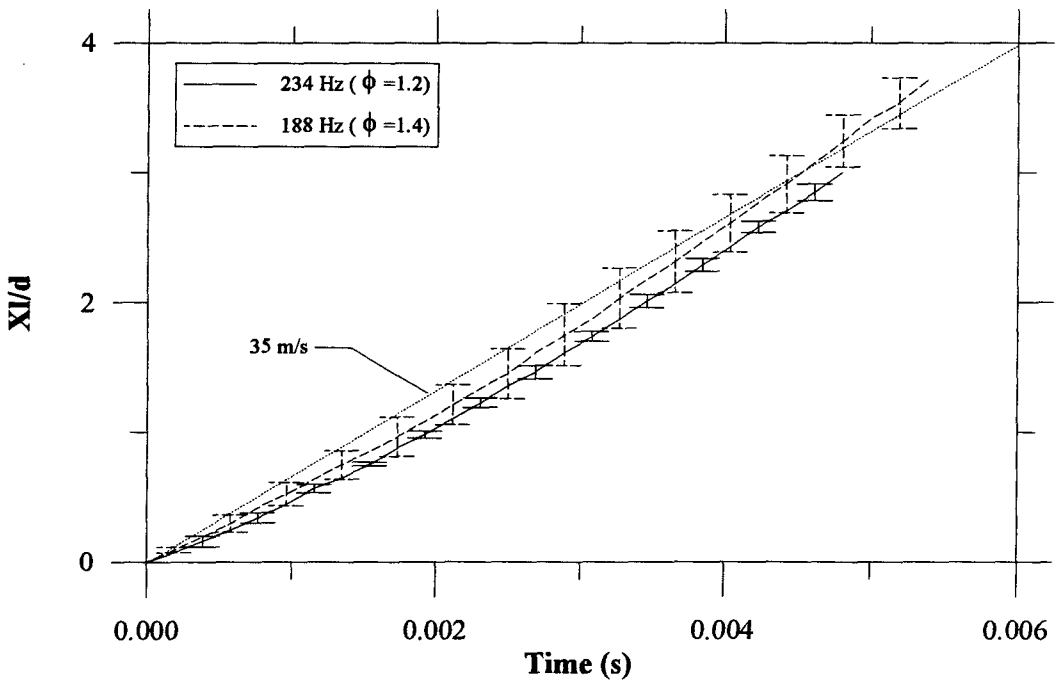

Figure 3.25b: X_l variation with time for two $\nu_{shedding}$: 5.08 cm duct, $V_{dump} = 35 m/s$.

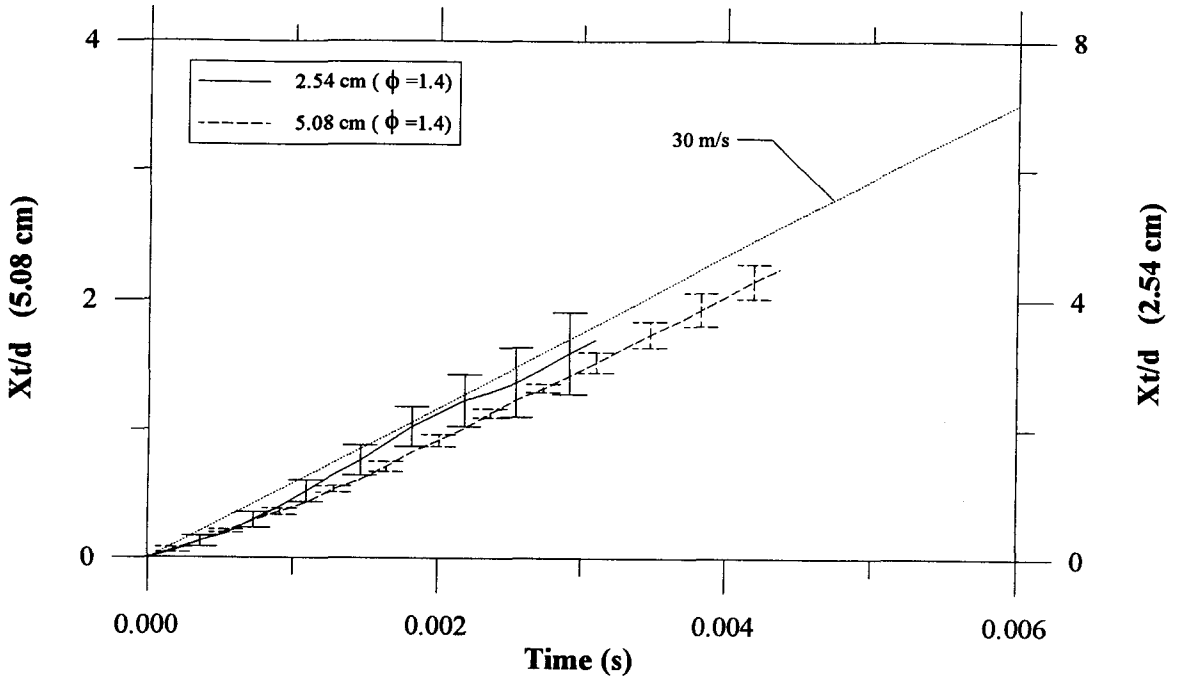

Figure 3.26a: X_t variation with time for two duct heights: $\phi = 1.4$, $V_{dump} = 30 m/s$.

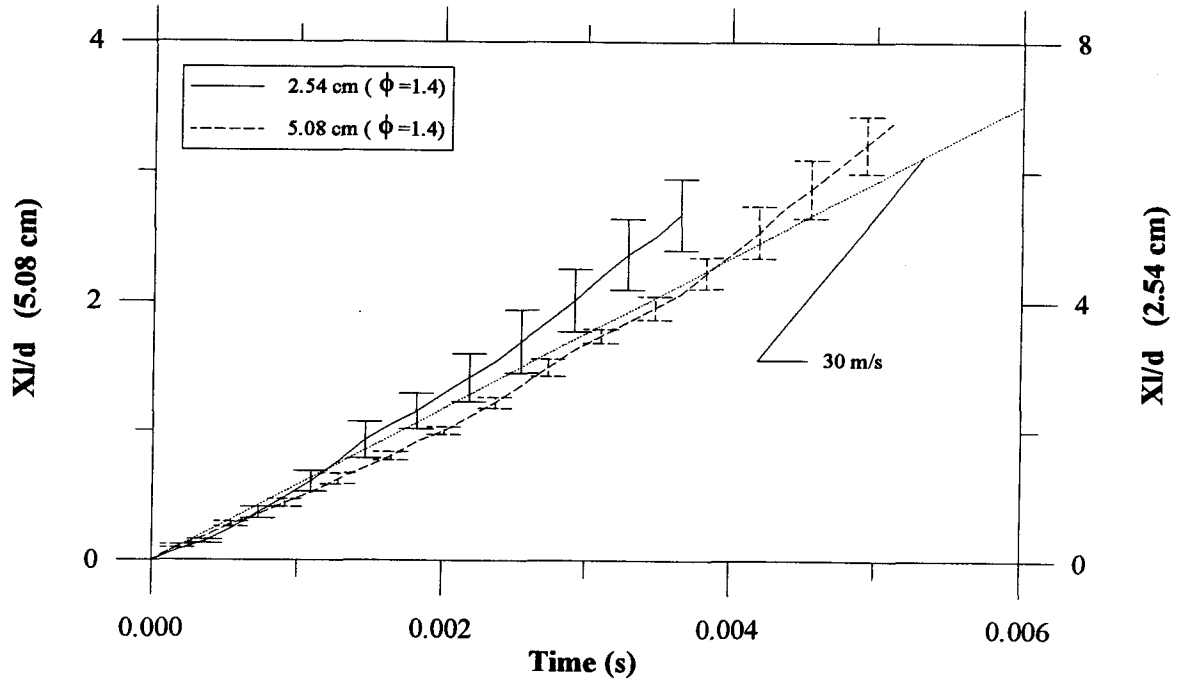

Figure 3.26b: X_l variation with time for two duct heights: $\phi = 1.4$, $V_{dump} = 30 m/s$.

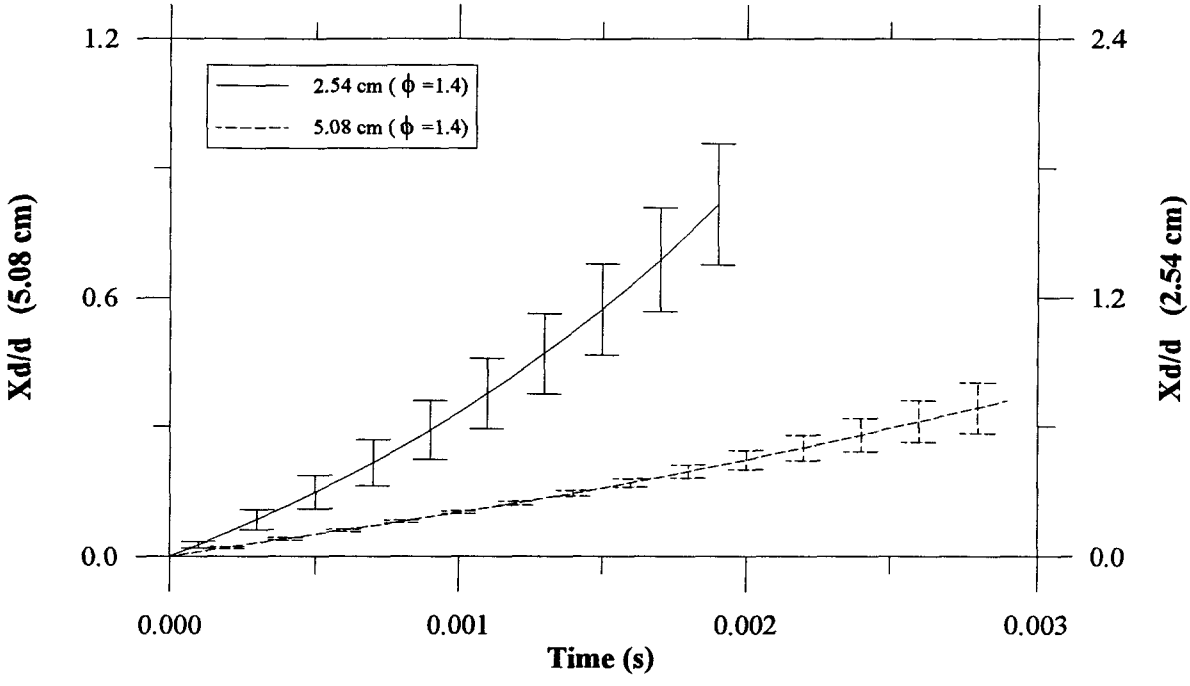

Figure 3.27a: X_d variation with time for two duct heights: $\phi = 1.4$, $V_{dump} = 30\ m/s$.

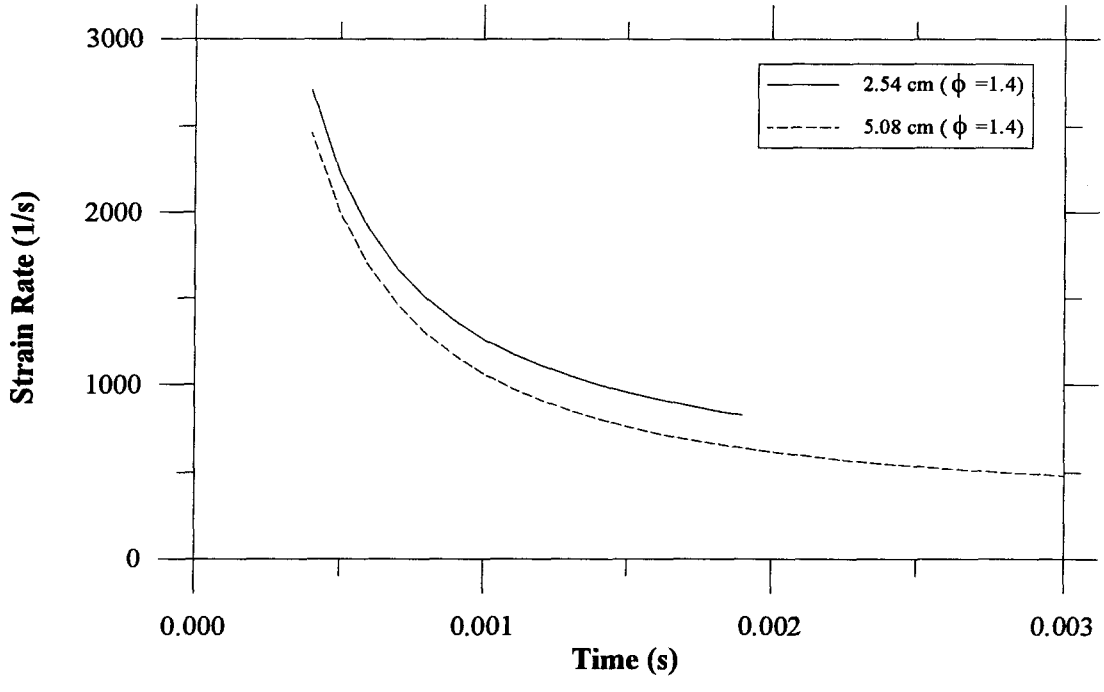

Figure 3.27b: X_d based strain rate for two duct heights: $\phi = 1.4$, $V_{dump} = 30\ m/s$.

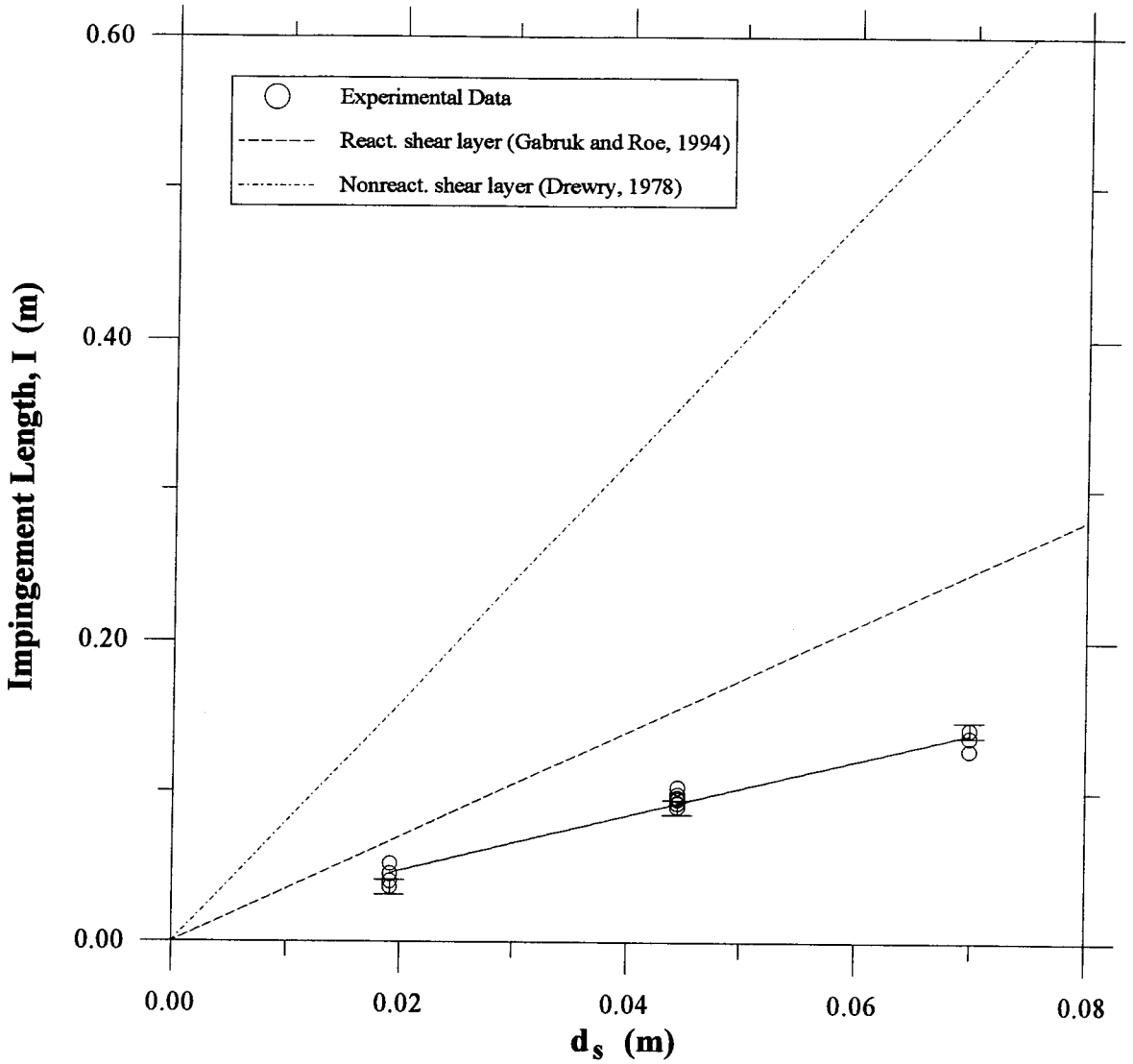

Figure 3.28: Vortex impingement location, I, versus step height, d_s.

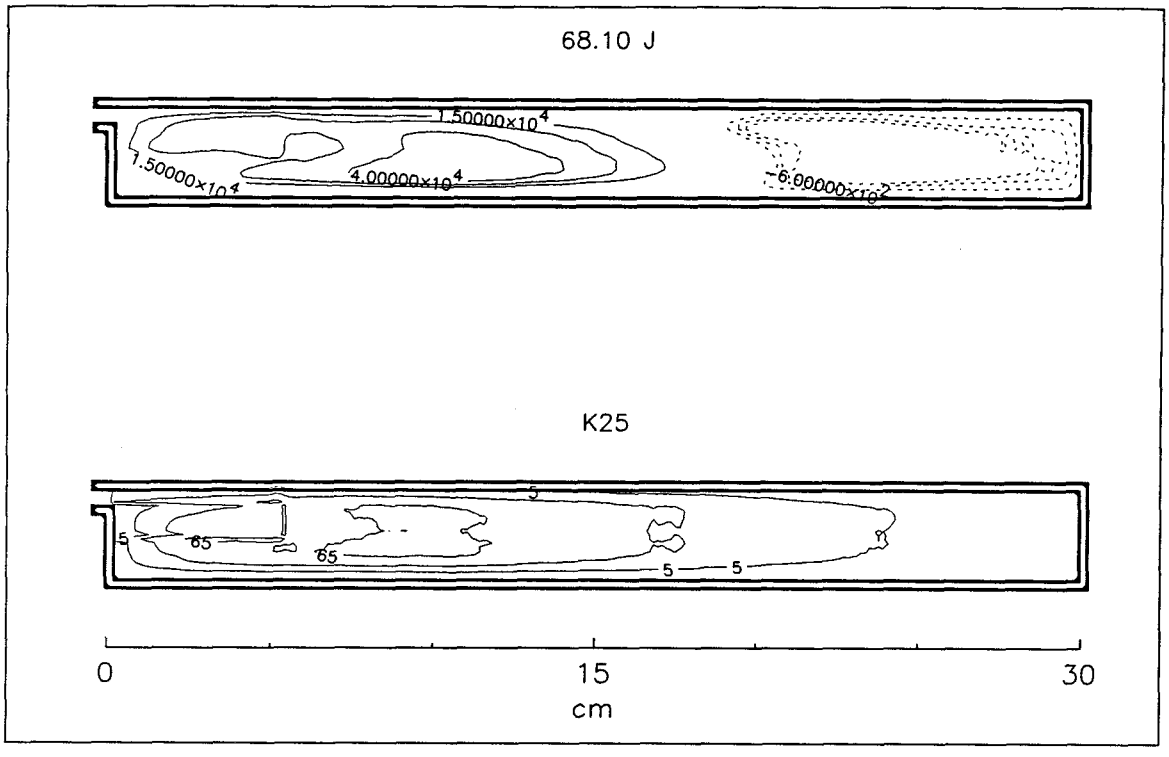

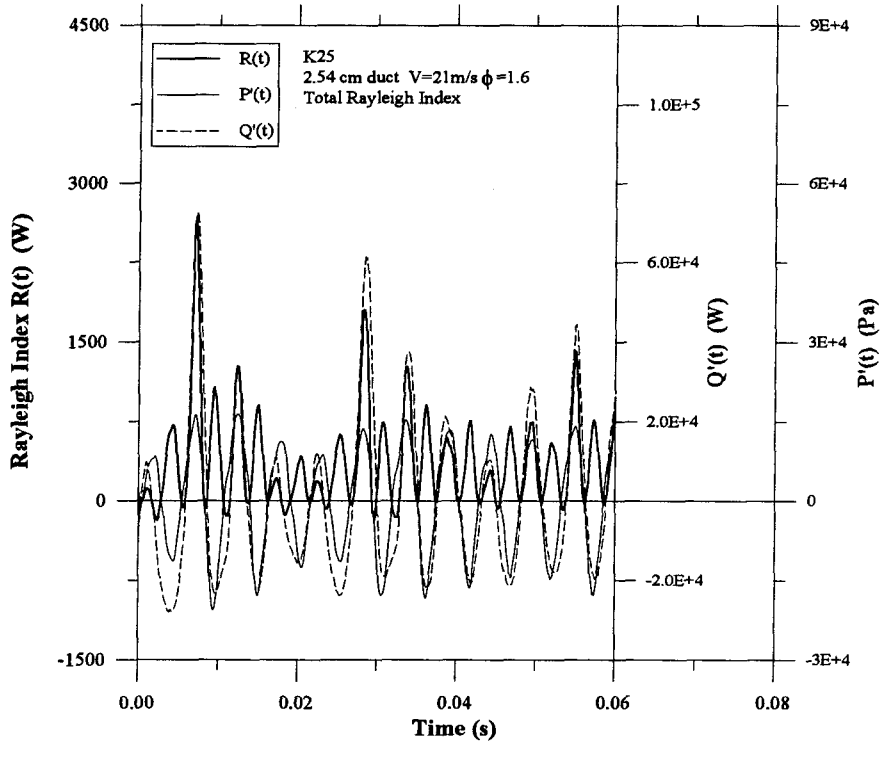

Figure 3.29: Two-dimensional Rayleigh Index (top), intensity (middle) and time-varying Rayleigh Index (bottom) plots: 2.54 cm duct, 21 m/s, $\phi = 1.6$.

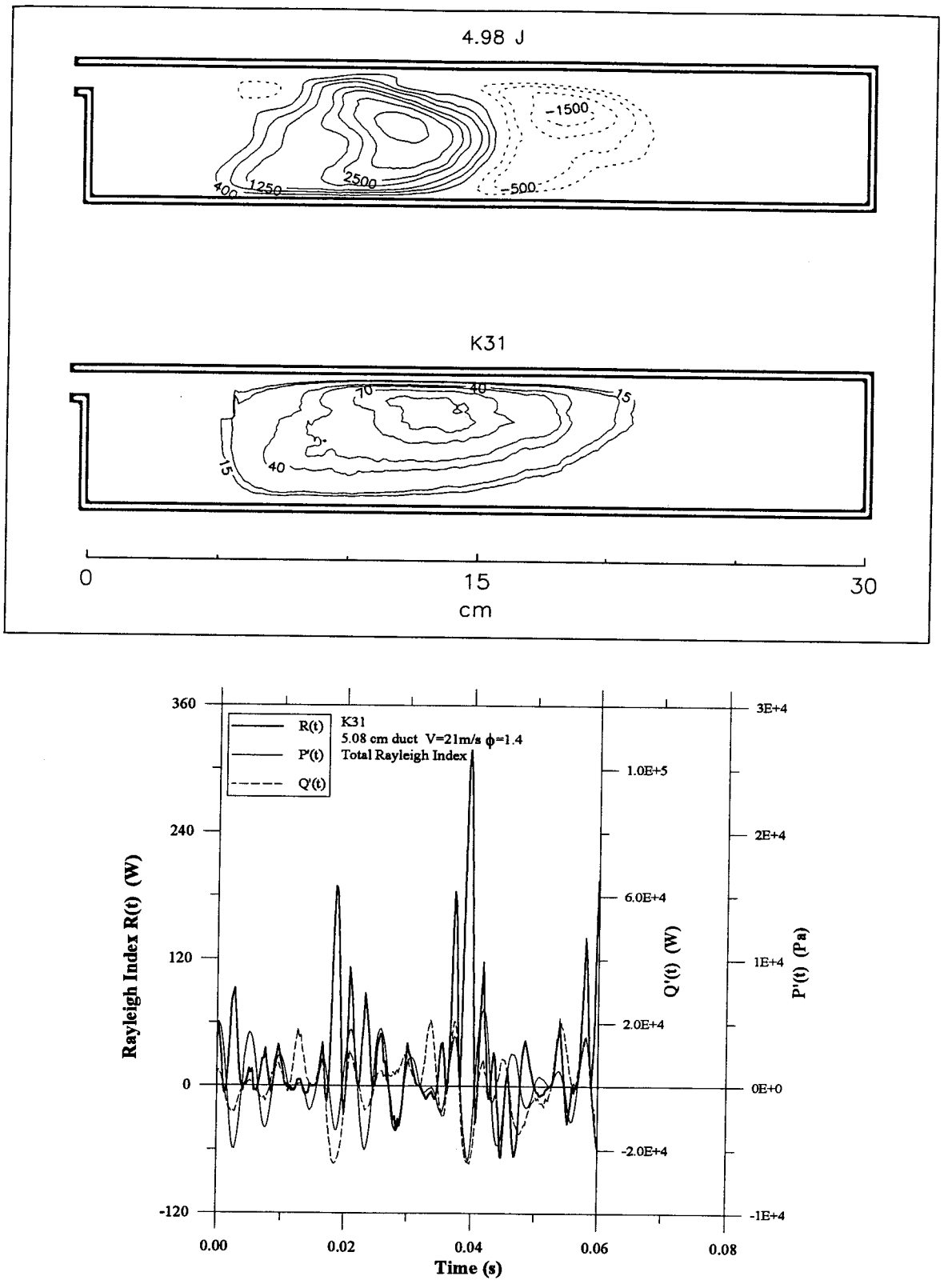

Figure 3.30: Two-dimensional Rayleigh Index (top), intensity (middle) and time-varying Rayleigh Index (bottom) plots: 5.08 cm duct, 21 m/s, $\phi = 1.4$.

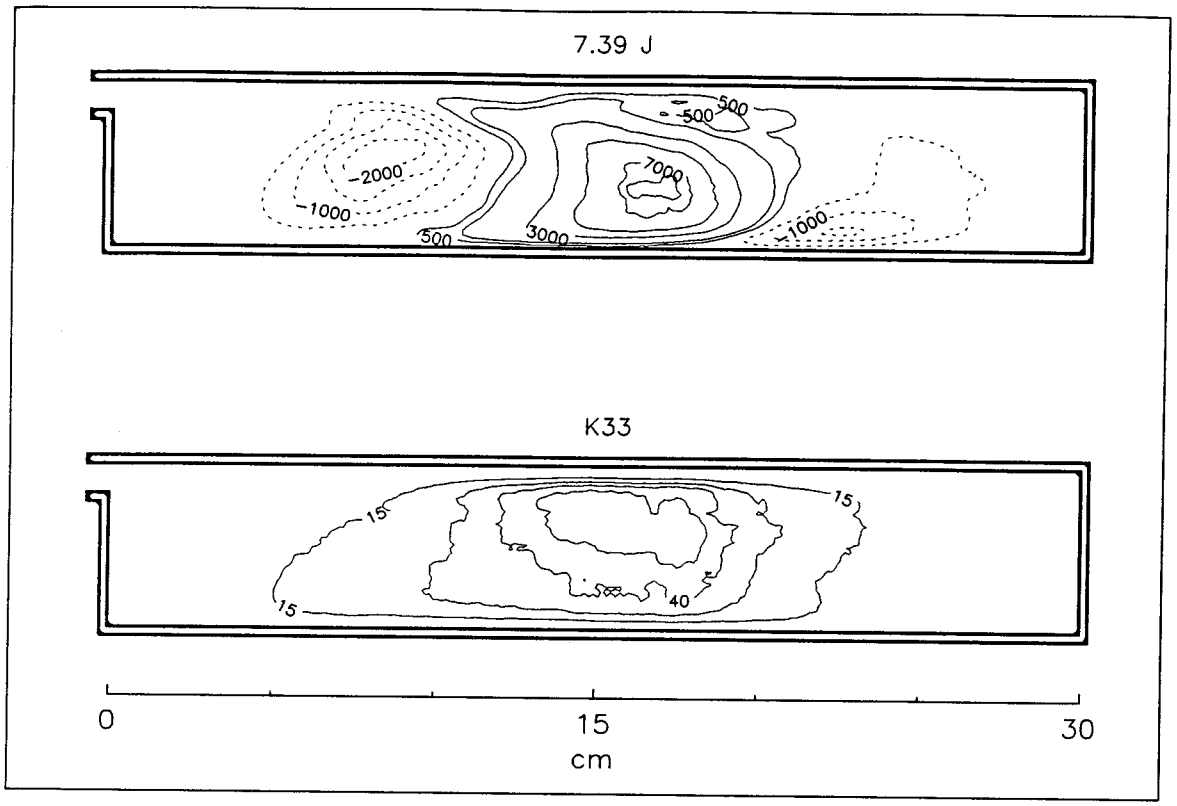

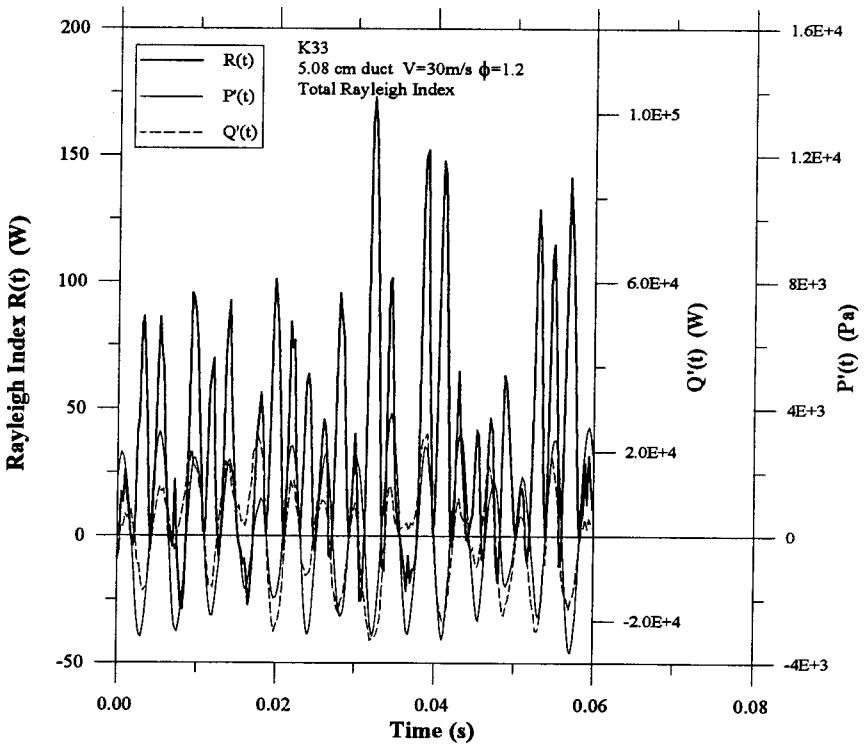

Figure 3.31: Two-dimensional Rayleigh Index (top), intensity (middle) and time-varying Rayleigh Index (bottom) plots: 5.08 cm duct, 30 m/s, $\phi = 1.2$.

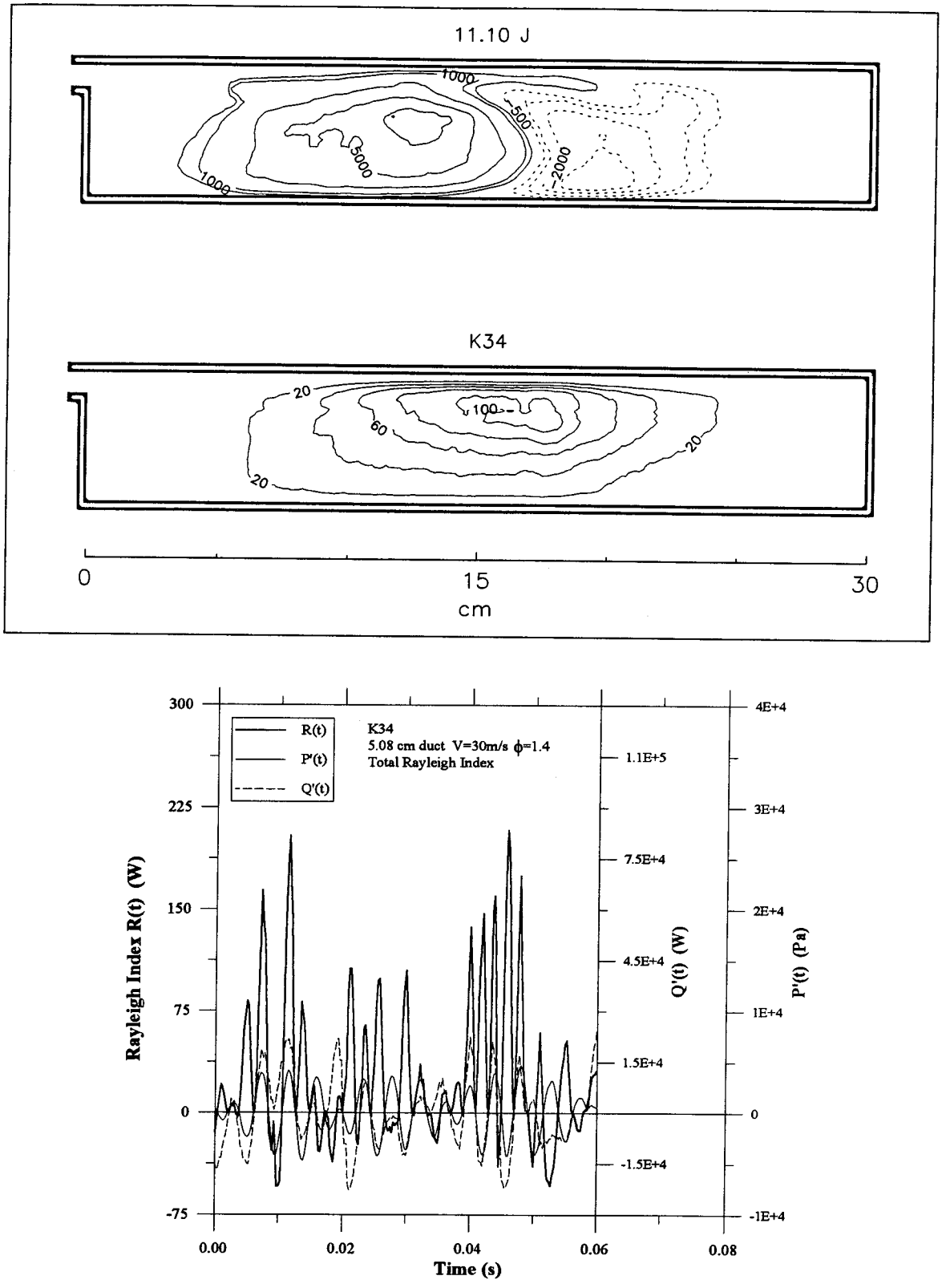

Figure 3.32: Two-dimensional Rayleigh Index (top), intensity (middle) and time-varying Rayleigh Index (bottom) plots: 5.08 cm duct, 30 m/s, $\phi = 1.4$.

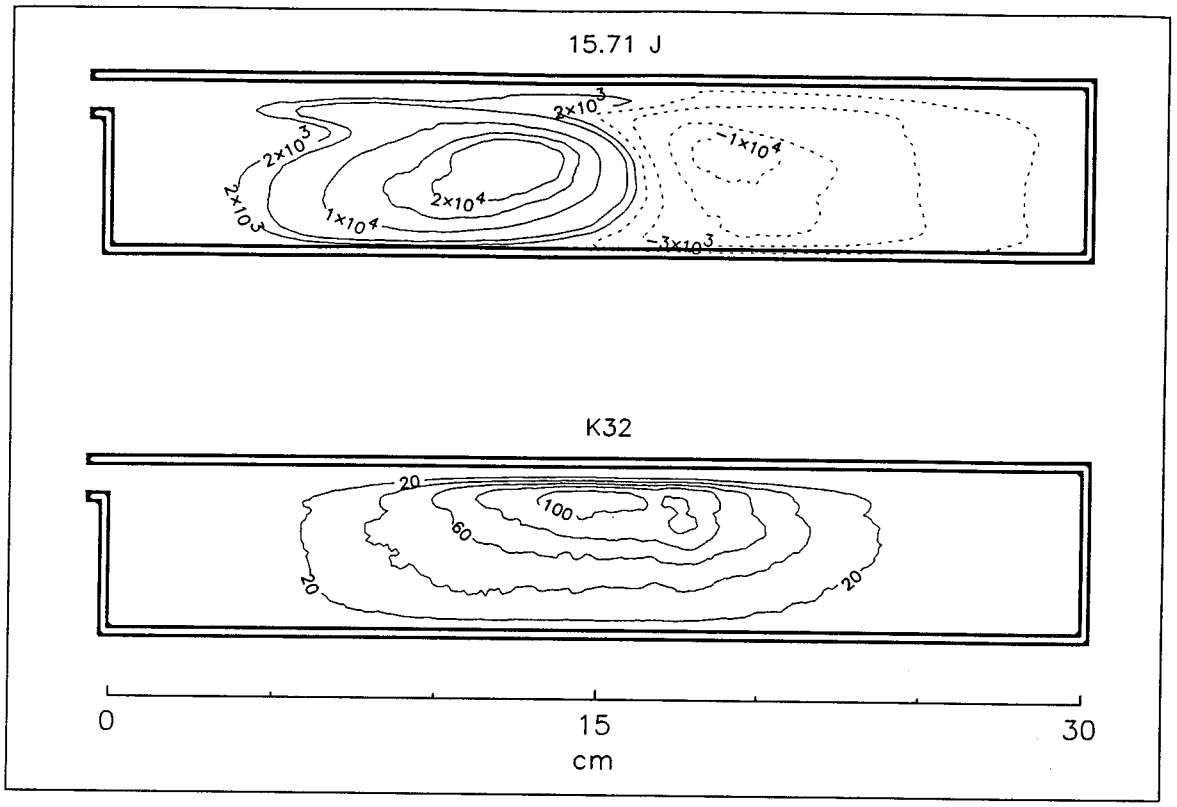

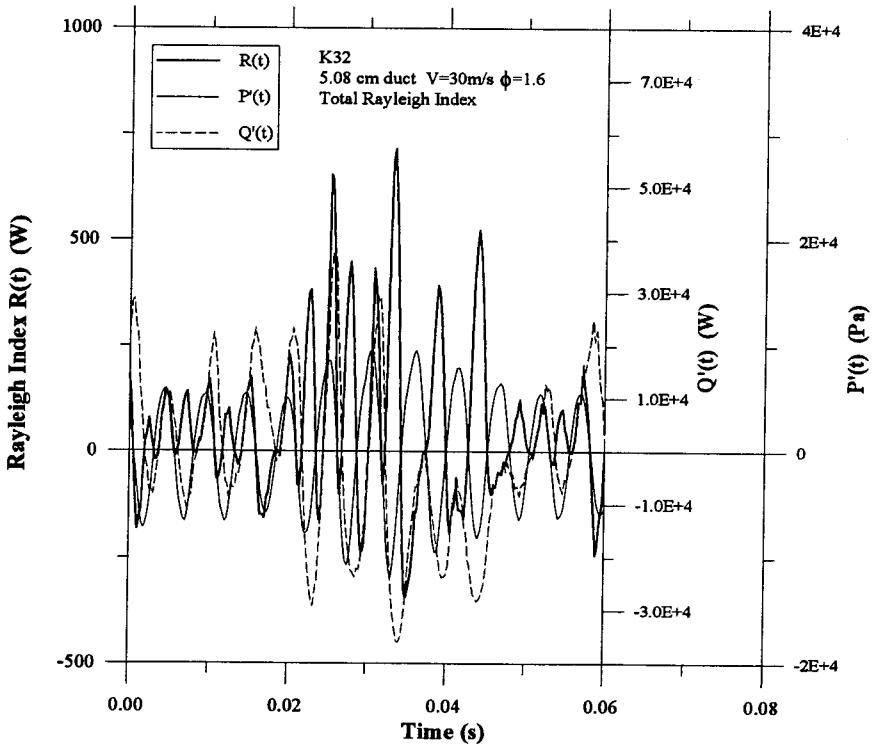

Figure 3.33: Two-dimensional Rayleigh Index (top), intensity (middle) and time-varying Rayleigh Index (bottom) plots: 5.08 cm duct, 30 m/s, $\phi = 1.6$.

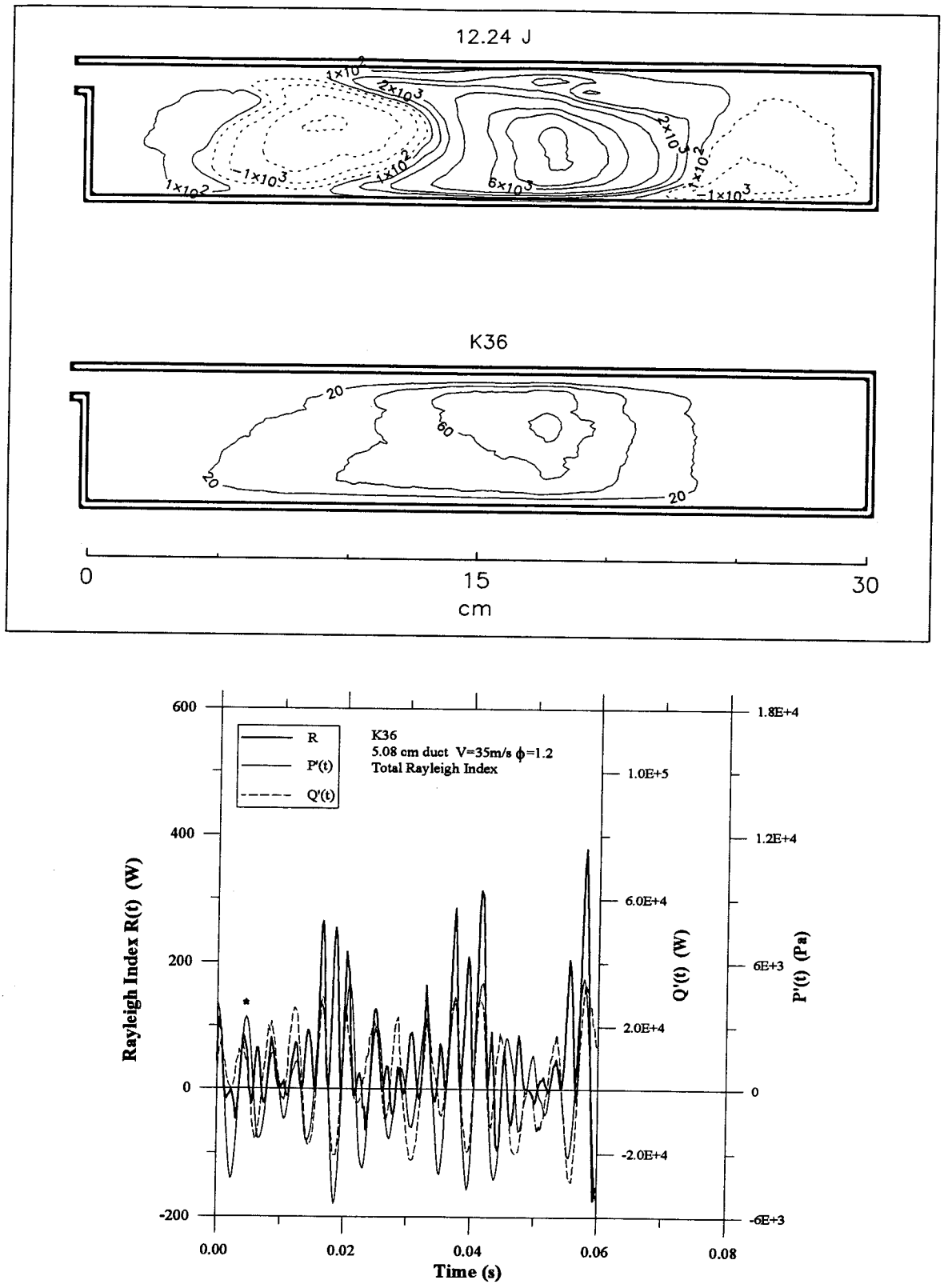

Figure 3.34: Two-dimensional Rayleigh Index (top), intensity (middle) and time-varying Rayleigh Index (bottom) plots: 5.08 cm duct, 35 m/s, $\phi = 1.2$.

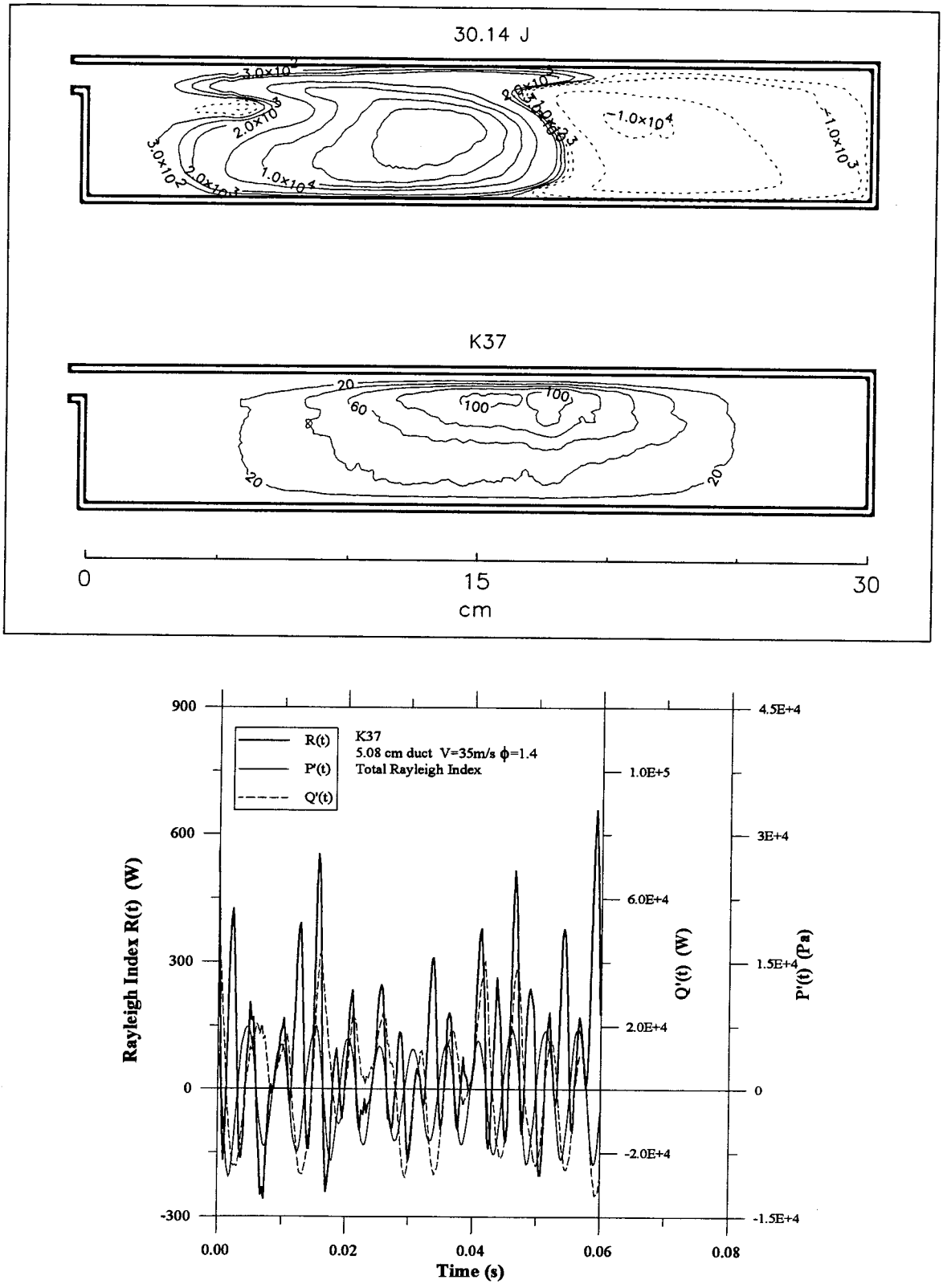

Figure 3.35: Two-dimensional Rayleigh Index (top), intensity (middle) and time-varying Rayleigh Index (bottom) plots: 5.08 cm duct, 35 m/s, $\phi = 1.4$.

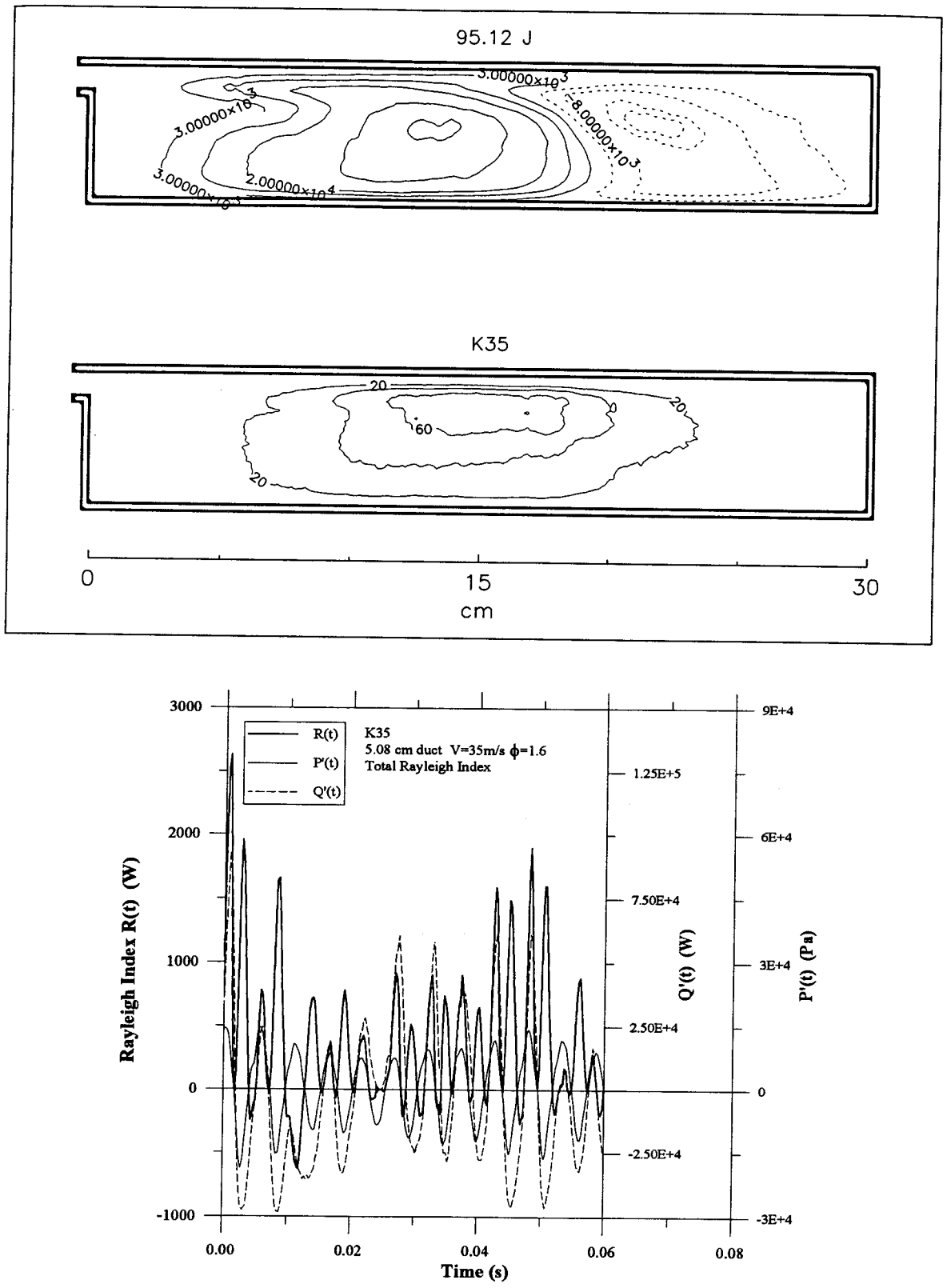

Figure 3.36: Two-dimensional Rayleigh Index (top), intensity (middle) and time-varying Rayleigh Index (bottom) plots: 5.08 cm duct, 35 m/s, $\phi = 1.6$.

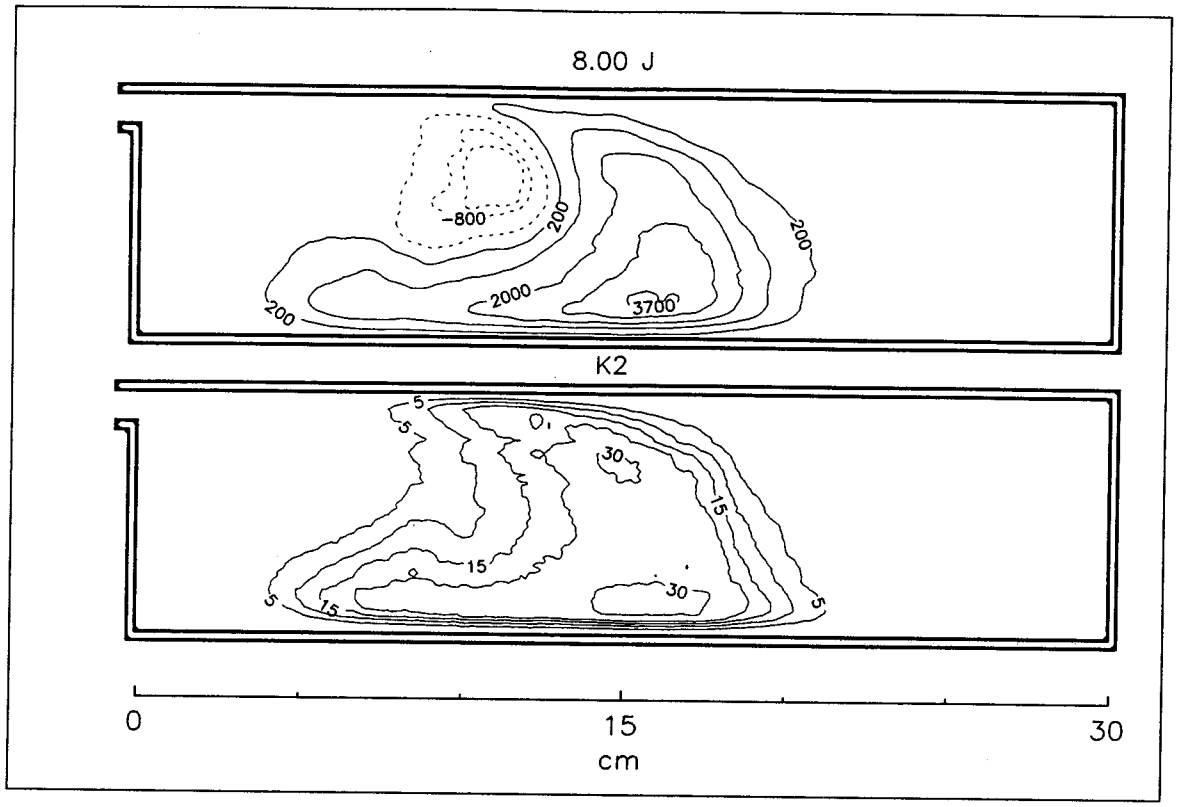

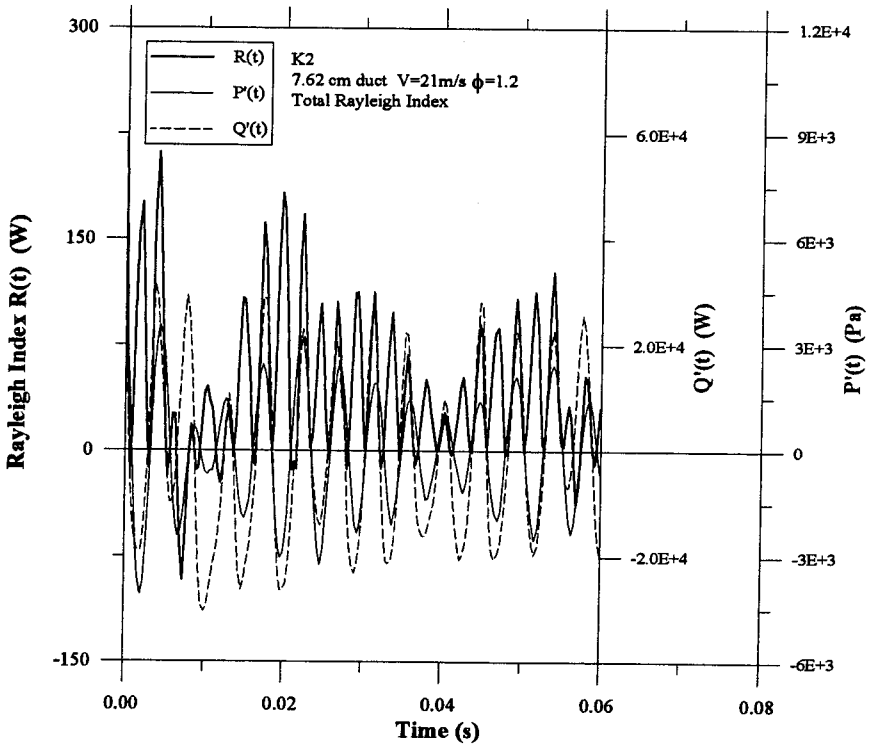

Figure 3.37: Two-dimensional Rayleigh Index (top), intensity (middle) and time-varying Rayleigh Index (bottom) plots: 7.62 cm duct, 21 m/s, $\phi = 1.2$.

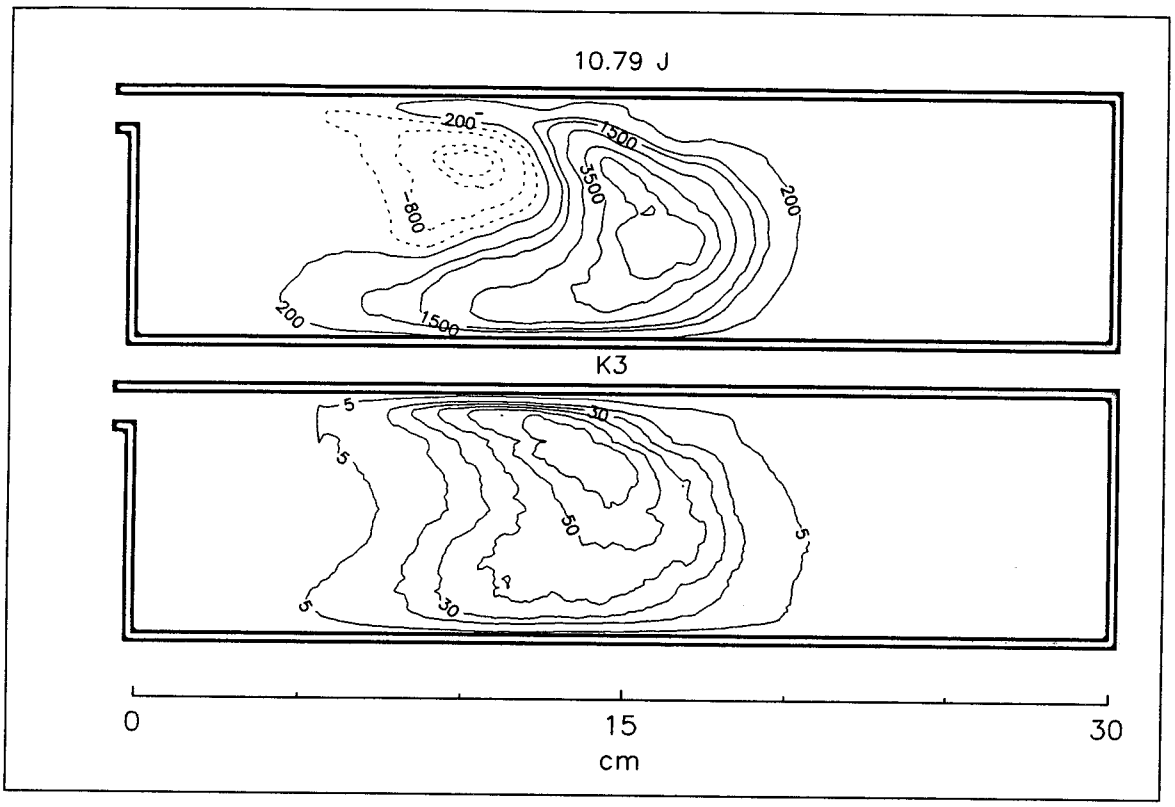

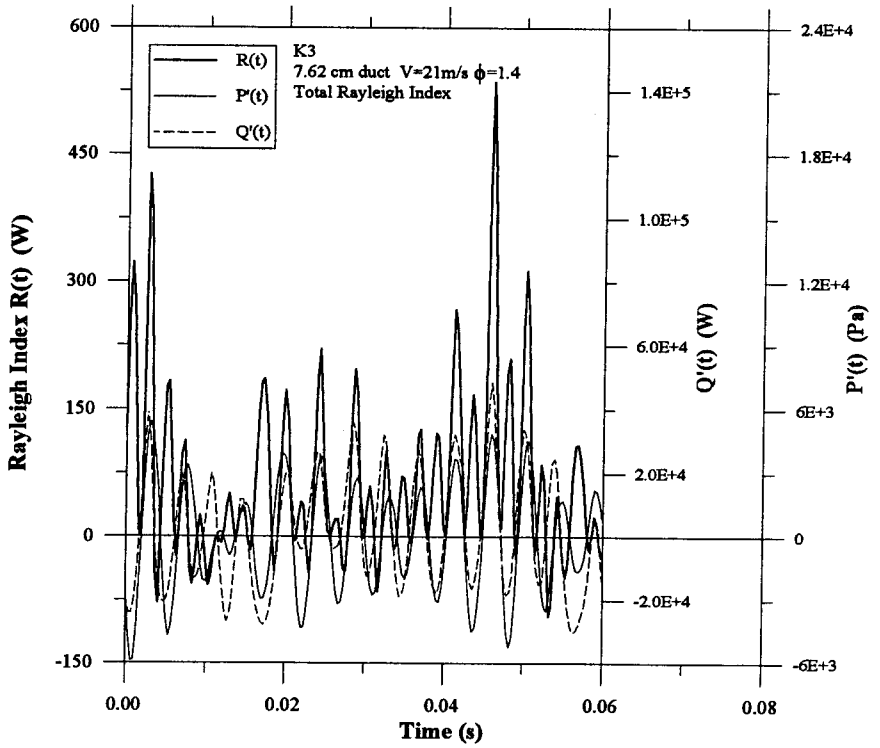

Figure 3.38: Two-dimensional Rayleigh Index (top), intensity (middle) and time-varying Rayleigh Index (bottom) plots: 7.62 cm duct, 21 m/s, $\phi = 1.4$.

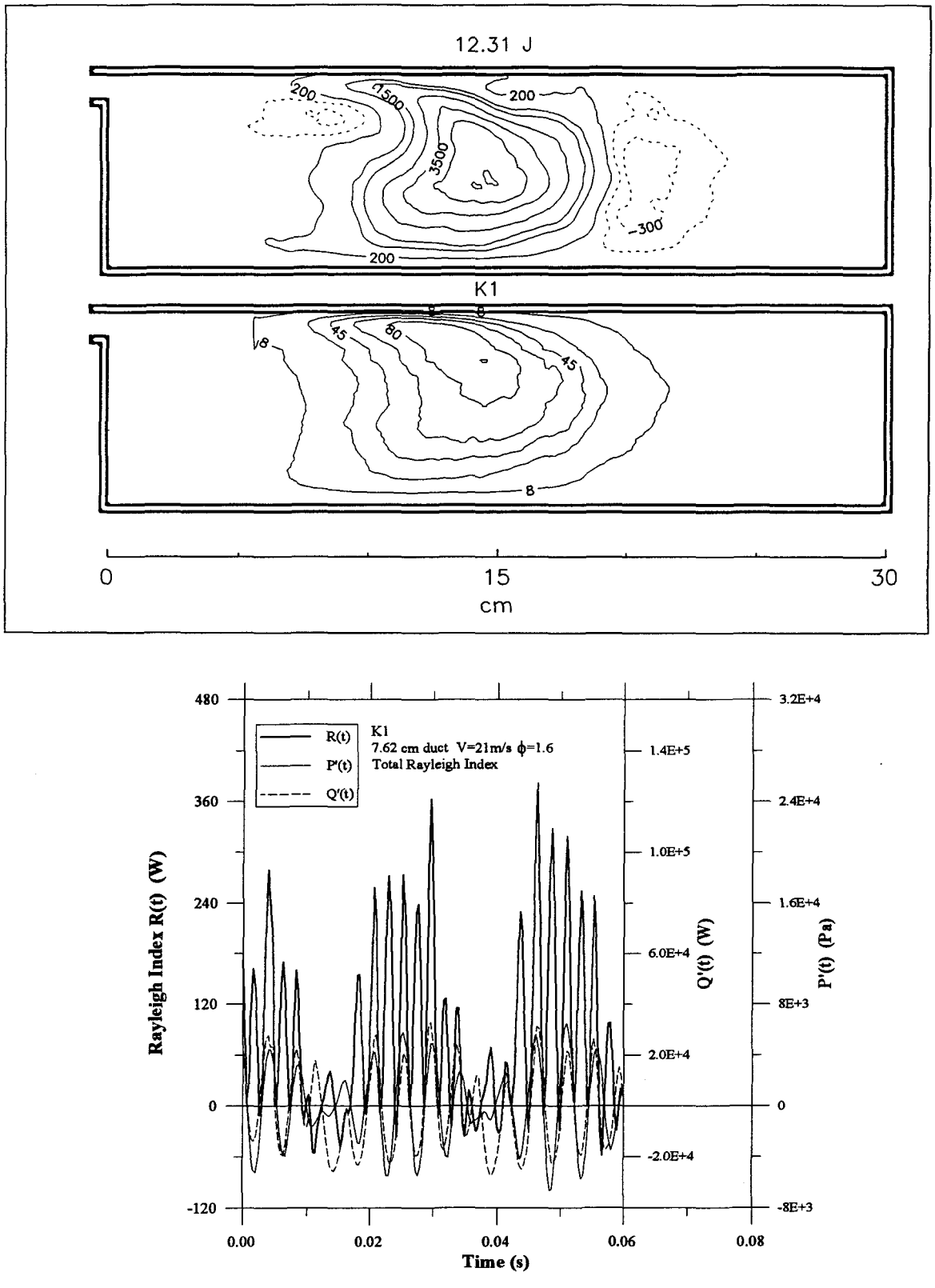

Figure 3.39: Two-dimensional Rayleigh Index (top), intensity (middle) and time-varying Rayleigh Index (bottom) plots: 7.62 cm duct, 21 m/s, $\phi = 1.6$.

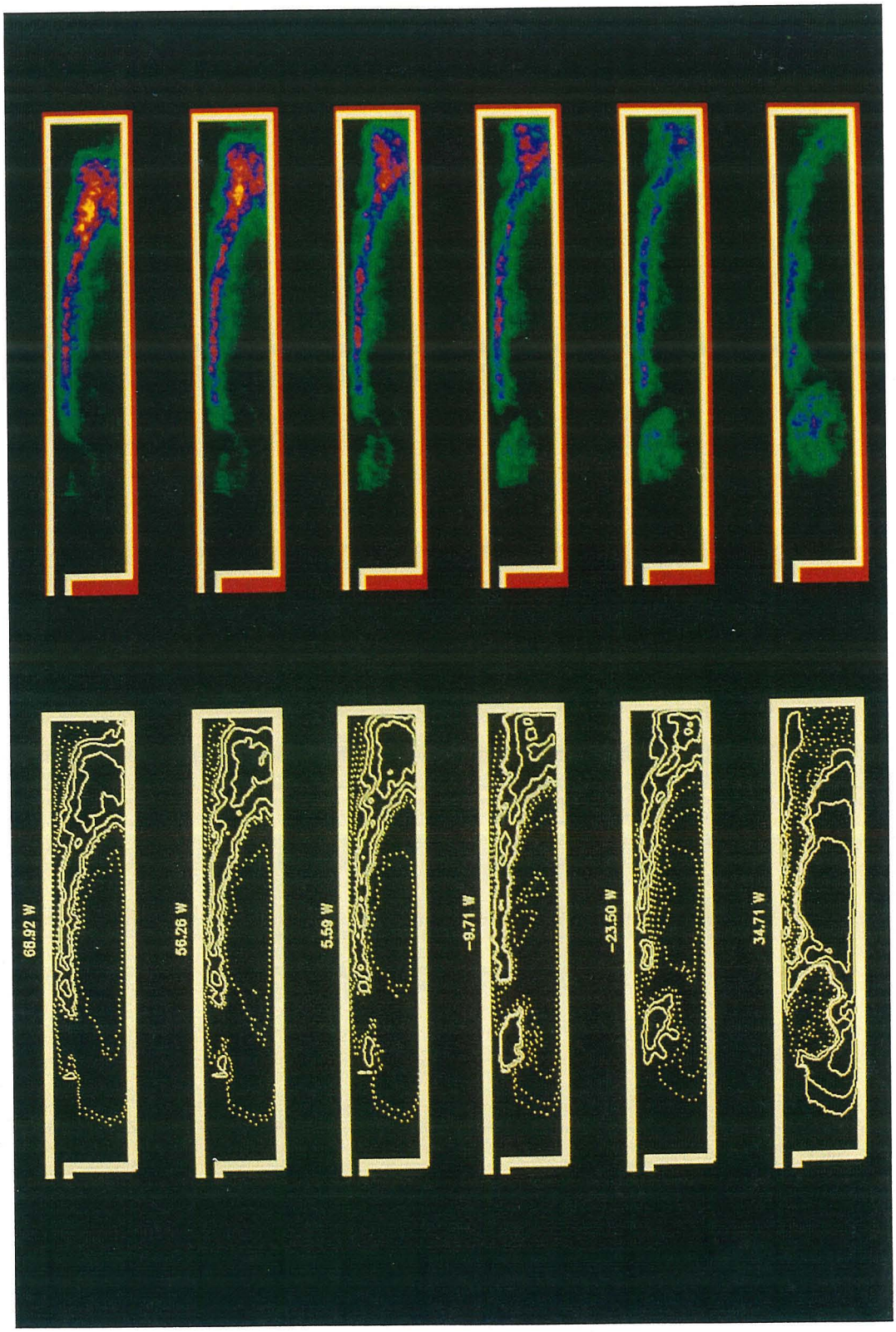

Figure 3.40a: Temporal evolution of Rayleigh Index: 5.08 cm duct, 35 m/s, $\phi = 1.2$.

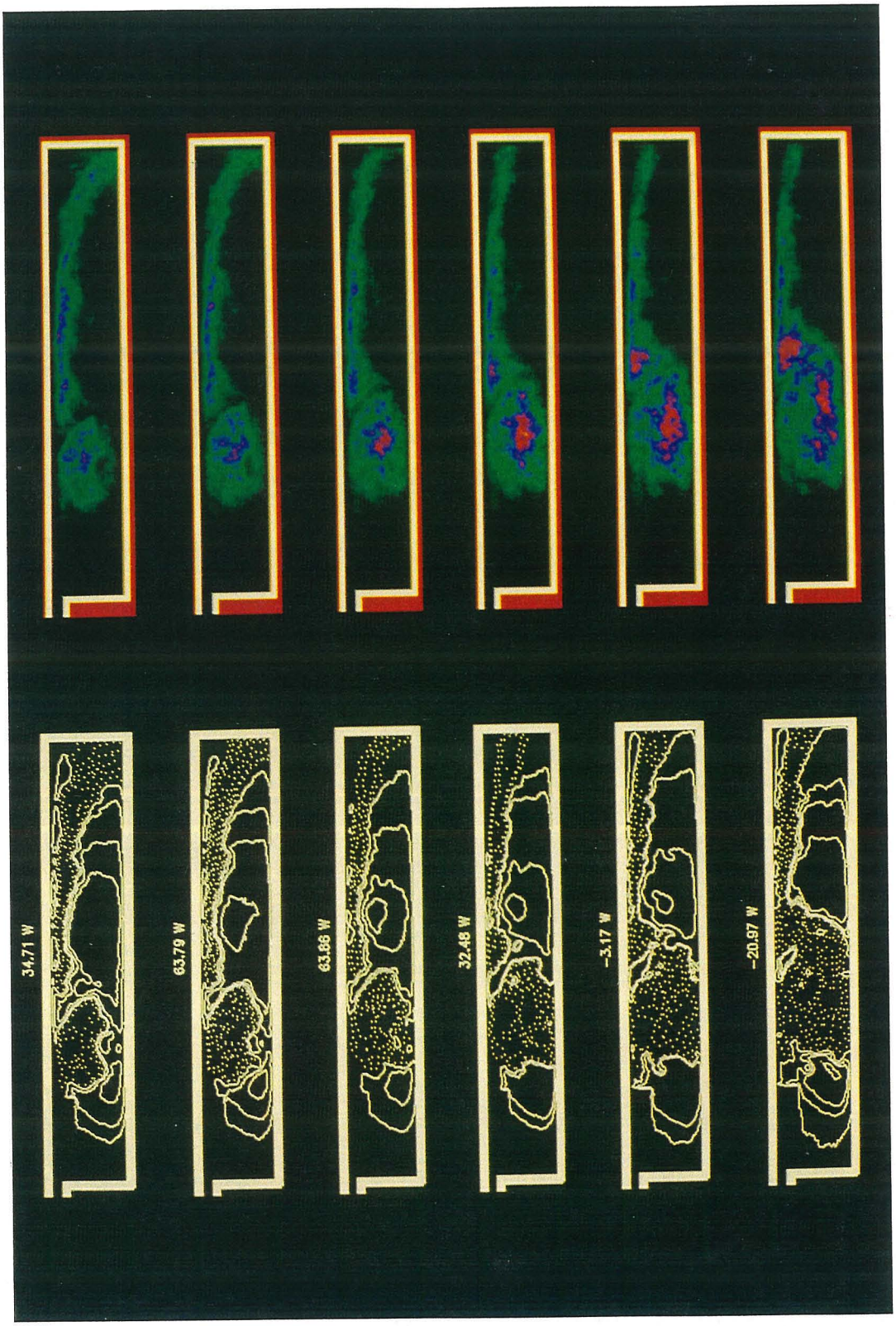

Figure 3.40b: Temporal evolution of Rayleigh Index: 5.08 cm duct, 35 m/s, $\phi = 1.2$.

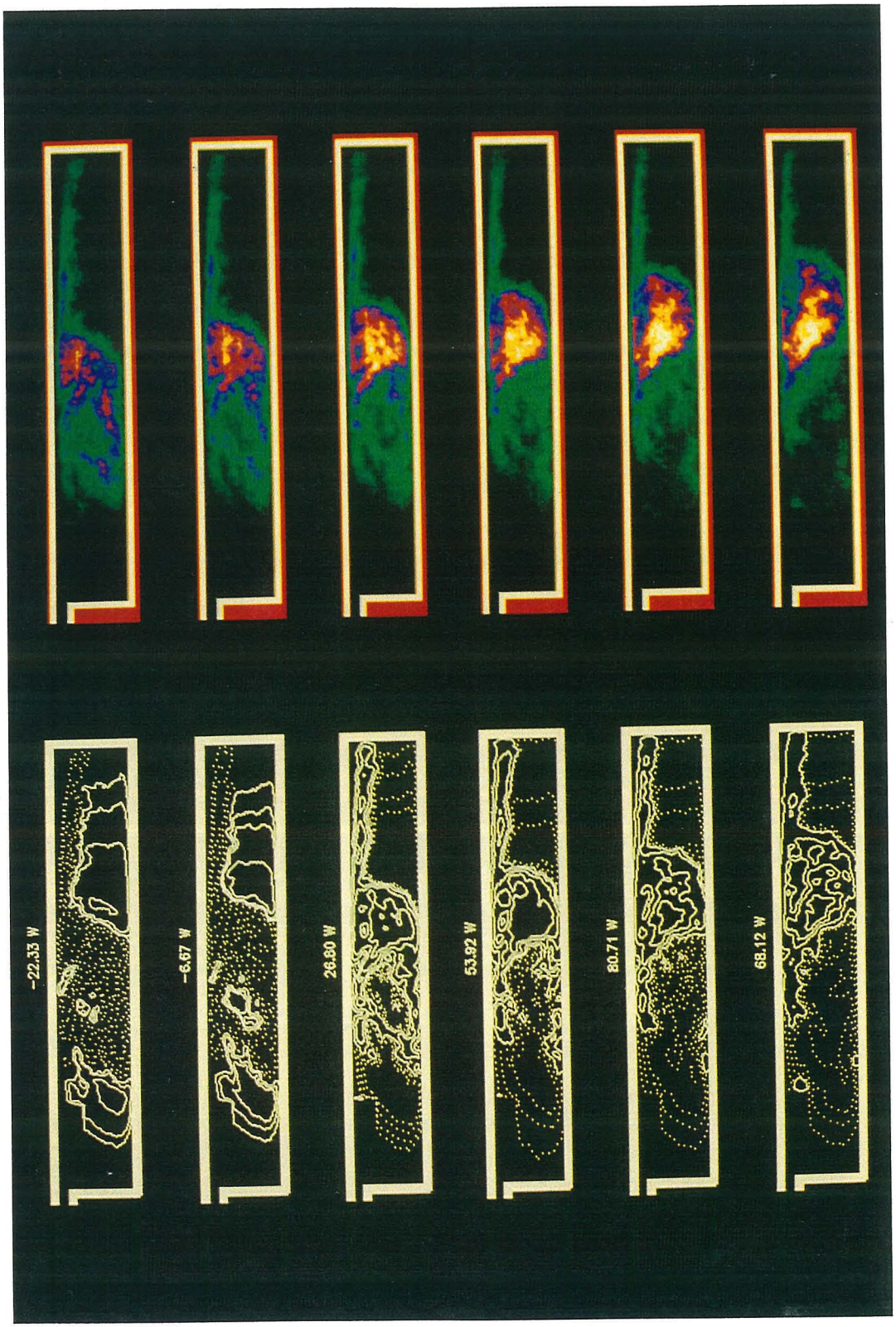

Figure 3.40c: Temporal evolution of Rayleigh Index: 5.08 cm duct, 35 m/s, $\phi = 1.2$.

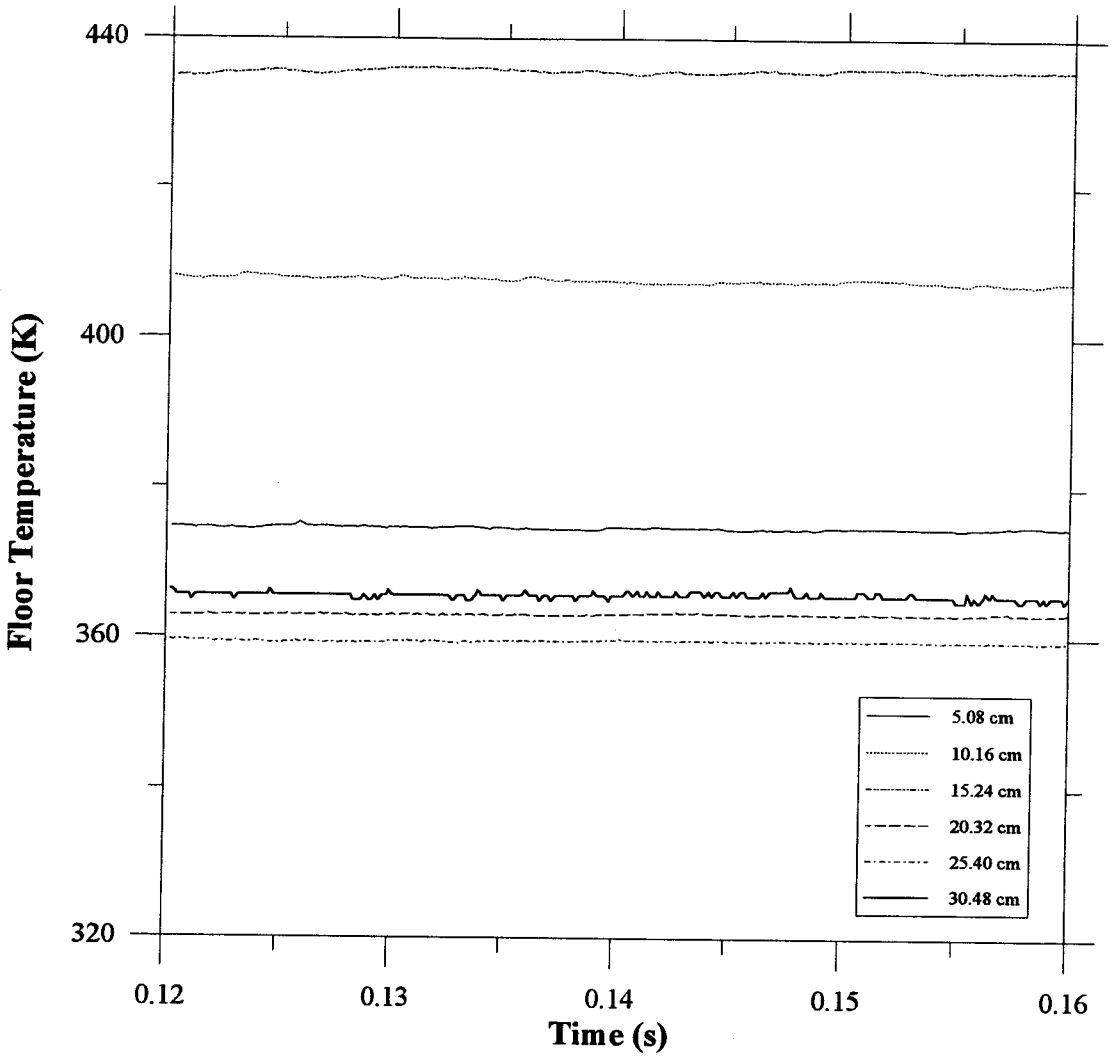

Figure 3.41: Temperature-time traces for 7.62 cm duct, $V_{dump} = 21\ m/s$, $\phi = 1.4$.

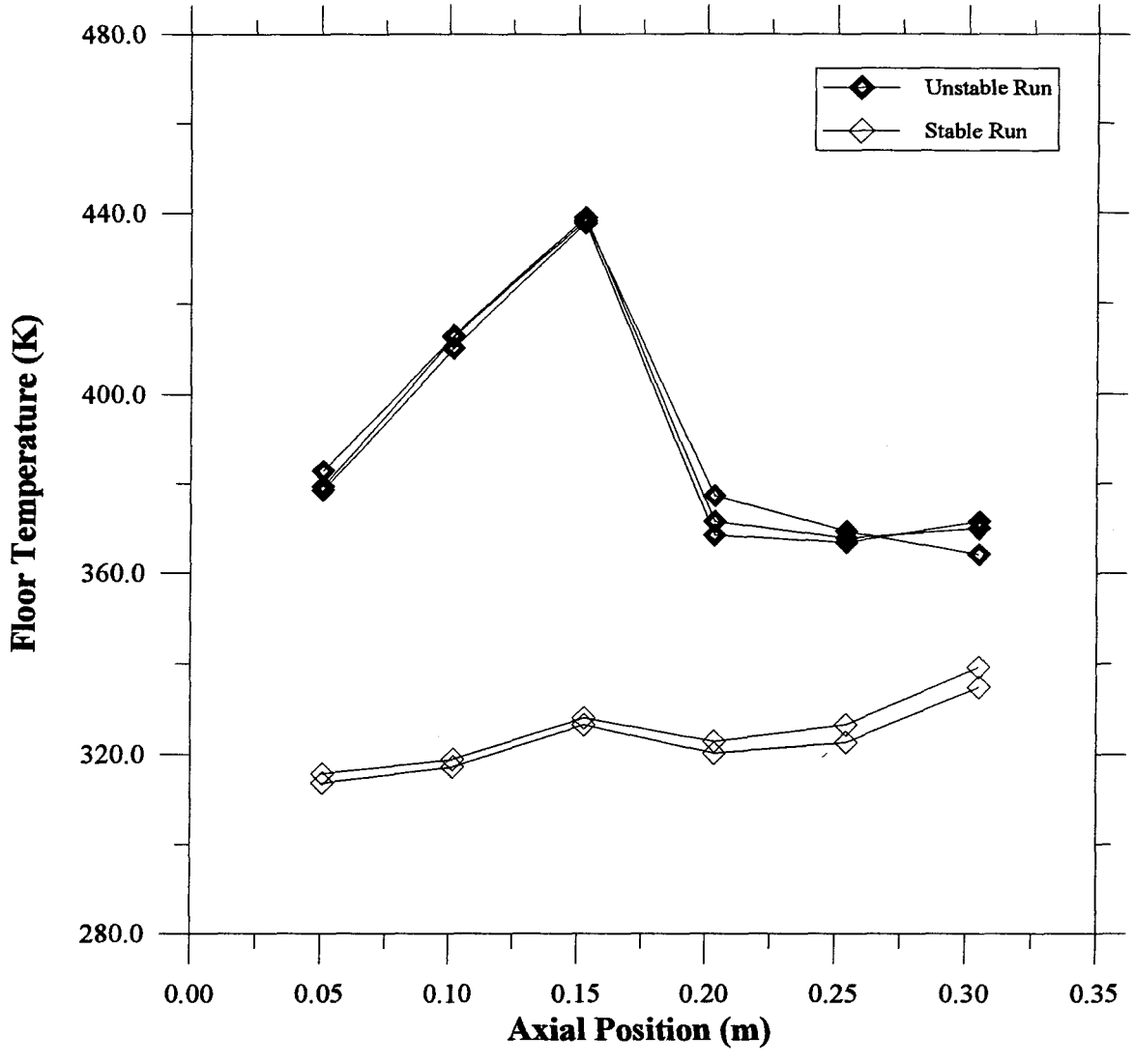

Figure 3.42a: Unstable/stable comparison: 7.62 cm duct, $V_{dump} = 21m/s$, $\phi = 1.4$.

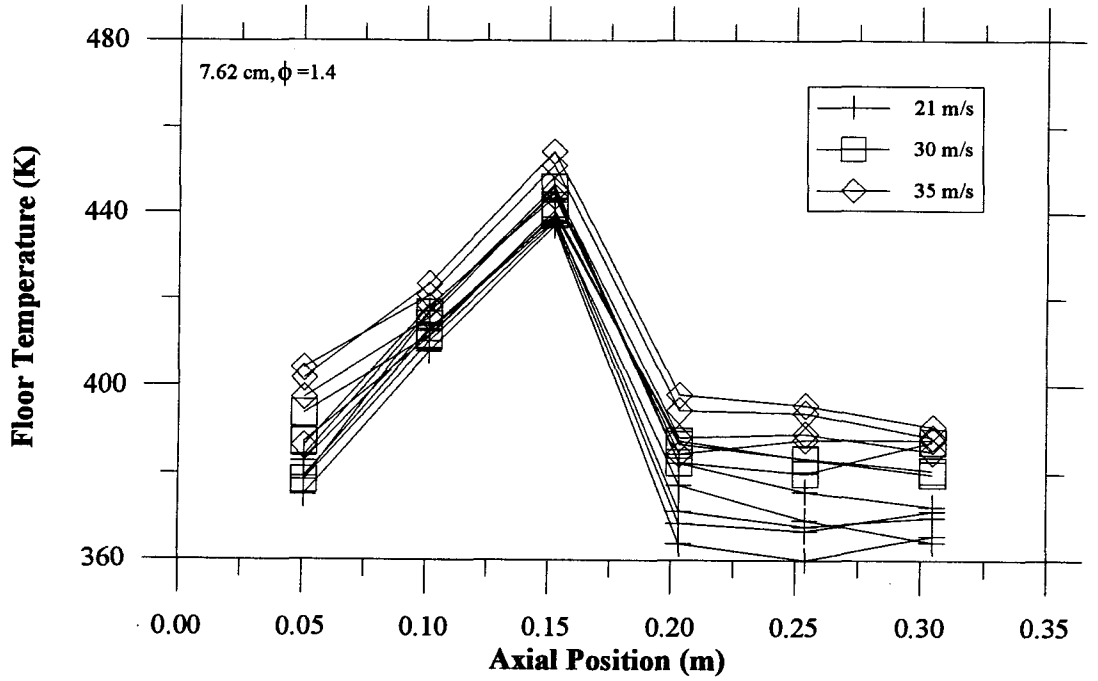

Figure 3.42b: Velocity effects: 7.62 cm, $\phi = 1.4$.

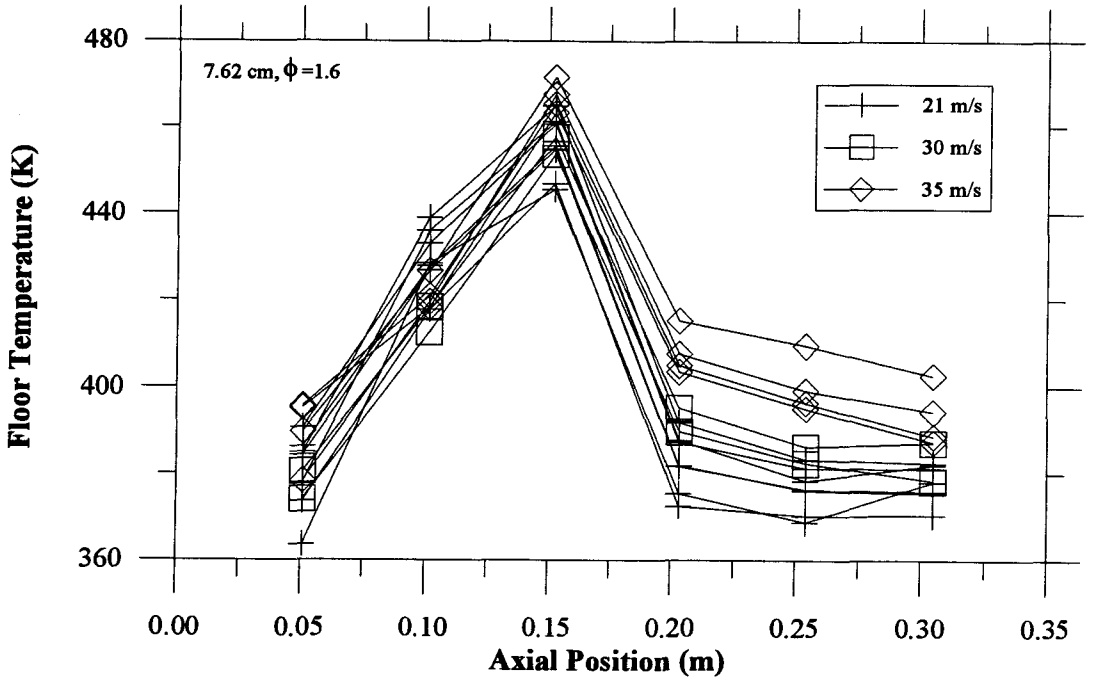

Figure 3.42c: Velocity effects: 7.62 cm, $\phi = 1.6$.

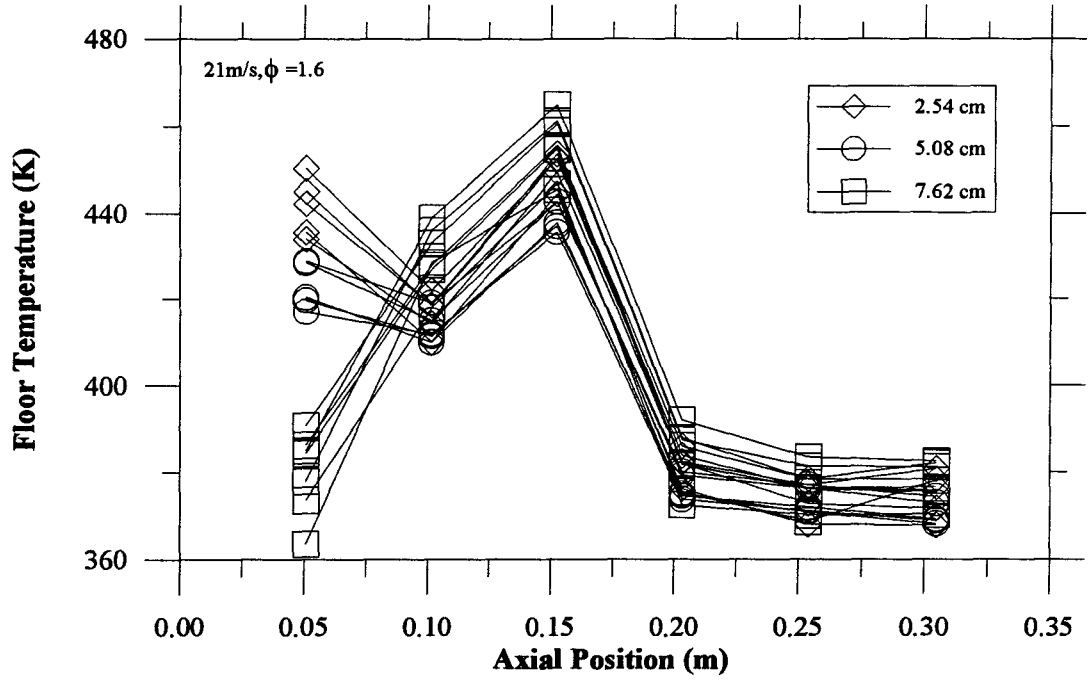

Figure 3.43a: Geometric effects: $V_{dump} = 21m/s$, $\phi = 1.6$.

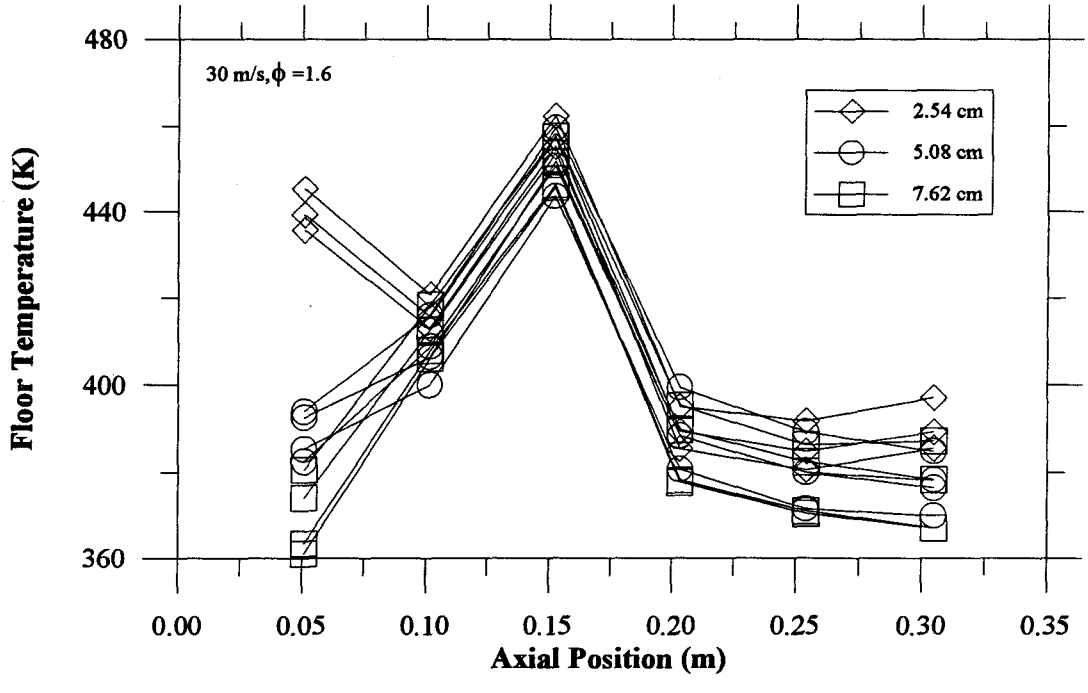

Figure 3.43b: Geometric effects: $V_{dump} = 30m/s$, $\phi = 1.6$.

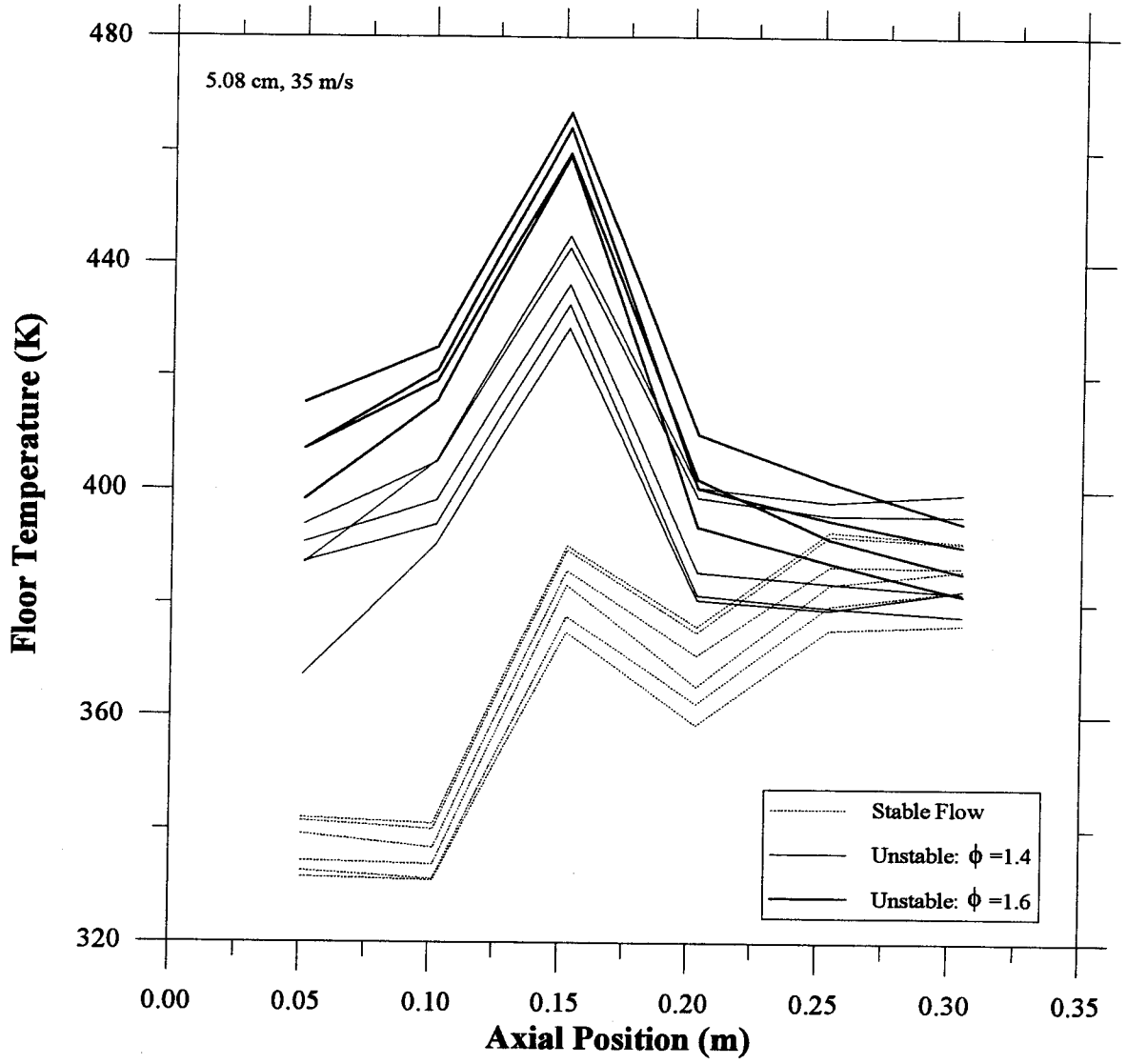

Figure 3.44: Shedding frequency effects: 5.08 cm duct, 35 m/s.

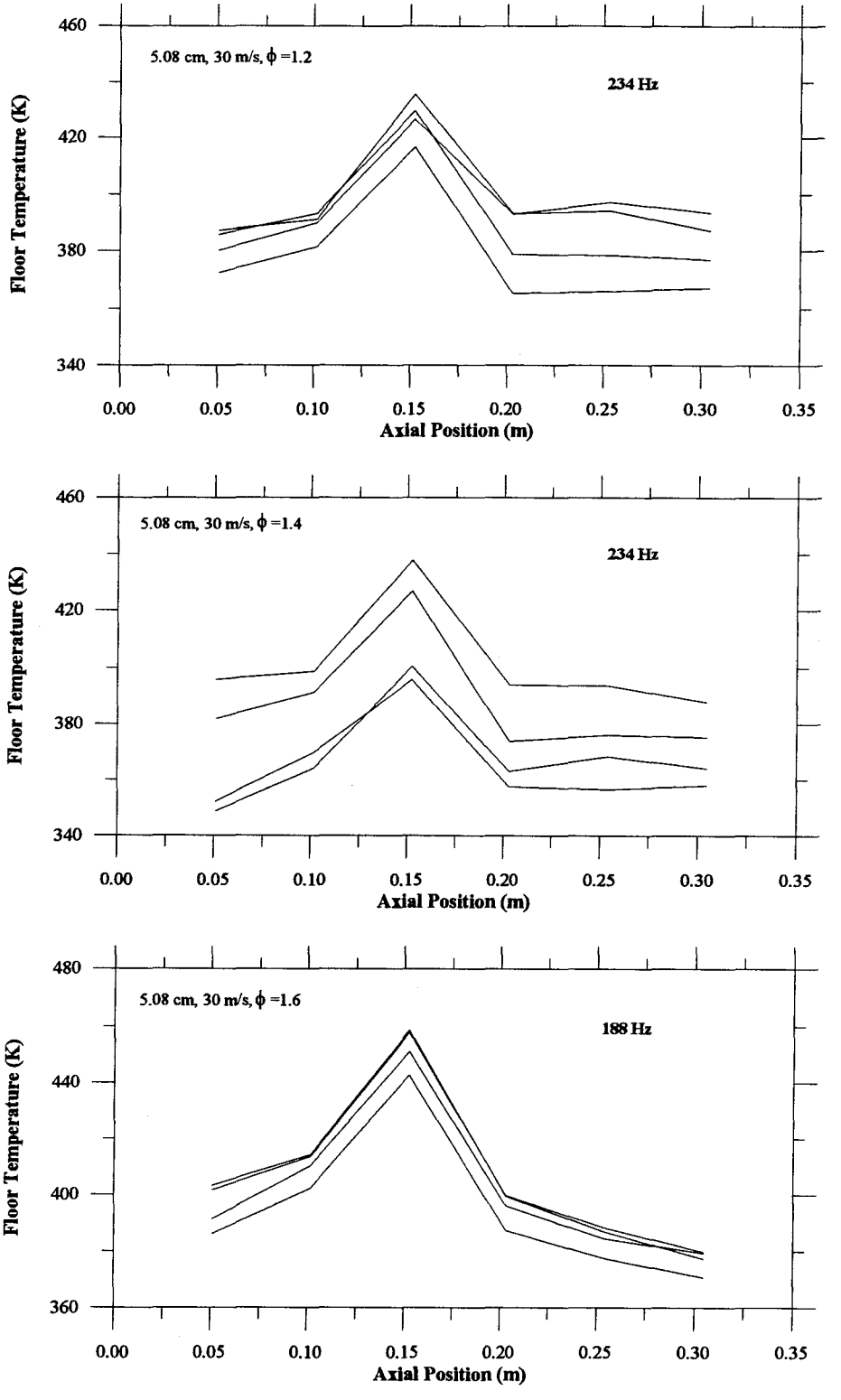

Figure 3.45: Shedding frequency effects: 5.08 cm, $V_{dump} = 30 m / s$.

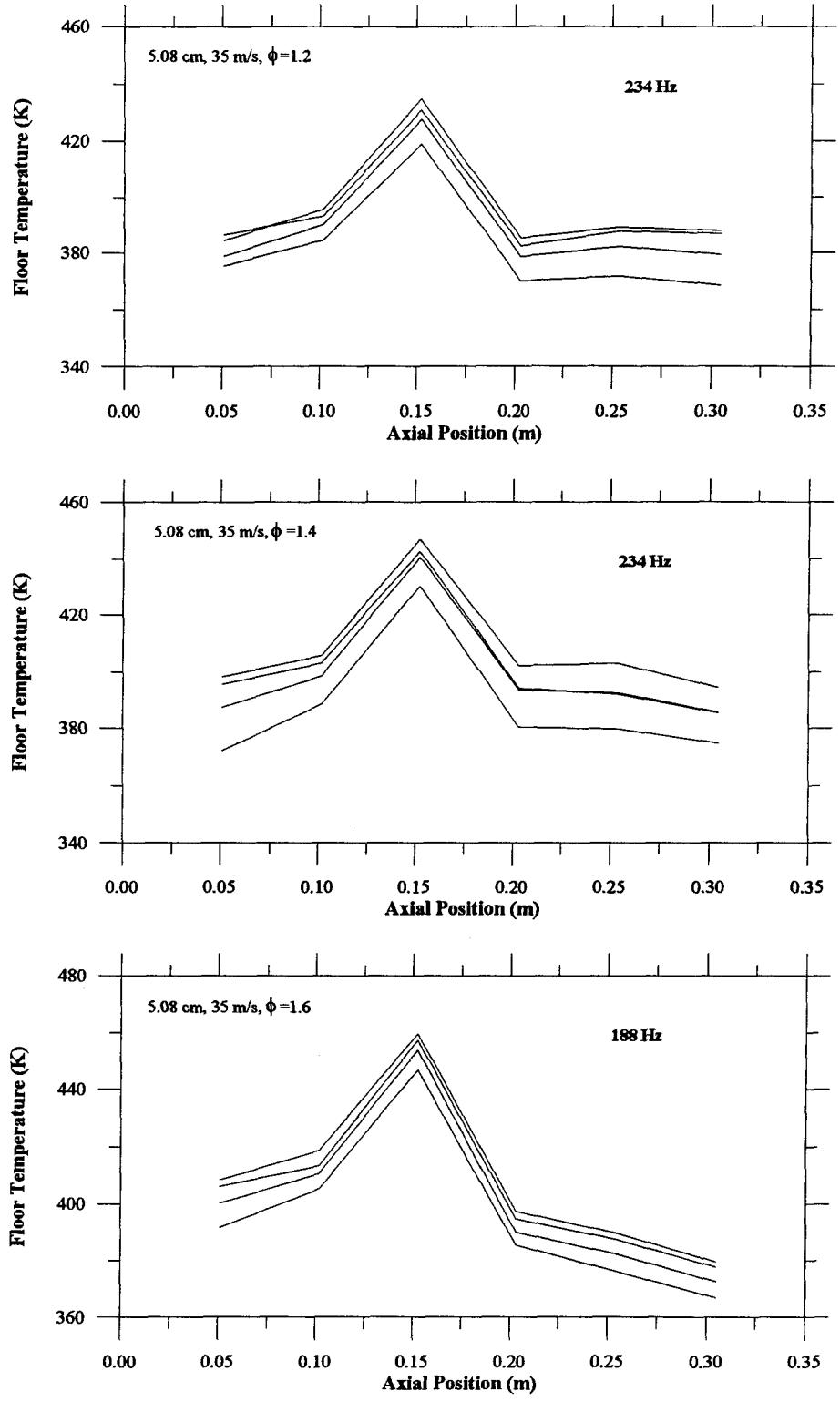

Figure 3.46: Shedding frequency effects: 5.08 cm, $V_{dump} = 35m/s$.

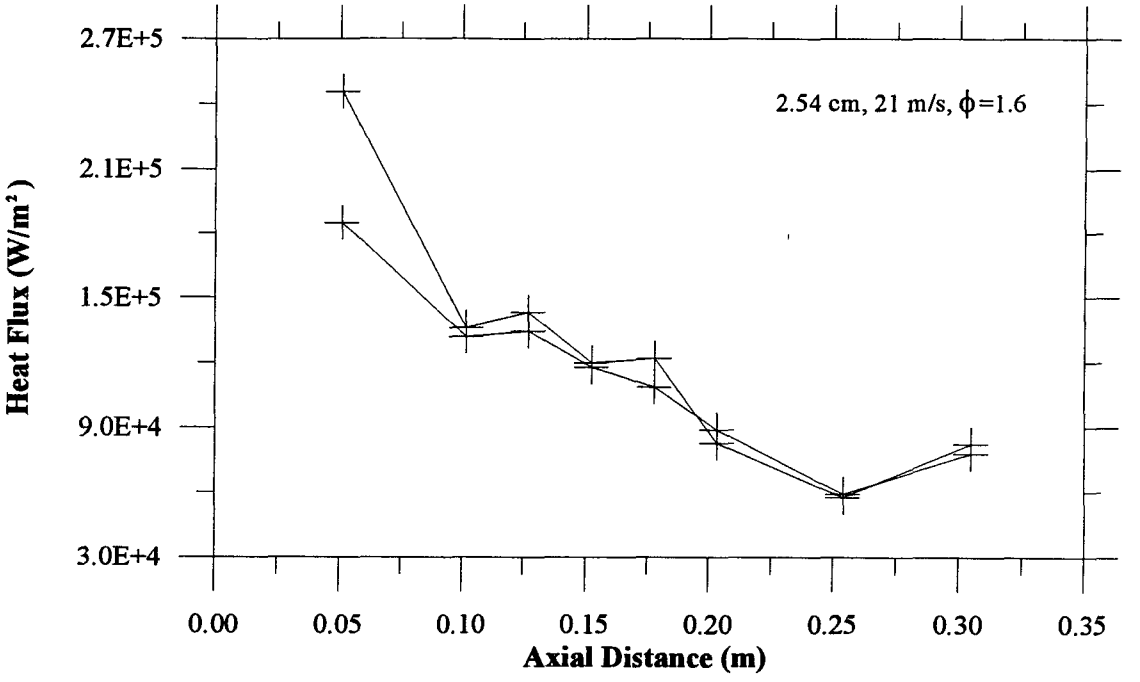

Figure 3.47a: Axial heat flux distribution: 2.54 cm, $V_{dump} = 21m/s$, $\phi = 1.6$.

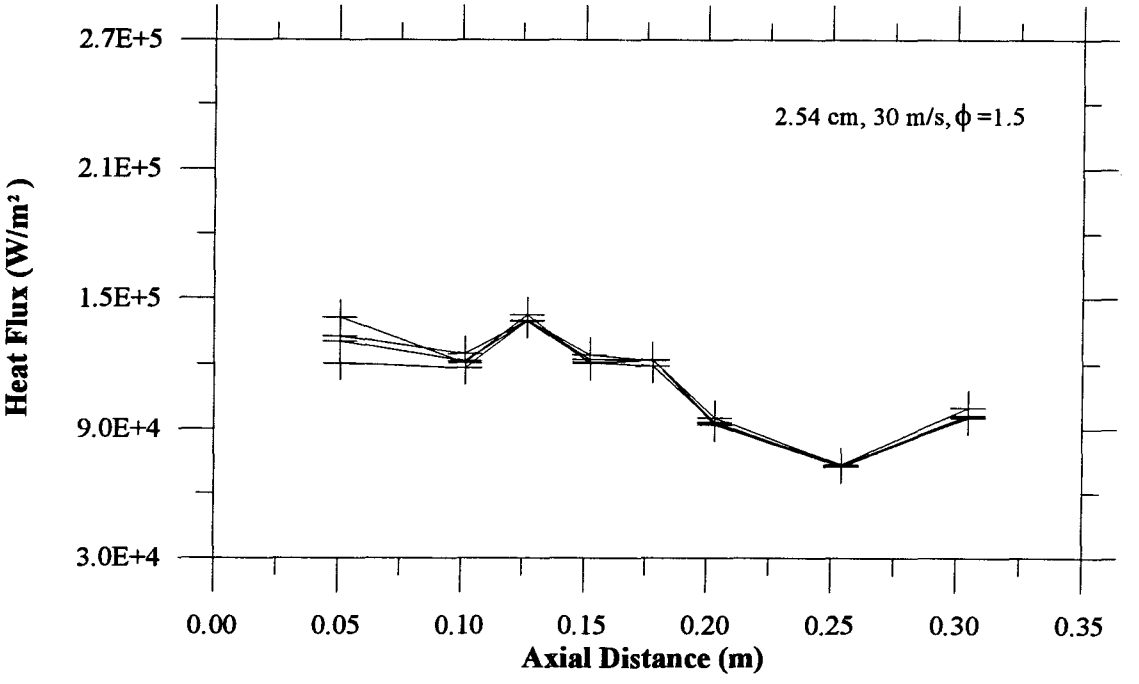

Figure 3.47b: Axial heat flux distribution: 2.54 cm, $V_{dump} = 30m/s$, $\phi = 1.5$.

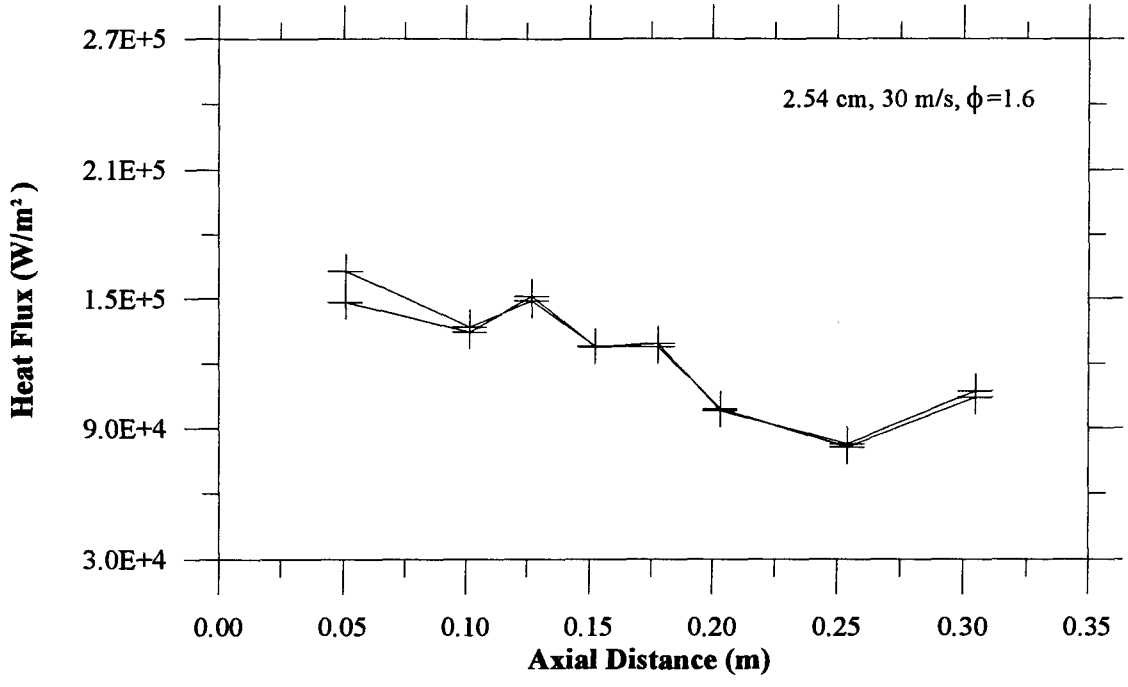

Figure 3.47c: Axial heat flux distribution: 2.54 cm, $V_{dump} = 30m/s$, $\phi = 1.6$.

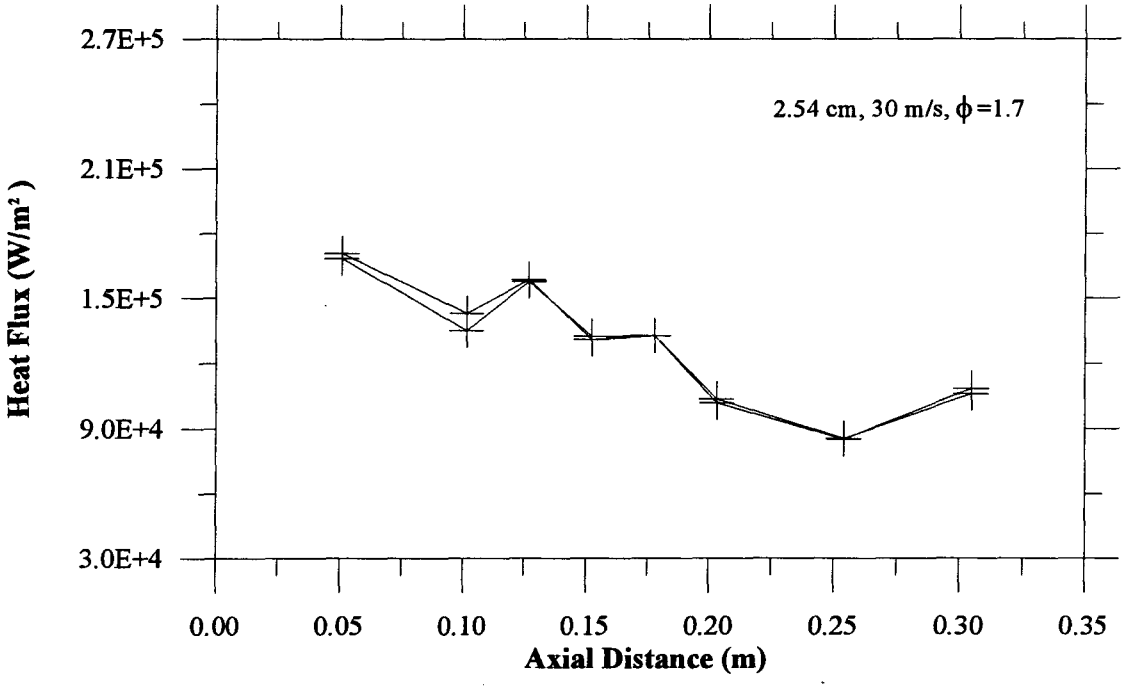

Figure 3.47d: Axial heat flux distribution: 2.54 cm, $V_{dump} = 30m/s$, $\phi = 1.7$.

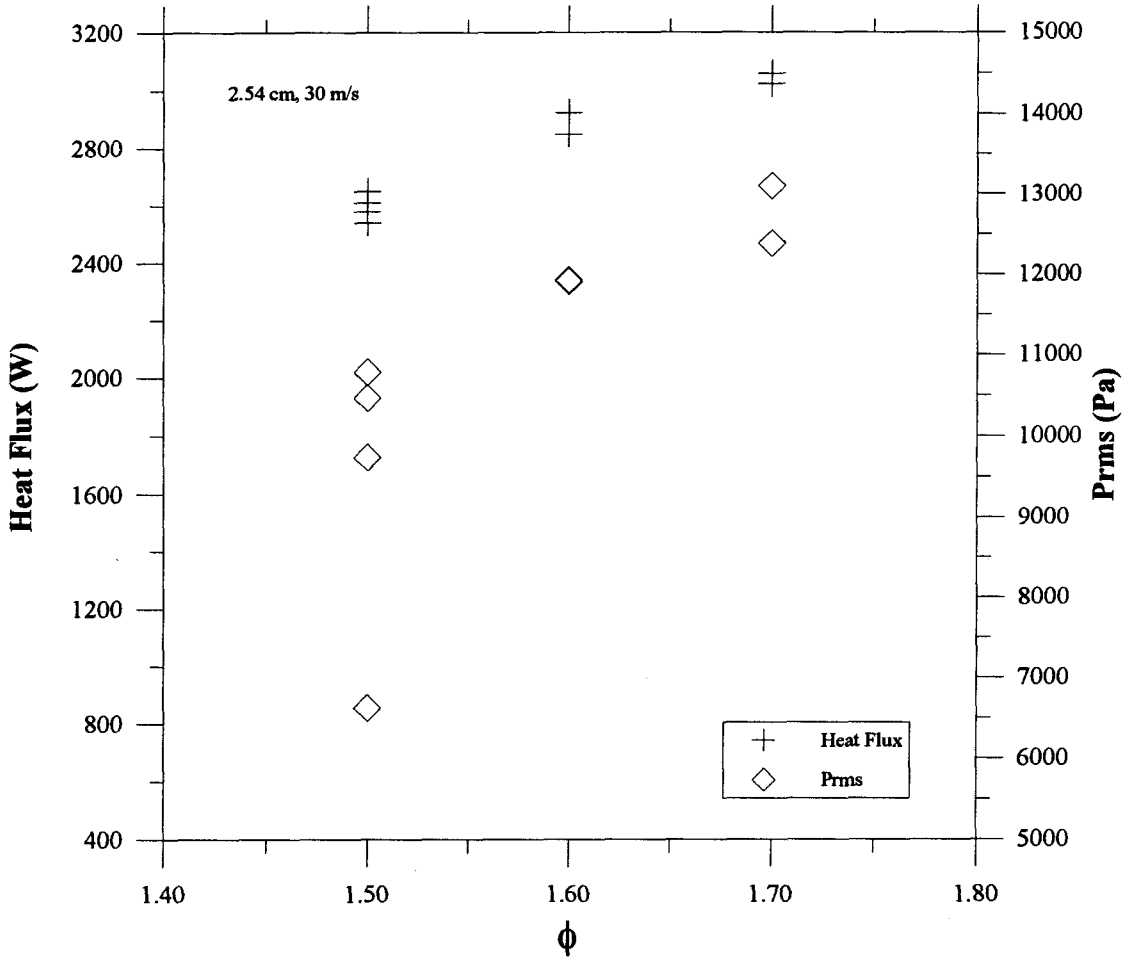

Figure 3.48: Total heat flux versus ϕ: 2.54 cm duct, 30 m/s.

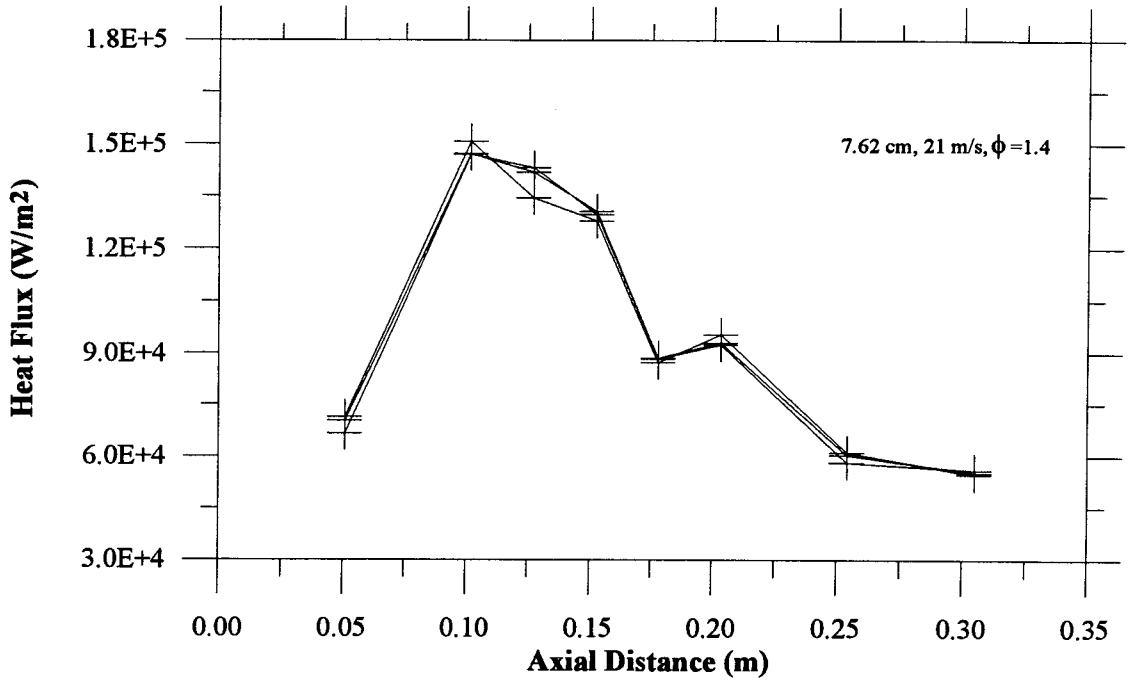

Figure 3.49a: Axial heat flux distribution: 7.62 cm, $V_{dump} = 21m/s$, $\phi = 1.4$.

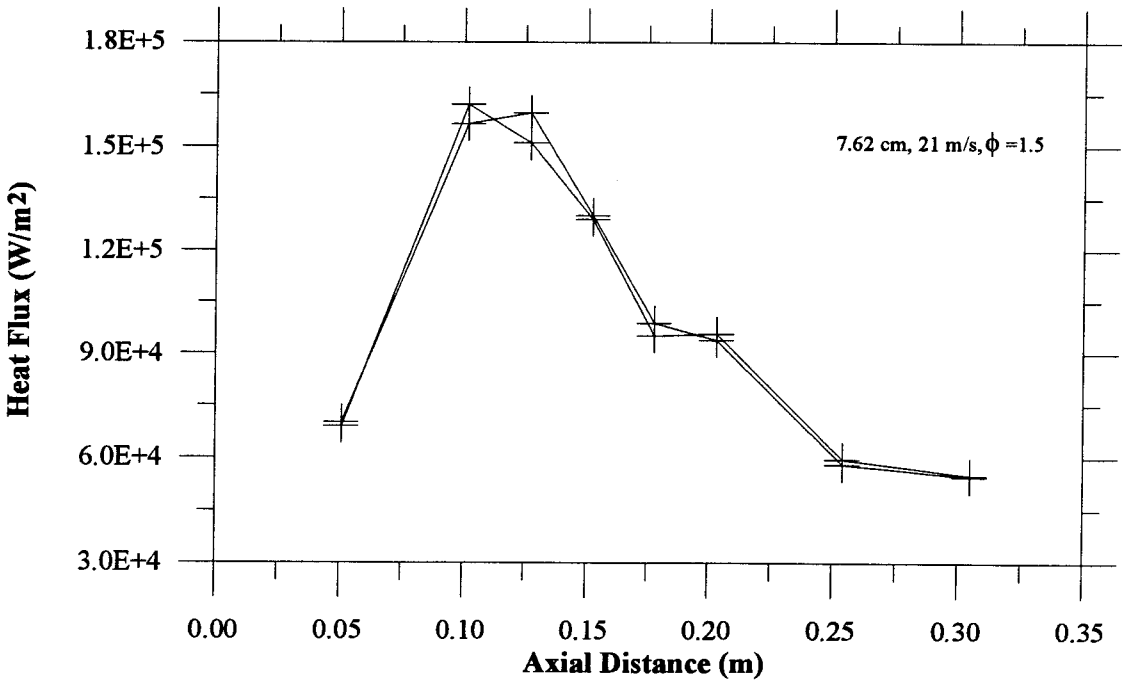

Figure 3.49b: Axial heat flux distribution: 7.62 cm, $V_{dump} = 21m/s$, $\phi = 1.5$.

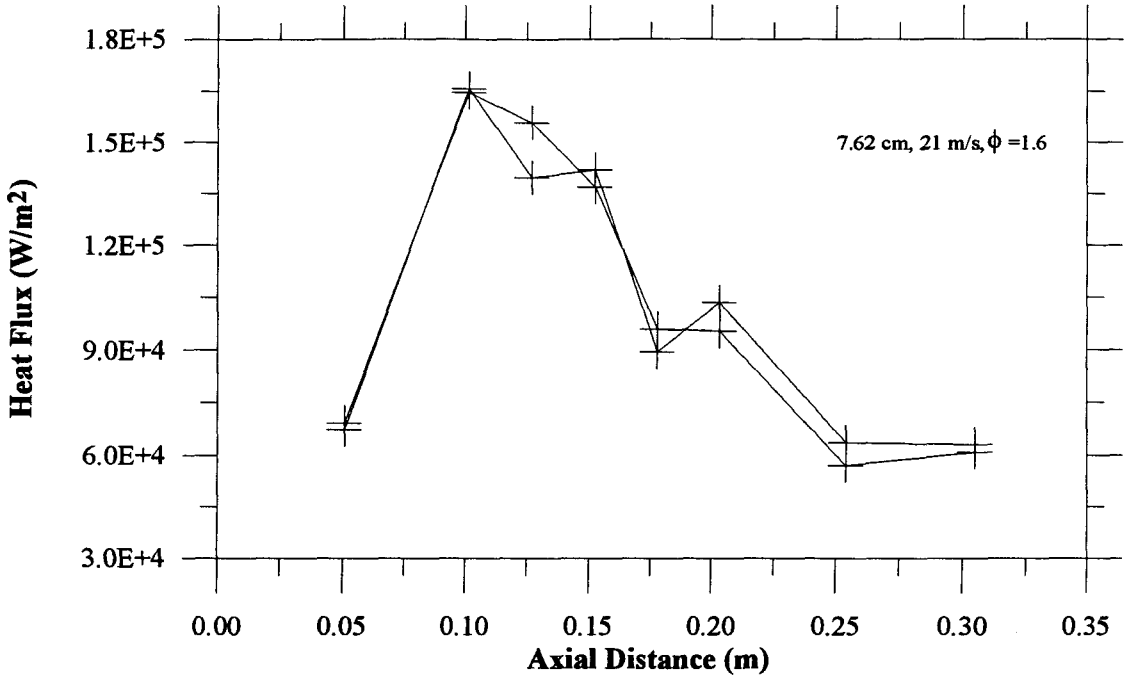

Figure 3.49c: Axial heat flux distribution: 7.62 cm, $V_{dump} = 21m/s$, $\phi = 1.6$.

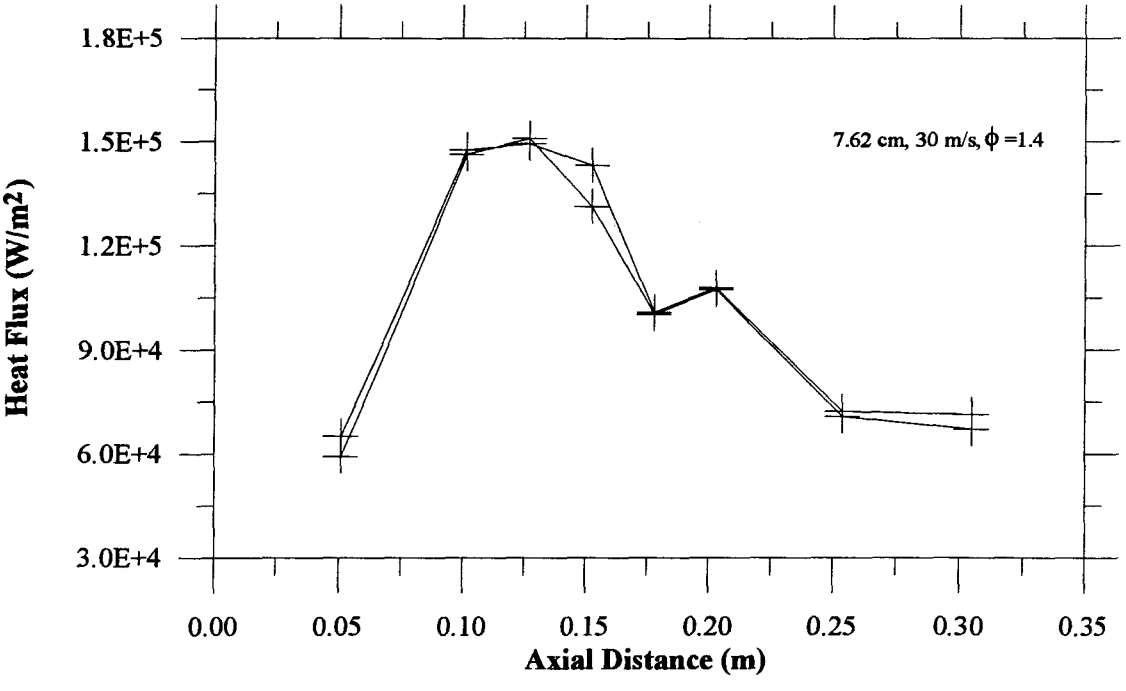

Figure 3.49d: Axial heat flux distribution: 7.62 cm, $V_{dump} = 30m/s$, $\phi = 1.4$.

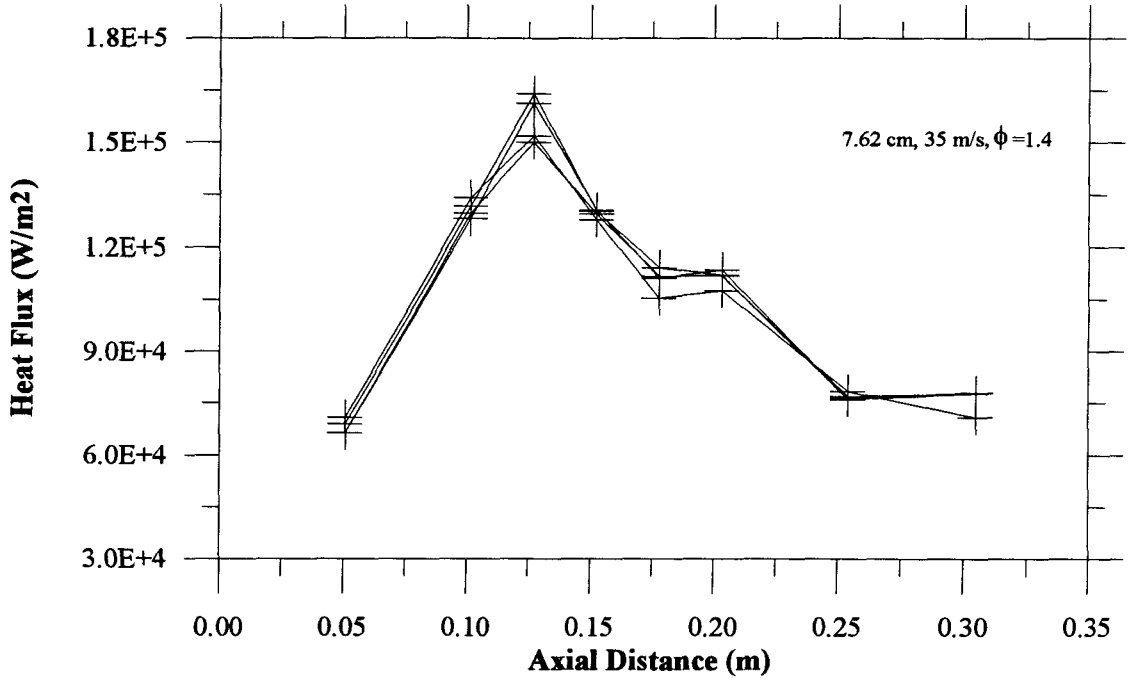

Figure 3.49e: Axial heat flux distribution: $V_{dump} = 35m/s,\ \phi = 1.4.$

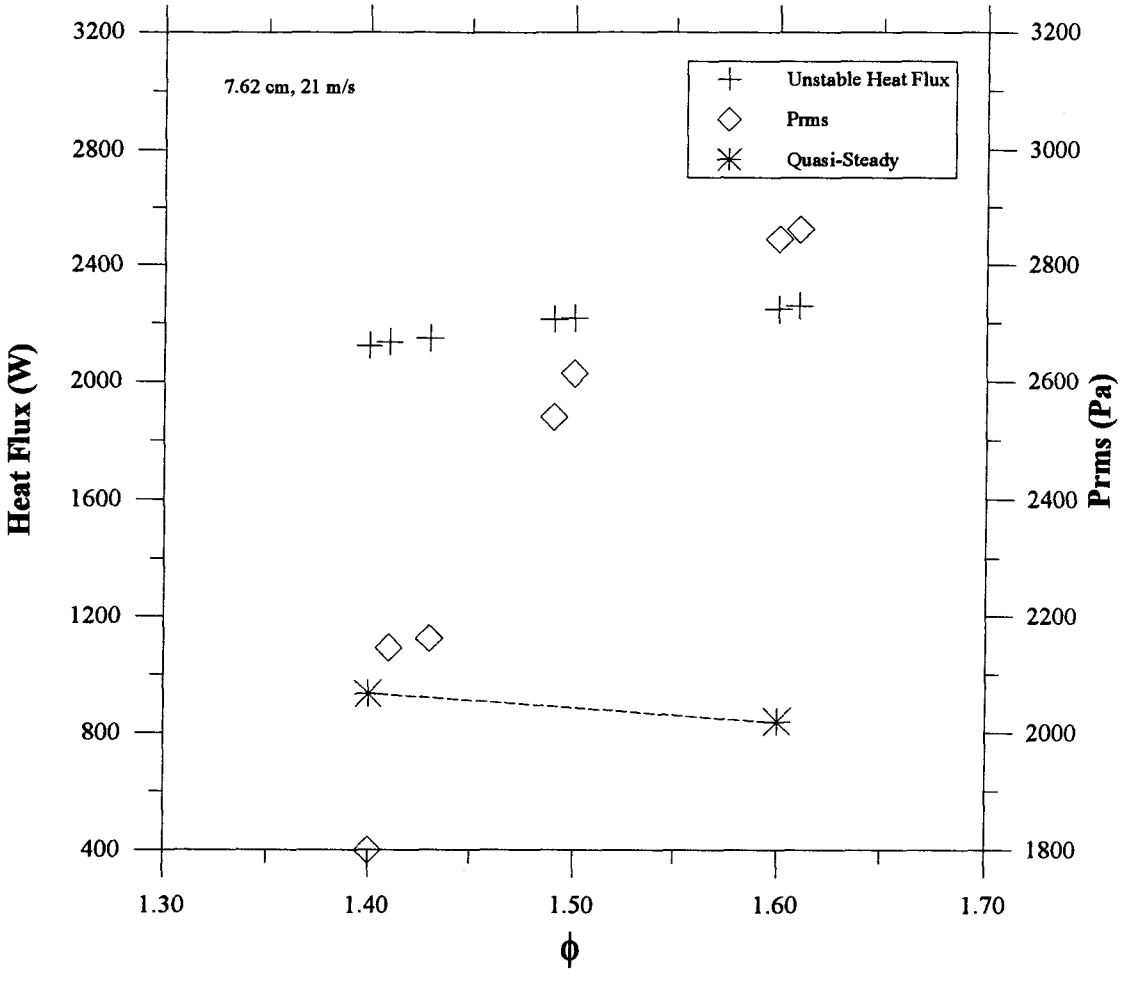

Figure 3.50: Total heat flux versus ϕ: 7.62 cm duct, 21 m/s.

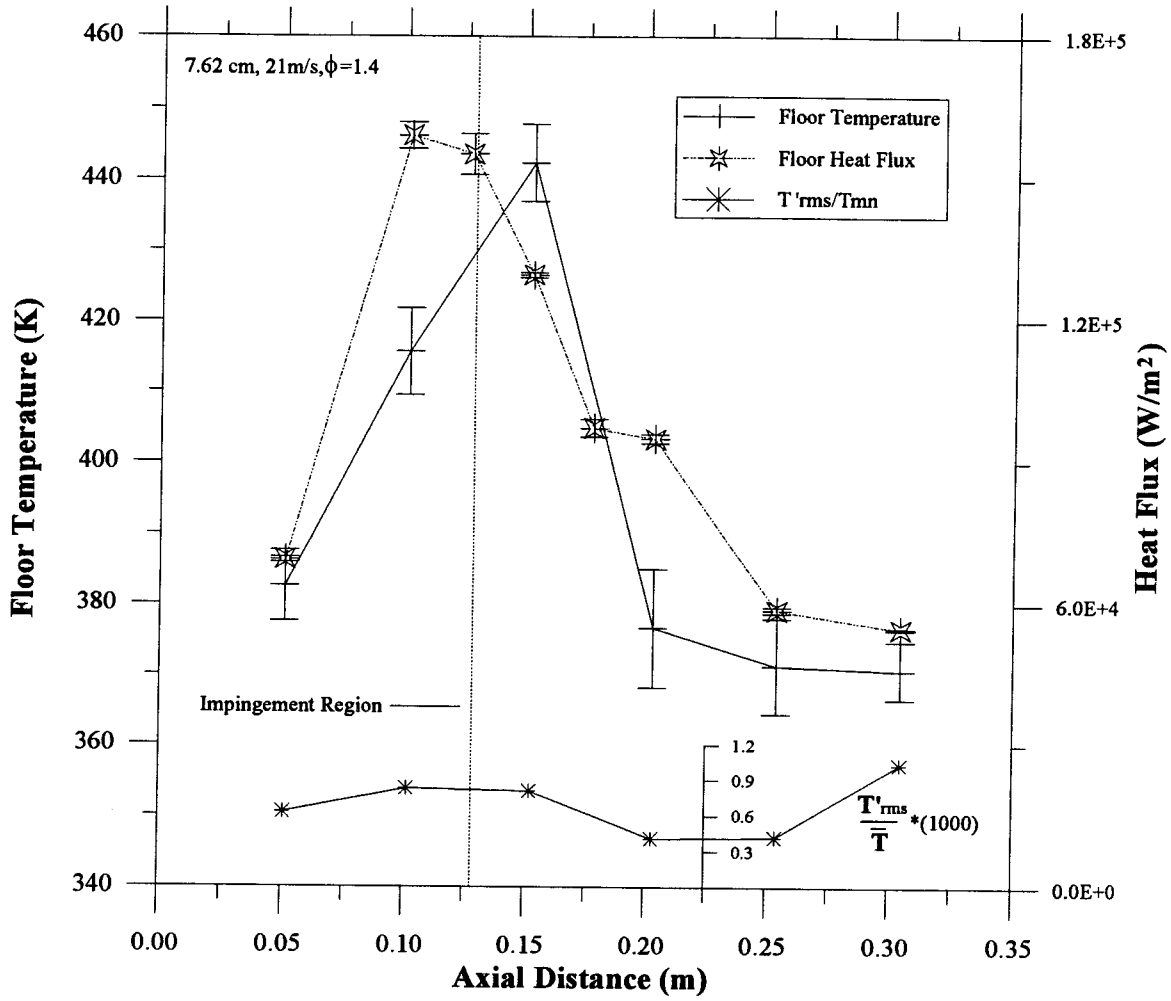

Figure 3.51: Summary of floor temperature and heat flux measurements: 7.62 cm, $V_{dump} = 21m/s$, $\phi = 1.4$.

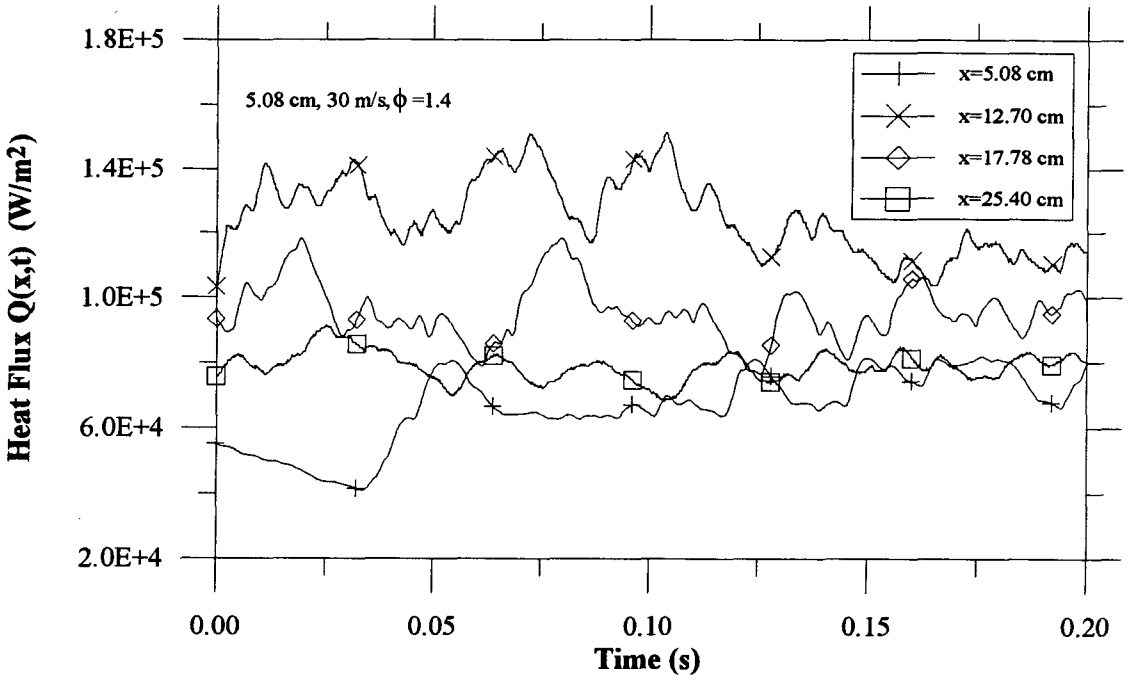

Figure 3.52a: Heat flux versus time: 5.08 cm, $V_{dump} = 30 m/s$, $\phi = 1.4$.

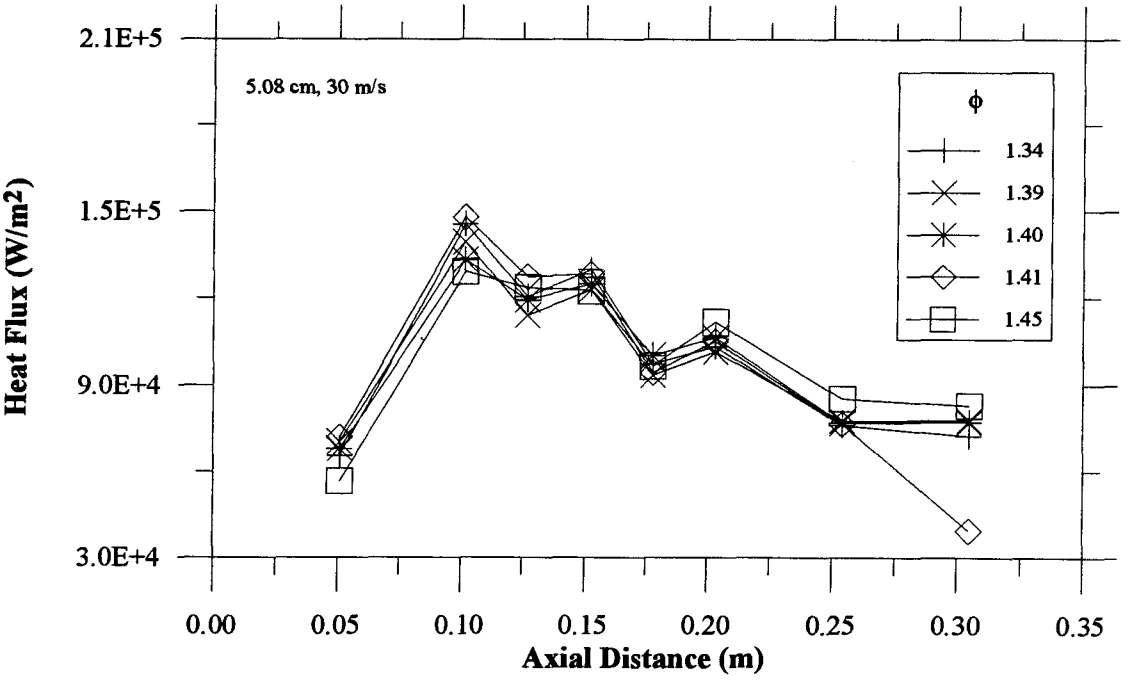

Figure 3.52b: Axial heat flux distribution versus ϕ: 5.08 cm, $V_{dump} = 30 m/s$.

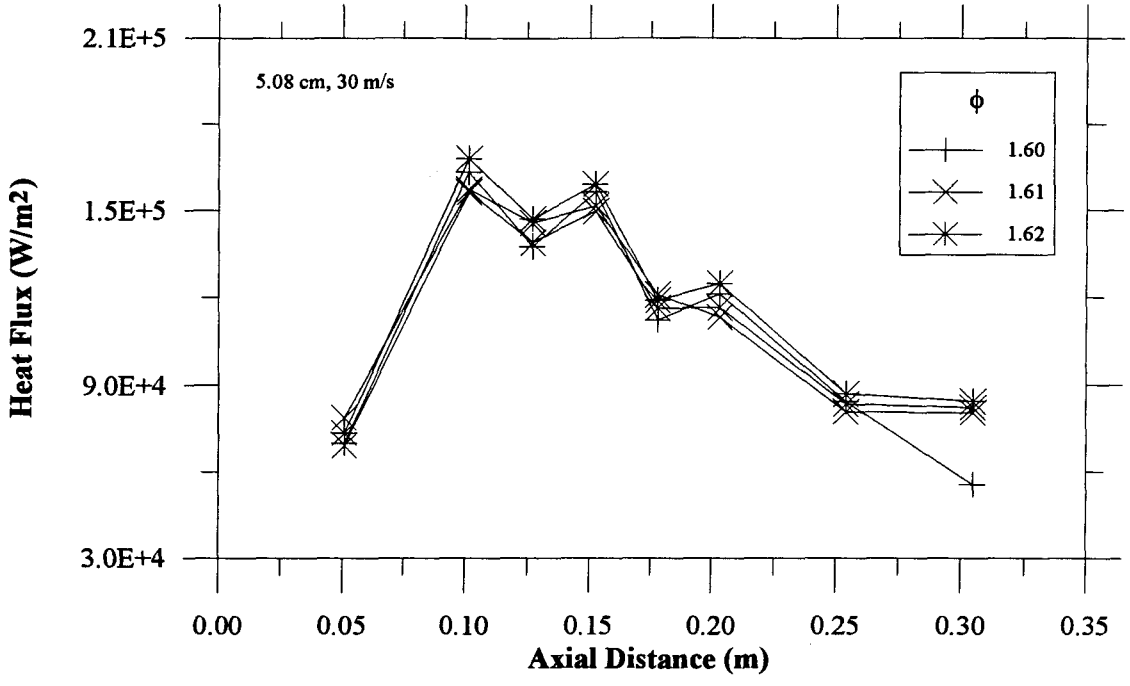

Figure 3.52c: Axial heat flux distribution versus ϕ: 5.08 cm, $V_{dump} = 30 m/s$.

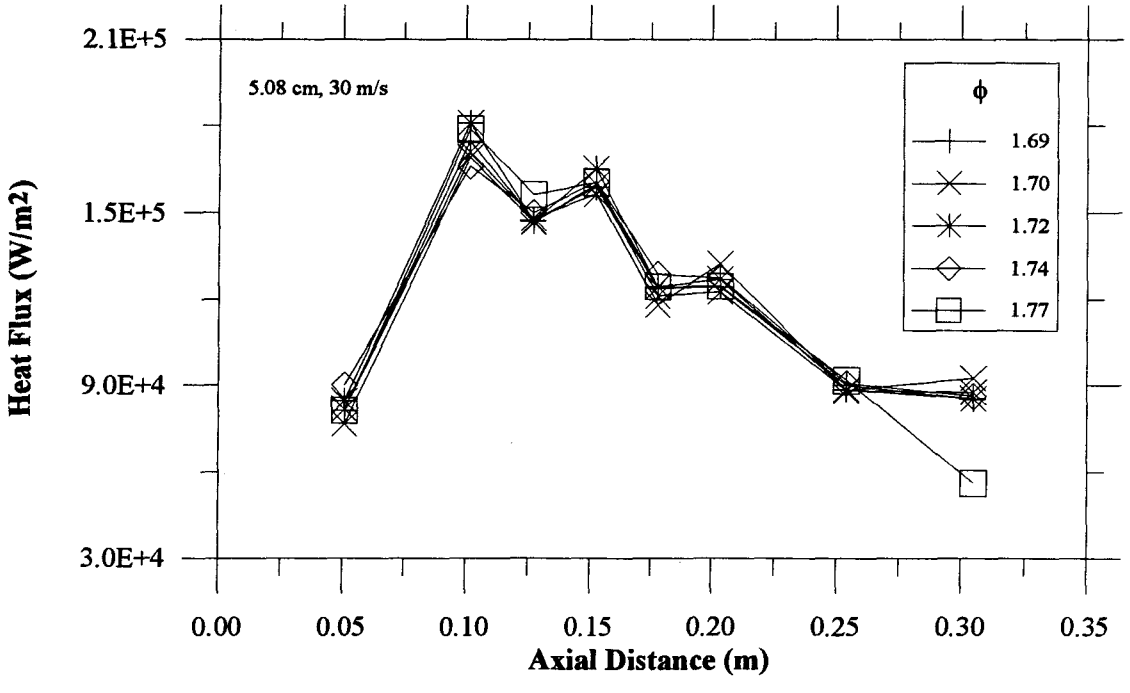

Figure 3.52d: Axial heat flux distribution versus ϕ: 5.08 cm, $V_{dump} = 30 m/s$.

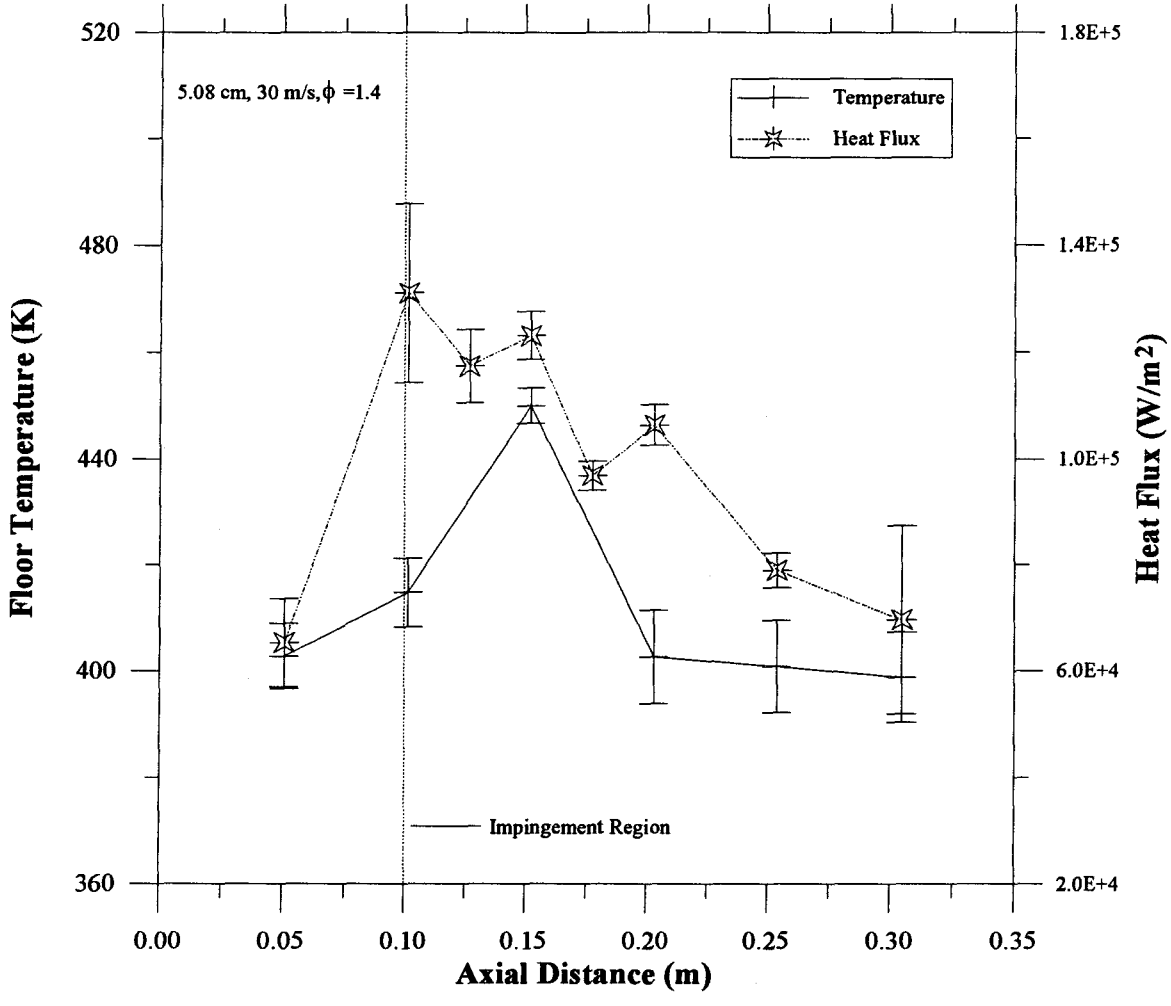

Figure 3.53: Summary of floor temperature and heat flux measurements: 5.08 cm, $V_{dump} = 30 m/s$, $\phi = 1.4$.

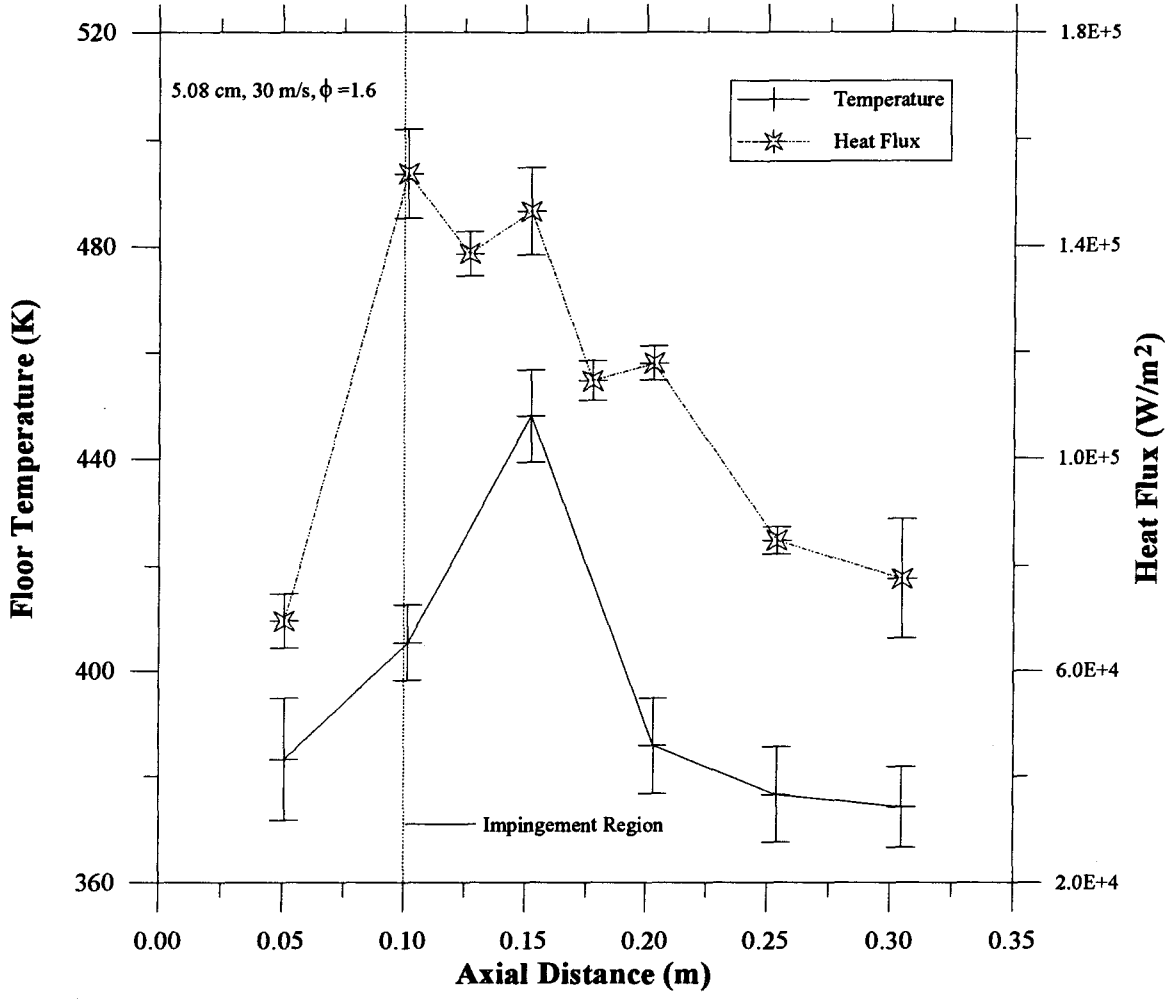

Figure 3.54: Summary of floor temperature and heat flux measurements: 5.08 cm, $V_{dump} = 30 m/s$, $\phi = 1.6$.

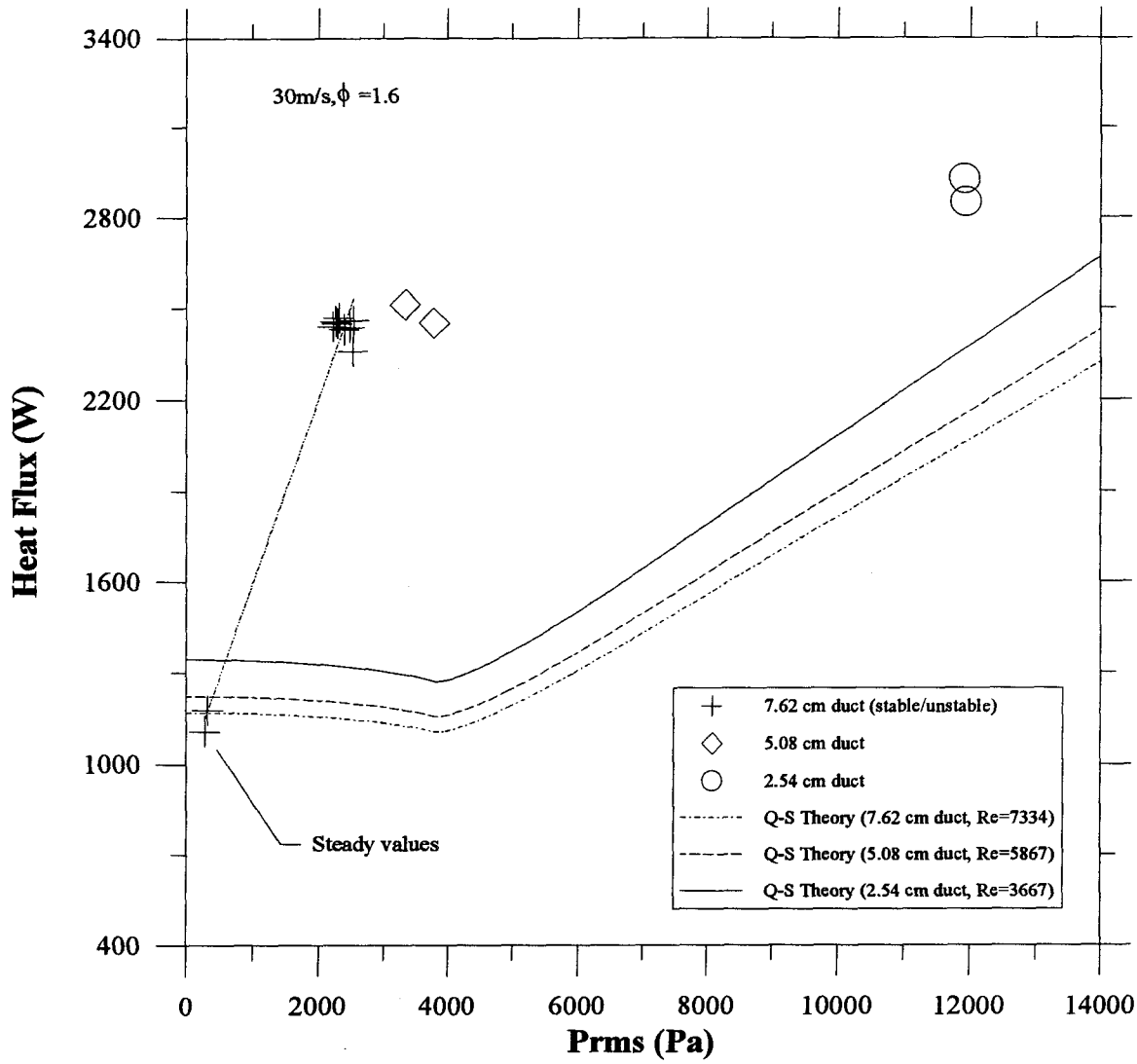

Figure 3.55: Summary of floor heat flux values with Quasi-Steady Theory.

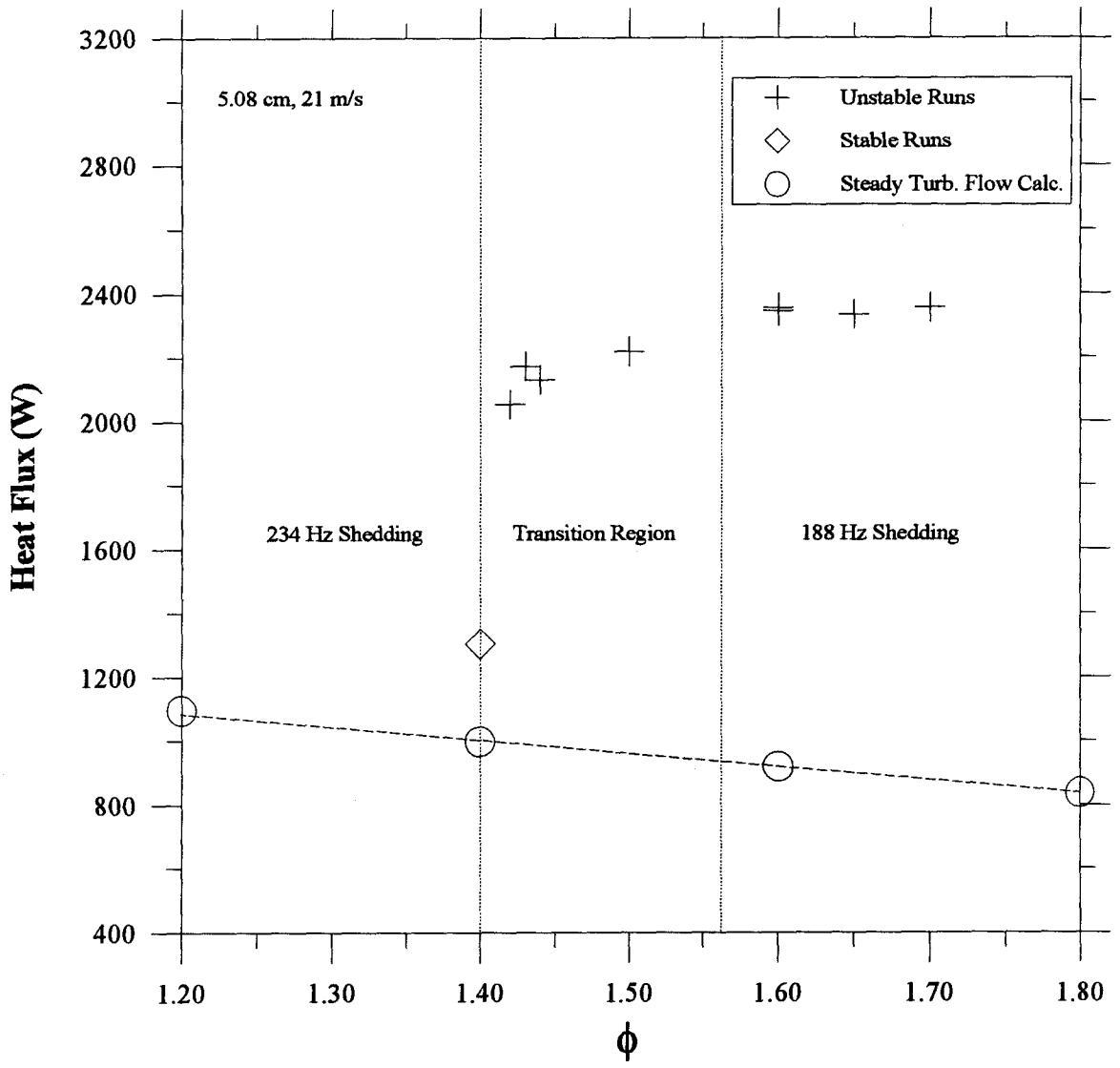

Figure 3.56: $\dot{Q}_{floor}$ transition data: 5.08 cm duct, 21 m/s.

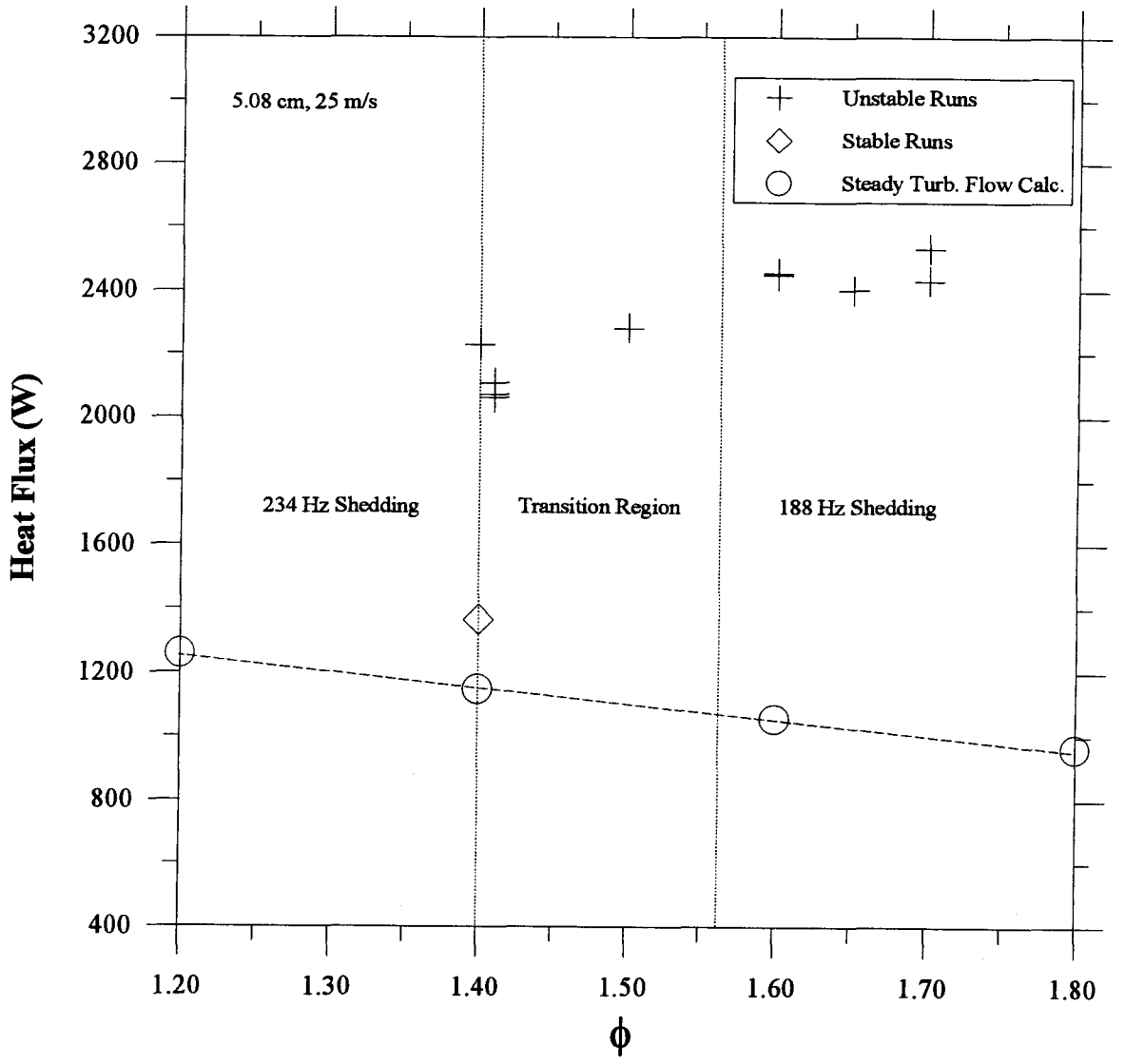

Figure 3.57: $\dot{Q}_{floor}$ transition data: 5.08 cm duct, 25 m/s.

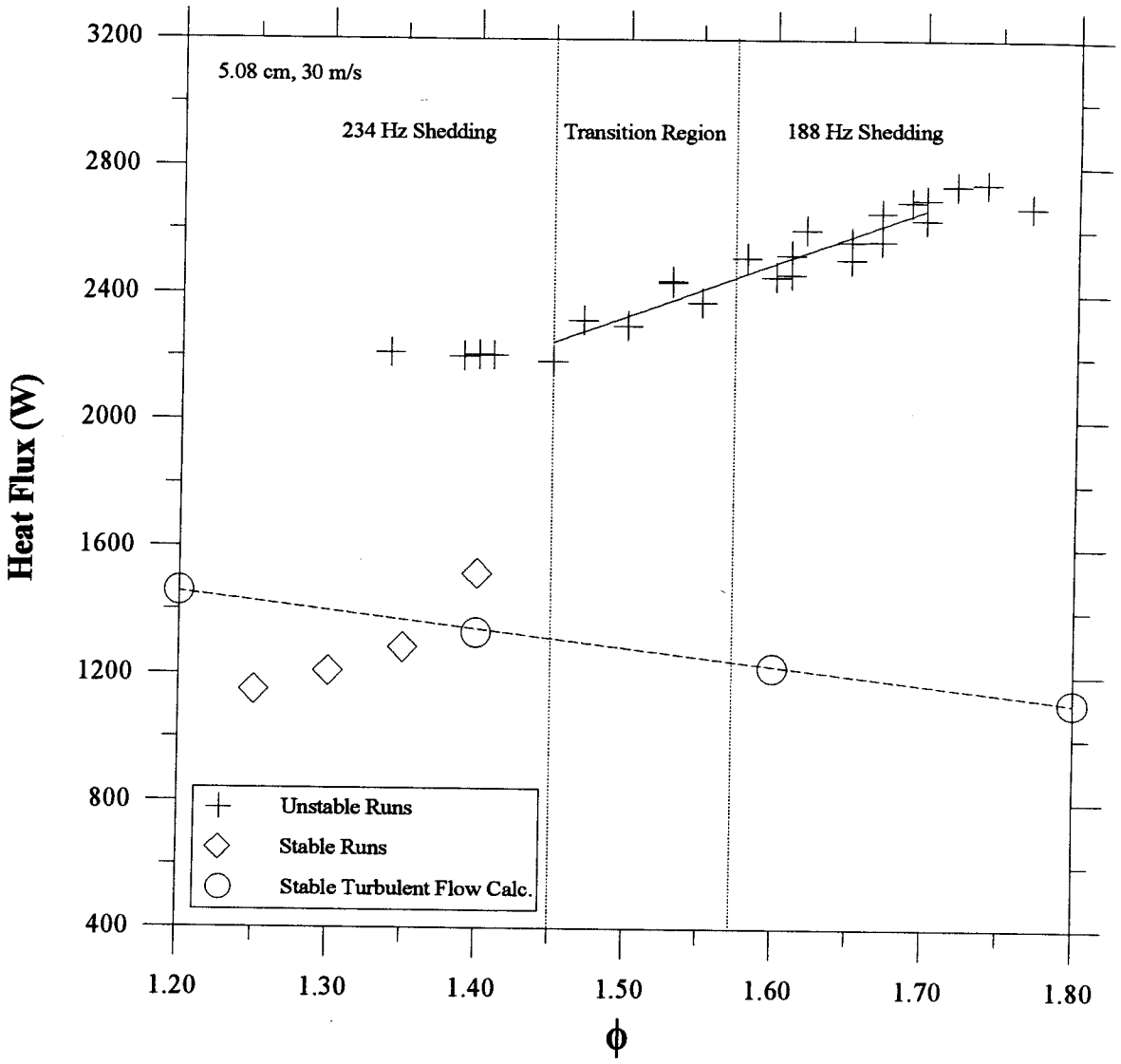

Figure 3.58: $\dot{Q}_{floor}$ transition data: 5.08 cm duct, 30 m/s.

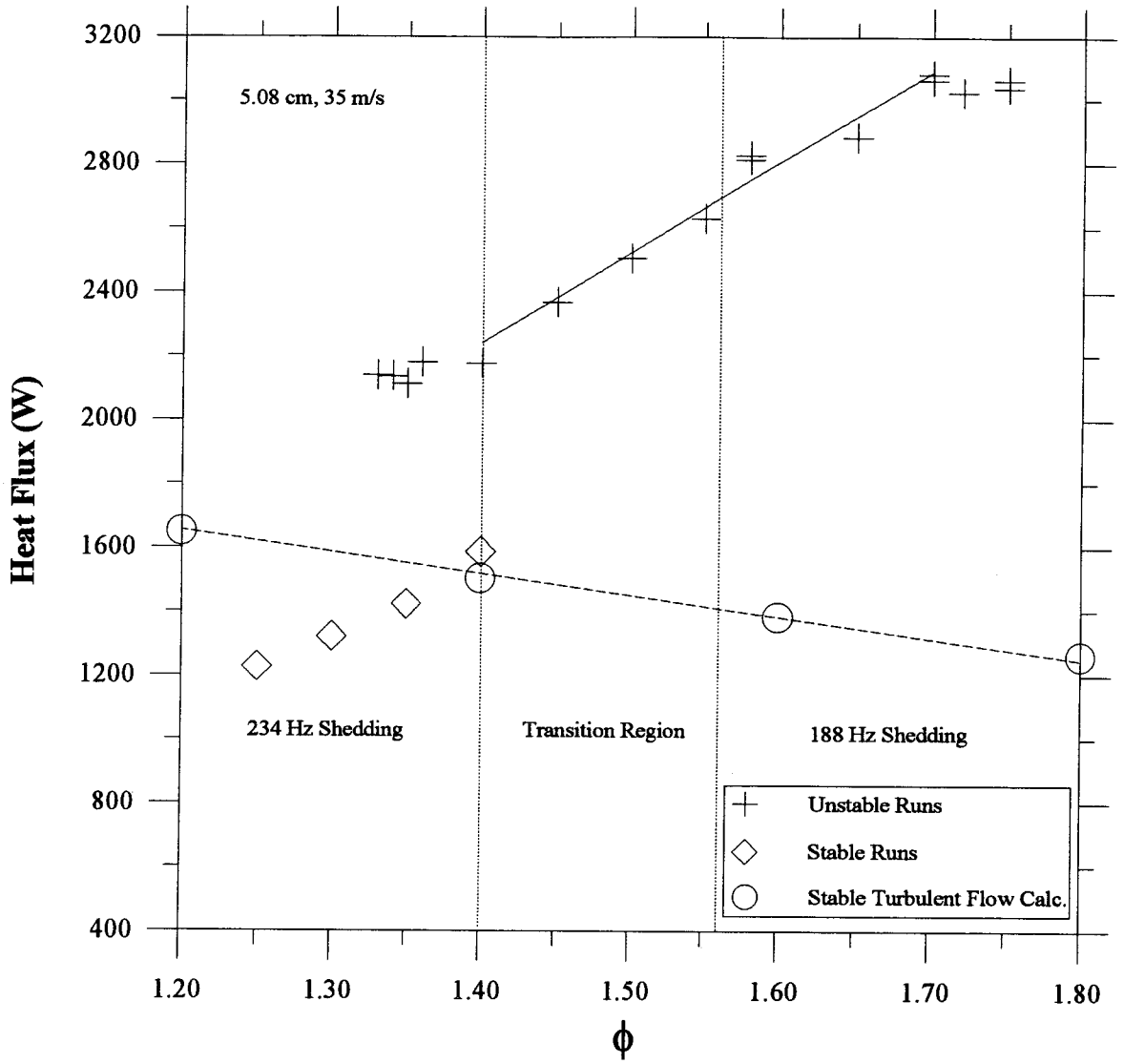

Figure 3.59: $\dot{Q}_{floor}$ transition data: 5.08 cm duct, 35 m/s.

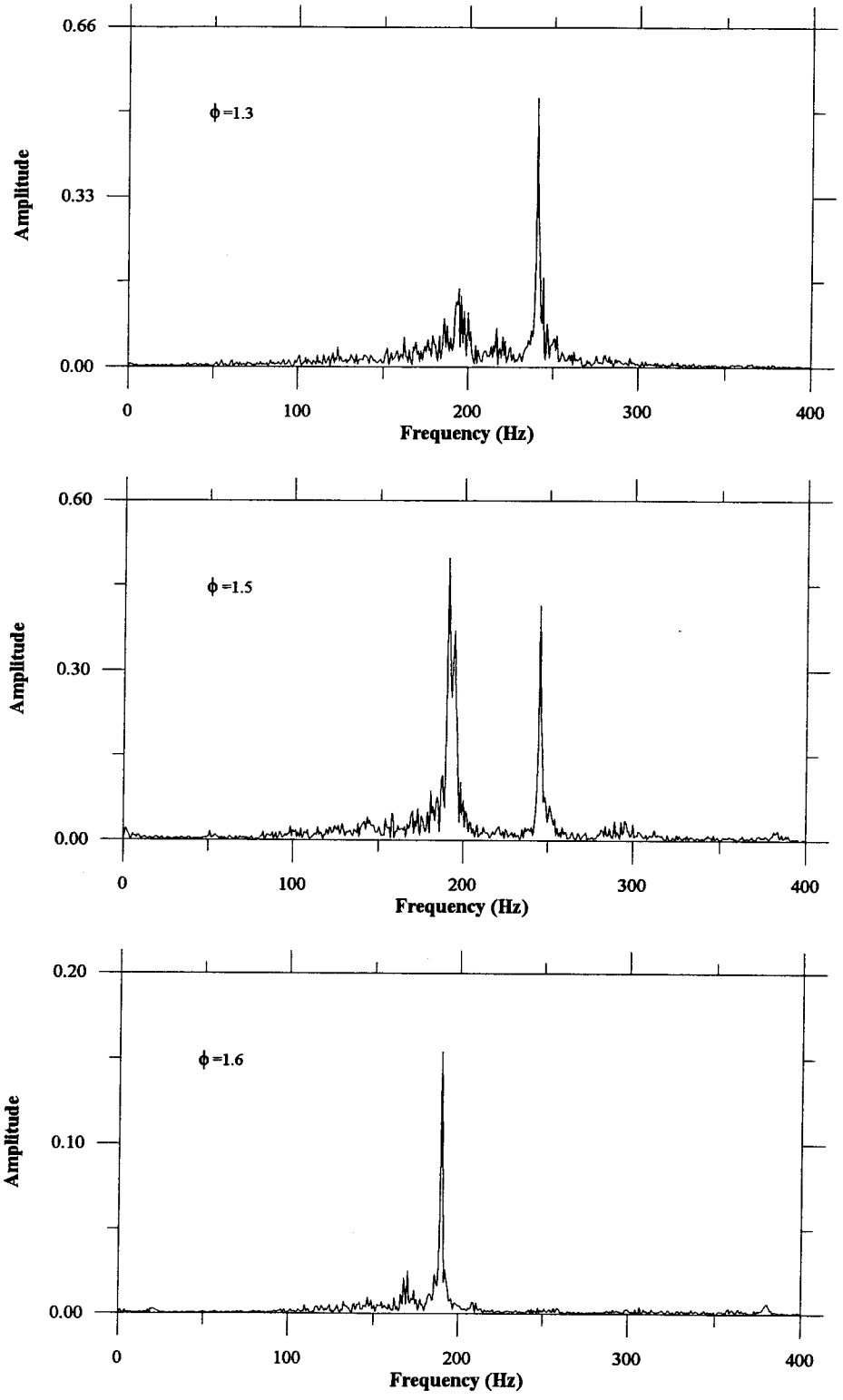

Figure 3.60: Sequence of transitional pressure FFTs.

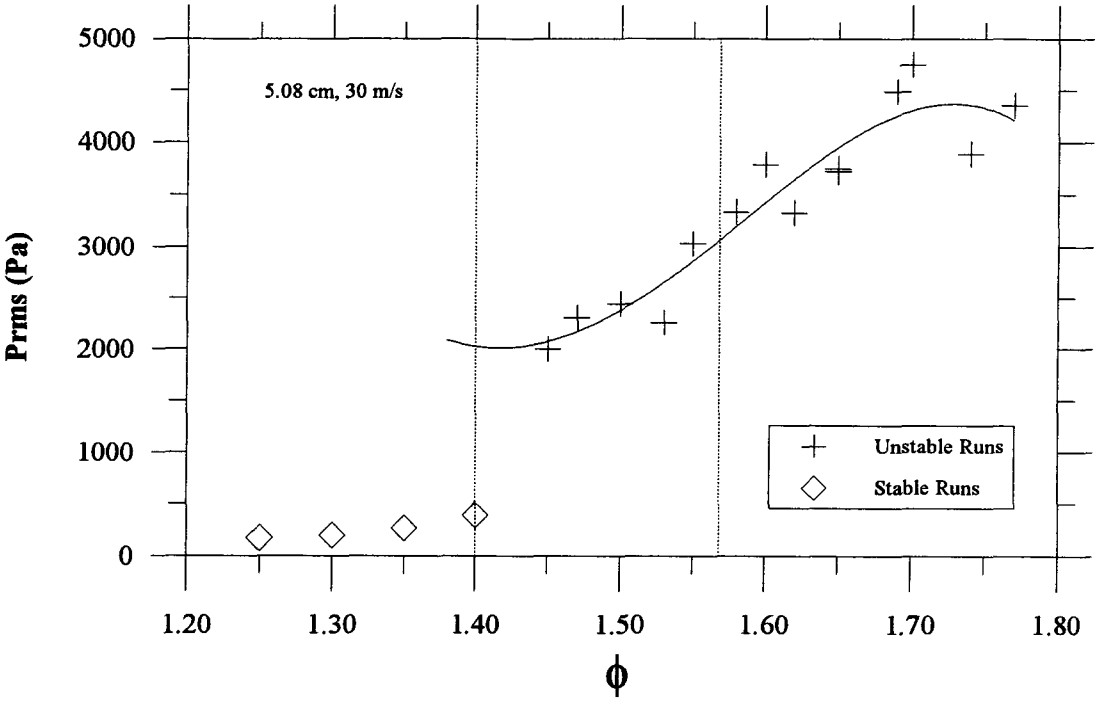

Figure 3.61: Transitional pressure values: 5.08 cm, 30 m/s.

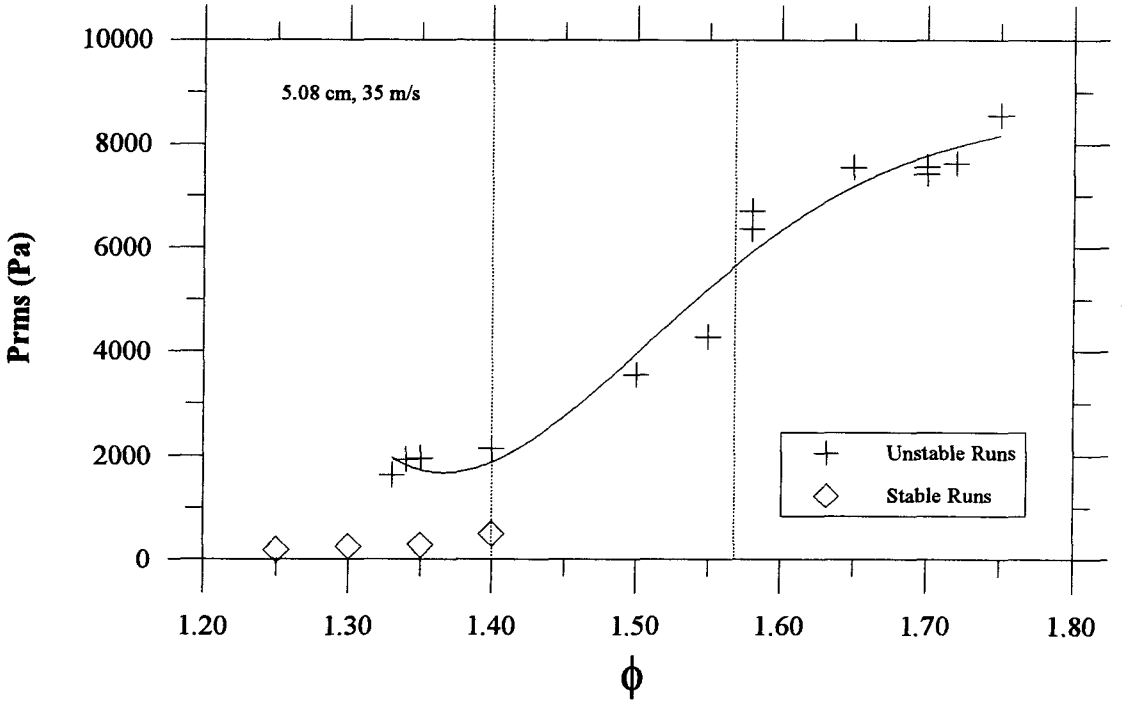

Figure 3.62: Transitional pressure values: 5.08 cm, 35 m/s.

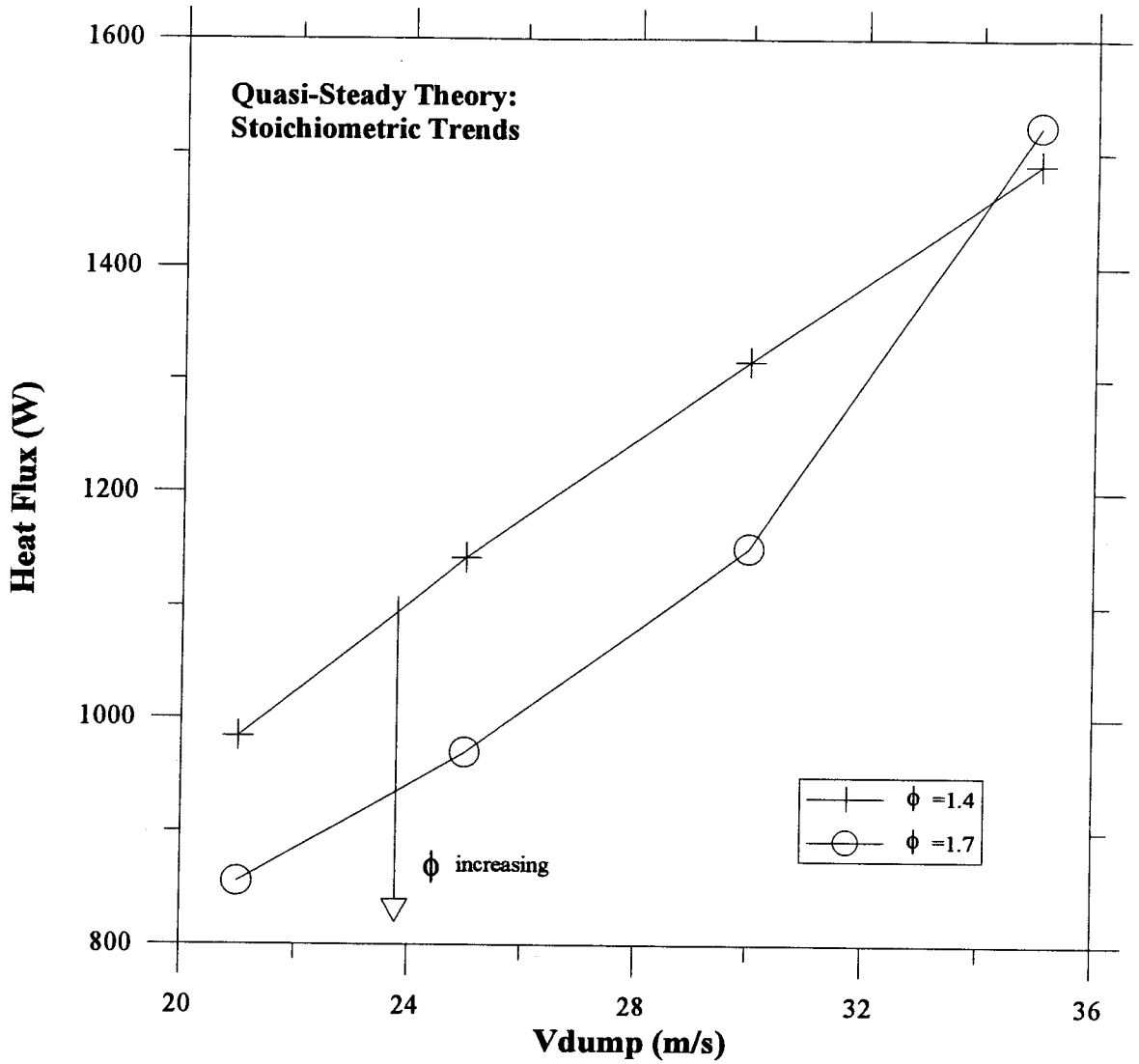

Figure 3.63: Quasi-Steady trends with ϕ: 5.08 cm.

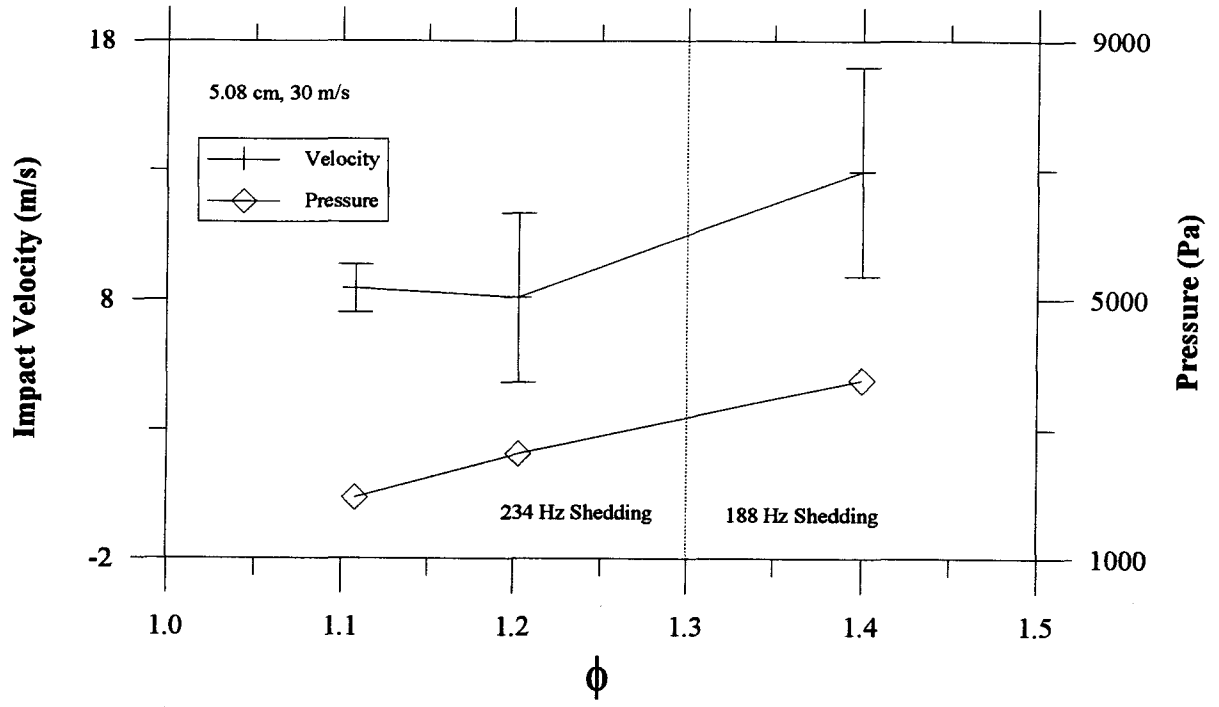

Figure 3.64a: Impact velocity versus ϕ: 5.08 cm, 30 m/s.

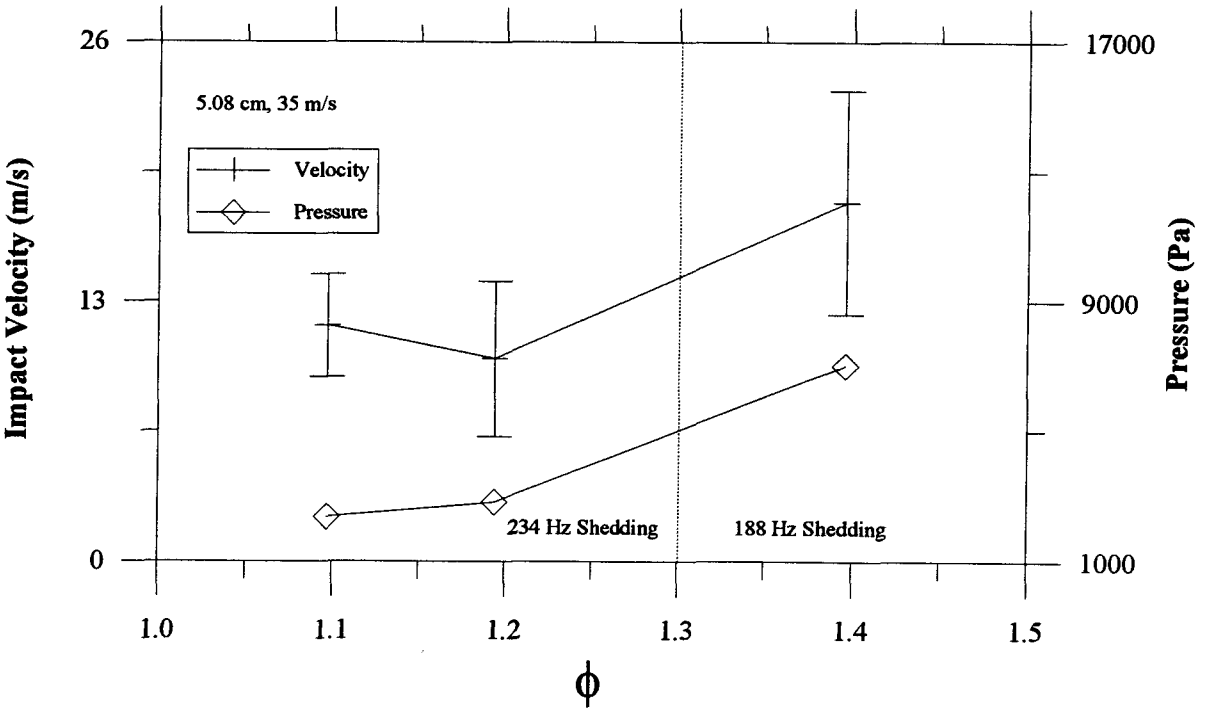

Figure 3.64b: Impact velocity versus ϕ: 5.08 cm, 35 m/s.

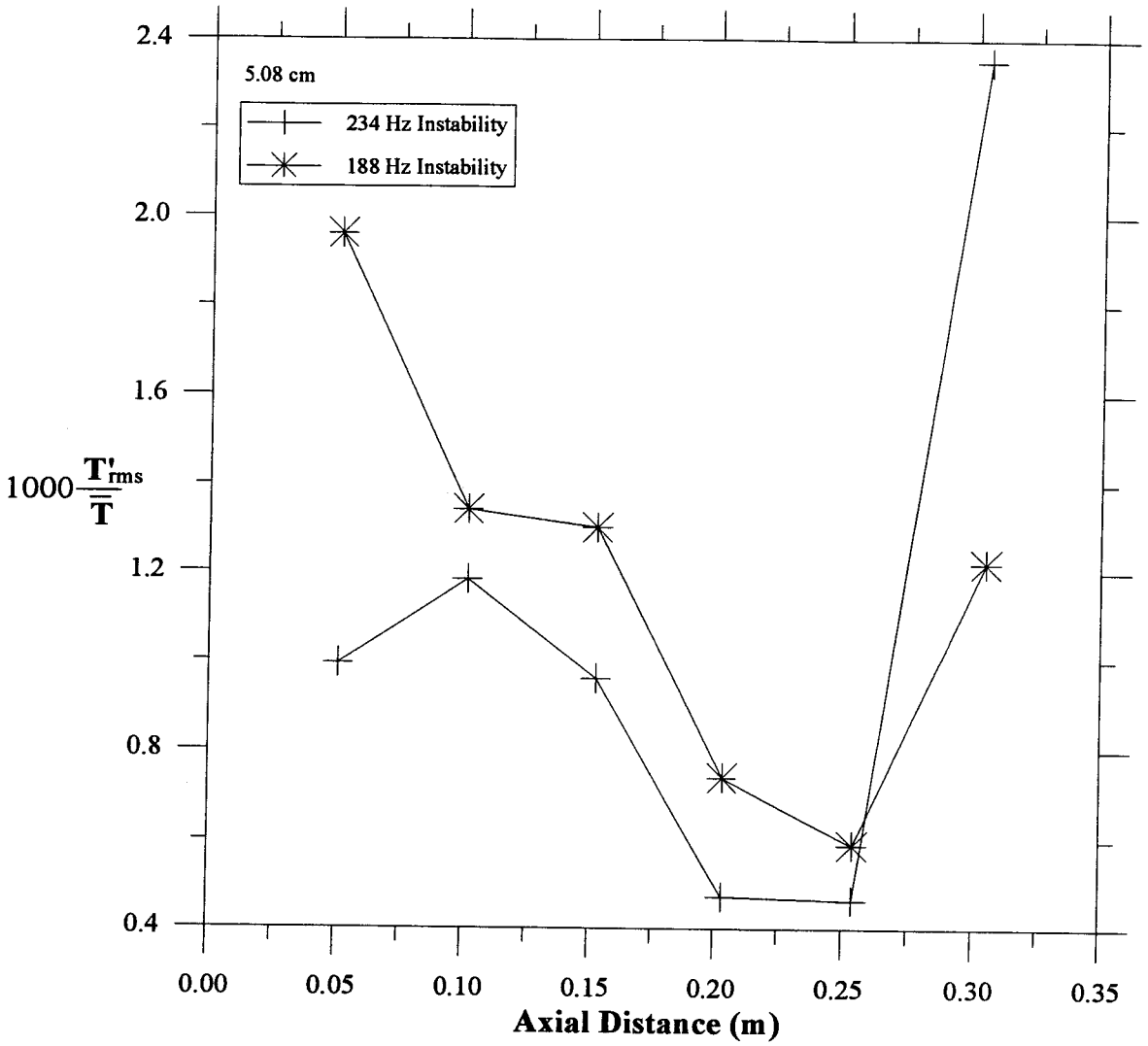

Figure 3.65: Comparison of floor, rms temperature fluctuations, T'_{rms}, under a mode transition nondimensionalized by average floor temperature, $\overline{T}(x)$: 5.08 cm, 30 m/s.

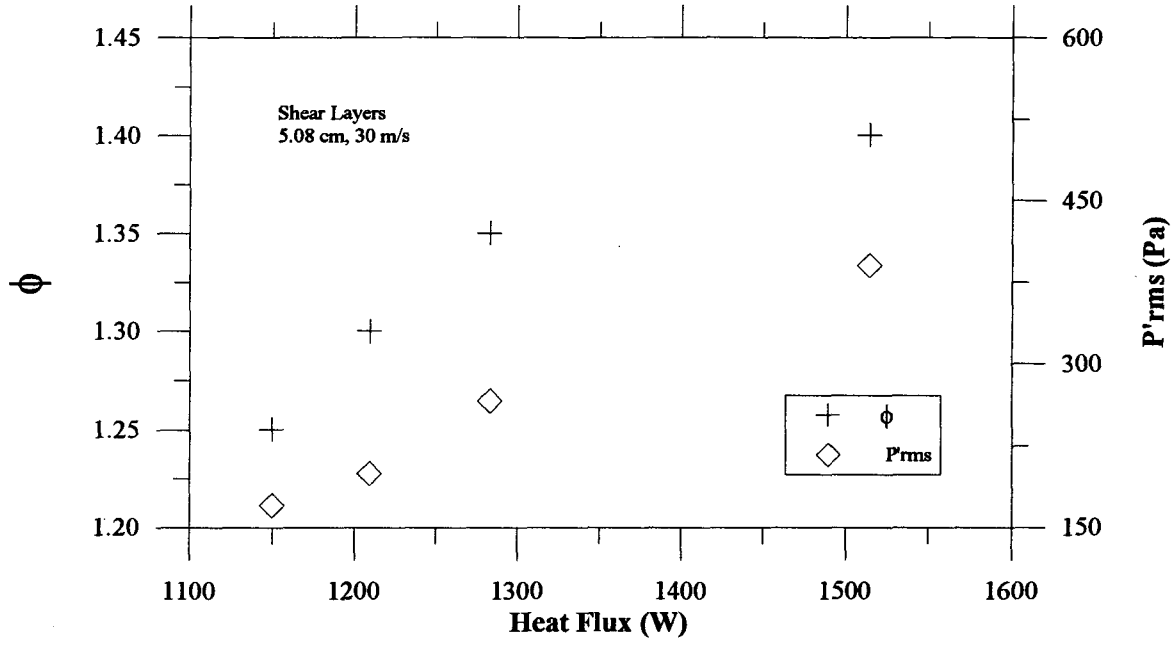

Figure 3.66a: Shear layer heat flux values: 5.08 cm, 30 m/s.

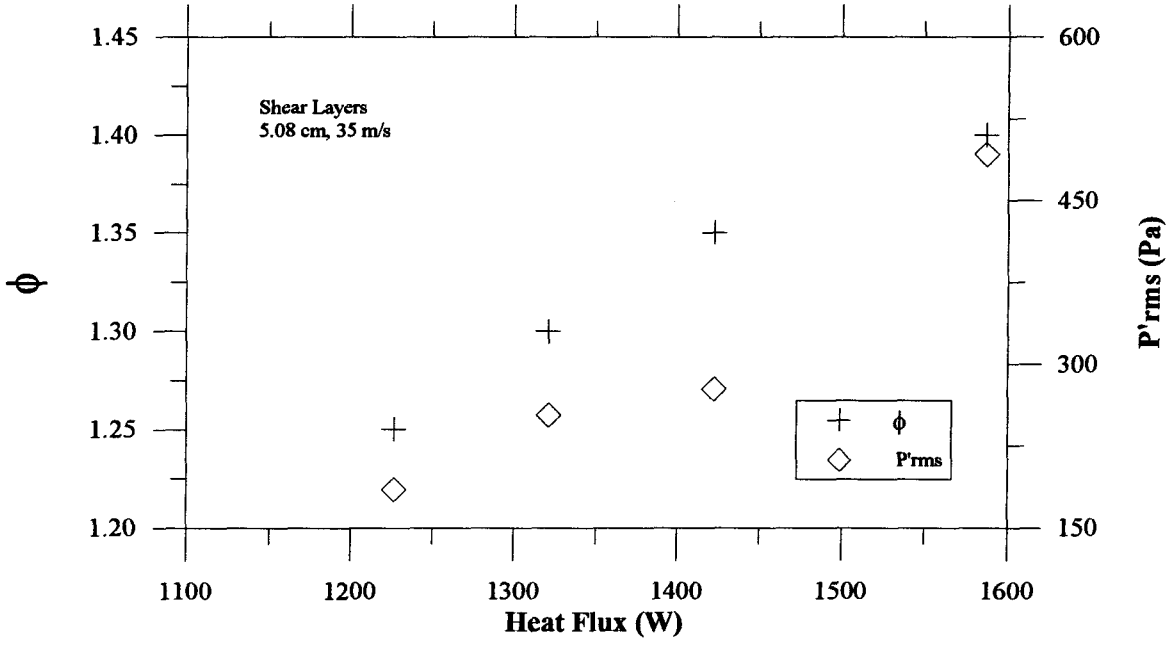

Figure 3.66b: Shear layer heat flux values: 5.08 cm, 35 m/s.

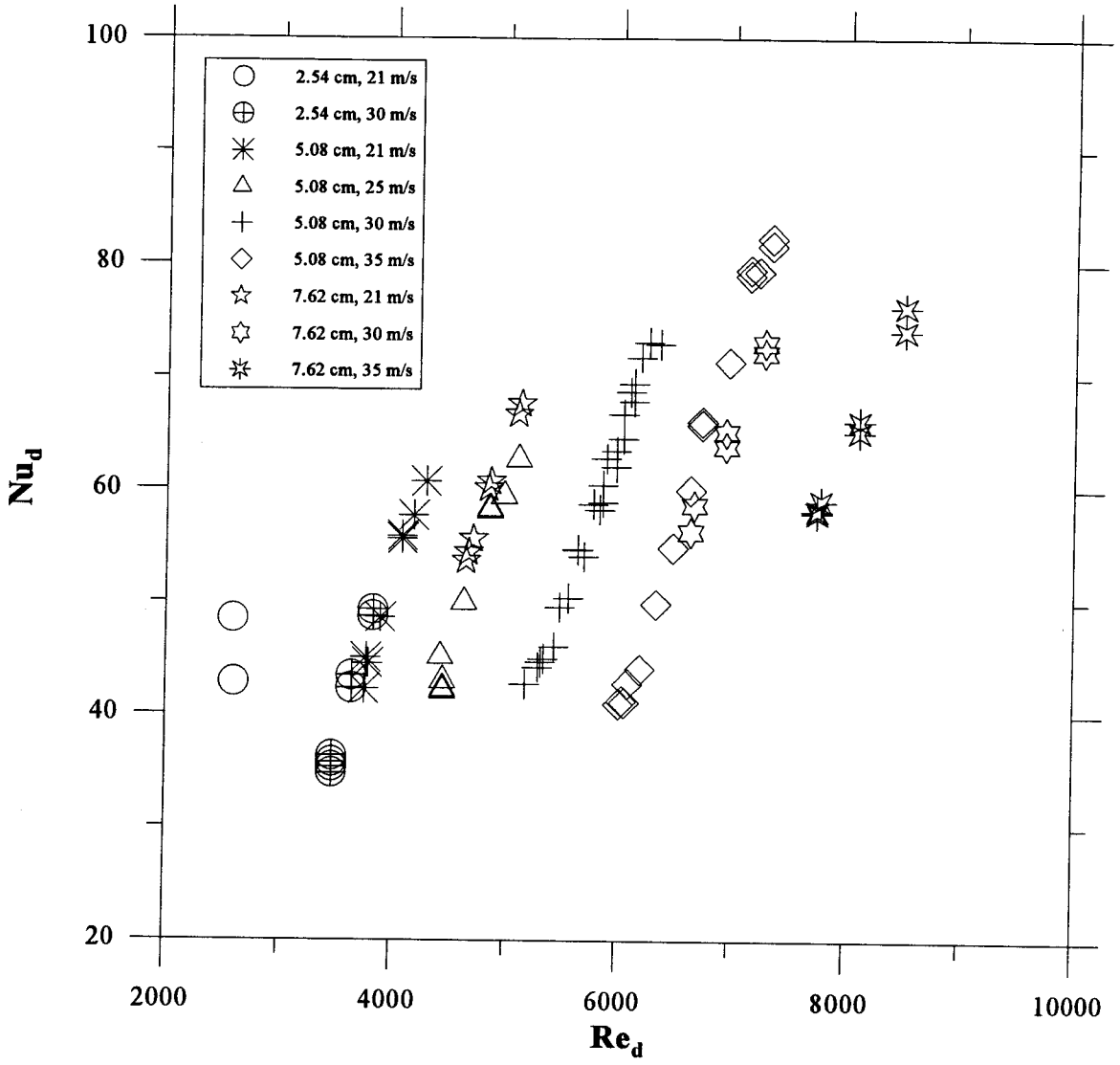

Figure 3.67: Summary of all heat flux data.

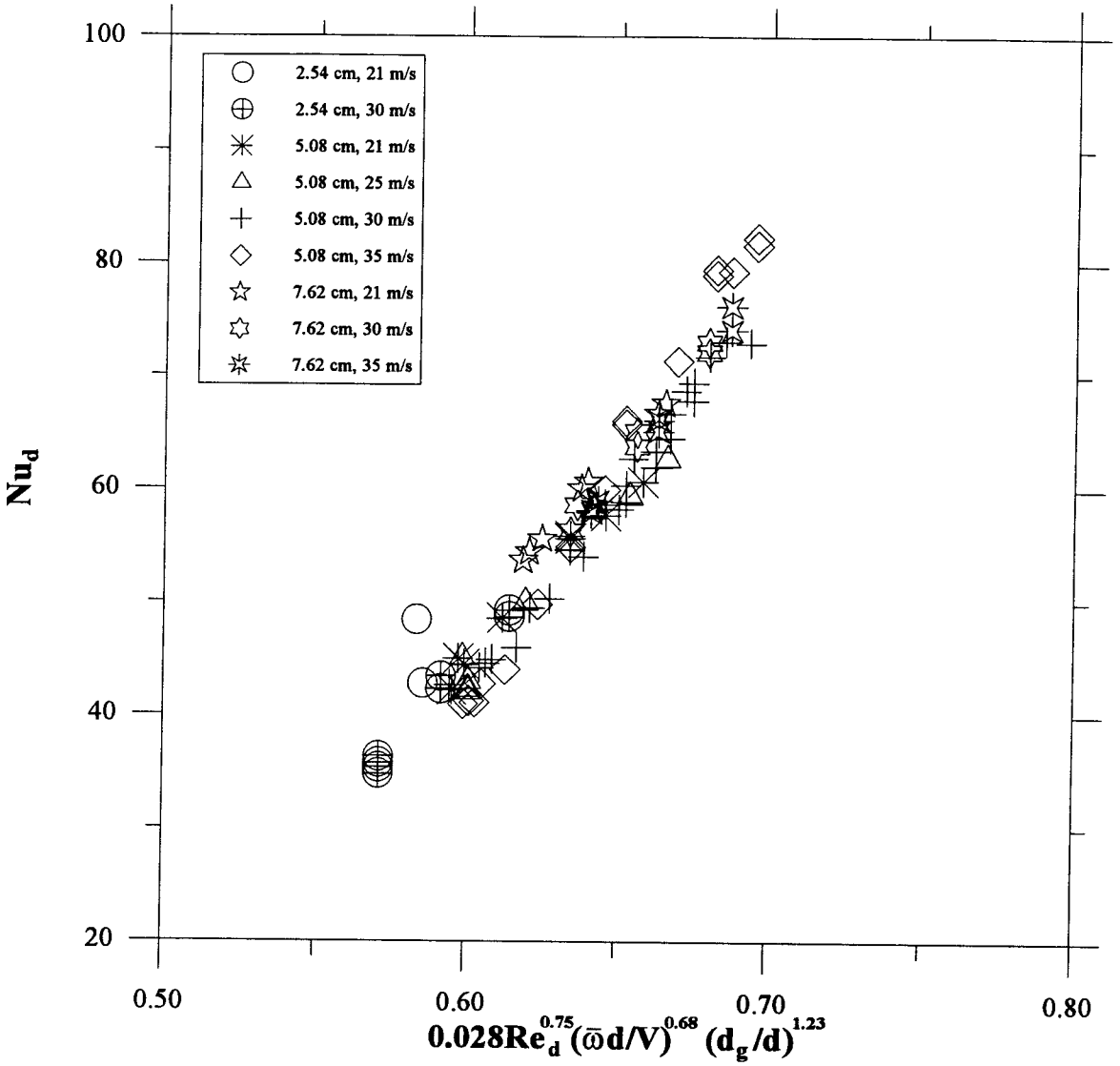

Figure 3.68: Correlation of all heat flux data.

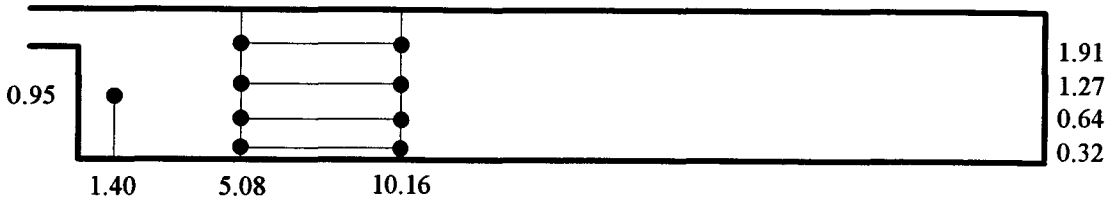

Figure 3.69: 2.54 cm duct temperature measurement locations: 21 m/s, $\phi = 1.3$. (Dimensions are in cm).

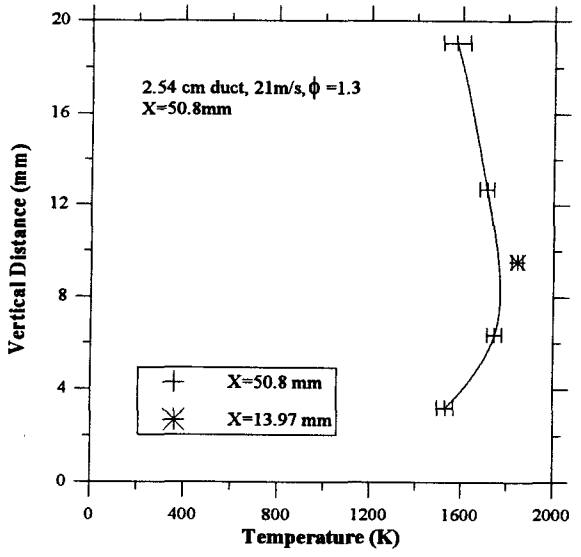

Figure 3.70: 2.54 cm duct temperature measurements: x=50.8 mm.

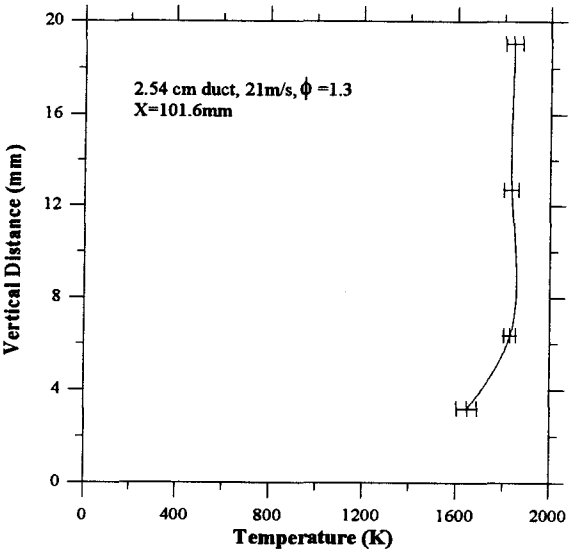

Figure 3.71: 2.54 cm duct temperature measurements: x=101.6 mm.

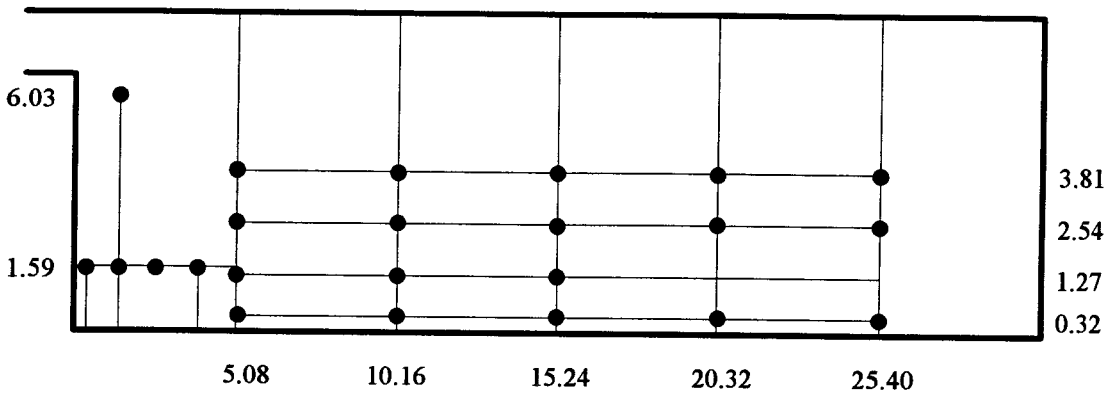

Figure 3.72: 7.62 cm duct temperature measurement locations: 21 m/s, $\phi = 1.3$. (Dimensions are in cm).

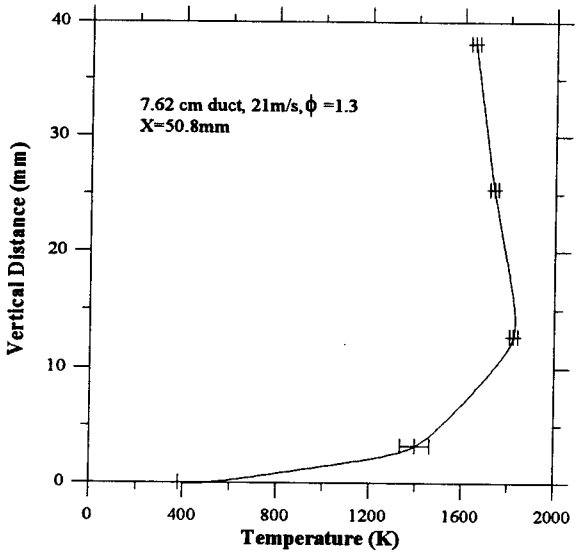

Figure 3.73: 7.62 cm duct temperature measurements: x=50.8 mm.

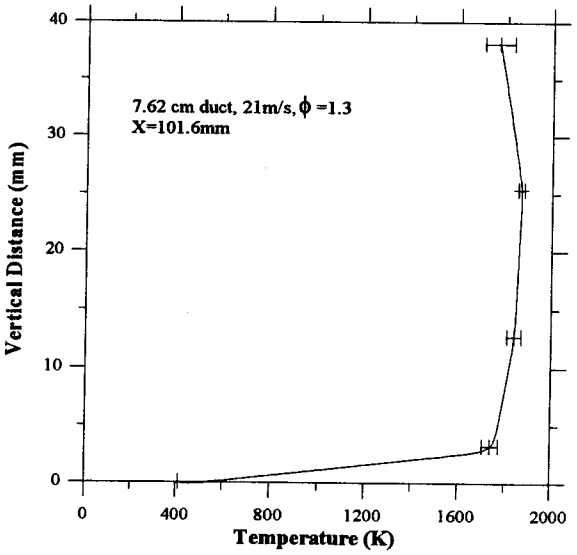

Figure 3.74: 7.62 cm duct temperature measurements: x=101.6 mm.

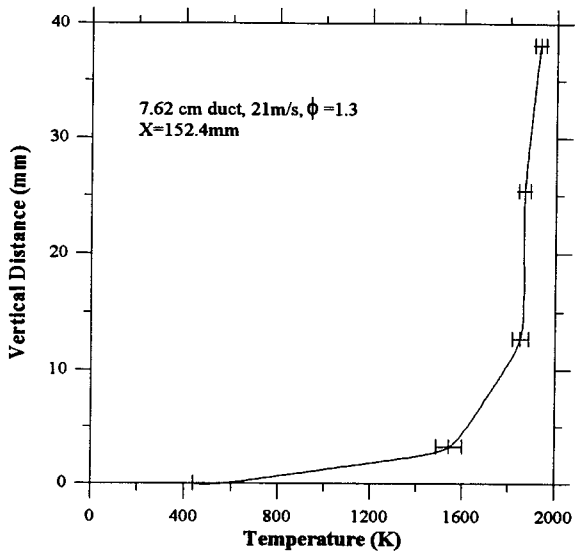

Figure 3.75: 7.62 cm duct temperature measurements: x=152.4 mm.

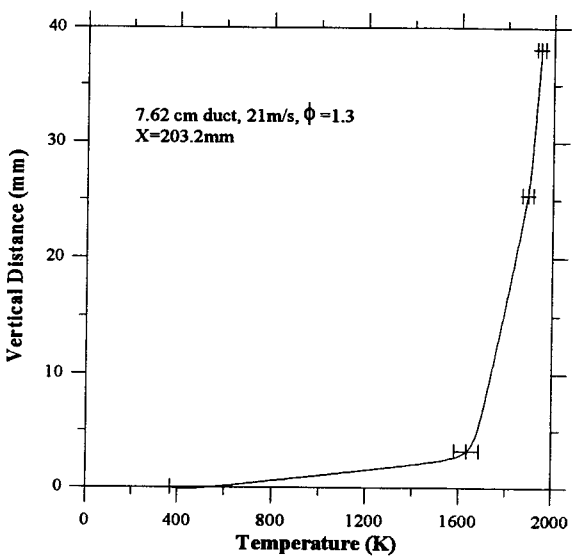

Figure 3.76: 7.62 cm duct temperature measurements: x=203.2 mm.

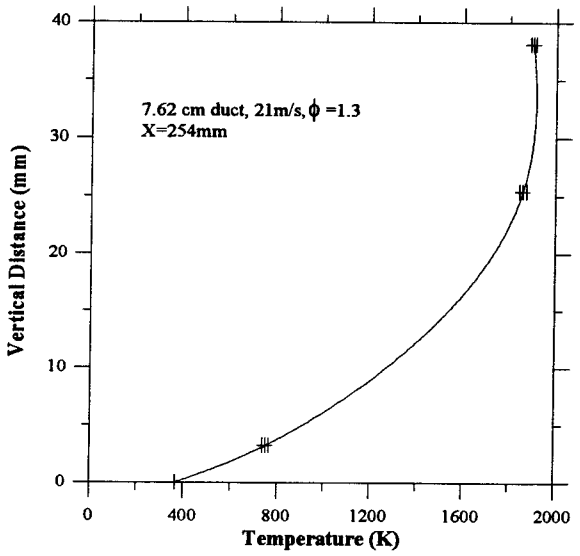

Figure 3.77: 7.62 cm duct temperature measurements: x=254 mm.

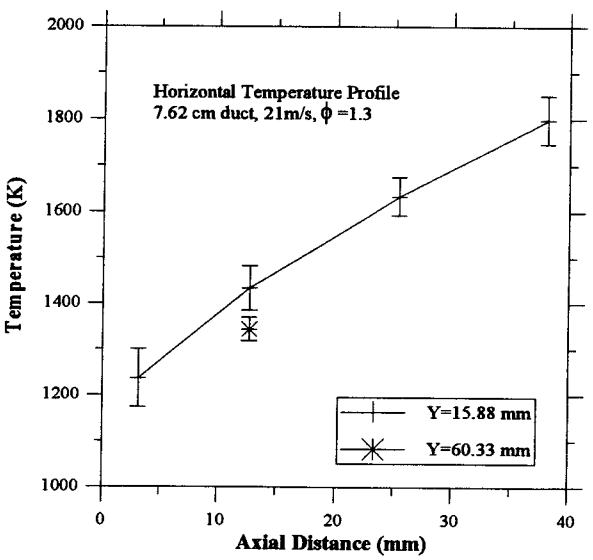

Figure 3.78: 7.62 cm duct temperature measurements: y=15.9 mm, y=60.3 mm.

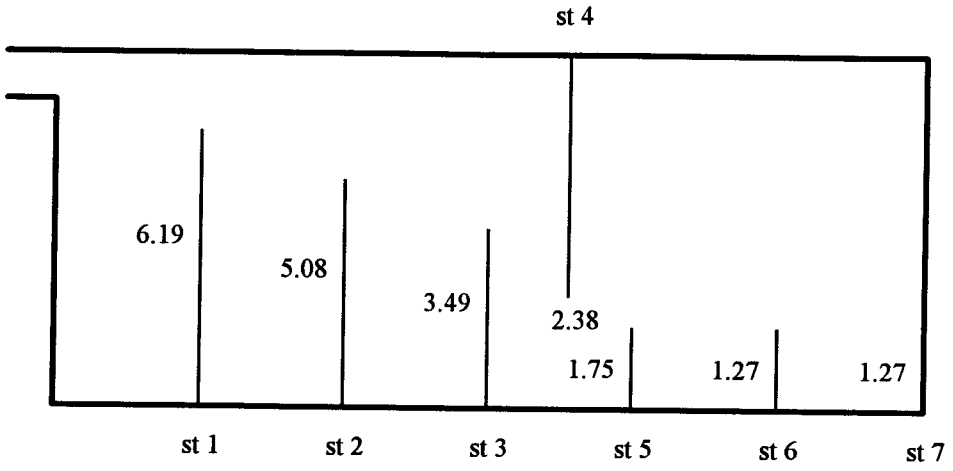

Figure 3.79: Thermocouple placement for 7.62 cm duct Hycam movies. (Dimensions are in cm).

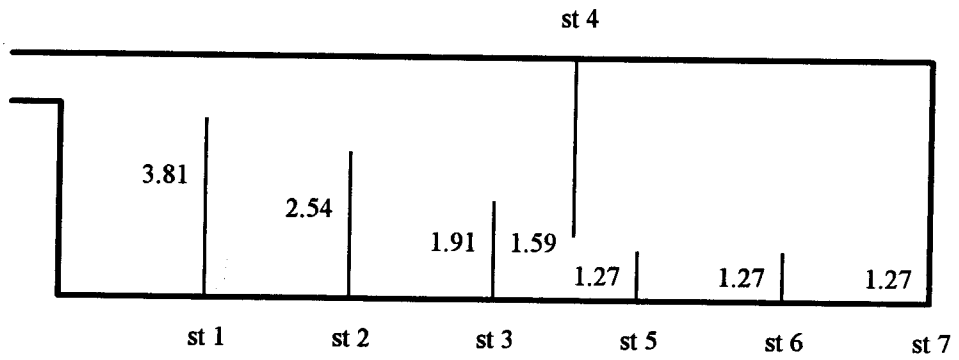

Figure 3.80: Thermocouple placement for 5.08 cm duct Hycam movies. (Dimensions are in cm).

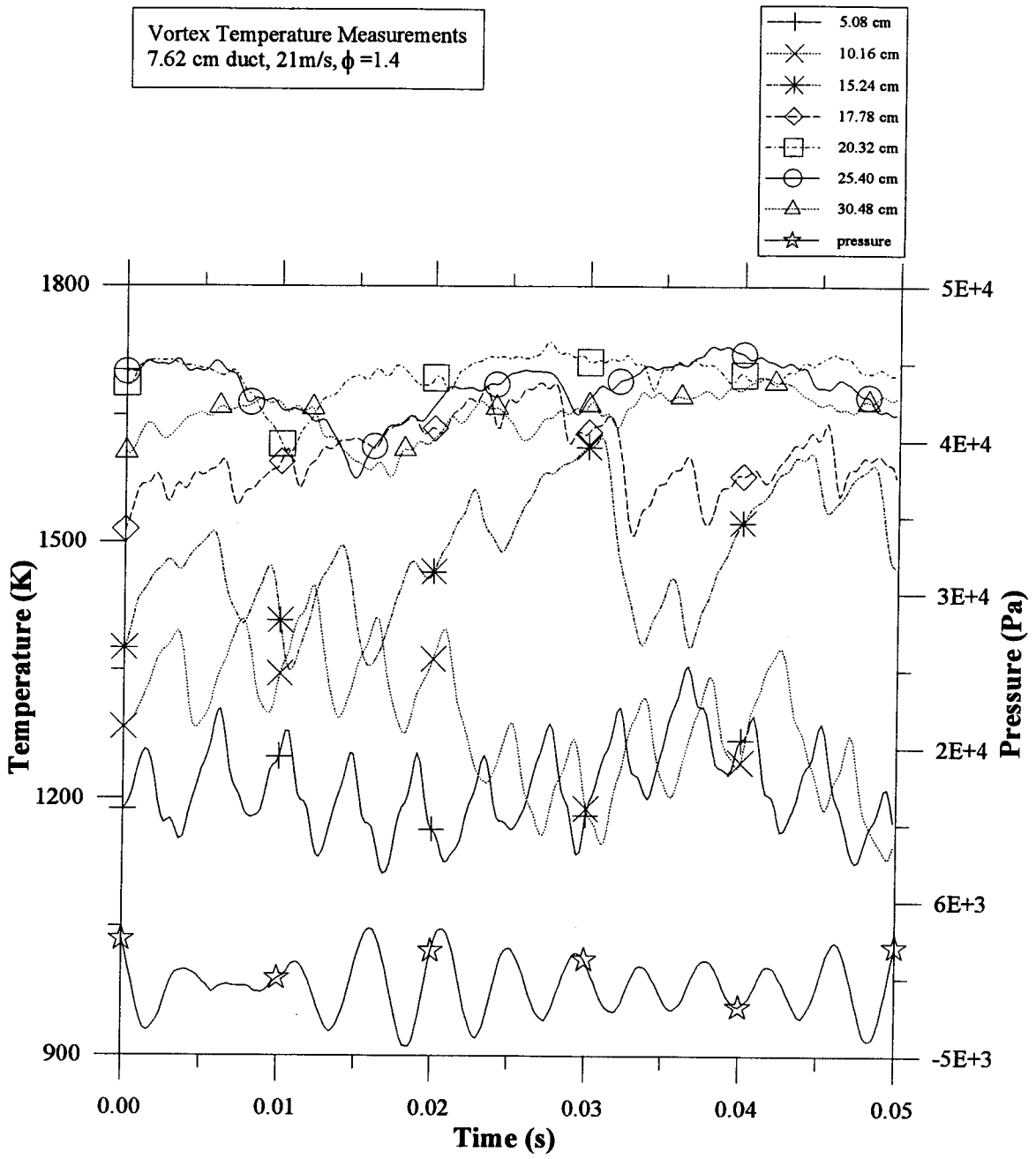

Figure 3.81: Time-resolved vortex temperature measurements for the seven measurement stations: 7.62 cm duct, 21 m/s, $\phi = 1.4$.

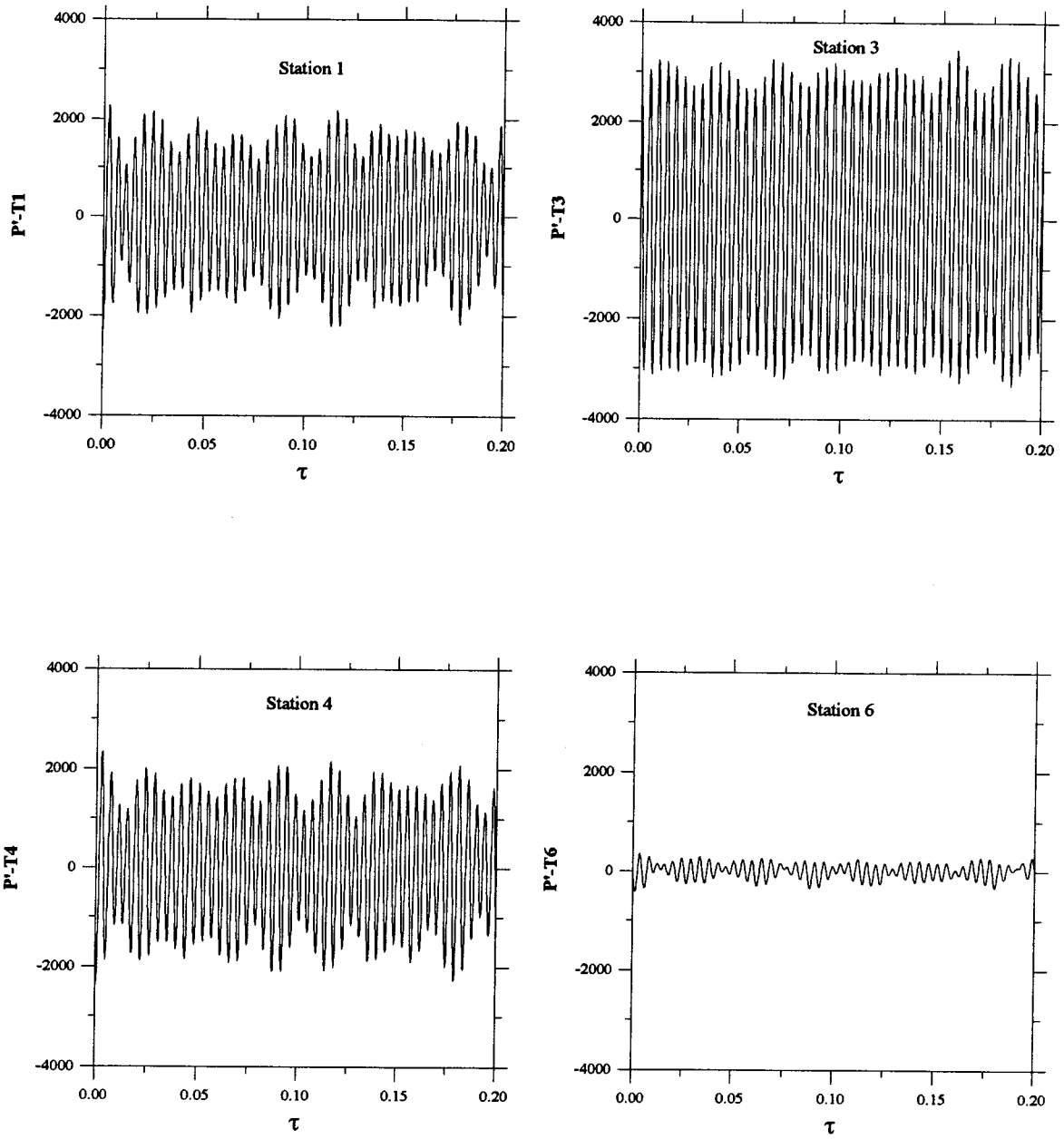

Figure 3.82: Cross-correlation between the pressure and temperature signals: 7.62 cm duct, 21 m/s, $\phi = 1.4$. τ denotes time-delay (s).

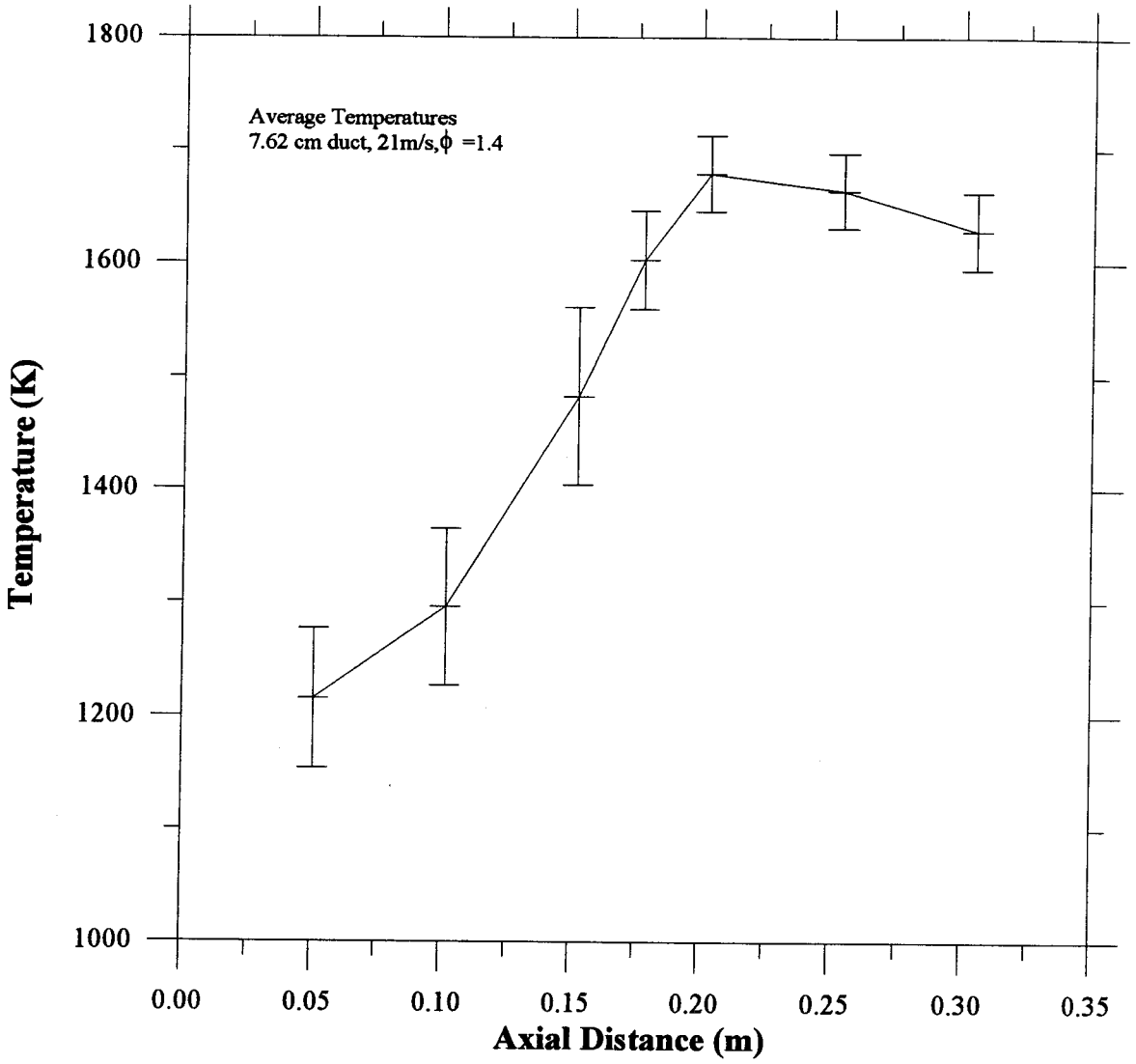

Figure 3.83: Average station temperatures: 7.62 cm duct, 21 m/s, $\phi = 1.4$.

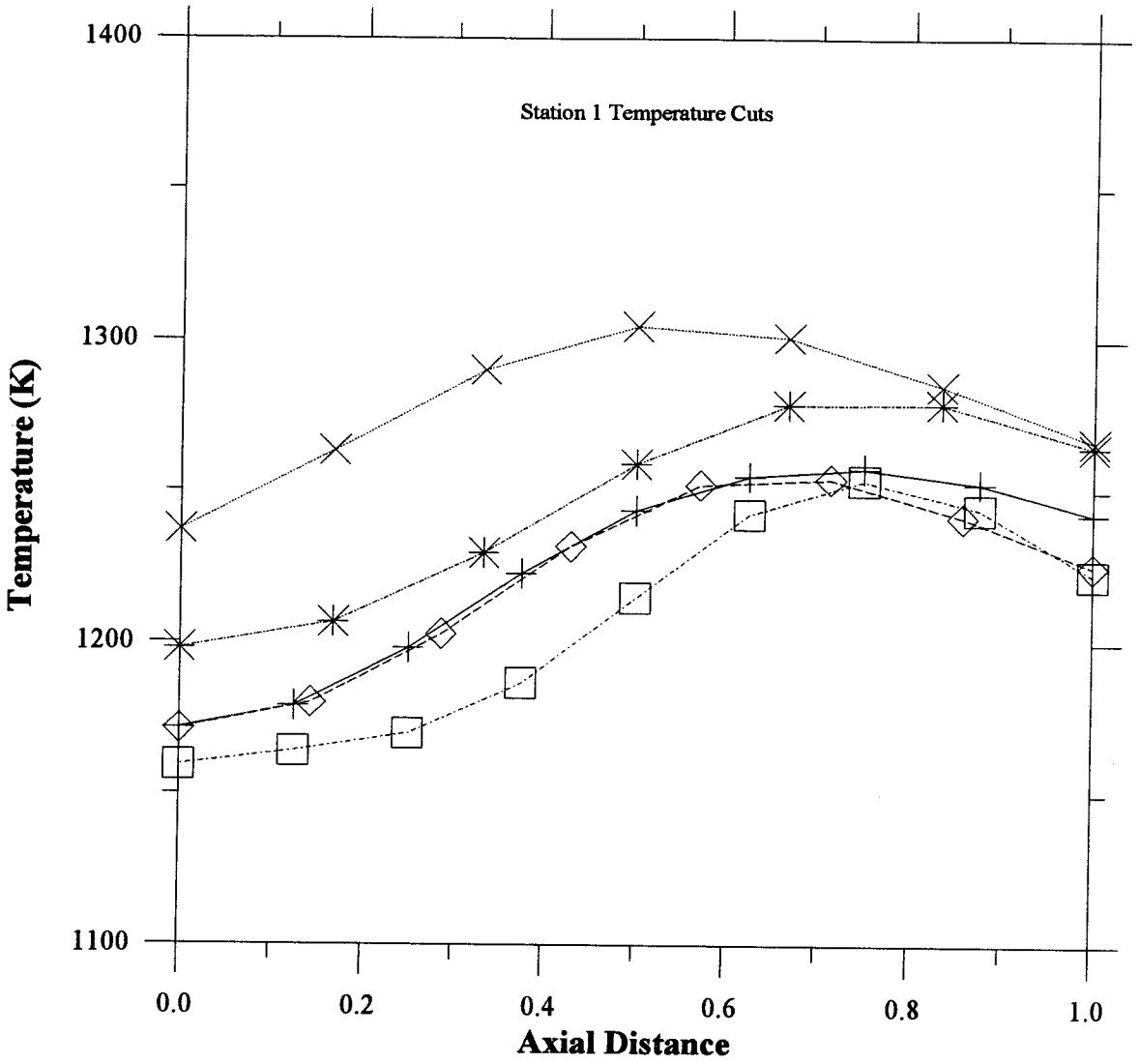

Figure 3.84: Cross-sectional temperature cuts: 7.62 cm duct, 21 m/s, $\phi = 1.4$.

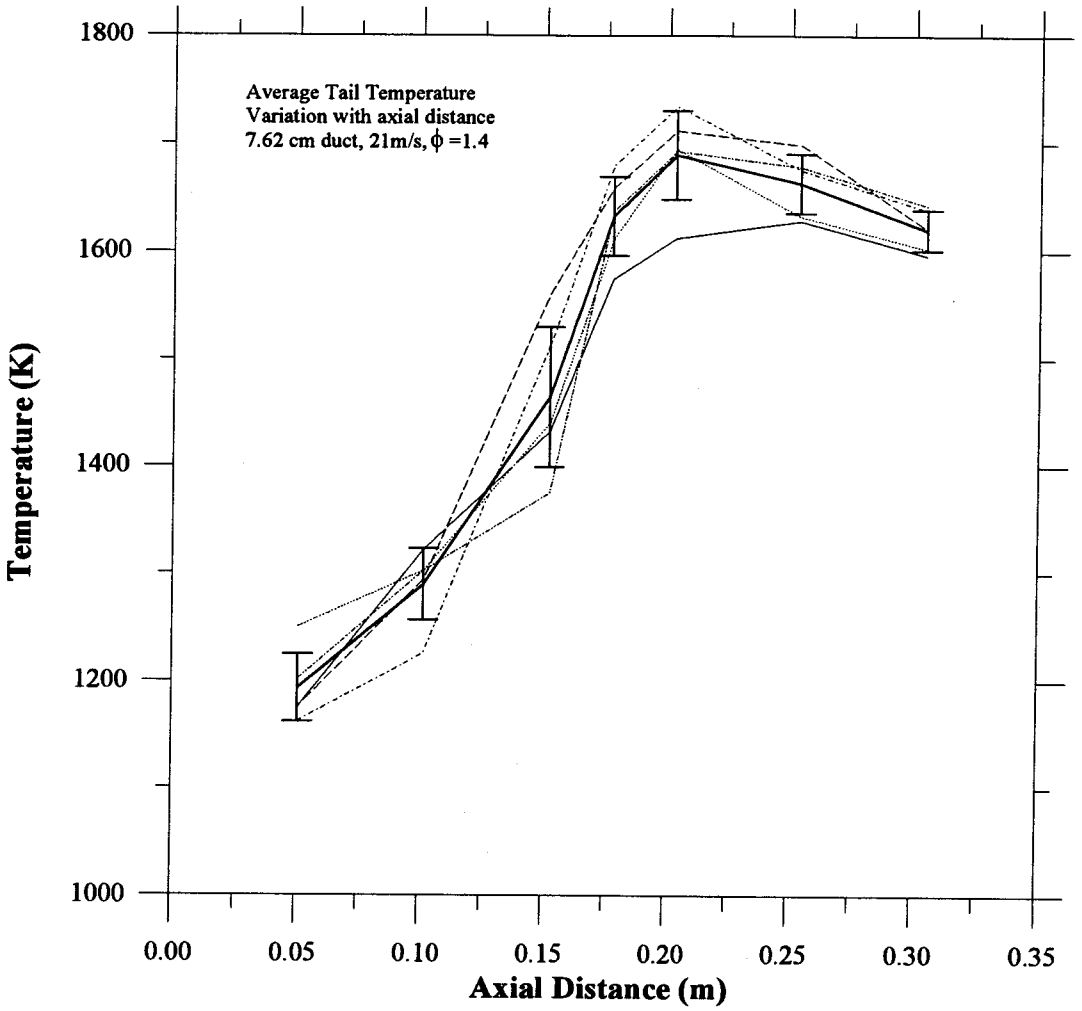

Figure 3.85: Average T_{tail} measurements: 7.62 cm duct, 21 m/s, $\phi = 1.4$.

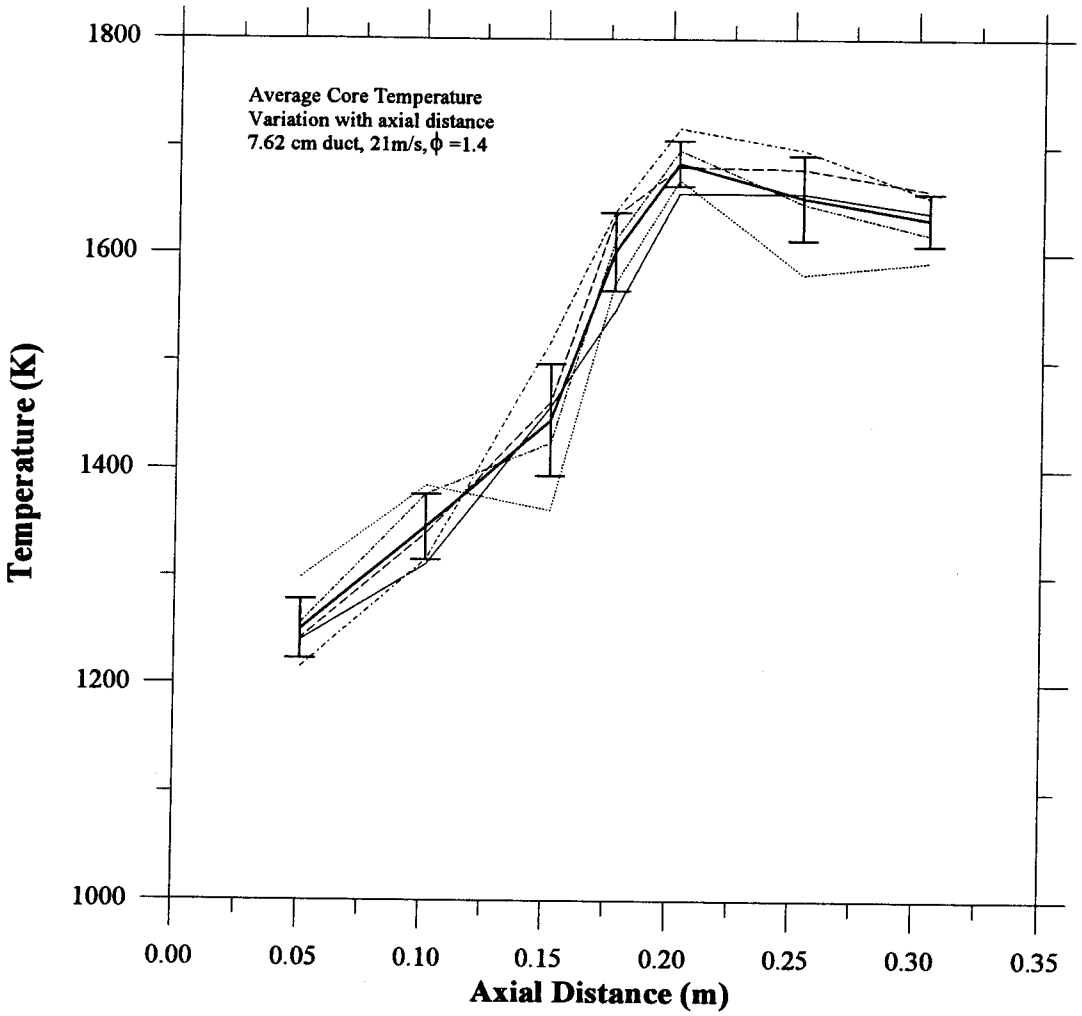

Figure 3.86: Average T_{core} measurements: 7.62 cm duct, 21 m/s, $\phi = 1.4$.

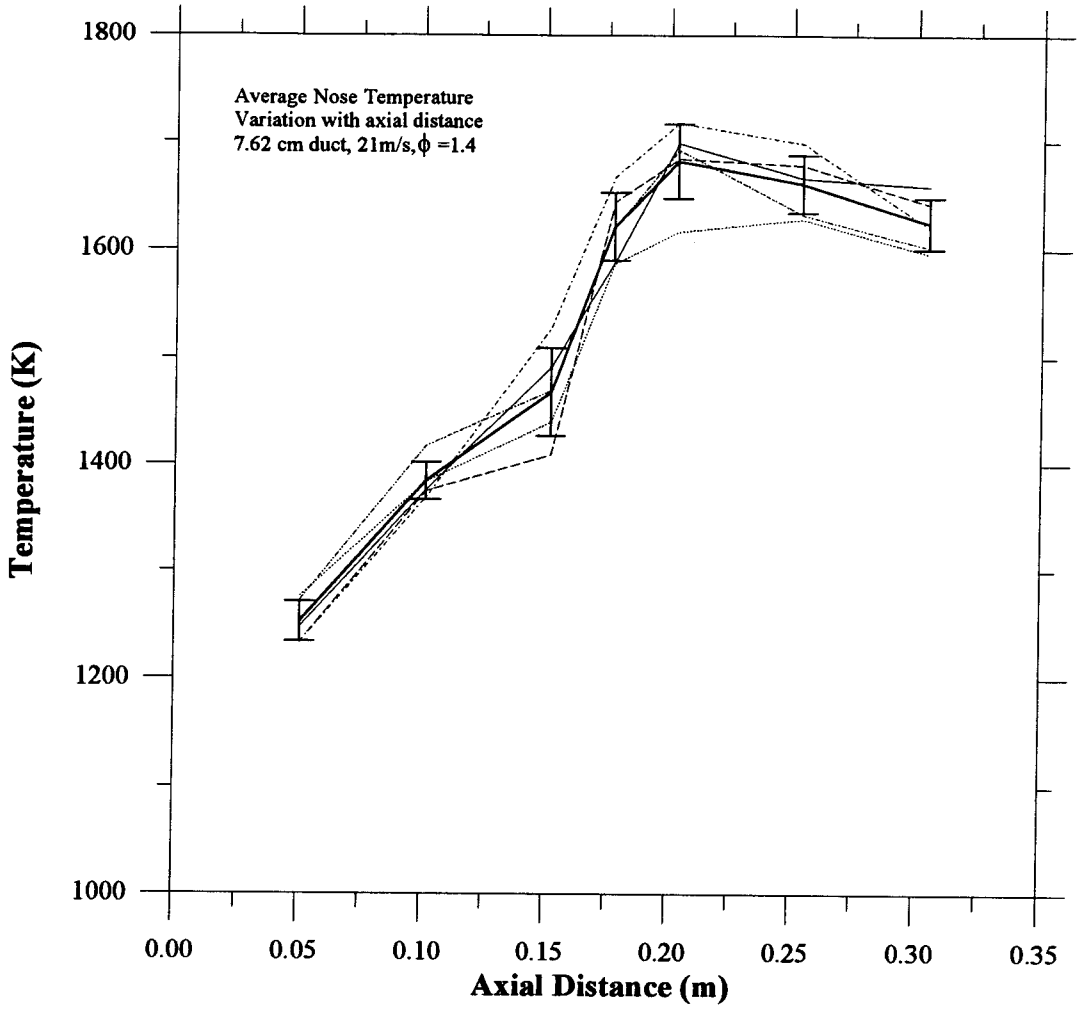

Figure 3.87: Average T_{nose} measurements: 7.62 cm duct, 21 m/s, $\phi = 1.4$.

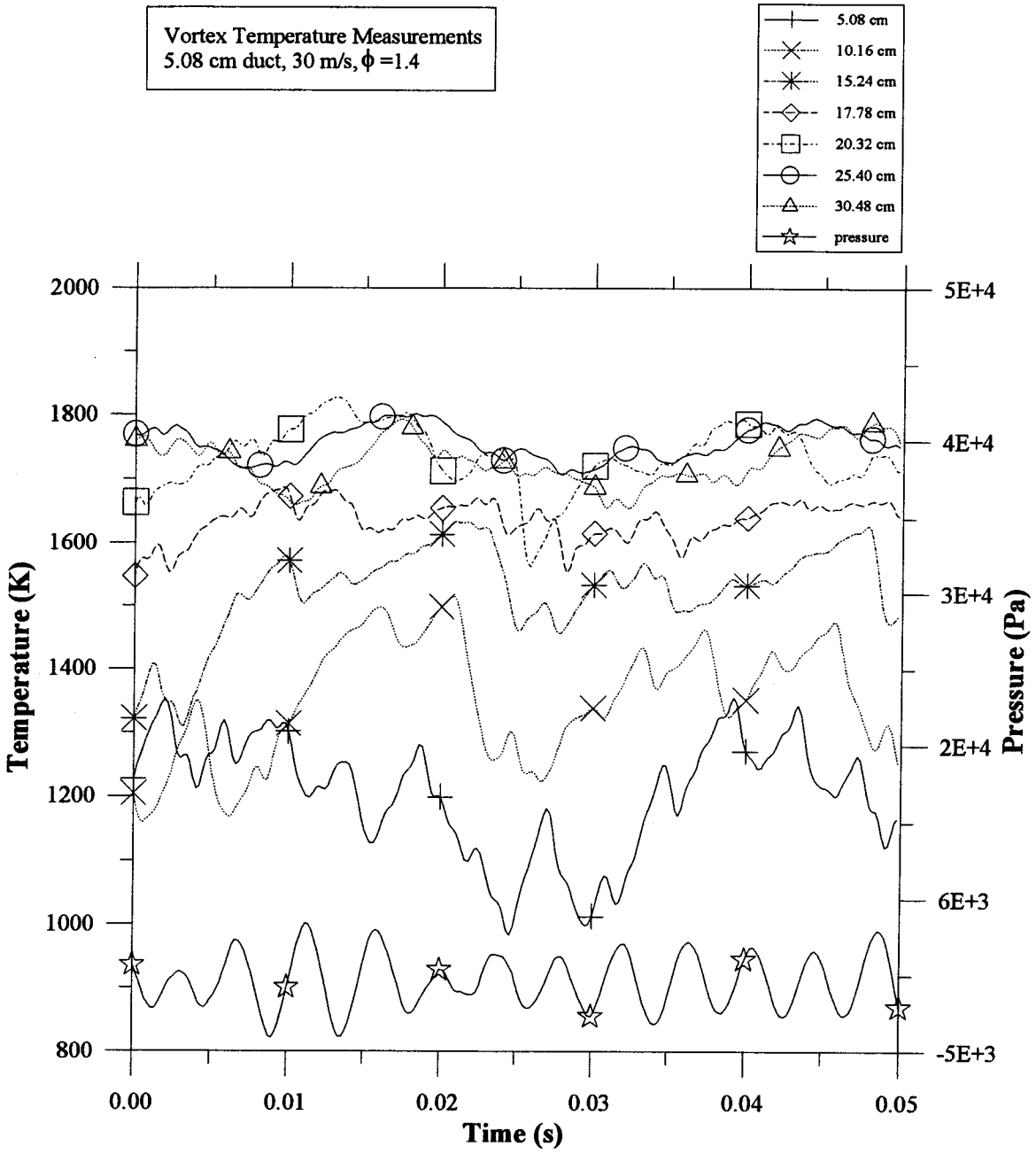

Figure 3.88: Time-resolved vortex temperature measurements for the seven measurement stations: 5.08 cm duct, 30 m/s, $\phi = 1.4$.

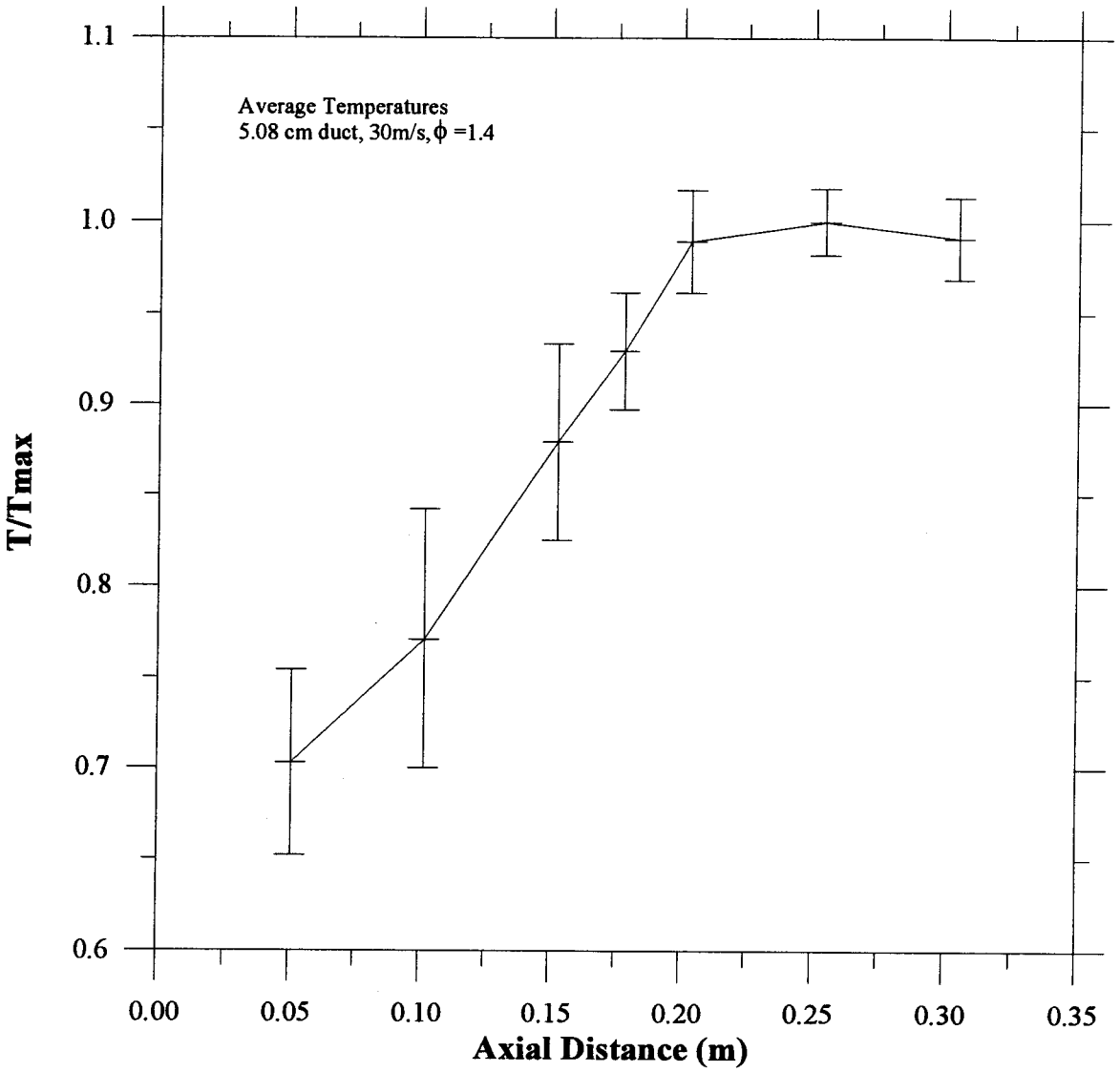

Figure 3.89: Normalized average station temperatures: 5.08 cm duct, 30 m/s, $\phi = 1.4$.

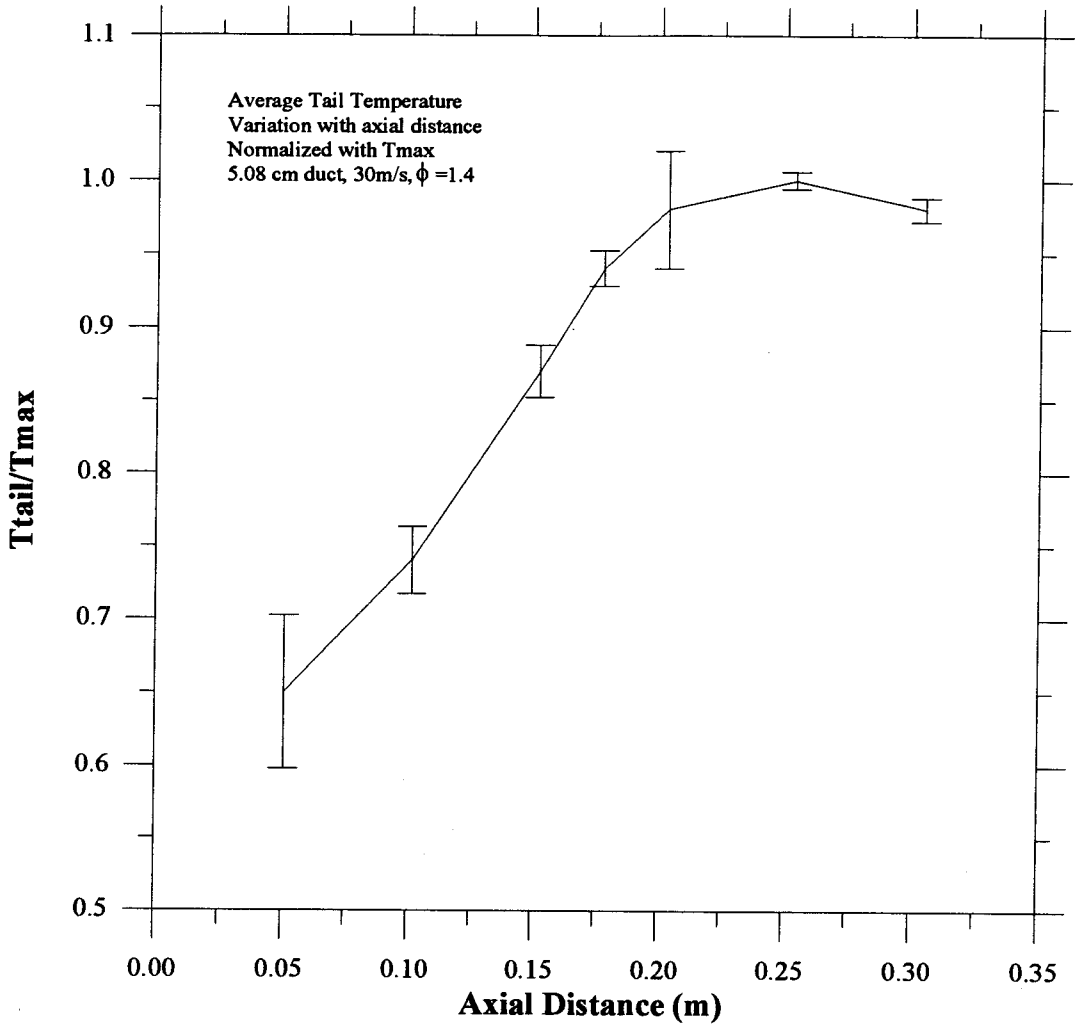

Figure 3.90: Normalized average T_{tail} measurements: 5.08 cm duct, 30 m/s, $\phi = 1.4$.

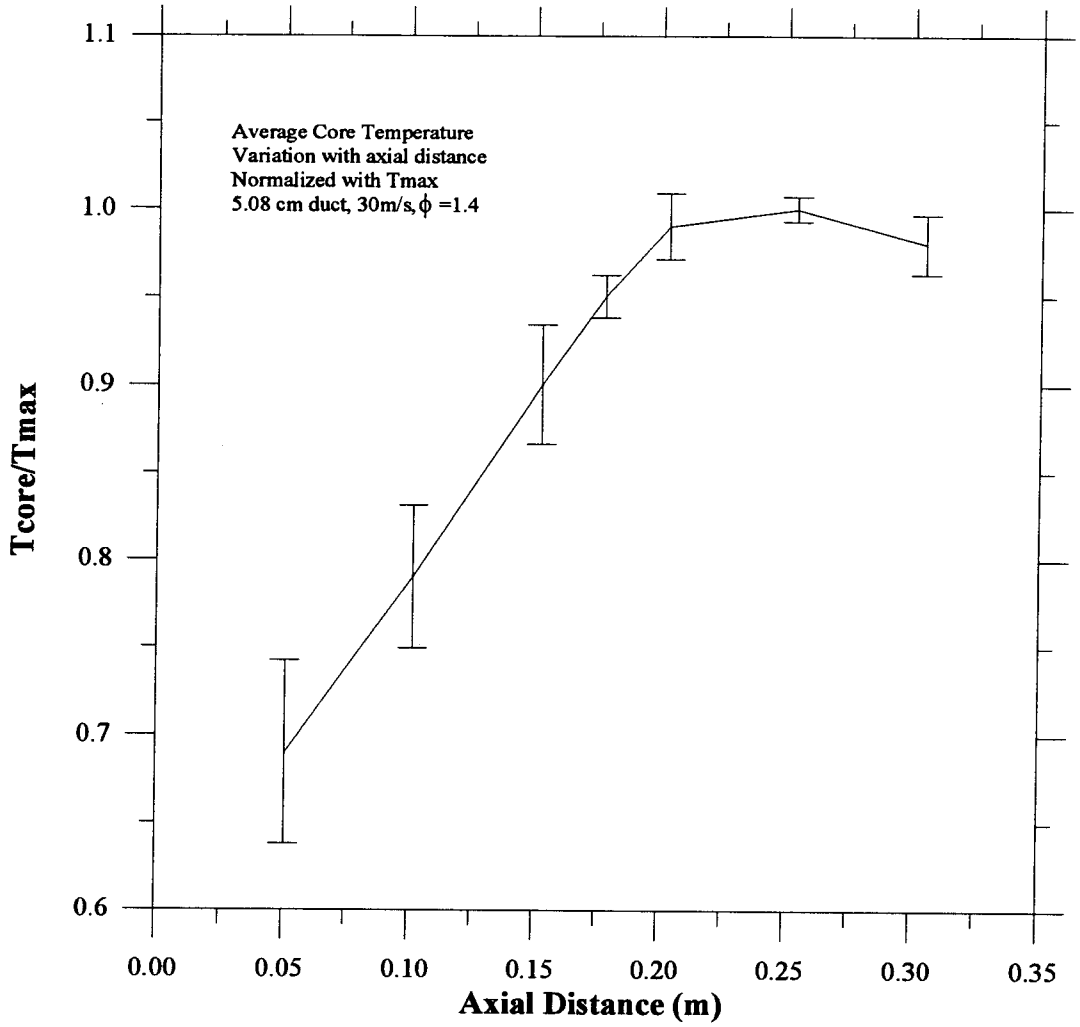

Figure 3.91: Normalized average T_{core} measurements: 5.08 cm duct, 30 m/s, $\phi = 1.4$.

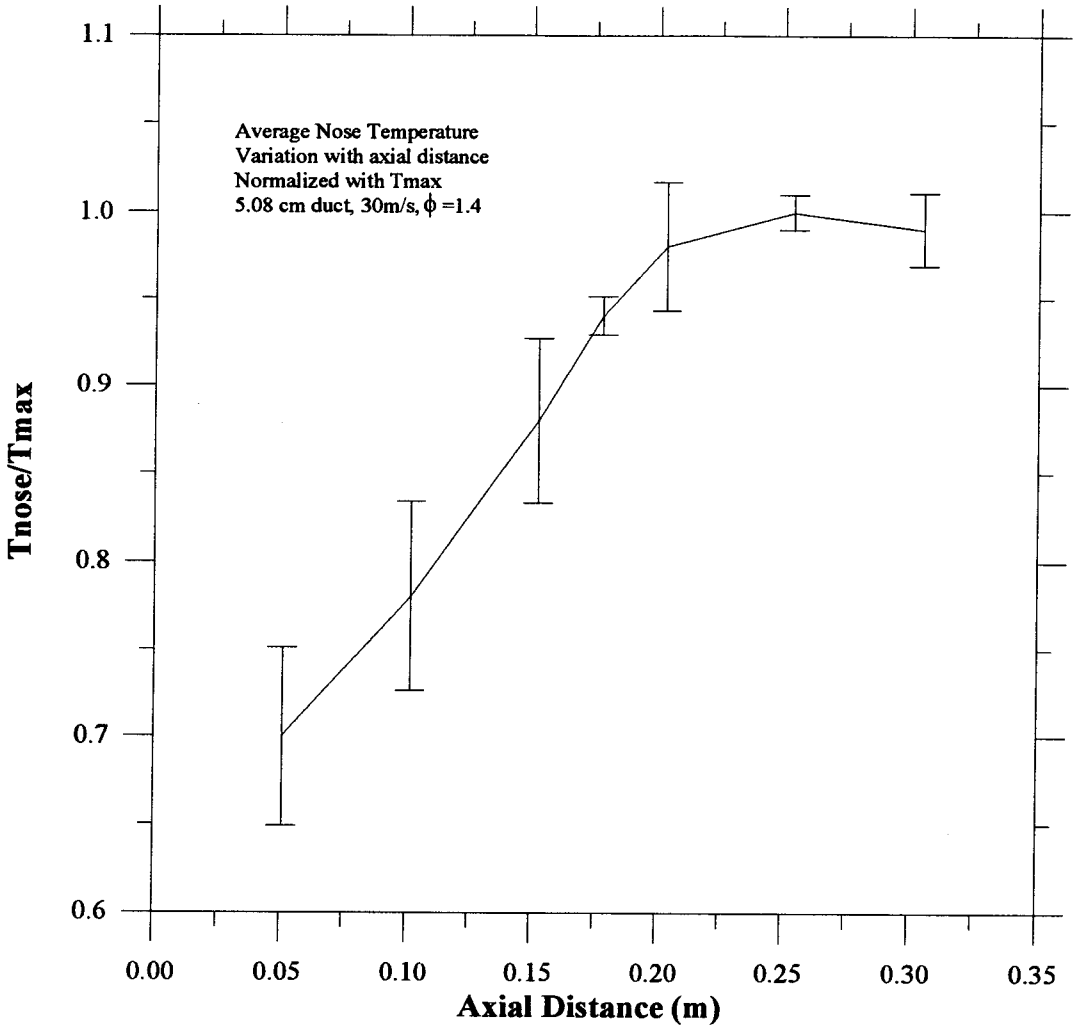

Figure 3.92: Normalized average T_{nose} measurements: 5.08 cm duct, 30 m/s, $\phi = 1.4$.

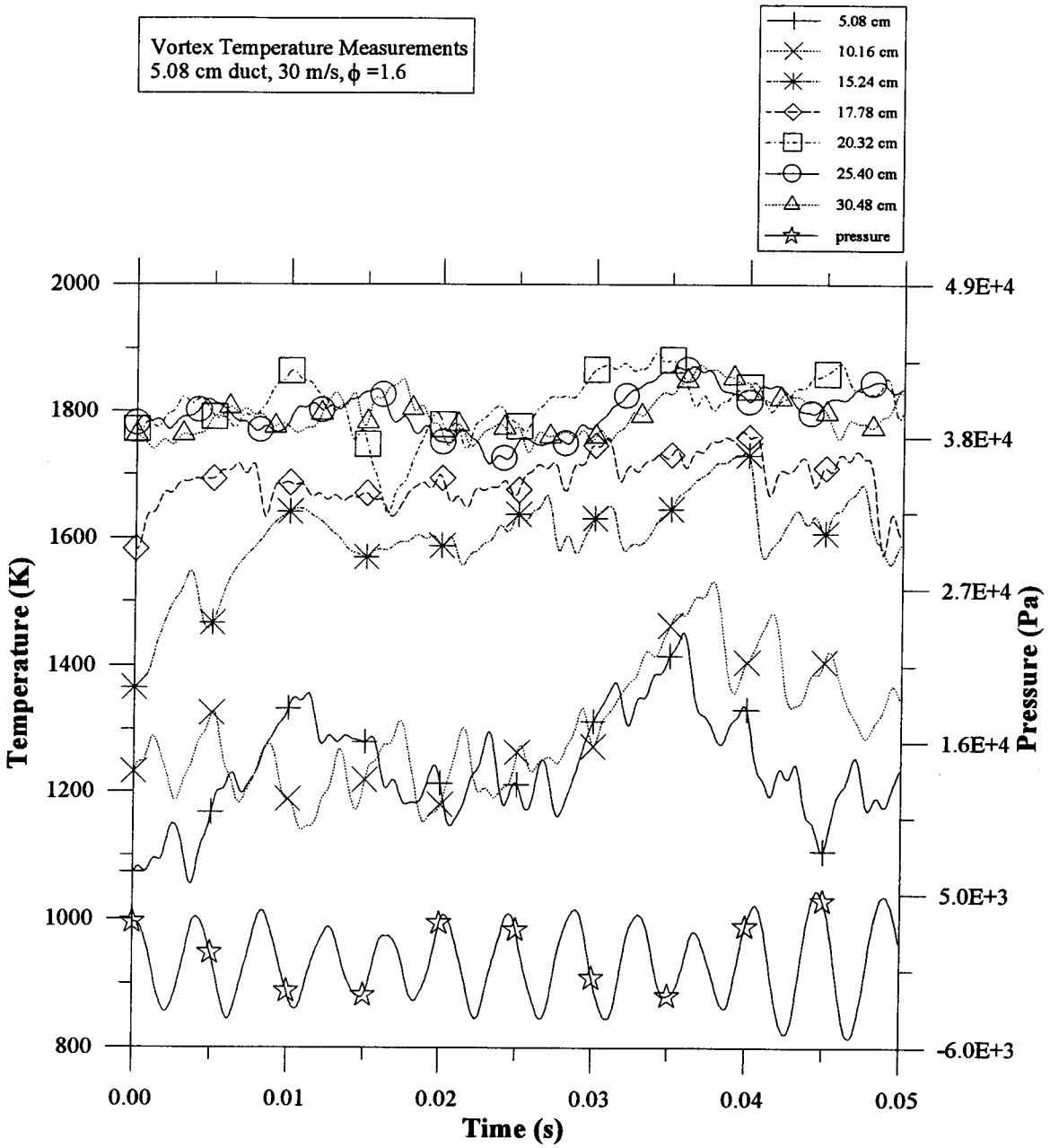

Figure 3.93: Time-resolved vortex temperature measurements for the seven measurement stations: 5.08 cm duct, 30 m/s, $\phi = 1.6$.

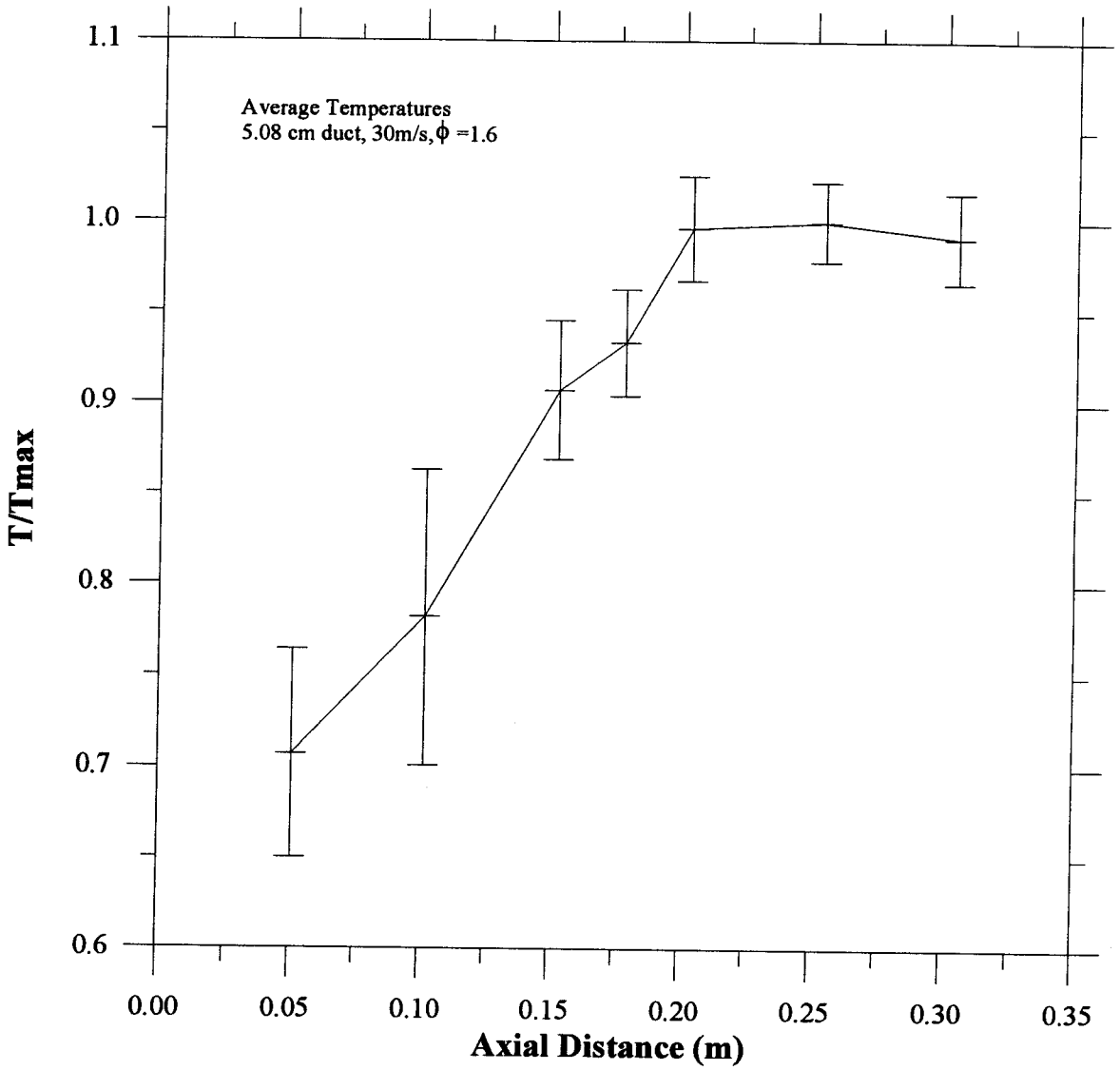

Figure 3.94: Normalized average station temperatures: 5.08 cm duct, 30 m/s, $\phi = 1.6$.

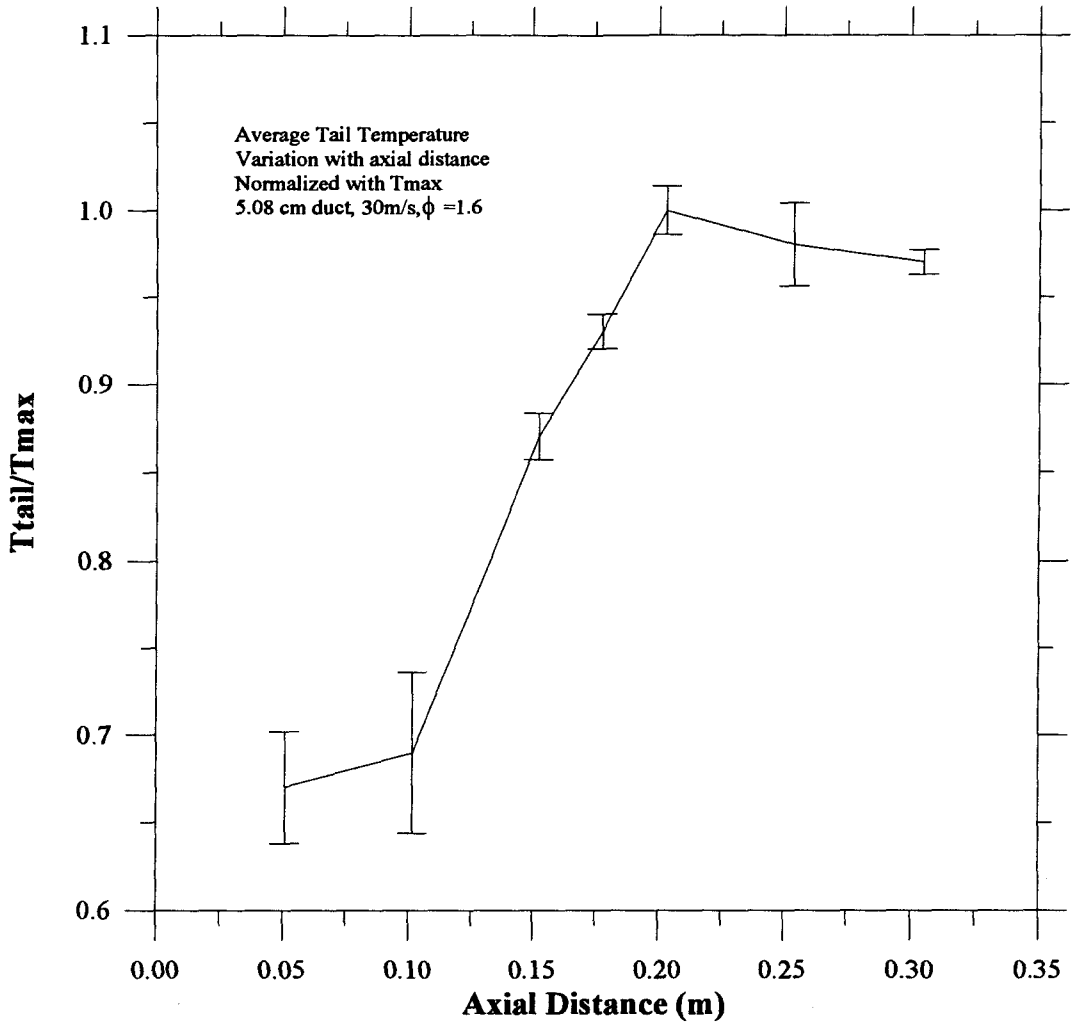

Figure 3.95: Normalized average T_{tail} measurements: 5.08 cm duct, 30 m/s, $\phi = 1.6$.

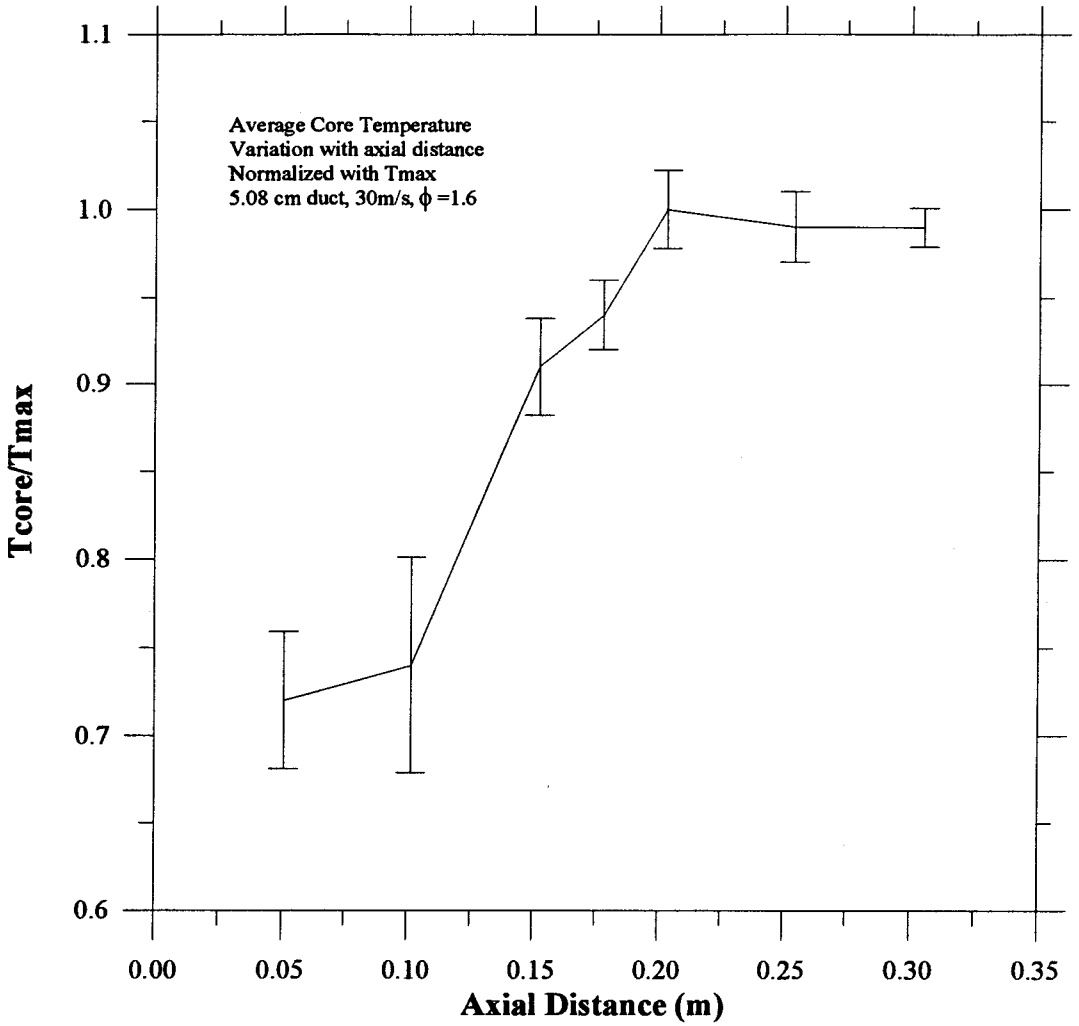

Figure 3.96: Normalized average T_{core} measurements: 5.08 cm duct, 30 m/s, $\phi = 1.6$.

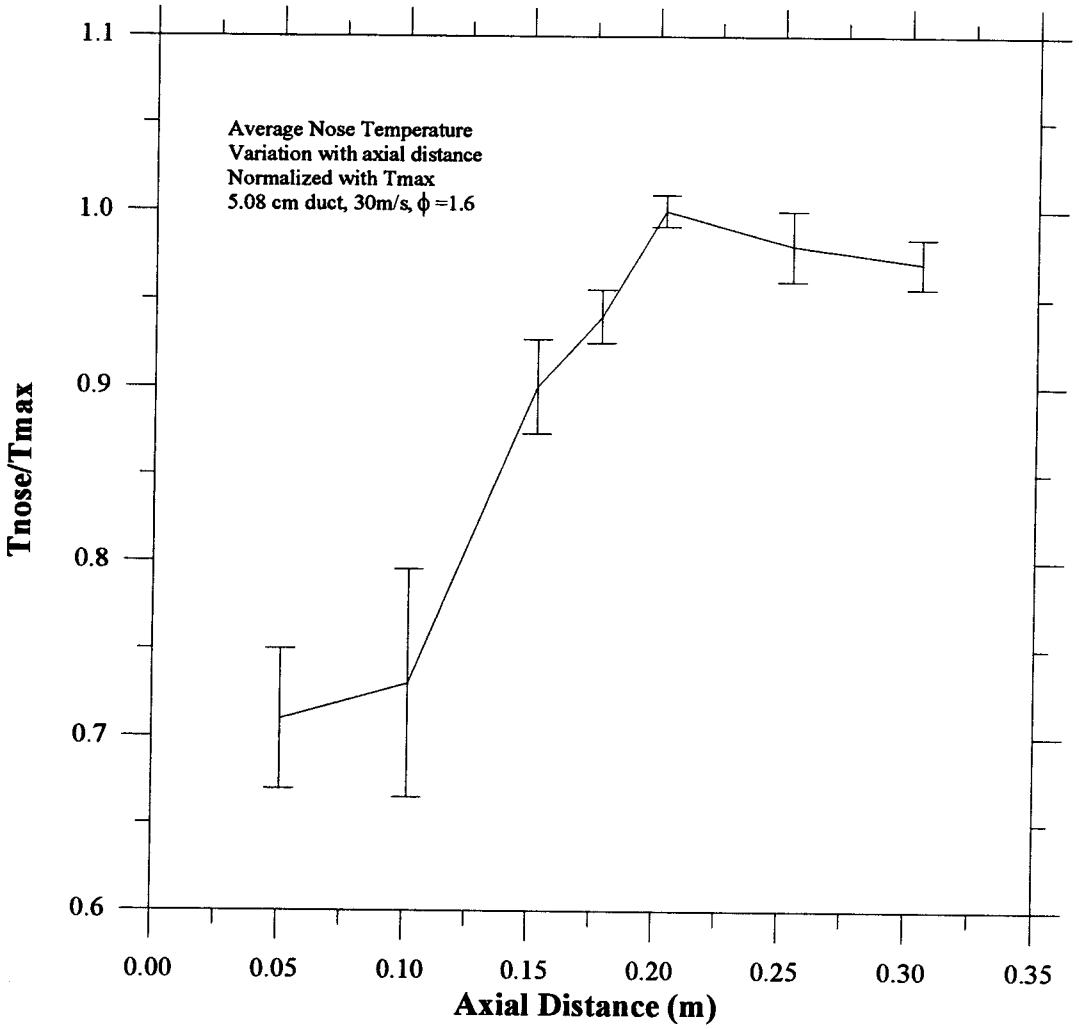

Figure 3.97: Normalized average T_{nose} measurements: 5.08 cm duct, 30 m/s, $\phi = 1.6$.

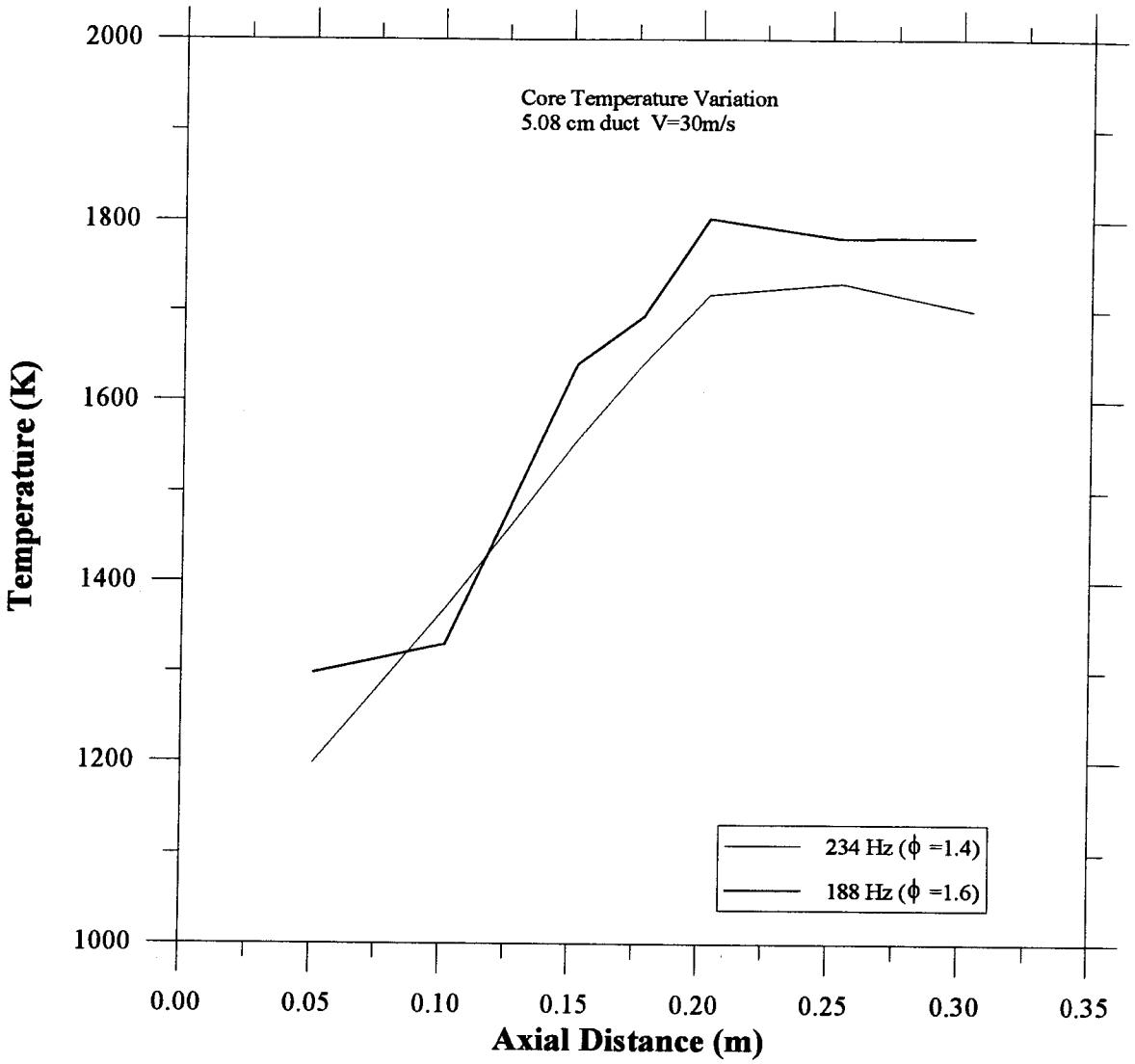

Figure 3.98: Summary of T_{core} measurements: 5.08 cm duct, 30 m/s, $\phi = 1.4$ and $\phi = 1.6$.

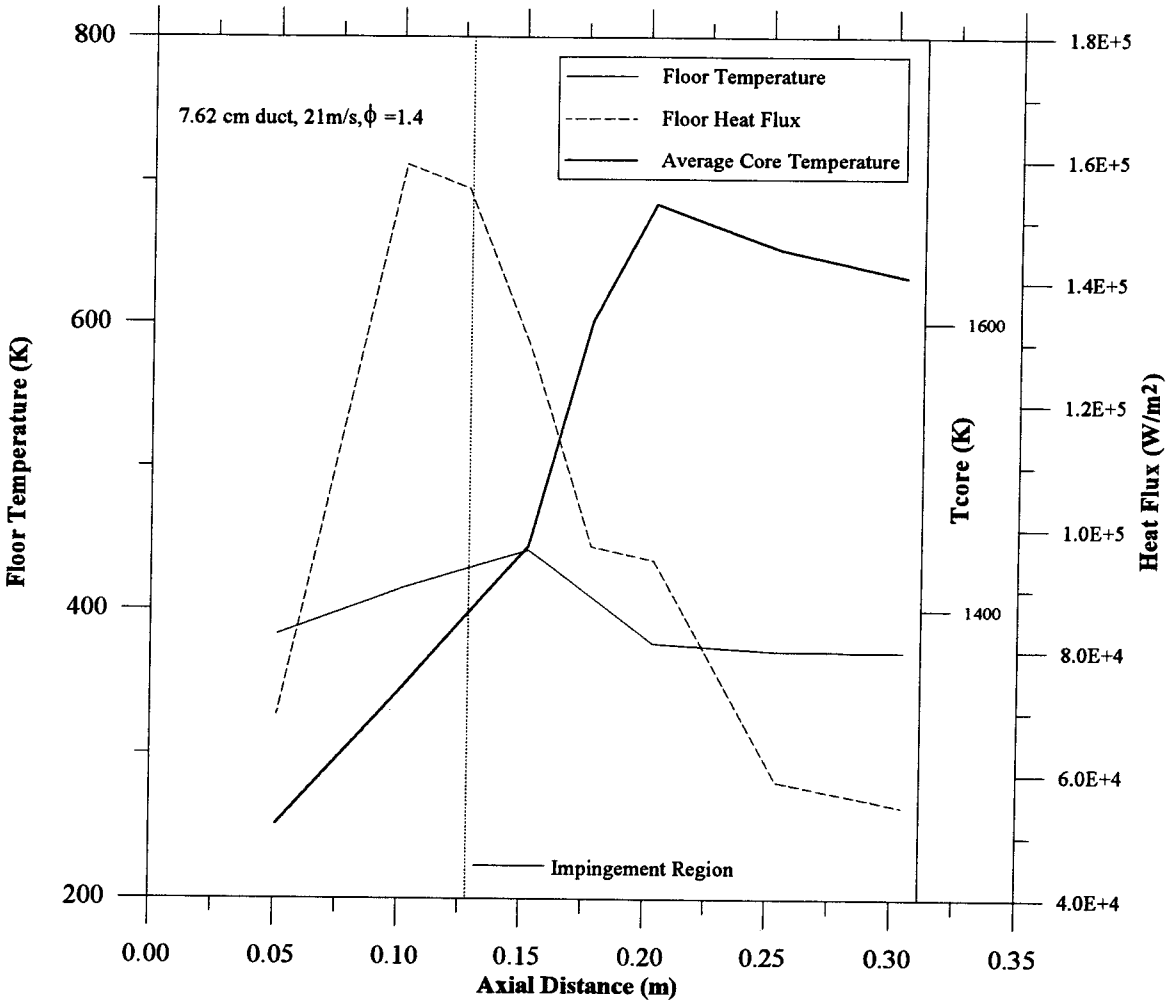

Figure 3.99: Summary of T_{core}, $\dot{Q}_{floor}$ and T_{floor} measurements: 7.62 cm duct, 21 m/s, $\phi = 1.4$.

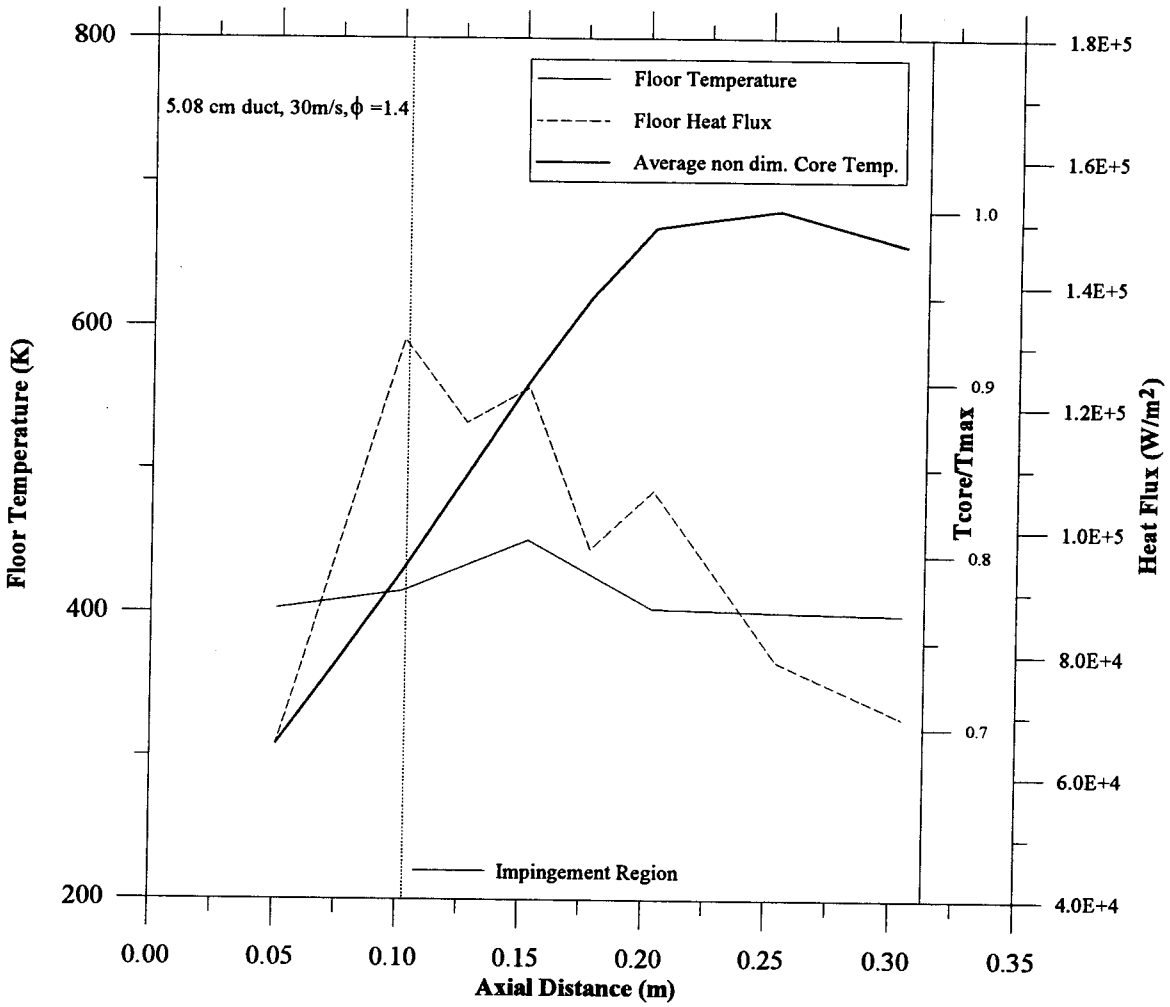

Figure 3.100: Summary of T_{core}, $\dot{Q}_{floor}$ and T_{floor} measurements: 5.08 cm duct, 30 m/s, $\phi = 1.4$.

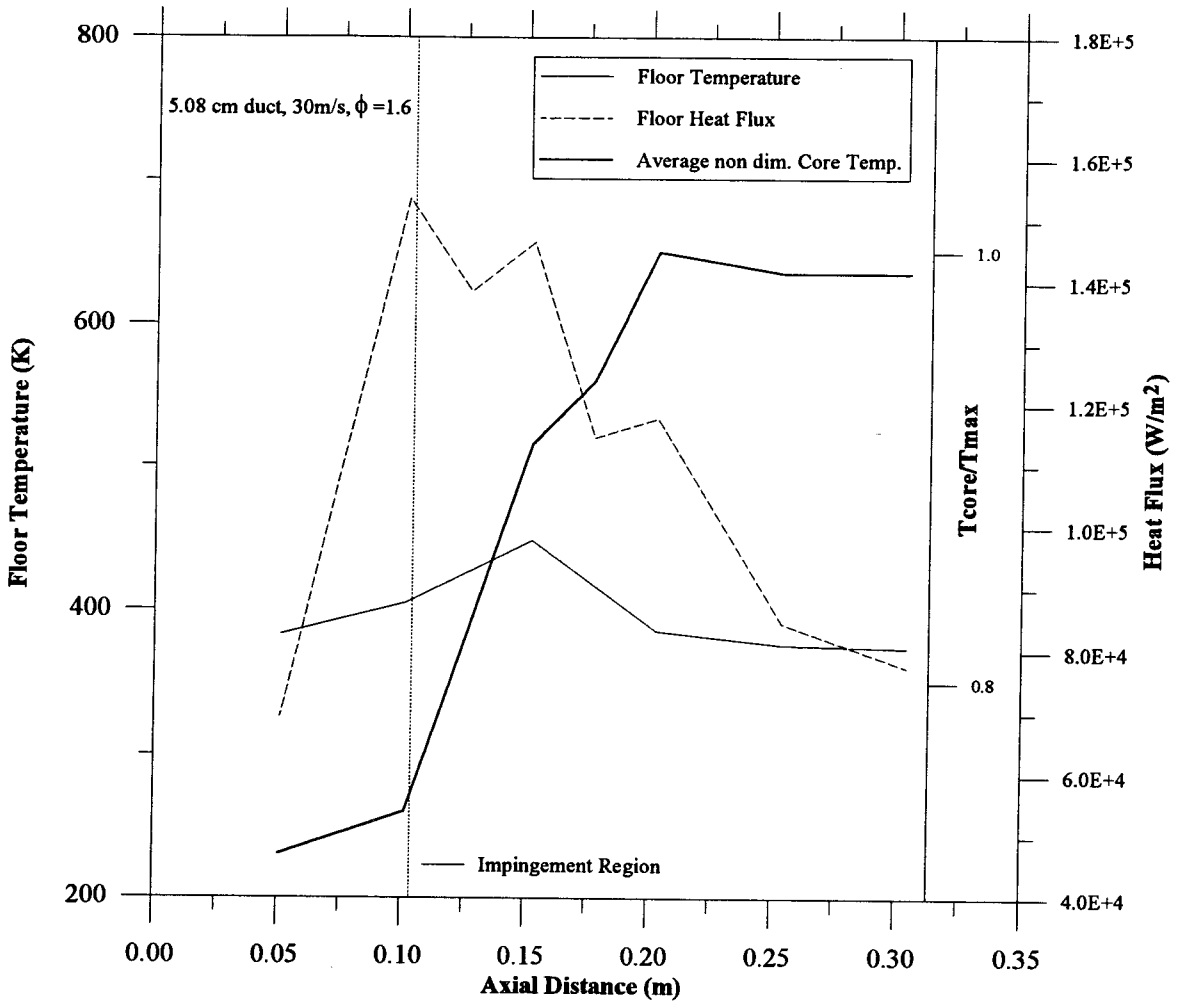

Figure 3.101: Summary of T_{core}, $\dot{Q}_{floor}$ and T_{floor} measurements: 5.08 cm duct, 30 m/s, $\phi = 1.6$.

CHAPTER FOUR
EXPLANATION OF OBSERVED MODE SHIFTS

The combustor can exhibit a wide dynamical range of vortex shedding frequencies through a careful selection of the governing flow variables: ϕ, V_{dump} and duct height, d. The ultimate effect can be the attenuation or augmentation of combustor pressure and velocity fluctuations at the step or the switching of shedding frequencies. Such trends are best demonstrated by examining the 5.08 *cm* duct cases which reveal $\nu_{shedding}$ changes accompany modest ϕ variations for the two V_{dump} values investigated. A summary of six pressure FFTs for these 5.08 *cm* cases appears in *Figures 4.1* and *4.2*. This phenomena of mode shifts occurring for the 5.08 *cm* duct will be addressed in this chapter. It will be shown that there are typically three mechanisms operating which are most likely responsible for these $\nu_{shedding}$ changes: (1) changes in $\tau_{\max}$ accompanying the increase in stoichiometry, (2) $\dot{Q}_{floor}$ variations which induce changes in the expected pressure spectra and (3) vortex straining which has been seen to physically delay the heat pulse for some of the cycles comprising the 35 *m/s* transition.

Items (1) and (2) will be investigated both theoretically and numerically while item (3) will be addressed using experimental results. Emphasis will be placed on the 30 *m/s* transition but references to other dump plane speeds and geometries will also be made.

4.1 MODE SELECTION BASED ON JUMPS IN τ_{max}

4.1.1 Fundamental Issues

The fundamental requirement necessary in sustaining combustion driven oscillations was first made by Rayleigh (Rayleigh, 1878) and later adapted by Chu (Chu, 1956, 1965). Stated simply, reinforcement of the instability is achieved by applying the heat pulse at moments of positive fluctuating pressure. Paramount, therefore, is understanding the phasing between the ensuing heat pulse and pressure trace and this hinges on evaluating the flowfield's influence on τ_{max} (time from when a structure is shed to when one sees it associated intensity spike) which will be show to detune, quell or switch vortex shedding frequencies.

4.1.2 Typical Burning Sequence for a Structure in a 30m/s Transition

Examination of the injection, ignition and combustion processes for the 30 *m/s* transition revealed many similarities irrespective of $\nu_{shedding}$. *Figures 4.3* through *4.5* depict the oscillatory velocity, pressure and heat release traces for each of the three runs comprising the change in fuel-air ratio corresponding to $\phi = 1.2, 1.4, 1.6$. Consult *Figure 4.1* for their respective pressure FFTs. It should be noted that the corresponding velocity spectra were nearly identical to their pressure counterparts. The pressure and velocity mode shapes are shown in *Figure 4.6* as discussed in Section 3.1. As a structure is shed near a V'_{min},[2] the structure entrains hot recirculating product from the recirculation zone and from immediately shed vortices into its core and/or along its edges. Ignition was seen to occur predominately along the outer edge due to a straining imbalance some 1.5 *ms*

[2] Slight cycle to cycle variations caused some previously discussed variations to this rule.

later (Section 3.1), irrespective of ϕ. As the geometric influence of the floor is felt some 9 *cm* downstream at impingement, more vigorous mixing of the still unburnt inner charge is achieved. More time elapses (~0.75 *ms*) until finally, full combustion of the structure is seen, characterized by an intensity maximum in the heat release traces (refer to *Figure 4.3*, for instance). The complete sequence with approximate time scales is shown pictorially in *Figure 4.7*.

The unusual trend appearing on closer examination of the data traces is the drop in τ_{max} despite the ϕ increase which is known to increase ignition times (Barr et al., 1990). Consult *Figure 4.8* for τ_{max} values for the 30 *m/s* transitional cases. More importantly, there is a shifting in the point at which the heat pulse arrives with respect to the pressure peak. For the 234 *Hz* instability, heat release peaks arrive ~ 45°–0° *before* P'_{max} (*Figure 4.3*) while for the 188 *Hz* instability, the heat pulse arrives ~ 45° *after* P'_{max} (*Figure 4.5*). The apparent discrepancy lies in when the vortices are shed for each of the two modes. The leaner case (234 *Hz*) is seen to have its V'_{min} located further from P'_{max} while the richer case (188 *Hz*) has its V'_{min} much closer to P'_{max}. This disparity is crucial in understanding the mode switching process as when a vortex is shed generally dictates when its heat release is seen. Further investigation of the pressure/velocity phase difference, $\theta_{p'-v'}$, for a variety of runs exhibiting varying $\nu_{shedding}$, V_{dump}, and geometry revealed $\theta_{p'-v'}$ to depend predominately on $\nu_{shedding}$ (Table 4.1). That is, if a 188 *Hz* instability is engaged, $\theta_{p'-v'}$ will be approximately 127°±6° while if a 234 *Hz* instability is engaged, $\theta_{p'-v'}$ will drop considerably to 47°±5°. Phase angles have also been included for the weakly excited modes if apparent in the FFTs.[3]

[3] A positive phase angle represents velocity leading the pressure pulse.

Table 4.1: *Pressure/Velocity Phase Angles.*

Duct Ht. (*cm*)	ϕ	V_{dump} (m/s)	$\nu_{shedding}$ (Hz)	$\theta_{p'-v'}\|188Hz$ (°)	$\theta_{p'-v'}\|234Hz$ (°)
2.54	1.3	21	188	123	41
5.08	1.2	30	234	133	45
5.08	1.4	30	188/234	132	45
5.08	1.6	30	188	131	-
5.08	1.2	35	234	138	49
5.08	1.4	35	188	127	-
5.08	1.6	35	188	125	-
7.62	1.2	35	234	120	55
7.62	1.3	21	234	118	45

This phenomena is not predicted by linear acoustics (*Figure 4.9a* and *4.9b*) which predicts a 90° phase lag or is not due to lower sound speeds resulting from lower chamber temperatures resulting from increased stoichiometry (*Figure 4.10*). It may be attributed to nonlinear effects invoked from dissimilar dissipation within the duct (Culick, 1994; Yang, 1984). Examination of the *rms*, total heat release fluctuations (*Figure 4.11*) and floor heat flux values (Section 3.3) through a transition seems to agree with this speculation. Pictorially, the shedding and burning process for a 234 and 188 *Hz* mode is shown in *Figure 4.12*. The traces have been shifted such that "time zero" represents when a vortex is shed for both modes (based on $\theta_{p'-v'}$ values). Dotted vertical lines represent the approximate locations of τ_{max} for both 234 and 188 *Hz* modes: 6.79 *ms* and 5.5 *ms*, respectively. A 234 *Hz* structure is shed nearly one and a half cycles prior to its associated intensity spike while a 188 *Hz* is, conversely, shed only around one cycle before its associated intensity peak. The fundamental question still remains, however, as why there is a transition or dynamical "kick" from the 234 to 188 *Hz* mode.

4.1.3 Engaging the 188 Hz Mode from a 234 Hz Limit Cycle (30 m/s transition)

With the flowfield operating in a stable 234 *Hz* limit cycle, an increase in ϕ causes four things: (1) an increase in τ_{chem} (Barr and Keller, 1991) due to its influence on temperature, (2) a slight lengthening in the "188 *Hz*" period (see *Figure 4.1*) due to sound speed reductions, (3) a slight shortening in the "234 *Hz*" period (see *Figure 4.1*) and (4) an increase in the oscillatory pressure levels (*Figure 3.61*). It is speculated that τ_{chem} increases are not the typical mechanism for the temporal shift in the heat pulse due to earlier evidence on τ_{id} suggesting that the flowfield is dominated by more fluid dynamic, turbulent effects (Section 3.1). A plot of τ_{max} versus ϕ (*Figure 4.8*) shows a similar result. Inspection of *Figure 3.61* for this 30 *m/s* transition also shows that as one changes from 234 to 188 *Hz* shedding, oscillatory pressure levels continuously rise, even for a flowfield having bimodal FFTs: i.e.: during a transitional case. An increase in ϕ would indeed increase τ_{chem} but the τ_{id} and τ_{max} trends suggest the fluid dynamics overpower the opposing chemical effects as is typically found in highly turbulent, oscillatory flows (Heitor et al., 1984; Bray, 1980). As some of the 188 *Hz* instability is engaged through the overlapping of the finite width heat pulse in regions favourable to 188 *Hz* shedding (see *Figure 4.12*), pressure levels begin to rise since more energy is being added to the acoustic field (both 188 and 234 modes, but now less to the 234 *Hz* mode) assuming a leftward shift in Q' (to be discussed) and τ_{max} values will *drop* due to increased fluid dynamic mixing encouraging *lower* τ_{mech} values. This competition between fluid dynamical and chemical effects was seen in *Figure 3.98* which depicted the core vortex temperature, T_{core}, versus axial distance for both the 234 and 188 *Hz* modes comprising the 30 *m/s* transition. The 234 *Hz* instability incurred a linear T_{core} increase with distance while the 188 *Hz* instability showed a distinct initial delay. This initially slow growth rate, however, overtook its 234 *Hz* counterpart and core temperatures soon exceeded those of the leaner

run. The increased turbulent exchange which accompanies richer instabilities obviously overcomes opposing chemical effects imposed by the stoichiometry. The net effect would be a *leftward* shift in the location of the heat pulse. It will be shown that this is the usual trend in the direction of the heat pulse with increasing ϕ as it was seen for three, 7.62 *cm* cases exhibiting a constant 234 *Hz* shedding and for three 2.54 *cm* cases undergoing a 188 *Hz* instability.[4] As will be shown, there are some possibilities for *rightward* shifts in the location of the heat release but this necessitates a much more lengthy temporal shift as will be numerically verified. Furthermore, this would necessitate the heat pulse first passing through the pressure maximum of the 234 *Hz* instability (since the heat pulse typically lies to the left of P'_{max} in a 234 *Hz* mode), thus encouraging a stronger 234 *Hz* mode. It is still unclear, however, as to why there is even the first initial increase in pressure to facilitate the typically leftward shift in heat pulse invoked from drops in τ_{max}.

Effect (2) is induced by the stoichiometry and influences the exact values of the generic "188" and "234" *Hz* modes. Richer runs (higher ϕ) lower chamber temperatures, thereby dropping the sound speed and *generally* lengthening the acoustic period. This can be seen by the gradual lowering of the *exact* frequency values of the "188 *Hz*" mode with ϕ (*Figure 4.1*): 195.31, 190.73, 189.97 *Hz*. The similar trend holds for the 35 *m/s* pressure FFTs (*Figure 4.2*): 194.55, 189.97, 187.68 *Hz*. This would *stretch* the rightmost "188 *Hz*" peak *rightward* (assuming the shedding location is fixed which is reasonable on examination of the $\theta_{p'-v'}$ data), closer to the location of the heat pulse (consult *Figure 4.12*).

---

[4] The reason for the invariance in shedding frequency for the smallest and largest duct heights with ϕ is due to the shortening and lengthening, respectively, of τ_{max} with geometric changes. The 5.08 *cm* duct, therefore, represents a unique geometry. More will be said on this in Chapter Five.

Effect (3) also induces the 234 *Hz* peak to "follow" the movement of the heat pulse leftward. Both effects (2) and (3) combine to induce excitation of both modes as evidence from the middle FFT ($\phi = 1.4$) in *Figure 4.1* since the heat pulse now straddles positive pressure regions of both modes and pressure levels consequently rise. As will be shown in the next section, a flowfield having bimodal FFT features causes the heat pulse to "jump" from one location to another due to the varying periods of the velocity trace which causes a nonuniform number of vortices to be shed over time.

As the stoichiometry is further increased and pressure levels continue to rise, the heat pulse arrives earlier due to further drops in τ_{max}. The continued lengthening of the 188 *Hz* period also serves to provide a more favourable heat-release/pressure phasing and the 188 *Hz* mode is further strengthened. By $\phi = 1.6$ (*Figure 4.5*), the heat pulse arrives after P'_{max} of the now 188 *Hz* excited mode and as further pressure increases occur shortening τ_{max}, the heat pulse continues to move closer to P'_{max}, further strengthening the instability. This can be seen by examining the $\phi = 1.4$ and $\phi = 1.6$ data traces for the 35 *m/s* transition which reflect slight leftward shift of the heat pulse (closer to P'_{max}) with ϕ (*Figure 4.13a* and *4.13b*). As will be shown in the next section, a noticeable compacting of the burning zone accompanies introduction of the 188 *Hz* mode, further enhancing the pressure-heat release coupling. It should be remarked that the mode change process is not progressive as hinted above, but rather the heat pulse "jumps" to its new location as will be seen in the next section.

There is a strange anomaly with the "234 *Hz*" mode as its frequency appears to increase with ϕ instead of dropping as is the usual case. Such anomalies are typically attributed to large temperature gradient existing within the duct (Laverdant et al., 1986) which may unequally effect different modes. As such, eigenfrequencies may not "....

change monotomically with equivalence ratio ....., hence the simplified prediction that eigenfrequencies are proportional to the square root of temperature fails." It is interesting that this proposed phenomena only effected the "234 *Hz*" mode.

Referring now to the corresponding two-dimensional Rayleigh Criteria for the 30 *m/s* transition (*Figure 3.31-3.33*), as the 188 *Hz* mode in engaged, driving regions enlarge and move upstream.[5] Both effects seem consistent with the observed strengthening of the 188 *Hz* mode with increasing ϕ as driving the instability over a greater axial length and closer to the pressure antinode (dump plane) are associated with stronger instabilities (Yang, 1984). The 234 *Hz* instability, conversely, is driven further downstream and over a smaller axial length. This explains the increasing $\eta_{Rayleigh}$ with introduction of the 188 *Hz* mode (Table 3.2, Section 3.2).

4.1.4 Competition between Modes

This section will illustrate the complex dynamical features associated with the $\phi = 1.4$, $V_{dump} = 30 m/s$ case whose pressure FFT (middle plot in *Figure 4.1*) shows distinct bimodal features. The significance of a beating data trace becomes important when referring to the velocity signal since it is at $V'_{\min}$ that vortices are typically shed. If the velocity signal beats, each cycle will exhibit irregular periods, thus causing a nonuniform number of vortices to be shed over time. As will be seen, this causes relocation of the heat pulse relative to the pressure trace, thereby inducing the apparent bimodal features seen in the velocity and pressure FFTs.

---

[5] Identical effect are seen for the other transitional case (35 *m/s*).

Figure 4.14a and *4.14b* show a sequence where the heat pulse arrives initially near P'_{max} but later shifts much later in the pressure cycle due to two closely shed vortices from an unusually short period in the velocity trace. The two vortices appear in the upper image (*Figure 4.14a*) and were taken as indicated in the data traces. The later structure is seen to burn earlier due to its close proximity to the earlier structure. As such, its associated heat pulse is attenuated and arrives too early as shown (Type I jump on *Figure 4.12*). The following structure is seen to burn near the zero-crossing in the pressure pulse *after* P'_{max} which, according to Rayleigh's Criterion, must lengthen the cycle's period (Keller et al., 1989). Examination of the corresponding pressure and velocity traces reflects this trend. The situation now resembles 188 *Hz* shedding characteristics. As discussed above, the relocation in Q' occurs in "jumps," rather than continuously. As *one* mode is engaged, however, the heat pulse tends to shift gradually as detailed for the 35 *m/s* transition (*Figure 4.13a* and *4.13b*).

Figures 4.15a and *4.15b* reflect a similar situation but due to three closely shed vortices caused by three successively short velocity periods. In this sequence, the heat pulse initially follows P'_{max}, then coincides, then follows P'_{max} again due to the "swallowing" of the middle structure by the most recently shed structure. Its heat pulse is consequently absorbed by this earliest structure. As expected, similar effects can be found for unusually long velocity periods. Careful inspection of the heat release traces reveals they are of unequal widths (some heat pulses appear narrow while others appear broad). As will be shown in the next section, this too contributes to the competition between modes as temporal variations in the width of the heat pulse may force one, the other or both modes simultaneously since forcing regions (region where the heat pulse overlaps positive regions of the pressure cycle) may enlarge or narrow.

A final example appears in *Figure 4.16a* and *4.16b* and shows the heat pulse almost skips a cycle. This phenomena was due to the instability going stable for a short instant (flowfield actually resembled a stable burning shear layer as shown) but later re-engaging (consult upper CCD image - *Figure 4.16*). Other images show that a structure is sometimes *not* shed at all at a V'_{min} if the velocity fluctuations at the step are small enough. These lengthy delays could suggest the possibility of a rightward shift in the heat pulse (Type II shift in *Figure 4.12*).

4.2 NUMERICAL VERIFICATION OF MODE SELECTION

The foregoing conjectures were numerically validated using a simplified version of Culick's expansion of the unsteady acoustic field as a summation of orthogonal modes (Culick, 1976). The model will show the timing of the heat releases with respect to the pressure pulse is paramount in mode selection as found by others (Keller and Westbrook, 1986; Tsujimoto and Machii, 1986) as it can detune and eventually quell the instability if timed appropriately. In addition, the model will show the generally undocumented result (Barr et al., 1990) of the importance of the temporal shape of the heat release distribution as it, too, may disrupt the delicate pressure/heat release coupling.

4.2.1 Model Description

Most numerical schemes have focused chiefly on reproducing pressure or velocity FFTs without regard to examining the influence of a more thorough heat release model on mode selection (Zsak, 1993; HA, 1992; Tsujimoto and Machii, 1986). Other researchers, however, have used detailed two-dimensional modeling but still have not communicated

its importance in the mode selection process (Bauwens and Daily, 1992; Ghoniem, 1991; Menon and Jou, 1991; Crump et al., 1985). In order to focus on the combustion occurring within the structures, a numerical model is proposed including only the pertinent heat source terms. Inclusion of an accurate heat release distribution incorporating time delays has been retained, therefore, at the expense of complex chemical kinetics, flame sheet modeling, etc. The methodology was developed by Culick (Culick, 1976, 1990, 1991) and entails reducing the complex combustion process into a series of coupled ordinary differential equations through a version of Galerkin's Method. The oscillatory pressure and velocity fields are expanded into orthogonal modes, characteristic of the present combustion chamber. As such, it was necessary to know these resonant modes or "eigenfrequencies" and mode shapes a priori so use of the past Jet Propulsion Center modeling was employed (Zsak, 1993; Sterling, 1987; Smith, 1985). Through a careful selection of the fundamental terms in the governing equations, many relevant physical phenomena can be retained (Sterling, 1991).

Complete formulation of the model will not be presented as it may be found in the literature (Culick, 1976, 1990, 1991). It is instructive, however, to outline some of its features. Assuming no body forces and an inviscid and nonconducting flow, the conservation equations (continuity, momentum and energy) are (Sterling, 1991):

$$\frac{\partial \rho}{\partial t} + \nabla \cdot (\bar{u}\rho) = 0, \tag{4.1}$$

$$\rho \frac{\partial \bar{u}}{\partial t} + \rho \bar{u} \cdot \nabla \bar{u} = -\nabla p, \tag{4.2}$$

$$\frac{\partial p}{\partial t} + \gamma p \nabla \cdot \bar{u} + \bar{u} \cdot \nabla p = (\gamma - 1) q, \tag{4.3}$$

where:

$\rho = density$
$p = pressure$
$\vec{u} = velocity$
$q = rate\ of\ heat\ addition\ per\ volume.$

The above equations are linearized by representing all dependent variables as the sum of a mean and fluctuating quantity. Manipulating the above conservation equations and relating all quantities to p' (useful in acoustic analysis) results in a nonlinear wave equation:

$$\nabla^2 p' - \frac{1}{\bar{a}^2}\frac{\partial^2 p'}{\partial t^2} = \boldsymbol{h}, \tag{4.4}$$

where $\boldsymbol{h} = (\gamma - 1)\frac{\partial q'}{\partial t}$ is the nonlinear driving term for the system and $\bar{a}$ is the average speed of sound. Inclusion of all source terms and second order fluctuations yields a more formidable nonlinear driving expression (Culick, 1988):

$$\boldsymbol{h} = -\bar{\rho}\nabla\cdot\left(\vec{\bar{u}}\cdot\nabla\vec{u}' + \vec{u}'\cdot\nabla\vec{\bar{u}}\right) + \frac{1}{\bar{a}^2}\vec{\bar{u}}\cdot\nabla\frac{\partial p'}{\partial t} + \frac{\bar{\gamma}}{\bar{a}^2}\frac{\partial p'}{\partial t}\nabla\cdot\vec{u} - \nabla\cdot\left(\bar{\rho}\vec{u}'\cdot\nabla\vec{u}' + \rho'\frac{\partial\vec{u}'}{\partial t}\right) +$$
$$\frac{1}{\bar{a}^2}\frac{\partial}{\partial t}\left(\vec{u}'\cdot\nabla p'\right) + \frac{\bar{\gamma}}{\bar{a}^2}\frac{\partial}{\partial t}\left(p'\nabla\cdot\vec{u}'\right) + \nabla\cdot\vec{\boldsymbol{F}}' - \frac{1}{\bar{a}^2}\frac{\partial\boldsymbol{P}'}{\partial t},$$

where $\vec{\boldsymbol{F}}'$ and $\boldsymbol{P}'$ are the fluctuating parts of:

$\vec{F}$ = *source term in momentum equation*
P = *source term in energy equation.*

Consult Culick (Culick, 1992, 1988) for his exact formulation. The above equation is solved with the accompanying boundary condition:

$$\hat{n} \cdot \nabla p' = -f, \tag{4.5}$$

where f is some prescribed function. For a rigid wall, for instance, all pressure perturbations must vanish which forces f to zero. The solution of the unperturbed problem ($h = f = 0$) can be formulated as the superposition of the normal acoustic modes $\Psi_n(\vec{r})$ requiring:

$$\begin{aligned} \nabla^2 \Psi_n + k_n{}^2 \Psi_n &= 0 \\ \hat{n} \cdot \nabla \Psi_n &= 0, \end{aligned} \tag{4.6}$$

where:

$$k_n = \frac{\omega_n}{a} \quad (\textit{wave number}).$$

ω_n denotes the particular frequency of mode n and for the present investigation n will be two (188 or 234 *Hz* shedding). A method of least residuals is employed whereby the pressure and velocity fields are expanded into normal acoustic modes $\Psi_n(\vec{r})$ with time varying amplitudes $\eta_n(t)$ given by:

$$\begin{aligned} p'(\vec{r},t) &= \bar{p} \sum \eta_n(t) \Psi_n(\vec{r}), \\ \vec{u}'(\vec{r},t) &= \sum \frac{\dot{\eta}_n}{\gamma k_n{}^2} \nabla \Psi_n(\vec{r}). \end{aligned} \tag{4.7}$$

The above expressions for pressure and velocity are not exact because they do not satisfy the boundary conditions but are correct in the case where $h = f = 0$. Provided that h and f are small ensures the validity of the above solutions and will be assumed hereafter (Culick, 1988).

The expression for $p'(\vec{r},t)$ is substituted into the wave equation (4.4) and then multiplied by the mode shape, Ψ_n. Equation (4.6) is then multiplied by p' and the resulting two equations are then subtracted and integrated over the chamber volume. Employing orthogonality of the mode shapes, Green's theorem and assuming ideal boundary conditions (f = 0), n ordinary differential equations are derived for the amplitudes $\eta_n(t)$:

$$\frac{d^2\eta_n}{dt^2} + \omega_n{}^2\eta_n = \frac{\gamma - 1}{\bar{p}E_n{}^2}\int_V \Psi_n \frac{\partial q'}{\partial t} dV, \tag{4.8}$$

where:

$$E_n{}^2 = \int_V \Psi_n{}^2 dV.$$

Hence the complex problem has been reduced to one characterized by a set of coupled oscillators driven by a nonlinear heat source term. Its inclusion as the only driving mechanism has been motivated by prior Jet Propulsion Center work (Sterling and Zukoski, 1991; Sterling, 1991) whereby the pressure oscillations were controlled almost exclusively by the Rayleigh Mechanism. A similar proof has been included in Section 3.2. This technique obviously neglects other mechanisms of energy transfer such as the viscous dissipation in the boundary layers and nonideal boundary conditions but these were shown to be negligible (Section 3.2).

4.2.1.1 Heat Release Modeling

The most critical components of the heat release distribution found from the experiments have been the spatial and temporal evolution of the heat supplied by the convecting vortices. Based on Hycam work (Section 3.1), vortices convect at approximately the average dump plane speed and are typically shed at velocity minimums either one to one and a half (2.54 and 5.08 *cm* ducts) or two cycles (7.62 *cm* duct) before their peak combustion (Section 4.1). Since it was found the phasing between the pressure and velocity traces are unique to $v_{shedding}$ and different from conventional acoustic predictions, $P'_{\max}$ was taken as the reference point from when structures are shed. The timing of the heat release was also found to vary on prior conditions within the duct as discussed in Section 3.1: structures characterized by larger resulting pressures amplitudes when they burn, generally provide more hot products for later structures and hence reduce subsequent ignition times and times to peak combustion. Consequently, the delay between when vortex i is shed at time j-1 to the time j corresponding to its peak combustion is modeled as a straight line depending on the combustion pressure at the time of shedding (j-1):

$$\tau_{d_i} = mP'_{\max_{j-1}} + b. \tag{4.9}$$

Here, the time delay for vortex i, τ_{d_i}, depends on the pressure amplitude, $P'_{\max}$, one cycle before its peak combustion which is precisely the pressure near the time of shedding. The constants m and b were found through linear fits of the experimental data depicted in *Figures 3.19a*. The above formulation provides the model with an effective means at stabilizing the pressure magnitudes as the heat pulse drifts and eventually locates itself where dissipation equilibrates with energy addition. In addition, average heat release distributions when plotted as surface plots (see *Figure 4.24a*, for instance) closely

resemble gaussian profiles. Including all of the above results leads to the following model for the total heat release distribution, $Q_{total}(x,t)$:

$$Q_{total}(x,t) = pow \sum_{i=1}^{novor} \frac{c_i}{\sigma_{a_i}\sqrt{2\pi}} \left\{ \exp\left[-\left(x_i - x_{rxn_i}\right)^2 / 2\sigma_{a_i}{}^2 \right] \right\} \times \left\{ \exp\left[-(x - x_i)^2 / 2\sigma_{b_i}{}^2 \right] \right\}, \tag{4.10}$$

where:

i = *vortex no.*

j = *time index*

$c_i = m_a P'_{\max_{j-1}} + b_a$; *constant for heat release pulse magnitude*

x_i = *position of vortex* $i = v_{v_i} t$

v_{v_i} = *speed of vortex i*

$x_{rxn_i} = v_{v_i} \tau_{d_i}$ = *location of peak heat release for vortex i*

σ_{a_i} = *standard deviation of gaussian envelop*

σ_{b_i} = *standard deviation of convecting vortex*

pow = factor to convert Q to watts.

When a pressure maximum is encountered, a structure convecting at the local dump plane speed is shed. The larger gaussian envelop (consult *Sketch 4.1* below), represented by the first exponential term above, depicts the height of the smaller convecting gaussian (second expression) whose area is representative of the heat content within the vortex at a particular instant. Compact heat distributions that occur at precise axial locations and with great intensity, for instance, can therefore be modeled with a gaussian envelop of small σ_{a_i} as this would effectively narrow the burning zone, thereby

assessing the significance of the shape of the burning distribution. When a structure reaches $x = 30\ cm$, it is extinguished as this represented the end of the combustion zone from examination of the CCD images. Fine tuning of the model to more correctly mimic experimental results can be achieved through a careful selection of the governing parameters. Varying the parameters in a systematic way will allow the important combustion effects to be analyzed separately.

Sketch 4.1

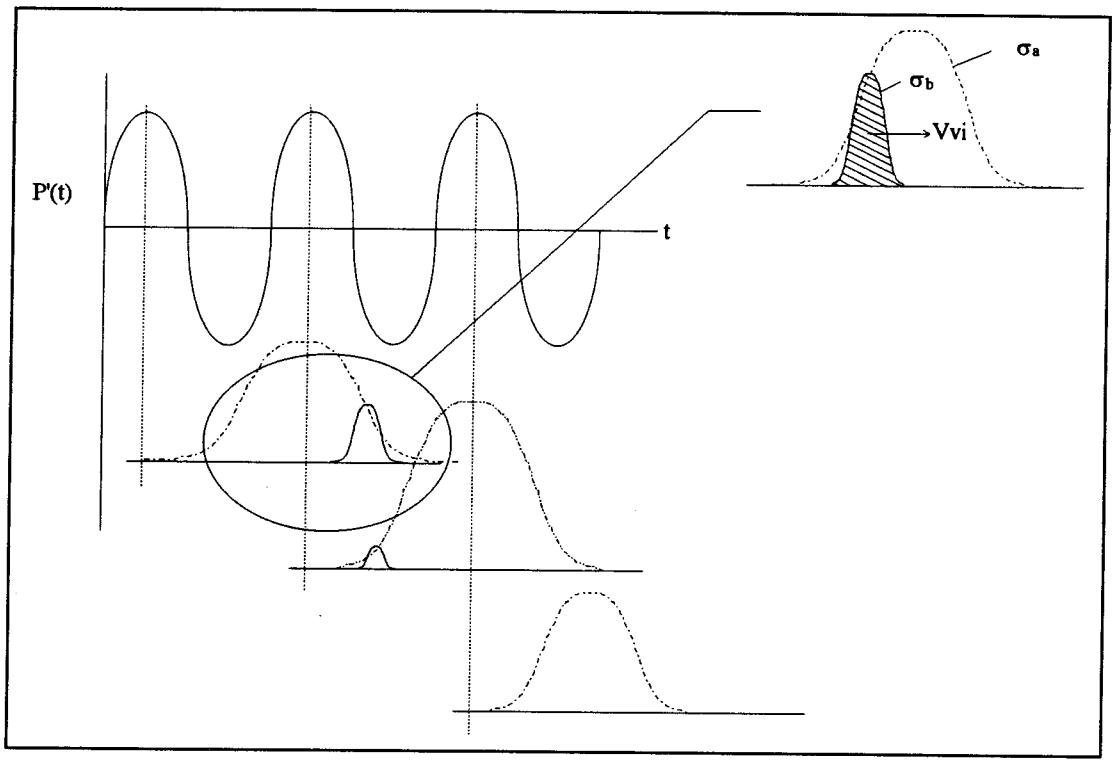

4.2.2 General Model Output

The model was run with a variety of input parameters to assess its stability. *Figures 4.17* and *4.18* reveal the model is accurate in stabilizing pressure oscillations which are initially smaller (Type I) or larger (Type II) than their limit cycle counterparts, respectively and reflects that the Rayleigh Mechanism is sufficient in providing driving or damping for stable limit cycles. In the previous two figures, initial pressure levels were chosen below and above their corresponding limit cycle counterparts, respectively. Since no other sources of damping were incorporated, the heat release pulse always settled straddling the zero-crossing of the pressure pulse, either before or after pressure maxima. Setting the parameter m to zero allowed the heat pulse to be manually located where desired and typically did not result in limit cycle behavior. A summary of the input parameters for both Type I and II convergence is presented in Table 4.2 below. It should be noted that since the model does not incorporate other damping sources (viscous dissipation in the boundary layers, nonideal end conditions, etc.), oscillatory pressure amplitudes will be over-predicted.

***Table 4.2:** Input Parameters for Figures 4.17 and 4.18*

Convergence	V_{dump} (m/s)	m	b	σ_{a_i}	$\dot{Q}_{total}$ (kW)
Type I	30	-1.796e-7	0.0057	0.01	20
Type II	30	-1.796e-7	0.0052	0.01	20

4.2.3 Verification of Jump in Time Delay invokes Mode Shifts

Section 4.1 postulated that jumps in τ_{max} could provide the necessary "kick" to induce a transition from 234 to 188 *Hz*. To model the temporal shift in Q', the formulation of τ_{d_i} was systematically varied by altering parameter b. Variation of this parameter would allow the heat pulse to drift and finally settling at a location once a limit cycle is established. Because one is interested only in the placement of the heat pulse, no other parameters were varied. Both forward (Type II shift; see *Sketch 4.2*) and backward (Type I) shifts in the location of the heat pulse were examined after first engaging a 234 *Hz* mode.

Sketch 4.2

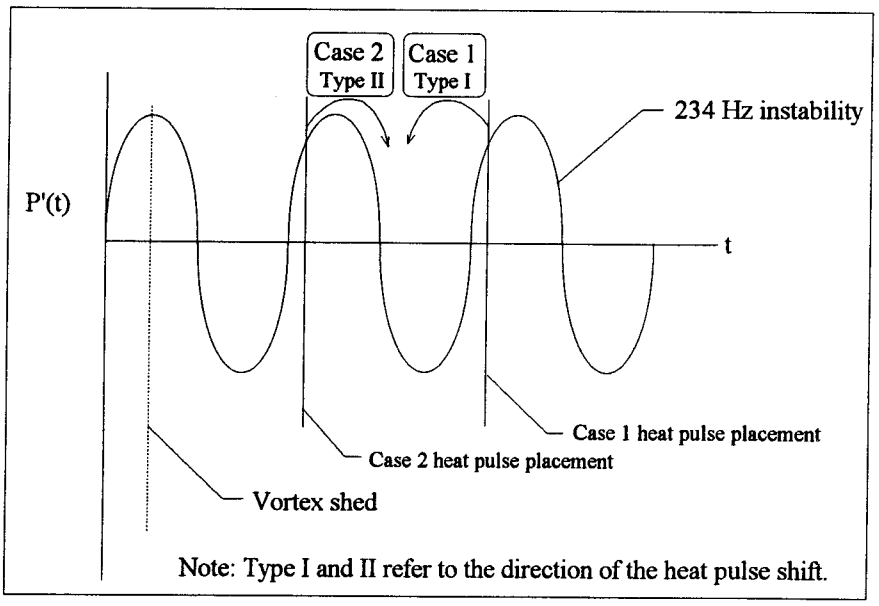

As expected, placing the heat pulse ~ 45° before P'_{max} by setting $b = 0.004$ (heat pulse arriving within one cycle after shedding; Case 2) or by setting $b = 0.0072$ (heat pulse arriving nearly two cycles after shedding; Case 1) indeed invoked 234 *Hz* shedding. This

was done to show both forward and backward movements of the heat pulse could invoke the 188 *Hz* instability. Compare the numerical and experiment pressure FFTs in *Figures 4.19* ($b = 0.004$) and *4.20* ($b = 0.0072$). Further increasing b to 0.0057 for the Case 2 route with $m = 0.0$ favoured energy addition to the 188 *Hz* mode, thus rendering a 188 *Hz* instability (*Figure 4.21*). Setting the parameter m to zero was necessary to force the heat pulse to the equilibrium point *after* P'_{max}. Continued increases in b with nonzero m values were insufficient in moving the heat pulse after P'_{max} due to mode "locking" and suggests there are preferred direction the heat pulse most likely takes. In addition, decreasing b to 0.0063 for the Case 1 situation also invoked the 188 *Hz* instability (*Figure 4.22*). It should be noticed that the leftward movement of the heat pulse (Case 1) to invoke a 188 *Hz* mode was achieved with less effort (smaller change in b) since the Type 1 transition did not have to negotiate the P'_{max} of the 234 *Hz* mode. The complete transition for the Case 2 transition is shown in *Figures 4.23a* through *4.23f*. The top plots represent the pressure (solid lines) and heat release (dashed lines) traces while the bottom plots are the associated pressure FFTs.

4.2.4 Effect of Heat Distribution Shape in Mode Selection

Figures 4.24 and *4.25* depict experimental average burner surface plots for two transitional cases (V_{dump} = 21 and 30 *m/s*, respectively) where $\nu_{shedding}$ gradually shifts from 234 to 188 *Hz* as ϕ increases from 1.2 to 1.6. The surface plots, averaged from over 50 cycles of pressure, were made using the software package PV-WAVE and were corrected for noise and normalized such that their volumes equal the average power output for their corresponding ϕ and V_{dump} (STANJAN, 1985). The "horizontal" and "vertical" dimensions are, respectively, the horizontal and vertical dimensions of the duct represented as pixel values: 239 pixels long (30.48 *cm*) by 48 pixels high (5.08 *cm*). As shown most explicitly

for the lowest dump plane speed (21 *m/s*), there is a gradual compacting of the burning zone as ϕ increases and as the 188 *Hz* mode is introduced. The goal of this section is to demonstrate the importance of the shape of the heat release distribution in mode selection. It has been documented, for instance, that narrowing the burning zone in numerical simulations increases $\eta_{Rayleigh}$ and consequently pressure (Barr and Dwyer, 1991). The shape of the heat release has not, conversely, seen to be crucial in mode selection except by possibly one researcher (Samaniego et al., 1993) who commented that the transition from a fuel-lean to fuel-rich instability "..... seems to be related to the evolution of the flame geometry with the equivalence ratio since the downstream reaction zone becomes more and more compact as ϕ increases."

The axial shortening could be related to the augmentation in turbulence levels accompanying the pressure increases which for turbulent flames causes well documented shortening of the flame length (Kuo, 1986; Yoshida and Tsuji, 1982; Bowditch, 1953; Wohl et al., 1953). Furthermore, 188 *Hz* instabilities are characterized by structures spaced further apart which would also reflect a more compact burning zone as fewer structures would be in the duct and consequently burning on average. Such trends are reflected in the narrower floor heat flux and temperature distributions for the 188 *Hz* modes (Section 3.3 and 3.4).

The above disparities in average burner profiles can be implemented into the model through a careful selection of the model parameter σ_{a_i}. It should be noted that slight changes in σ_{a_i} induced wide variations in Q' so appropriate adjustments in the constant *pow* were made to ensure accurate Q' values. The constants varied in these simulations were therefore *pow*, σ_{a_i} (0.01-0.07) and b (0.003-0.007). As such, the simulations depicted Case 2 transitions (forward moving heat pulse). This range of σ_{a_i} was chosen as

it represented the approximate burning lengths experimentally found (Compare *Figure 3.21* with *Figure 4.26*). *Figure 4.27* presents the results. Each dark triangle represents 188 *Hz* shedding while the lighter triangles are representative of 234 *Hz* shedding, with each case having some component of the other competing frequency. The dotted line represents the boundary separating shedding at either one or the other frequency. The most apparent and typically documented trend (Barr et al., 1990; Keller and Westbrook, 1986) is the shift in the excited mode accompanying b increases for constant σ_{a_i}. What is interesting is the transition from 234 to 188 *Hz* under constant σ_{a_i} becomes more resistant to changes in b as σ_{a_i} is lowered (until 0.02). Obviously, the 234 *Hz* mode is stronger dynamically with narrower heat distributions. The reason should be clear. As the spatial distribution is narrowed, the temporal distribution will also narrow as heat is being applied more compactly due to assumed relation between space and time ($x_{rxn} = v_v t$). Narrower heat pulses provide a more favourable phasing with the pressure pulse if applied at the same location, thus strengthening the instability typically and making it more resistant to external influences. The argument holds until $\sigma_{a_i} = 0.01$ but it should be noted that the exact temporal location of this heat pulse is different due to the different pressure amplitudes attained in the limit cycle.[6]

Another result which will become important later is, as expected, the closer one is to the dotted line, the more bimodal are the respective FFTs. As a result, the pressure FFTs for simulations with b=0.003 show an increasingly stronger 234 *Hz* content as σ_{a_i} is lowered from 0.07 to 0.02. Consequently, a broad heat release profile in a 234 *Hz* limit cycle with significant 188 *Hz* component in its respective FFTs - i.e.: a point close to the dotted line in *Figure 4.27* - would be easier to "kick" into a 188 Hz limit cycle. A situation

[6] The previous examples had more or less the same pressures in the limit cycles, thereby ensuring the heat pulse arrived at approximately the same location. The above statement only holds for identically placed heat pulses.

where the FFT reveals a much stronger 234 *Hz* component - i.e.: further away from the dotted line - would be, conversely, harder to coax into a new mode. This is interesting as experimentally determined 234 *Hz*, average heat release profiles show distinct broadening over their 188 *Hz* counterparts. Such spatial broadening of the heat release profile is not typically reflected in temporal broadening of the 234 *Hz* heat release traces when compared to 188 *Hz* profiles though there is some evidence of such a relation on examination of the first two 188 *Hz* heat pulses (*Figure 4.28*). This figure shows how the "height to width" ratio of the 188 *Hz* pulses is typically larger than its 234 *Hz* counterparts. Furthermore, the 234 *Hz* spectra (*Figures 4.1-4.2*) show significant 188 *Hz* components, placing these runs close to the transition boundary (dotted line) in *Figure 4.27*. According to the model, these cases should be easier to invoke mode shifts and was precisely what was found experimentally when compared to the 188 *Hz* cases which exhibited generally narrower heat release traces and therefore more dynamically resistant limit cycles.

Still another interesting result from the model is the new result that σ_{a_i} has significant influence in mode selection for constant *b*. The implications are as follows. If a bimodal limit cycle is engaged, as in the middle FFT appearing in *Figure 4.1*, broader heat release profiles favour 188 *Hz* shedding while narrower profiles force 234 *Hz* shedding. Evidently, narrower profile ensure more favourable energy addition to the 234 *Hz* mode while expanding the distribution spatially excites the 188 *Hz* mode. As profiles broaden, it should not seem unlikely that excitation of other existing yet less dominant modes could be achieved as one is forcing the bimodal pressure trace over a greater temporal length. It should be reiterated that these simulations reflect rightward shifts in Q', which was not the typical proposed route discussed earlier. The above influence of σ_{a_i} appears limited to a specific band of *b*, outside of which one sees the generally accepted result (Barr and

Dwyer, 1991; Barr et al., 1990; Crump et al., 1985) that σ_{a_i} has no bearing on $\nu_{shedding}$. This apparent discrepancy can typically be traced to many researchers (HA, 1992; Sterling, 1991) assuming the heat to be added all at once, rather than gradually. The simulation at $b = 0.005$, $\sigma_{a_i} = 0.02$ depicts an interesting "saddle" point (Wiggins, 1990) as any departure in σ_{a_i} from 0.02 invokes the 188 *Hz* mode. Consult *Figures 4.29a* to *4.29c* for their respective pressure FFTs.

Figure 4.30 depicts a summary of the pressures for all simulations versus the parameter b. A dotted line connects the runs having $\sigma_{a_i} = 0.05$ and reflects the experimentally found result that introduction of the 188 *Hz* mode incurs sizeable oscillatory pressure increases. This result should appear obvious since for a heat pulse of constant "width," the 188 *Hz* pressure cycle with its larger period has a larger *positive* region into which heat may be added relative to the shorter period 234 *Hz* pressure trace. A final note concerns the 234 *Hz* ($b = 0.003$) and 188 Hz ($b = 0.006$) which typically have their forcing function at the same location. They reflect the generally found result that for a fixed driving location, narrower profiles encourage more favourable pressure/heat release phasing as discussed earlier, thus augmenting pressure levels.

4.2.5 Desensitization of the 188 Hz Mode

Figures 4.31a and *4.31b* show how the placement of a narrow heat pulse ($\sigma_{a_i} = 0.01$) relative to the pressure maximum has severe implications to their corresponding pressure magnitudes and FFTs, respectively, as it can detune and eventually quell the instability (Keller and Westbrook, 1986). These figures should reinforce previous statements about the phasing between the pressure and heat release profiles i.e.: Rayleigh's Criterion.

By modeling the heat release as a convecting gaussian, the numerical model has shown the importance of the location of the heat release pulse relative to the pressure trace, located initially by the parameter b, and later allowed to drift until an equilibrium point was reached. Furthermore, the model has shown there are most likely preferred routes the heat pulse takes (as evidenced by larger changes in the parameter b necessary to invoke some transitions) and the importance of the *temporal* shape of the heat release distribution. The temporal shape of the model was directly related to the axial shape since it was assumed $x_{rxn} = v_v t$. This may, however, not be true in practice.

4.3 HEAT LOSS EFFECTS ON MODE SELECTION

Mode transitions incur sizeable increases in floor heat flux as previously shown (see Section 3.4). Table 4.3 below summarizes the results for the four dump plane speeds investigated. This section will address if such increases modify the resulting pressure spectra and hence $v_{shedding}$ through its inevitable effect on lowering the sound speed in the combustion chamber.

Table 4.3: *Floor Heat Flux Increases during Mode Transitions.*

V_{dump} (m/s)	$\Delta \dot{Q}_{floor}$ (W)
21	300
25	400
30	500
35	900

Motivated by others, heat losses to the surrounding walls in pulsed combustors have shown sizeable drops in Rayleigh Efficiency ($\eta_{Rayleigh}$) which inevitably lower pressure

magnitudes (Barr and Dwyer, 1991). The acoustic spectra with its dependence on combustor sound speed (Zsak, 1993) must consequently reflect some variation due to this mechanism of energy dissipation. Using a linear acoustic model (Zsak, 1993; Sterling, 1987; Smith, 1985), the combustion chamber sound speed was systematically lowered to see its effect on the resulting pressure spectra. The boundary condition at the exit plane of the combustor was altered to characterize the experimental result that the chamber temperature falls considerably along the duct, reaching approximately 900 K at the exit plane. *Figure 4.32* shows the resulting drop in maximum gas temperature corresponding to the stoichiometric variation and heat loss to the surrounding walls for two transitional cases: V_{dump} = 30 and 35 *m/s*. (To get an estimate of the total heat loss to all four walls throughout the 30 *cm* long combustion zone, the floor heat flux values were multiplied by three). For both dump plane speeds, a 300 *K* drop can be expected (STANJAN, 1985). *Figure 4.33* depicts how the relative amplitudes of both the 188 and 234 *Hz* modes respond to such a temperature drop. The 280 *Hz* mode is an acoustic mode that is excited only with fuels having shorter kinetic time scales ($H_2 - CH_4$ / *air* mixtures). Assuming an initial sound speed of 730 *m/s* (Sterling, 1987), the calculated temperature drops would invoke an approximate 50 to 60 *m/s* reduction in sound speed which clearly effects the relative amplitudes of the two competing frequencies. The acoustic model predicts an approximate 20 % reduction in the 234 *Hz* mode accompanied by a near 100 % increase in the 188 *Hz* mode. The net effect would be to favour a transition from 234 to 188 *Hz*. This effect was found only through changing the complex reflectance (Zsak, 1993) at the dump plane to reflect the temperature drop along the duct. If the original model configuration was used (constant duct temperature, therefore exit reflectance based on combustor temperature), the result was not seen. Such effects could be attributed to subtle movements of the heat addition location relative to the maxima in the acoustic mode shapes.

4.4 STRAINING ARGUMENT IN MODE SELECTION

Failure to notice any sizeable delay and/or shift in peak burning locations for the majority of the 5.08 *cm* cases (Consult Section 3.1 and *Figure 4.24* - all peaks in the burner surface plots occurred at the same axial location) suggests that ϕ variations do not play a major roll in delaying combustion (This by no means precludes its importance as was shown). As previously remarked, such highly turbulent flows are predominately controlled by turbulent exchange processes rather than chemical effects (Heitor et al., 1984; Bray, 1980). A careful analysis of the transition occurring at 35 *m/s* reveals, however, that there may be some chemical and/or mechanical mechanism at work. Comparing the average burning distributions for $\phi = 1.2$ (234 *Hz* shedding) and $\phi = 1.4$ (188 *Hz* shedding) and ensuring to average only those cycles having precisely the prescribed $\nu_{shedding}$ (subtle beating of the pressure signal invoked cycle-to-cycle variations in the period), an approximate 4 *cm* downstream shift in peak burning location was observed (*Figure 4.34*). This axial shift encourages speculation of a physical delay mechanism occurring throughout the development of the structure. There are two possible candidates for the above trend: (1) an increase in τ_{id} accompanying the ϕ increase or (2) existence of a mechanical delay such as straining. As detailed in Section 3.1, τ_{id} varies inversely with ϕ so speculation therefore focuses on a mechanical mechanism as straining to provide the necessary shift.

It has been reported that straining can provide the necessary delay mechanism to ensure the correct phasing between the pressure and heat release (Barr and Keller, 1991). This should come as no surprise since the effects of straining on laminar and turbulent flames are widely discussed (Kostiuk and Bray, 1994; Roberts et al., 1993; Kobayashi and Kitano, 1993; Poinsot et al., 1991; Rutland and Ferziger, 1991). In most situations,

aerodynamic stretching created by flowfield nonuniformities, flame curvature or prevailing unsteadiness exists and cannot be avoided. Its effect on laminar burning velocity, for instance, has been extensively documented (Law et al., 1986; Wu and Law, 1985; Yu et al., 1986). Stretching increases the area of a flame by the convolution or wrinkling of its surface, augmenting turbulence levels ahead of it (Driscoll et al., 1994) and consequently increases S_l (laminar burning velocity) (Law et al., 1986). As straining continues, it quenches the flame by any number of its side effects: it augments flame curvature (convex flame towards the reactants) which for Lewis number greater than unity mixtures (rich $CH_4 - air$ mixtures, for instance) reduces their local reaction rates by dropping temperatures (Roberts et al., 1993; Tsuji and Yamaoka, 1981) or it thins the reaction zone for confined flames which in turn causes incomplete reactions (Law et al., 1986), to name two. Furthermore, the response of the flame to prevailing strain fields may cause it to relocate near heat sinks, resulting in heat loss and eventual quenching (Robert et al., 1993; Law, 1988). All of the above effects can be accelerated using either richer or leaner mixtures. Experimental and numerical findings of the interactions of flames with vortices are clear indicators of its effect on the existence and modification of flames (Driscoll et al., 1994; Kobayashi and Kitano, 1993; Roberts et al., 1992, 1993; Rutland and Ferziger, 1991). Given the above statements and noting the present flowfield incorporates flame-vortex interactions, it is reasonable to expect straining to have some impact on combustion development.

Figures 4.35 and *4.36* depict the straining curves based on the vortex dimensions X_d and $L - \frac{1}{2}U_o t$, respectively (see Section 3.1 for a description of the dimensions), for the $\phi = 1.2$ (234 *Hz* shedding) and $\phi = 1.4$ (188 *Hz* shedding) transitions for a V_{dump} of 35 *m/s*. The curves are averaged from five vortices. Included on the plots are the laminar extinction limits taken from Law which states that richer mixtures have lower extinction

limits than their leaner counterparts (Law et al., 1986). This implies that the richer and consequently lower shedding cases must allow more time for straining rates to attain acceptable levels before the occurrence of full combustion. This does not preclude the fact that the structures may already be burning since not all regions are experiencing the same stretching due to its dependence on flame curvature, heat loss, etc. (Roberts et al., 1992). From the graphs, the time difference between when the two cases have their straining rates at acceptable levels corresponds closely to the difference in shedding periods ($1/188 - 1/240 \cong 2.83 - 1.53\ ms$). Furthermore, the downstream shift in peak burning location for the richer and consequently lower shedding case corresponds roughly to a 1.1 *ms* delay (4 *cm* / 35 *m/s*) between the two peak burning locations which is close to the difference in the shedding periods and time delay expected from straining. It could be suggested that straining may offer an additional physical delay mechanism, retarding the timing of the heat pulse. Further evidence of the roll straining might play is seen on the nose, core and tail temperature plots for the 30 *m/s*, $\phi = 1.6$ case discussed earlier (Section 3.5) which reflected a delay in temperature growth when compared to its leaner counterpart ($\phi = 1.4$, 234 *Hz* shedding). Although peak combustion occurred at approximately the same time, the initial difference in temperature growth rates between the two stoichiometric cases could be due to the extinction limit variations (i.e. strain related) between the cases. The fact that the time for straining rates to fall to acceptable levels (Section 3.1) constitutes more than half of the overall delay from shedding to maximum burning, τ_{max}, should also reflect its importance.

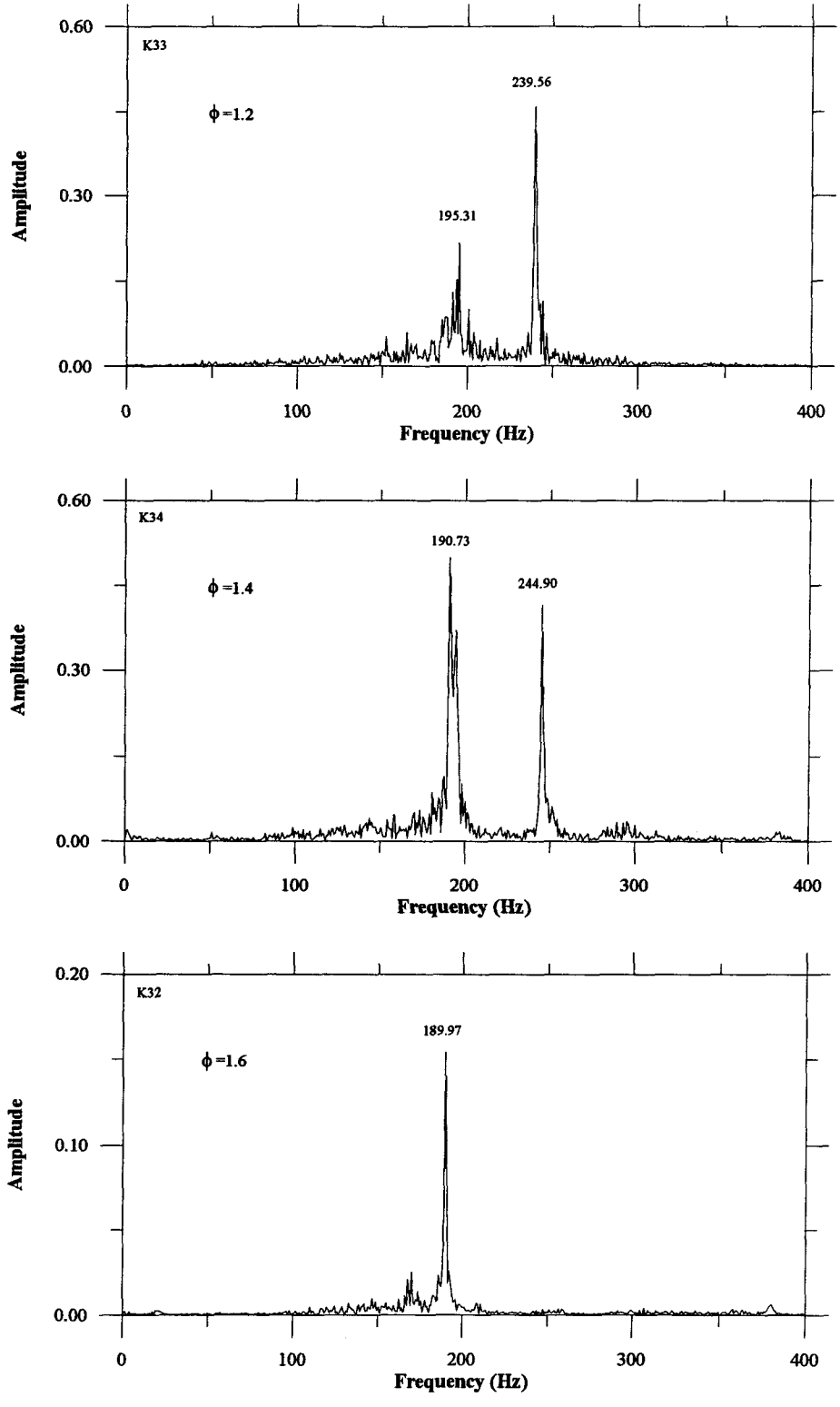

Figure 4.1: Pressure FFTs for mode transition: 5.08 cm, $V_{dump} = 30 m / s$.

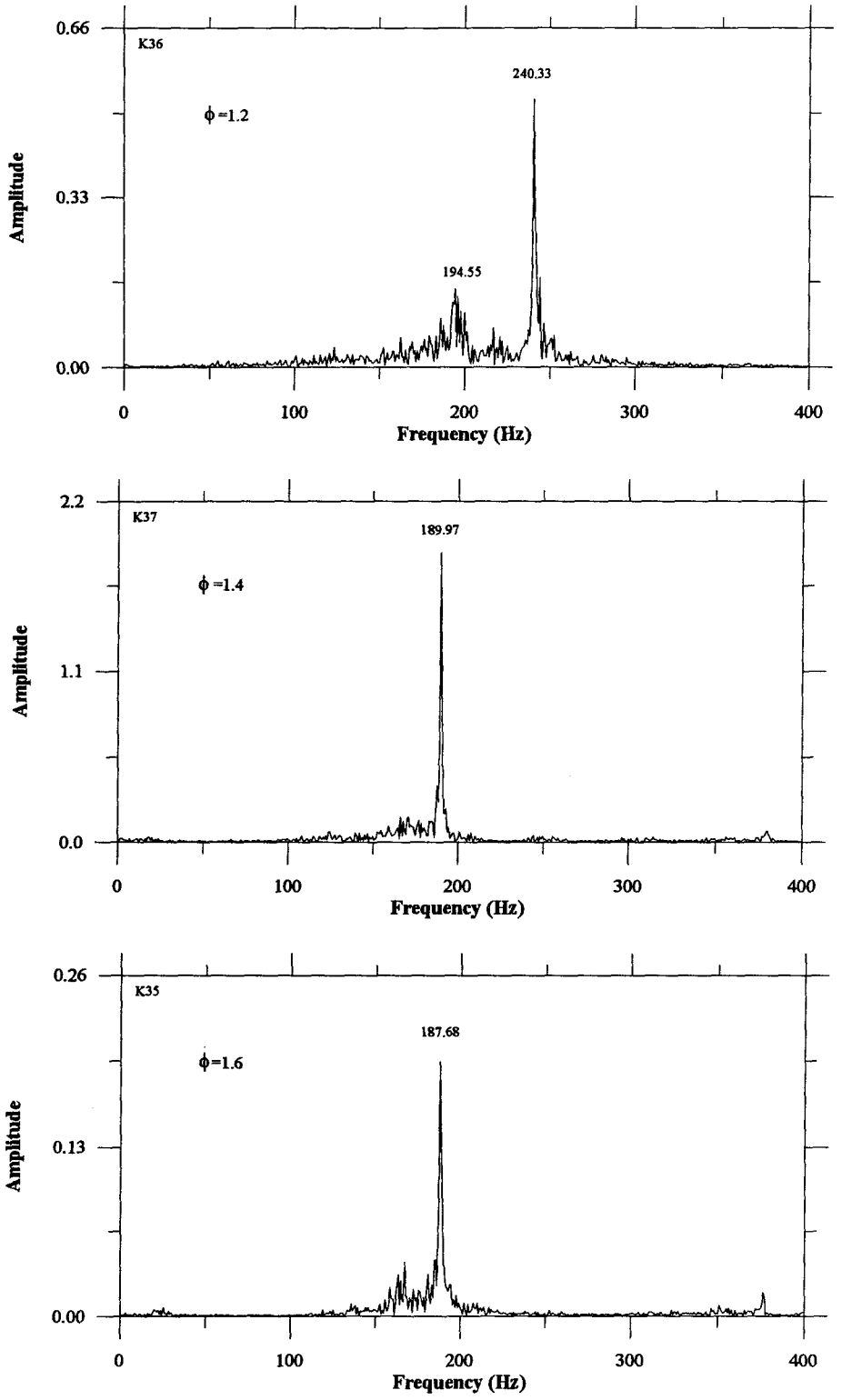

Figure 4.2: Pressure FFTs for mode transition: 5.08 cm, $V_{dump} = 35 m / s$.

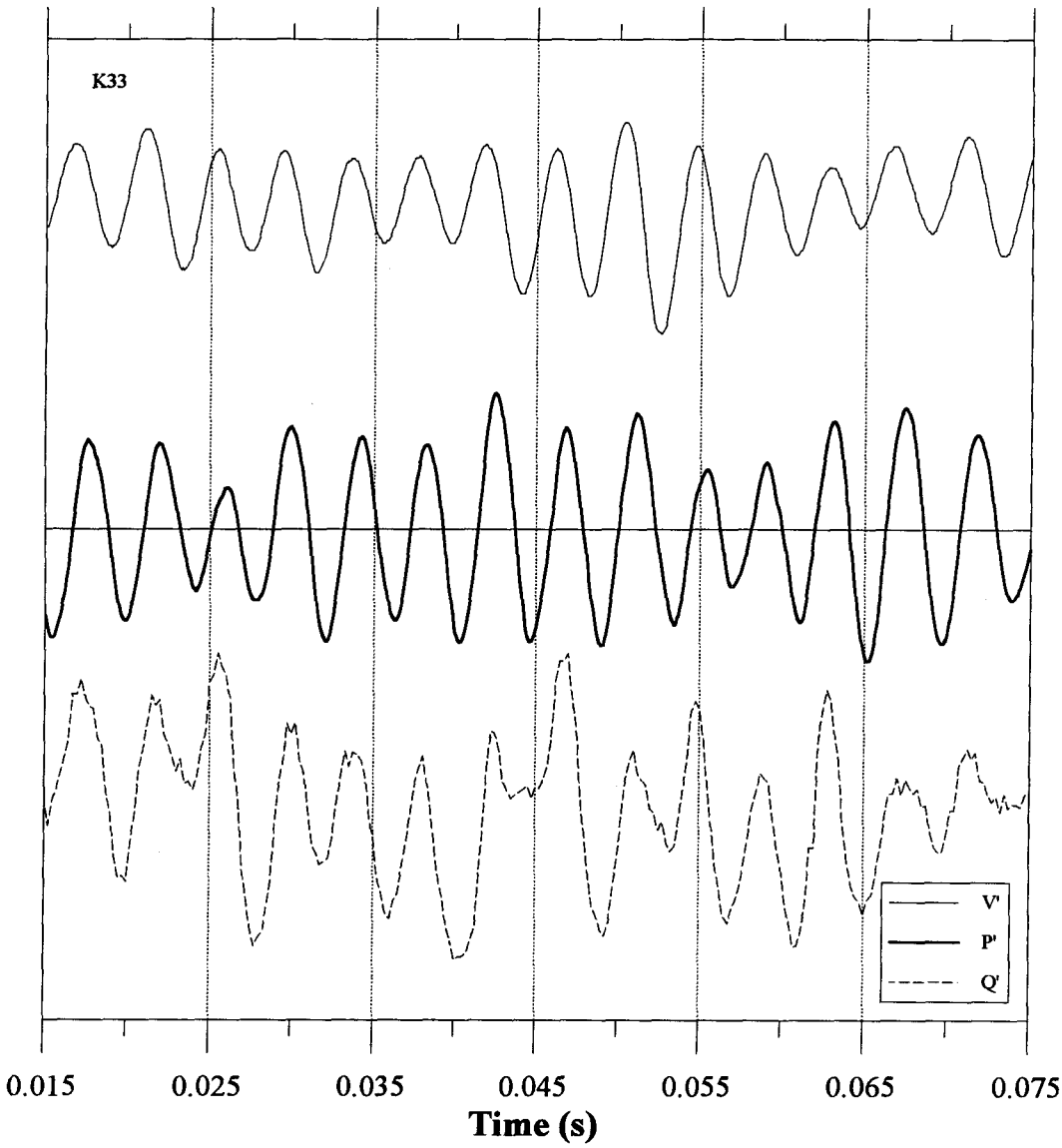

Figure 4.3: Experimental data traces: 5.08 cm duct, 30 m/s, $\phi = 1.2$.

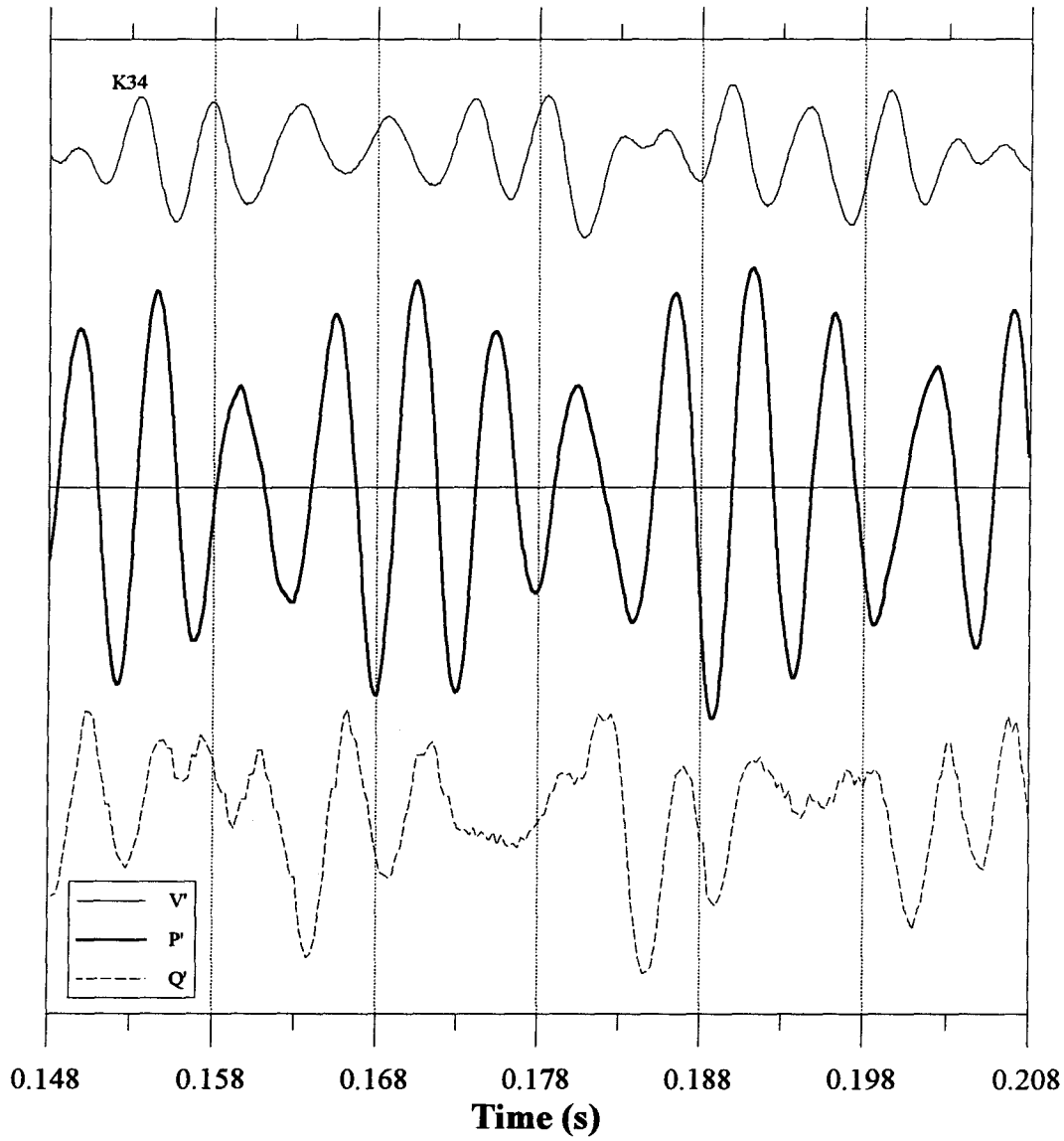

Figure 4.4: Experimental data traces: 5.08 cm duct, 30 m/s, $\phi = 1.4$.

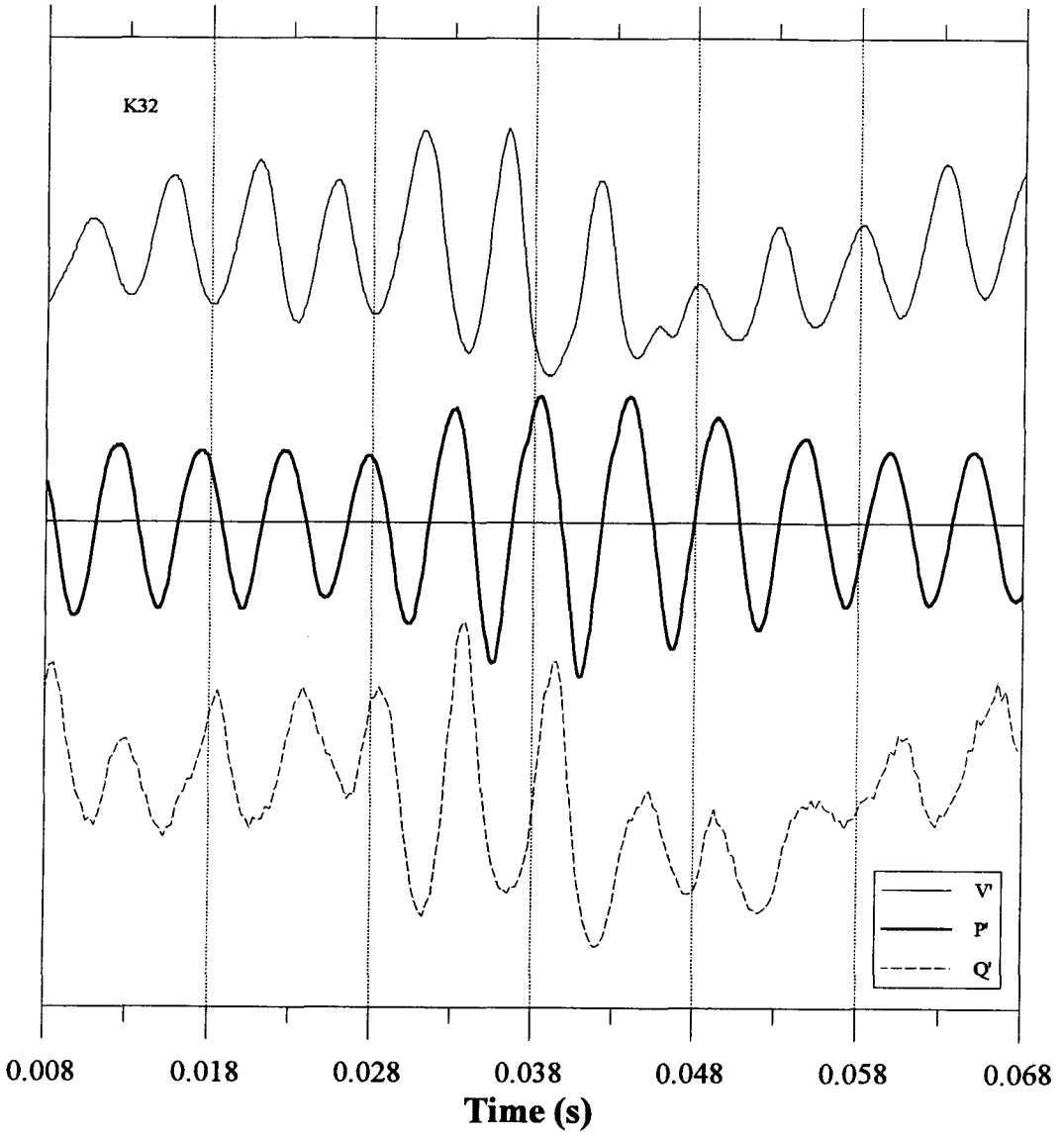

Figure 4.5: Experimental data traces: 5.08 cm duct, 30 m/s, $\phi = 1.6$.

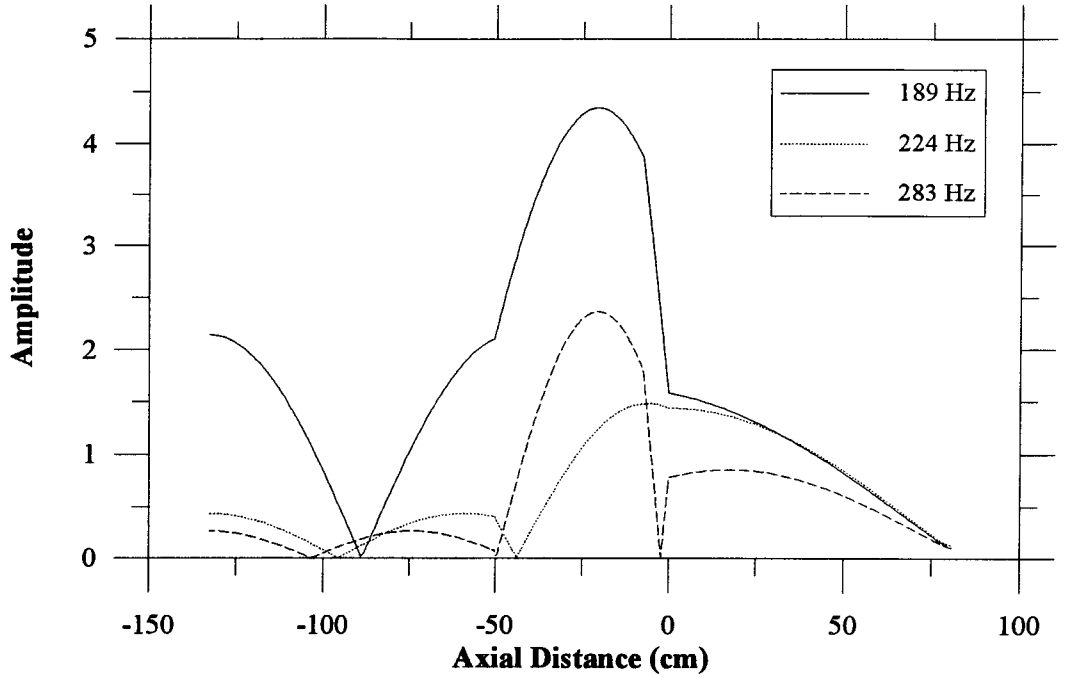

Figure 4.6a: Pressure mode shapes for 5.08 cm duct.

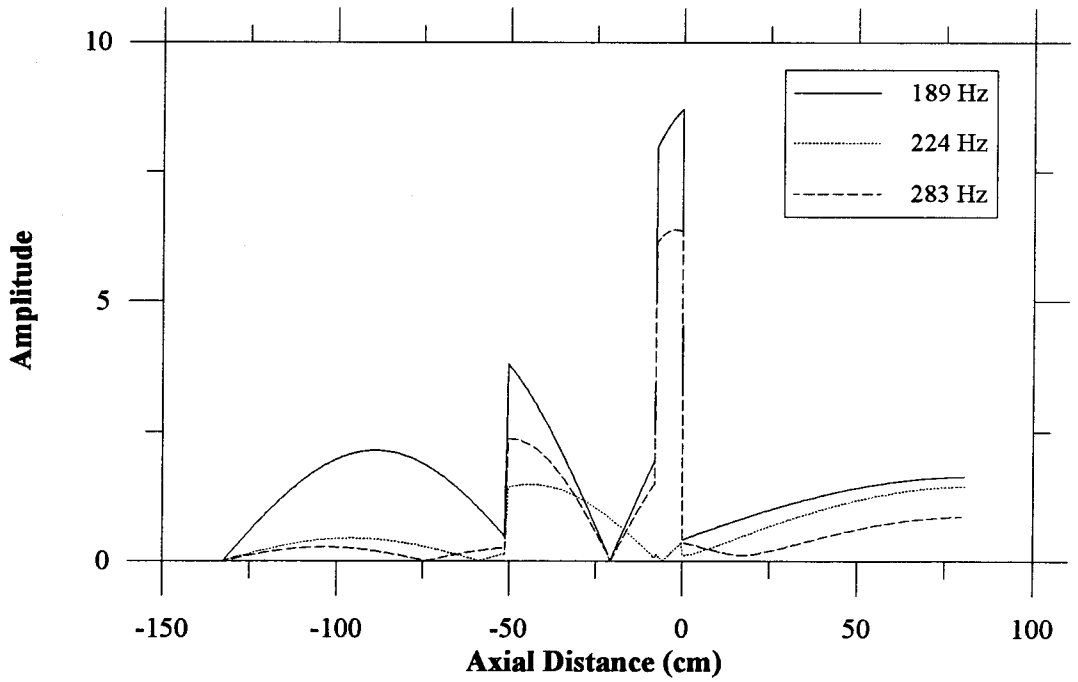

Figure 4.6b: Velocity mode shapes for 5.08 cm duct.

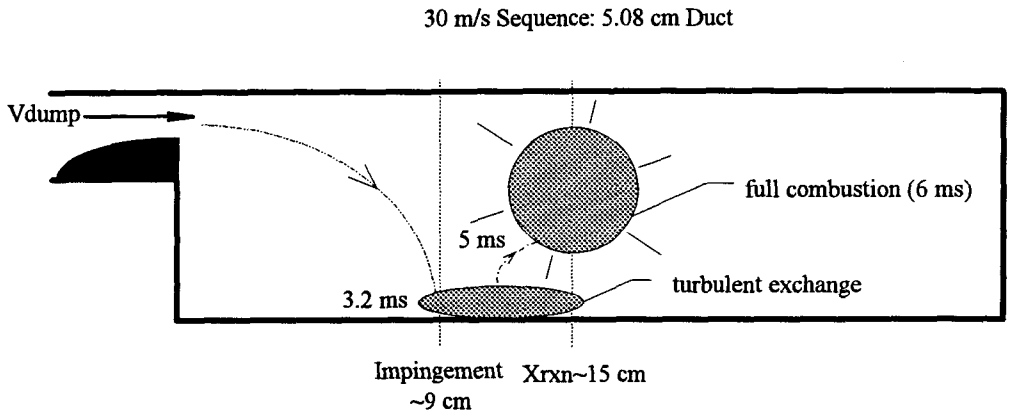

Figure 4.7: Typical burning sequence for a structure (30 m/s, 5.08 cm duct).

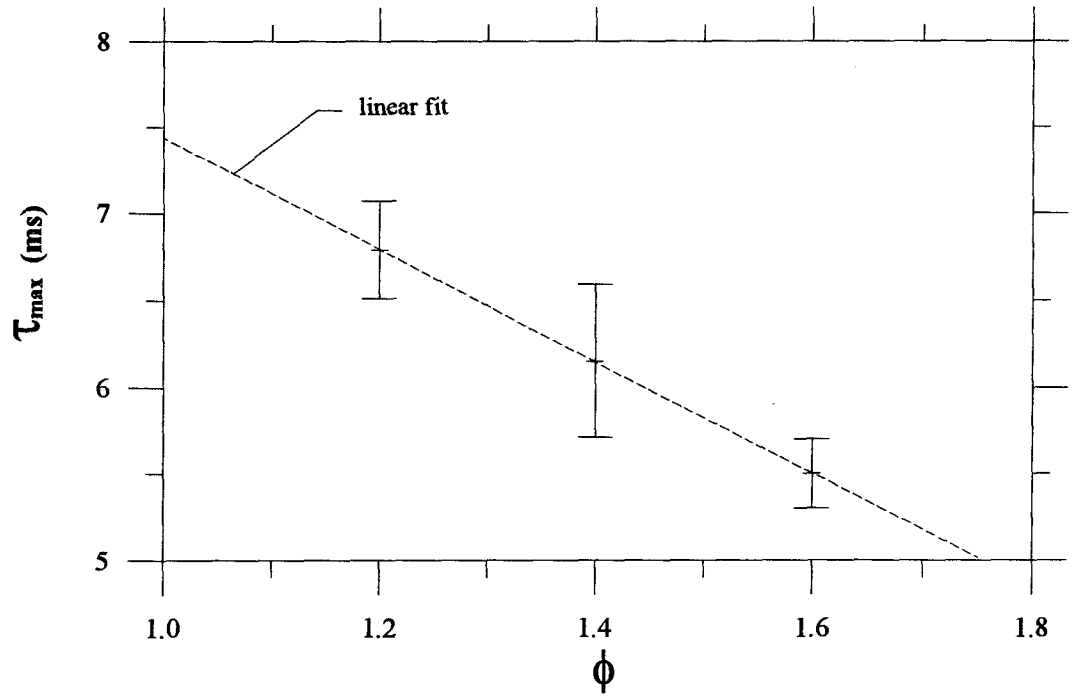

Figure 4.8: τ_{max} variation through a 30 m/s transition: 5.08 cm, 234 to 188 Hz.

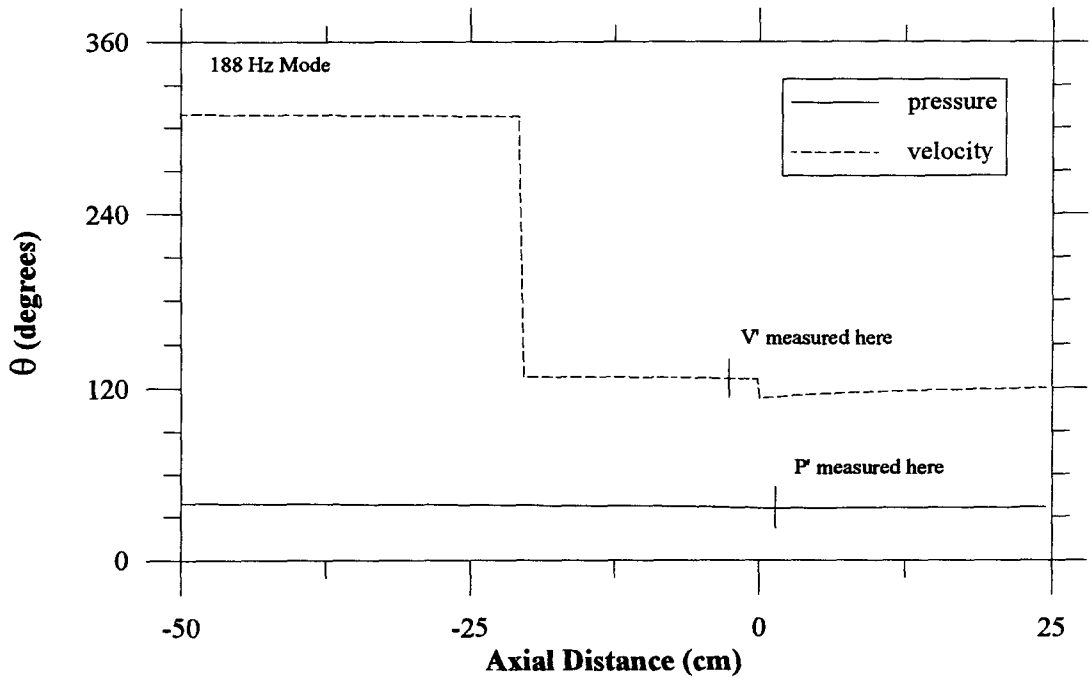

Figure 4.9a: Pressure and velocity phase angles for 188 Hz mode (linear acoustic model).

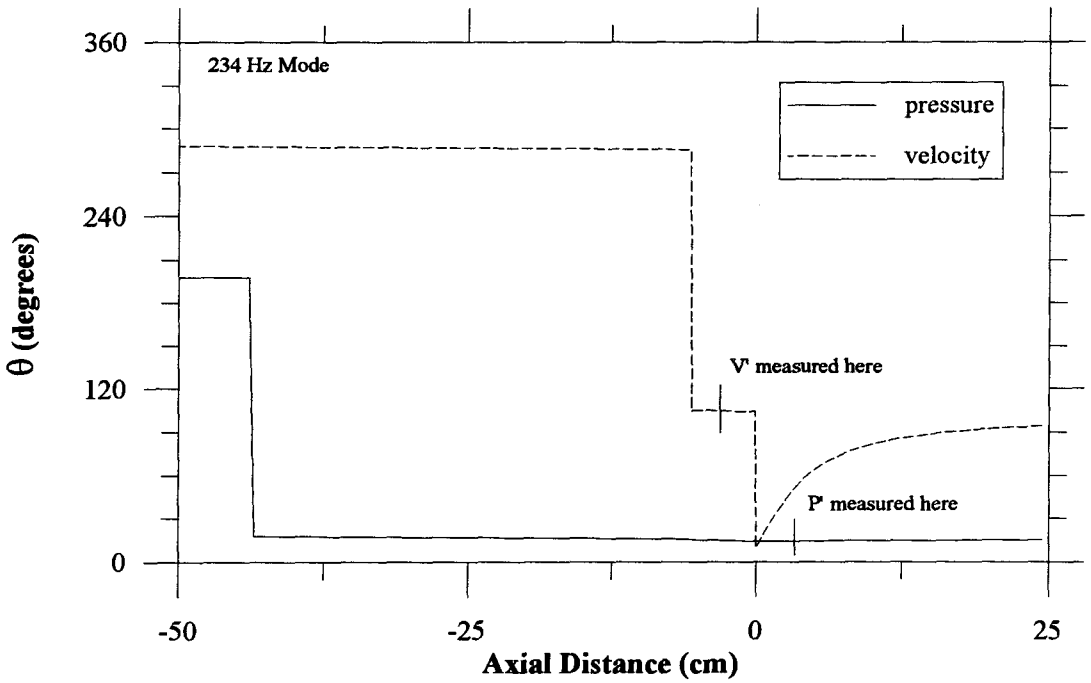

Figure 4.9b: Pressure and velocity phase angles for 234 Hz mode (linear acoustic model).

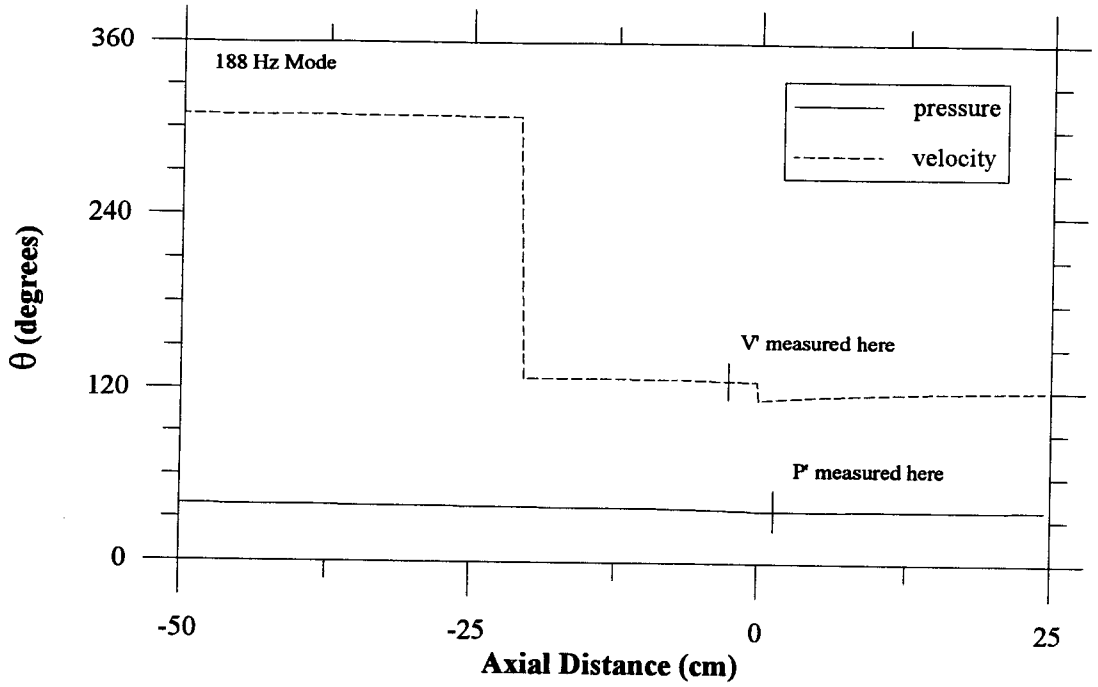

Figure 4.10: Phase angle dependency with combustor sound speed (linear acoustic model).

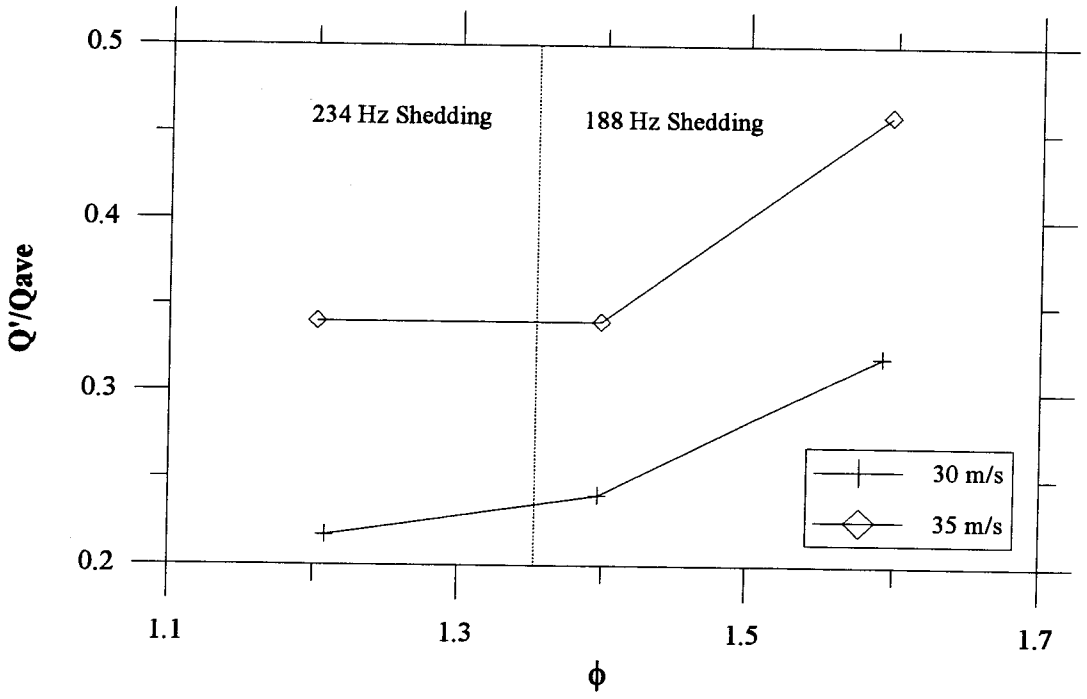

Figure 4.11: Heat flux increases through a transition.

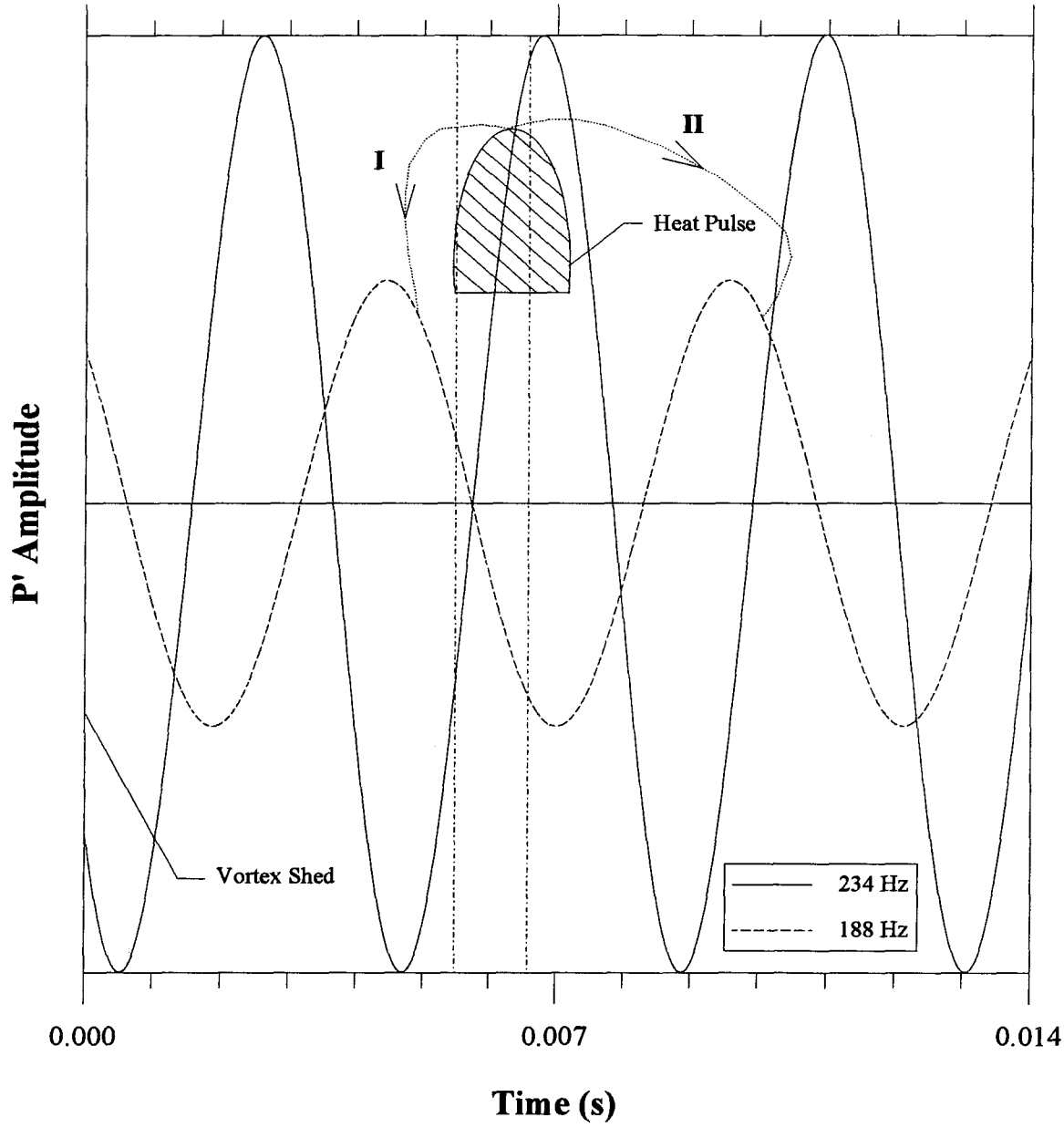

Figure 4.12: Pictorial sketch of mode transition at 30 m/s.

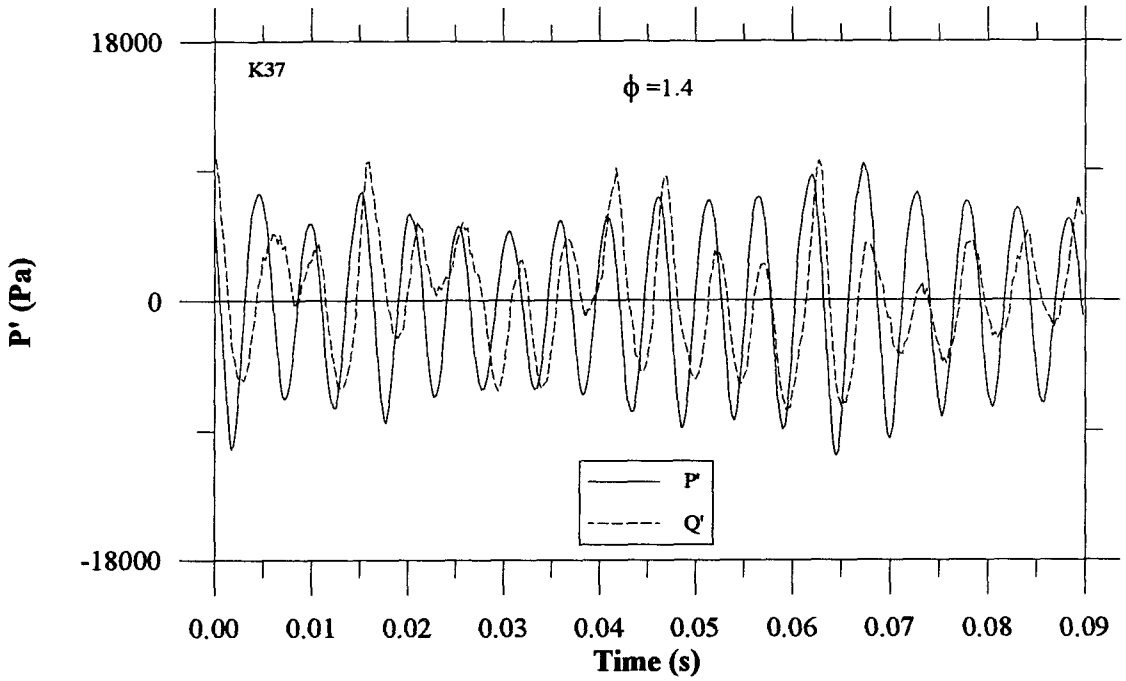

Figure 4.13a: Heat release and pressure traces for 5.08 cm duct, 35 m/s, $\phi = 1.4$.

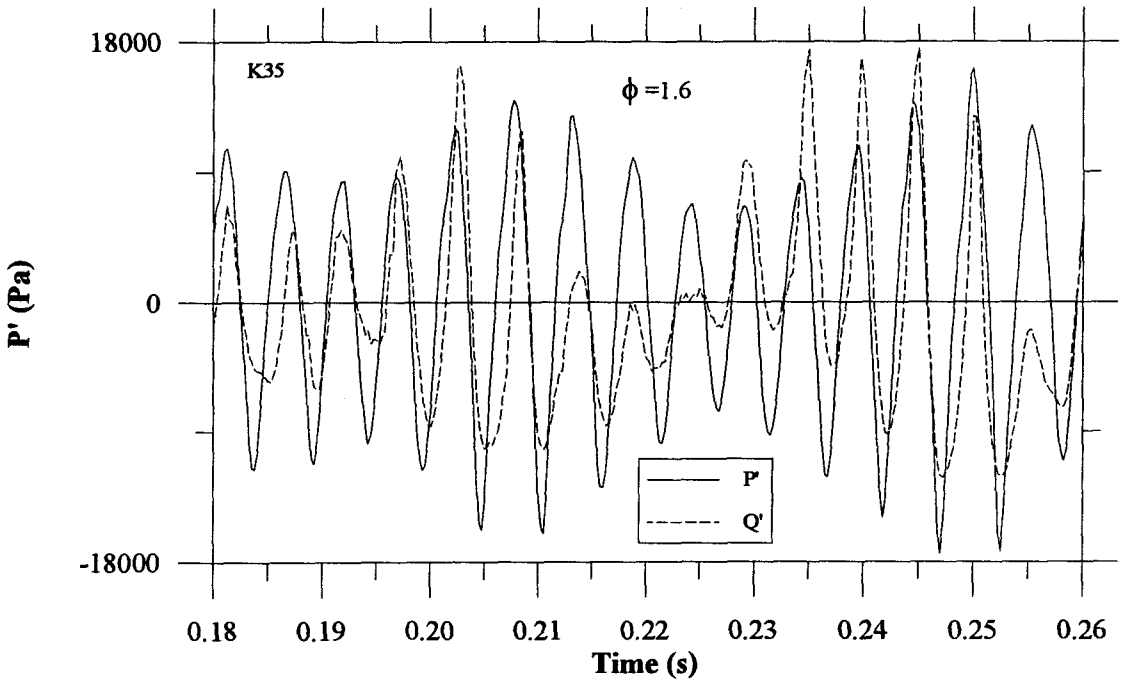

Figure 4.13b: Heat release and pressure traces for 5.08 cm duct, 35 m/s, $\phi = 1.6$.

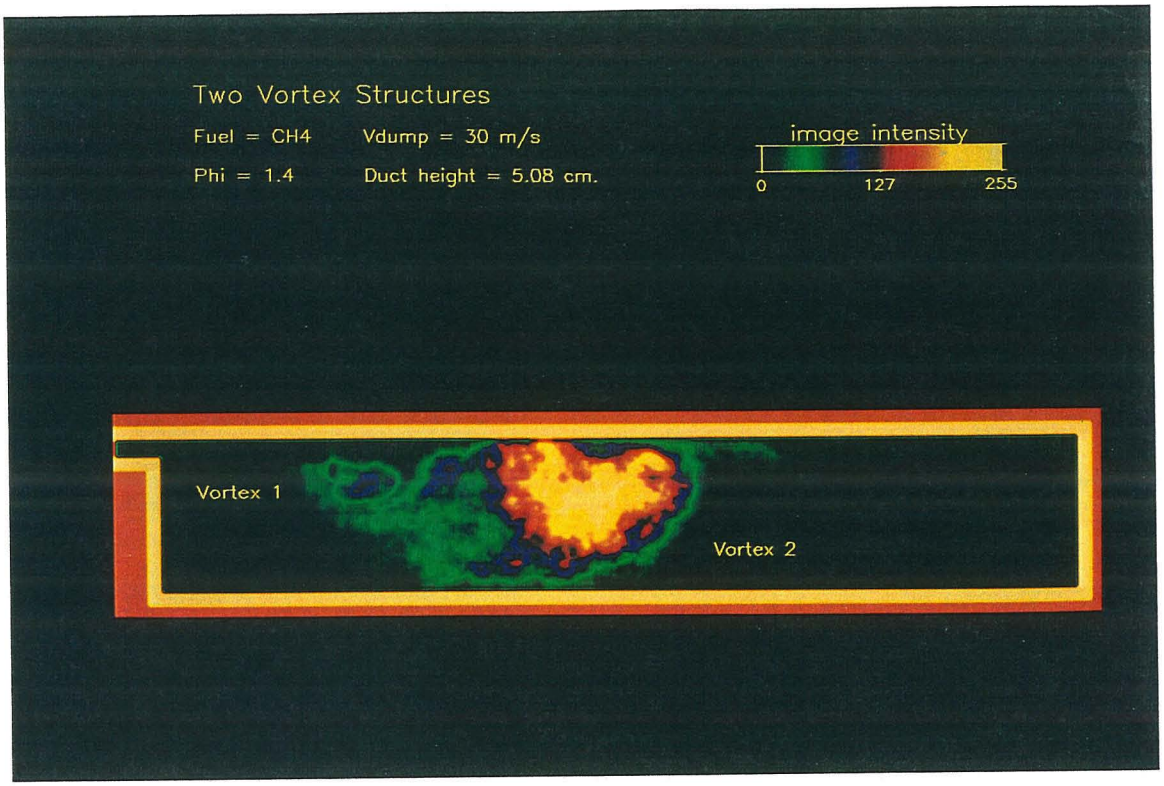

Figure 4.14a: CCD image of two closely spaced vortices.

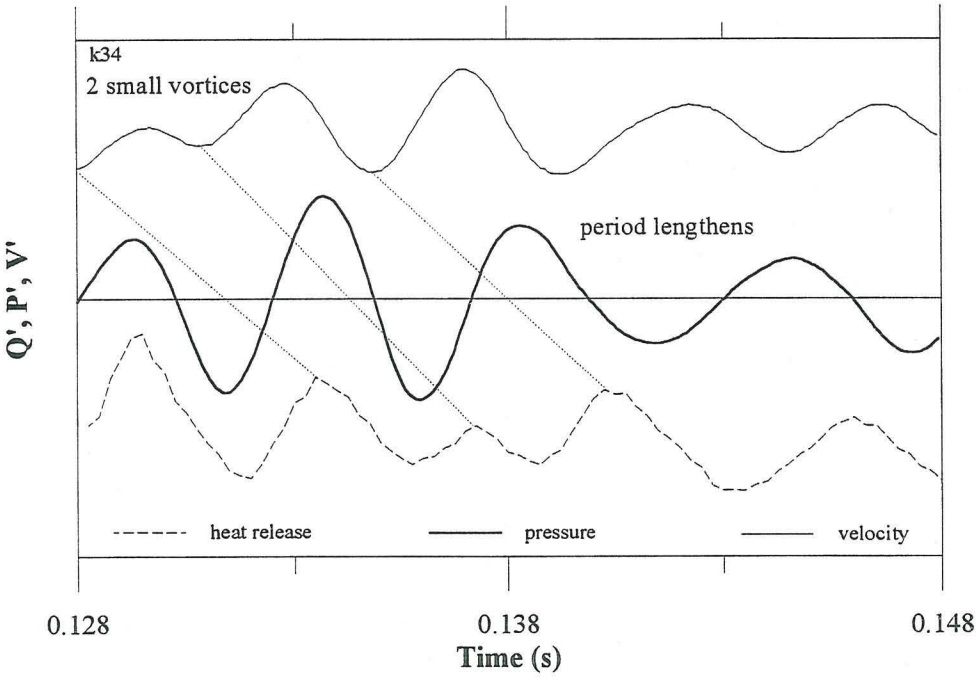

Figure 4.14b: Corresponding data traces: 5.08 cm duct, 30 m/s, $\phi = 1.4$.

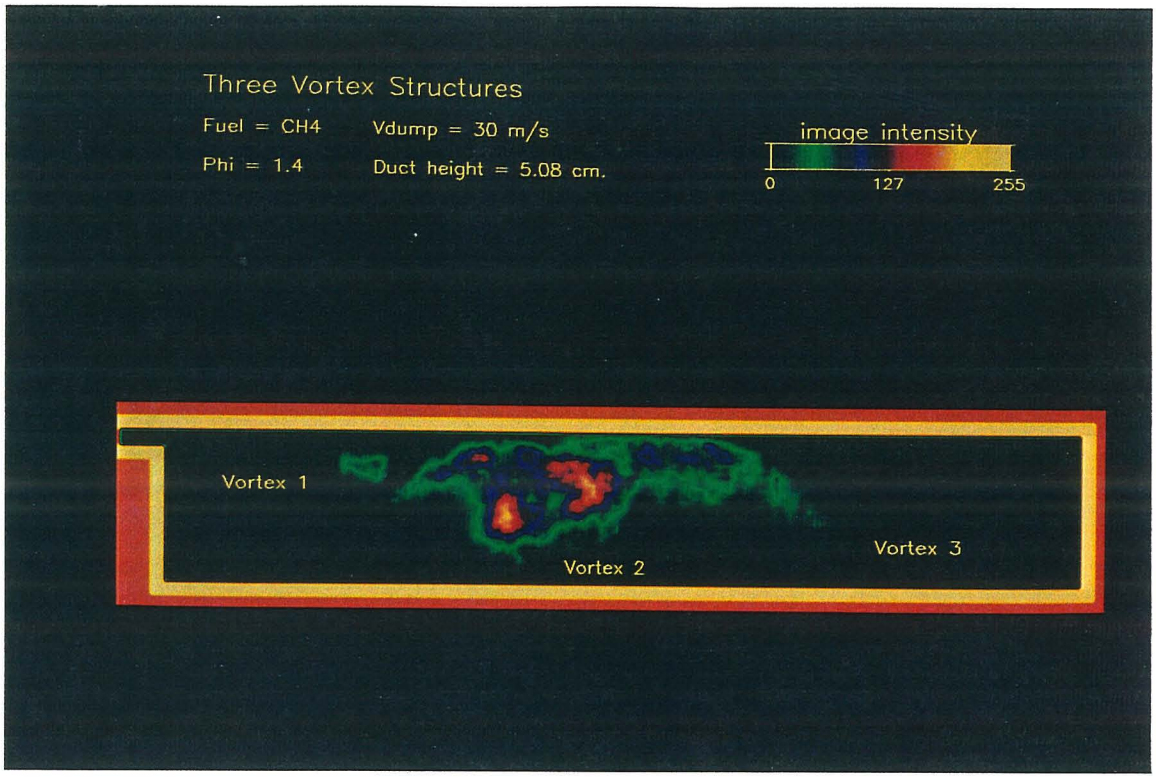

Figure 4.15a: CCD image of three closely spaced vortices.

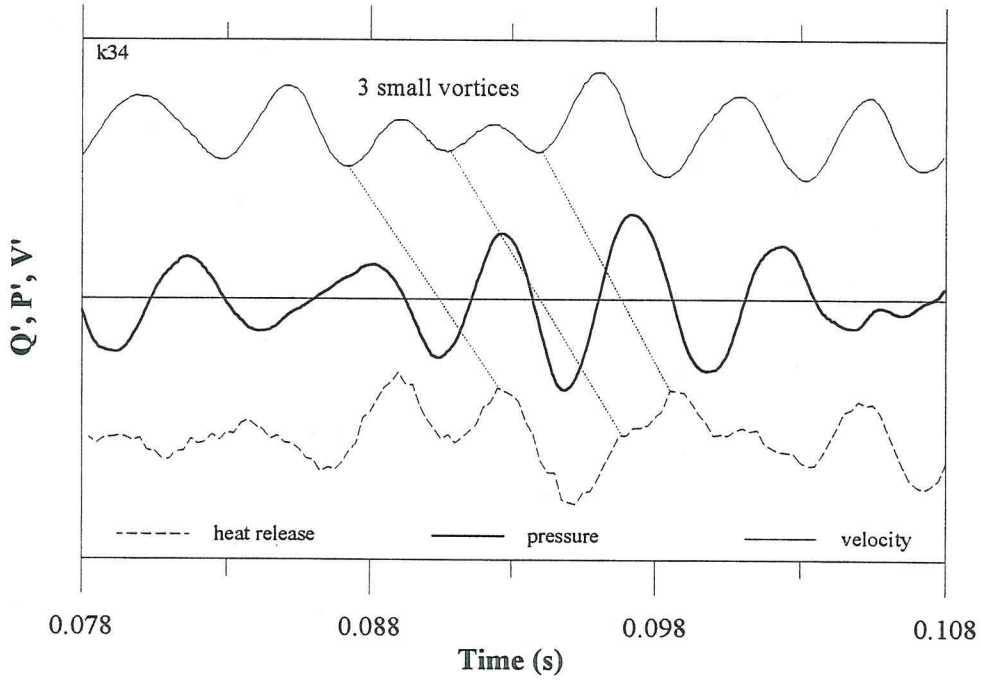

Figure 4.15b: Corresponding data traces: 5.08 cm duct, 30 m/s, $\phi = 1.4$.

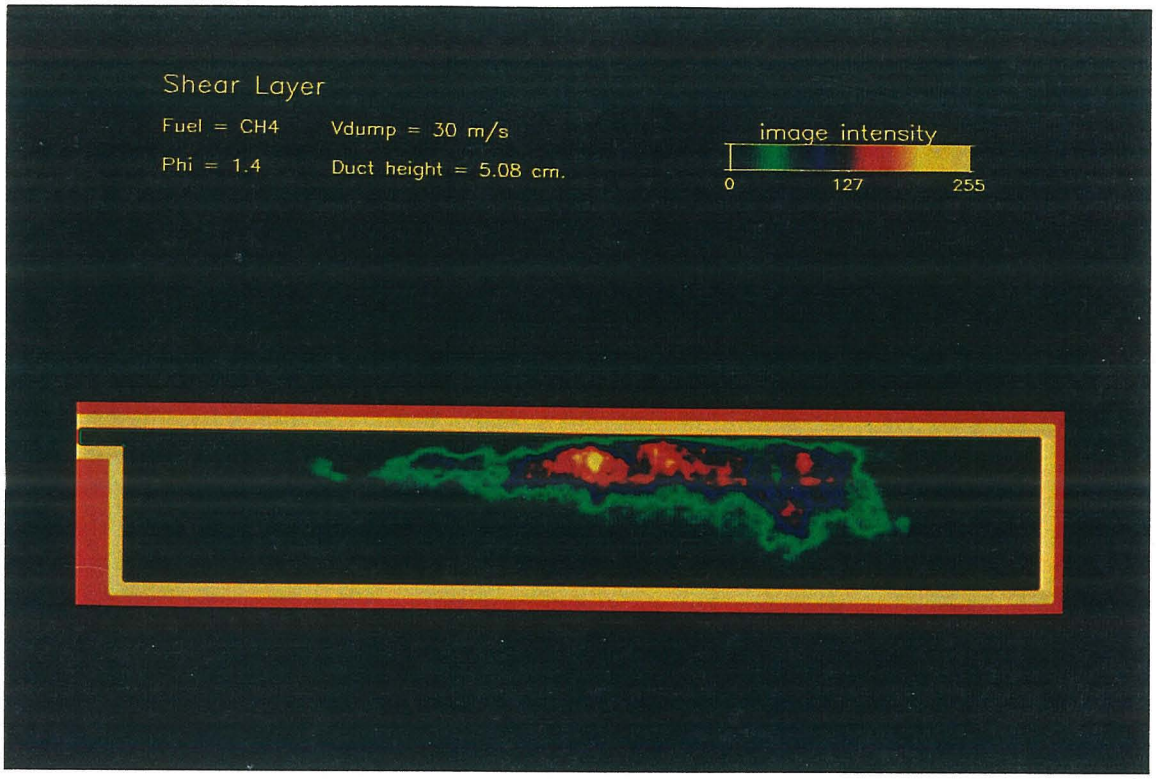

Figure 4.16a: CCD image of shear layer.

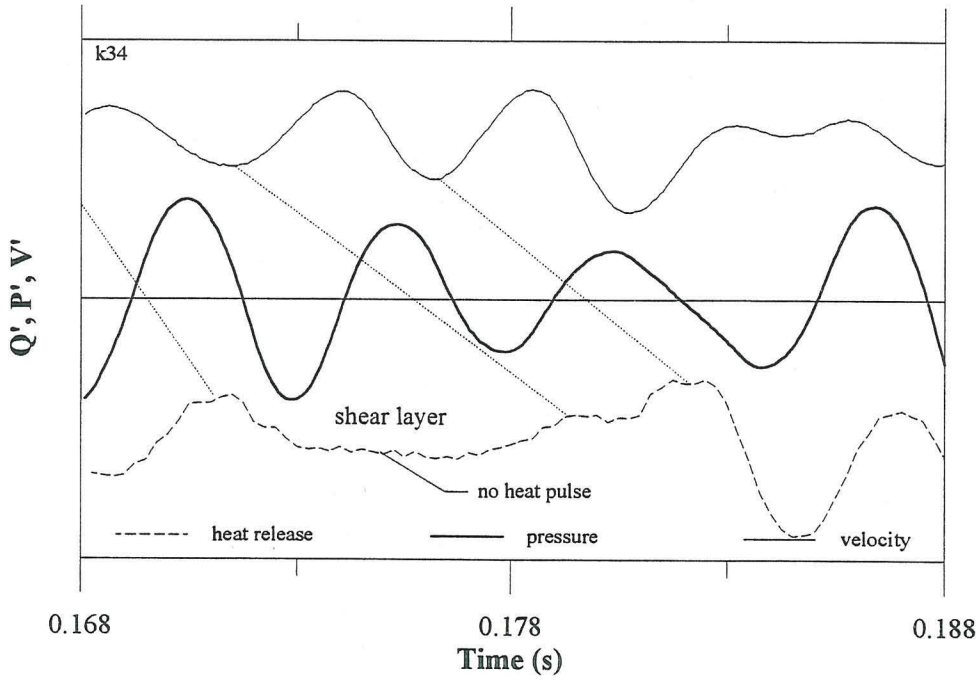

Figure 4.16b: Corresponding data traces: 5.08 cm duct, 30 m/s, $\phi = 1.4$.

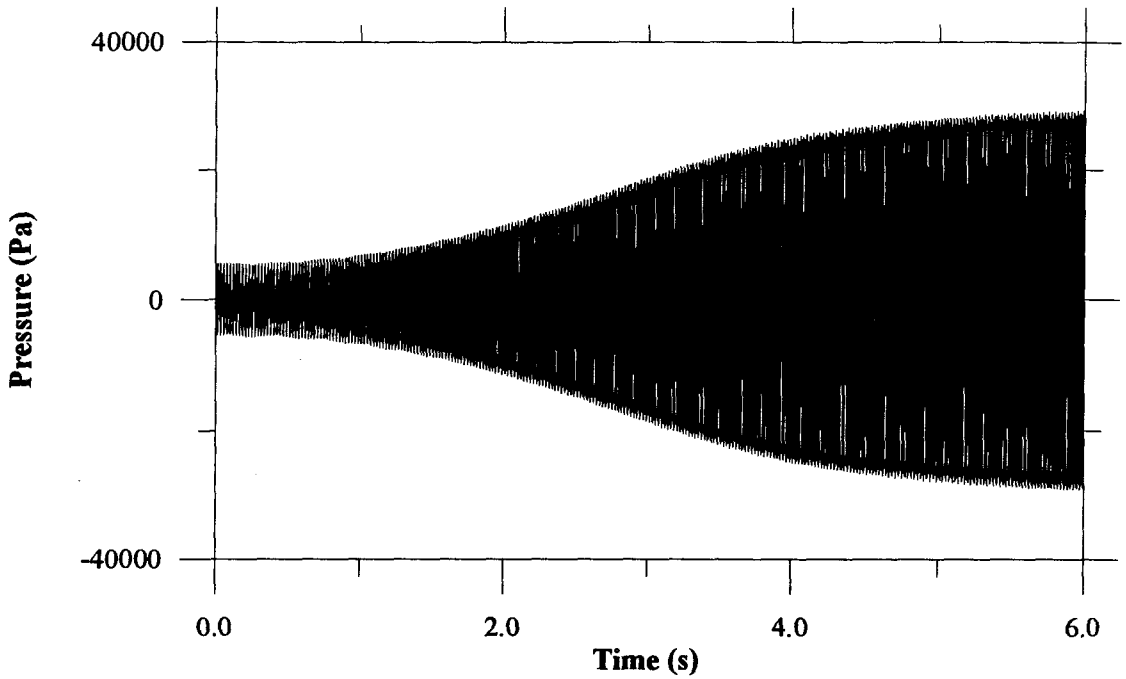

Figure 4.17: Convergence of numerical model Type I.

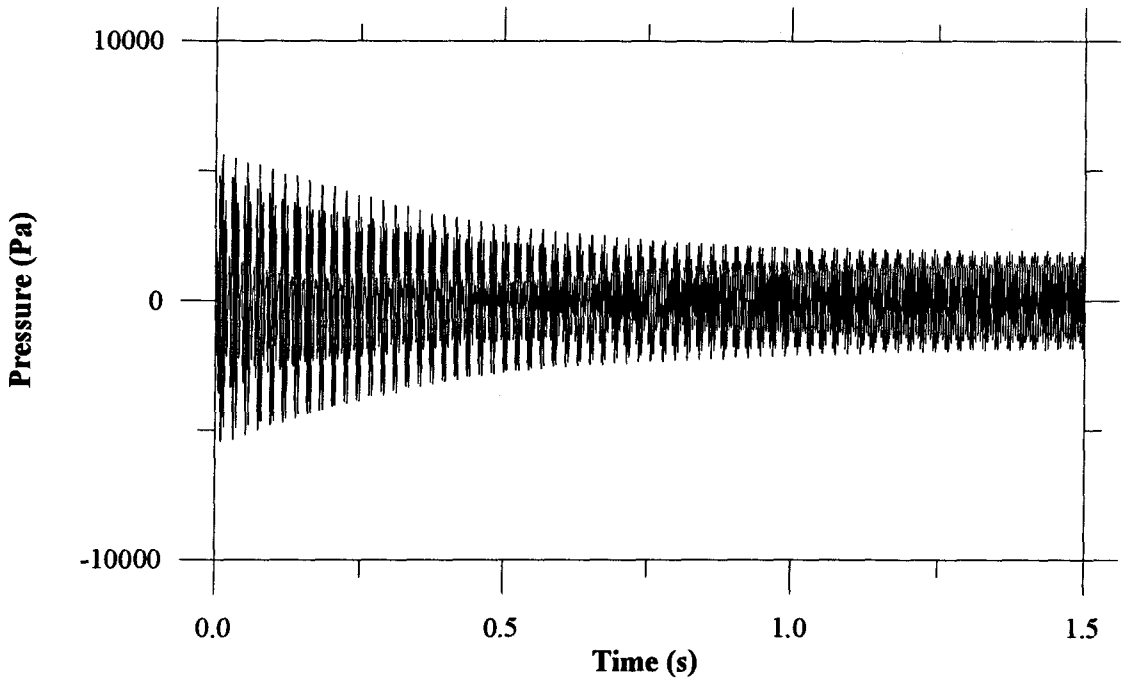

Figure 4.18: Convergence of numerical model Type II.

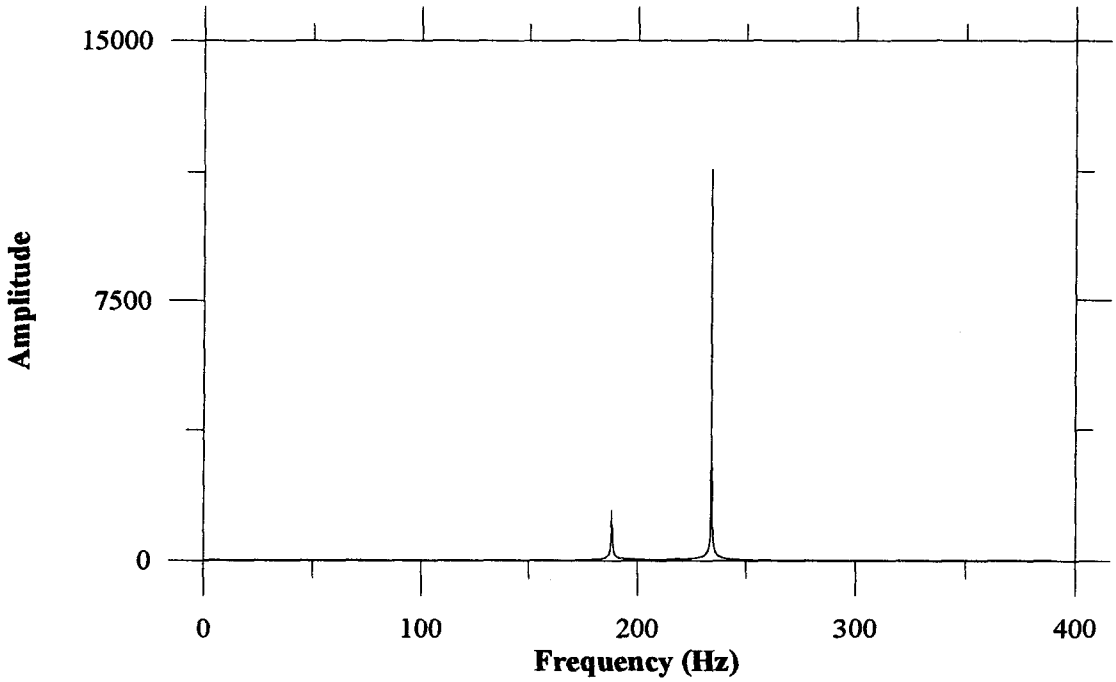

a) Numerical pressure FFT.

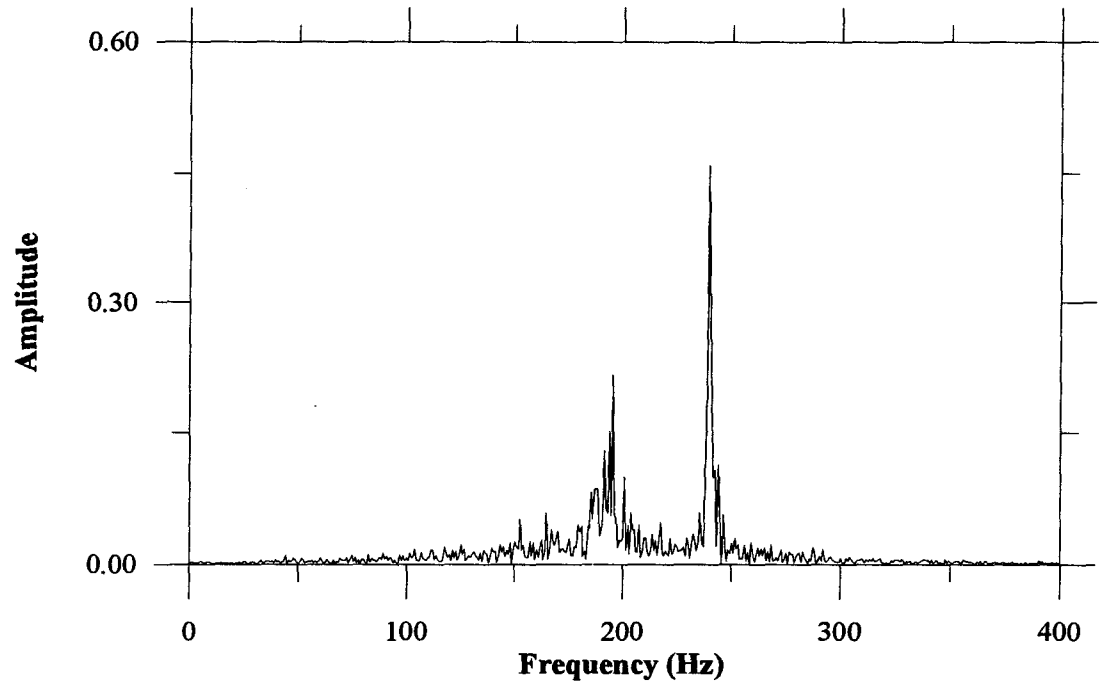

b) Experimental pressure FFT.

Figure 4.19: Comparison of numerical and experimental, 234 Hz pressure FFTs for a $V_{dump} = 30 m/s$ (b=0.004); Type II.

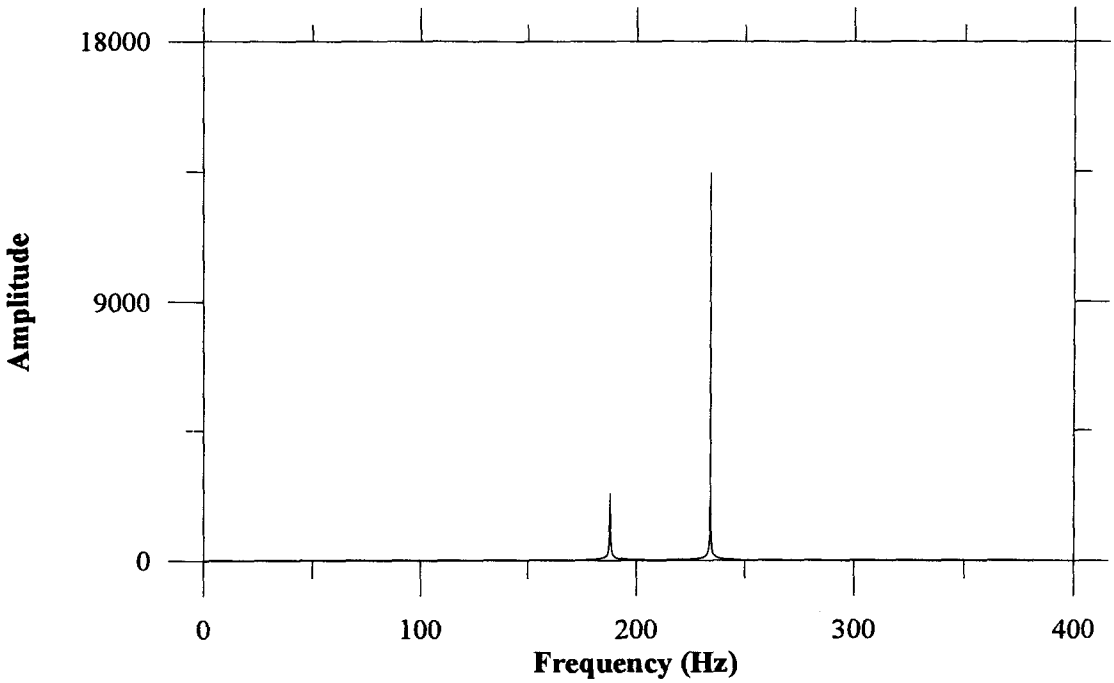

a) Numerical pressure FFT.

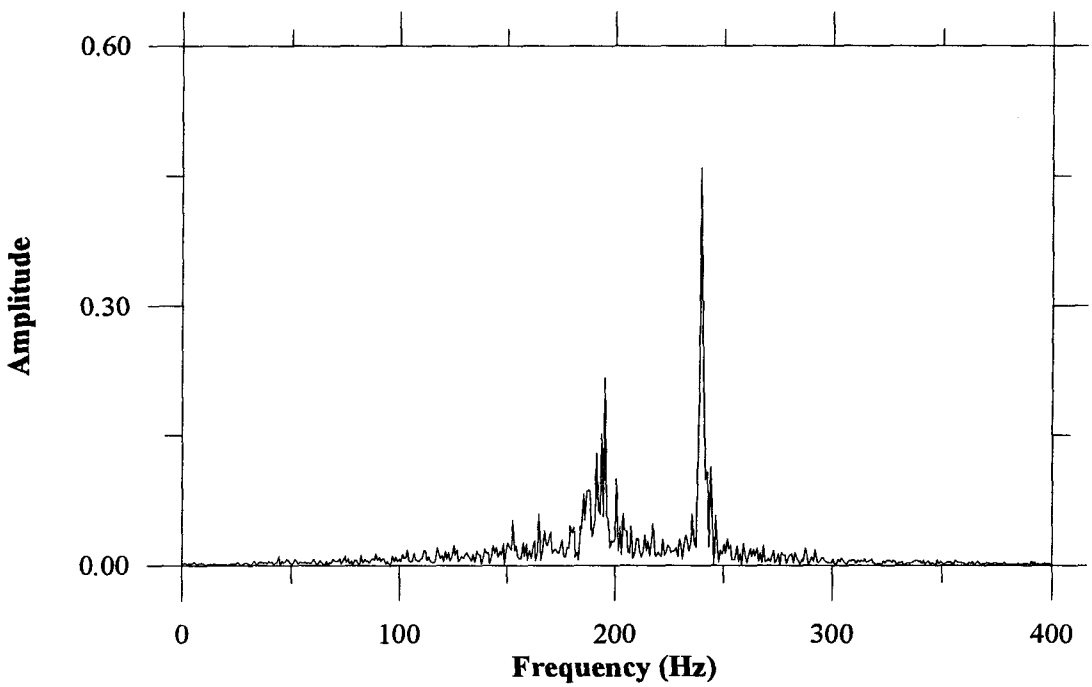

b) Experimental pressure FFT.

Figure 4.20: Comparison of numerical and experimental, 234 Hz pressure FFTs for a $V_{dump} = 30 m/s$ (b=0.0072); Type I.

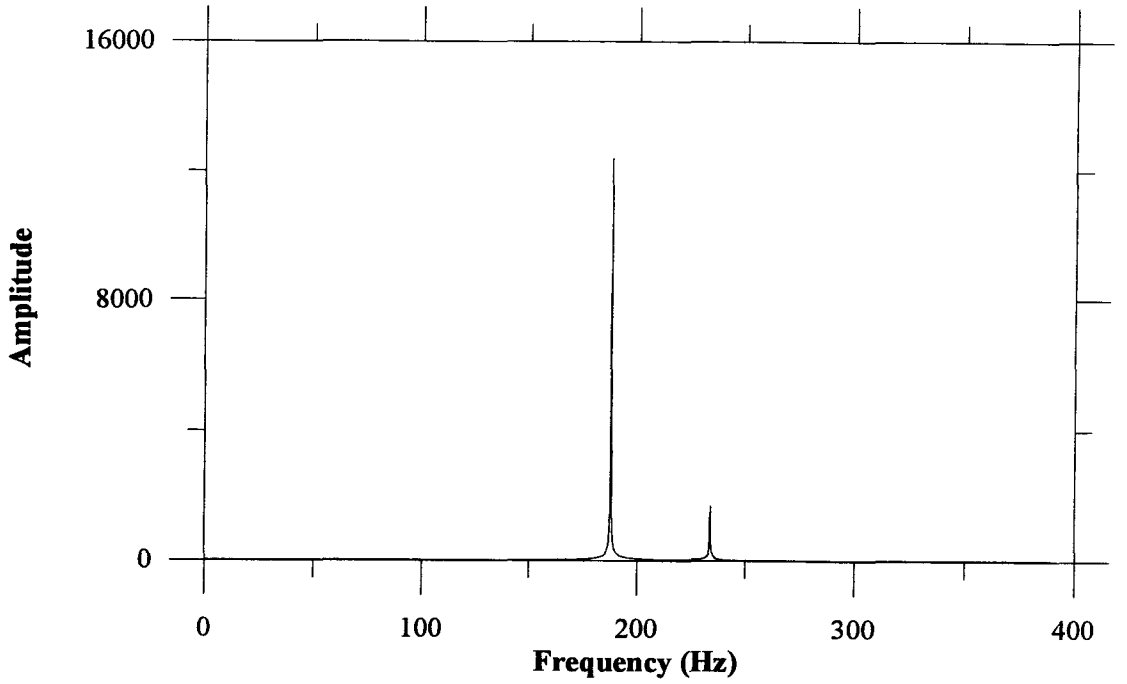

a) Numerical pressure FFT.

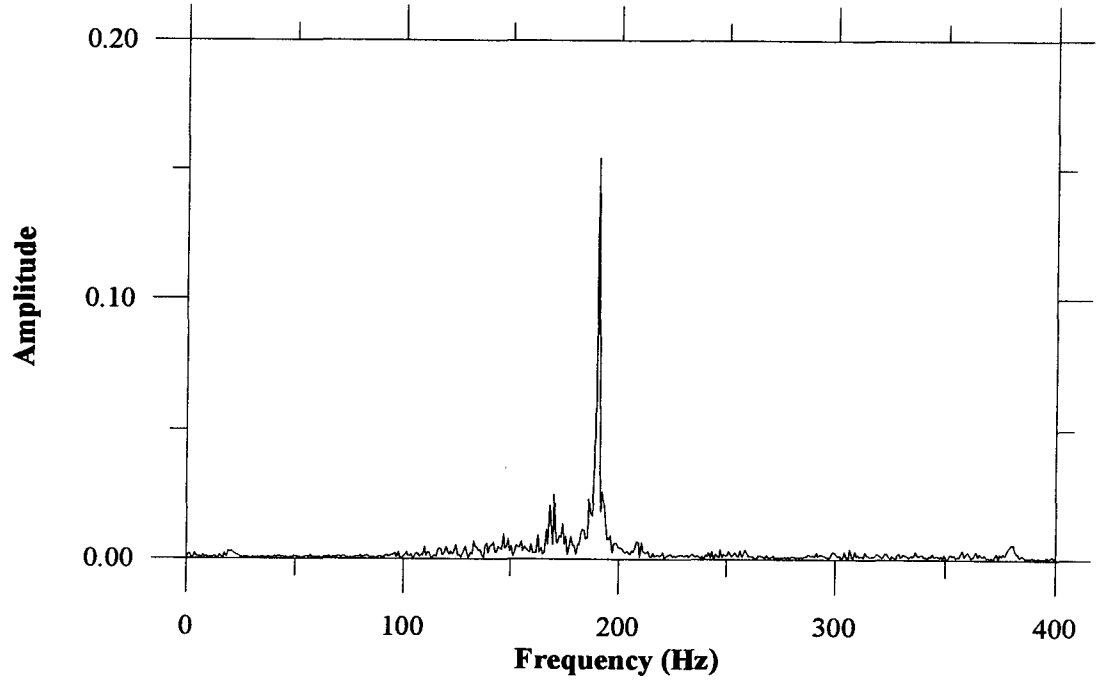

b) Experimental pressure FFT.

Figure 4.21: Comparison of numerical and experimental, 188 Hz pressure FFTs for a $V_{dump} = 30 m/s$ (b=0.0057, m=0.0); Type II.

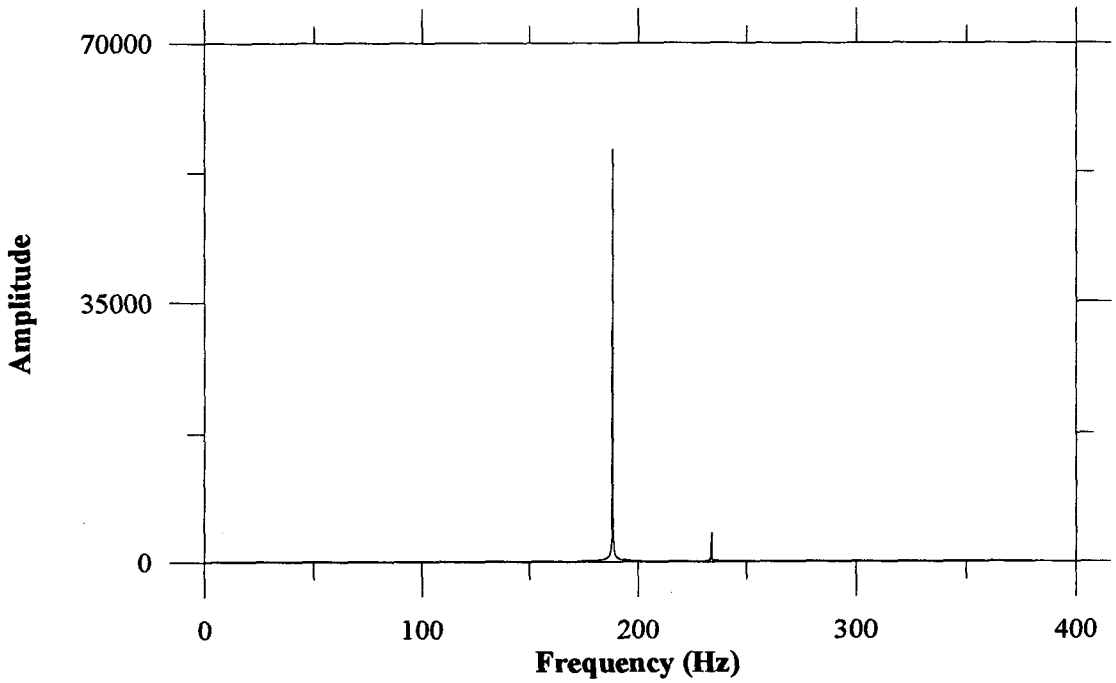

a) Numerical pressure FFT.

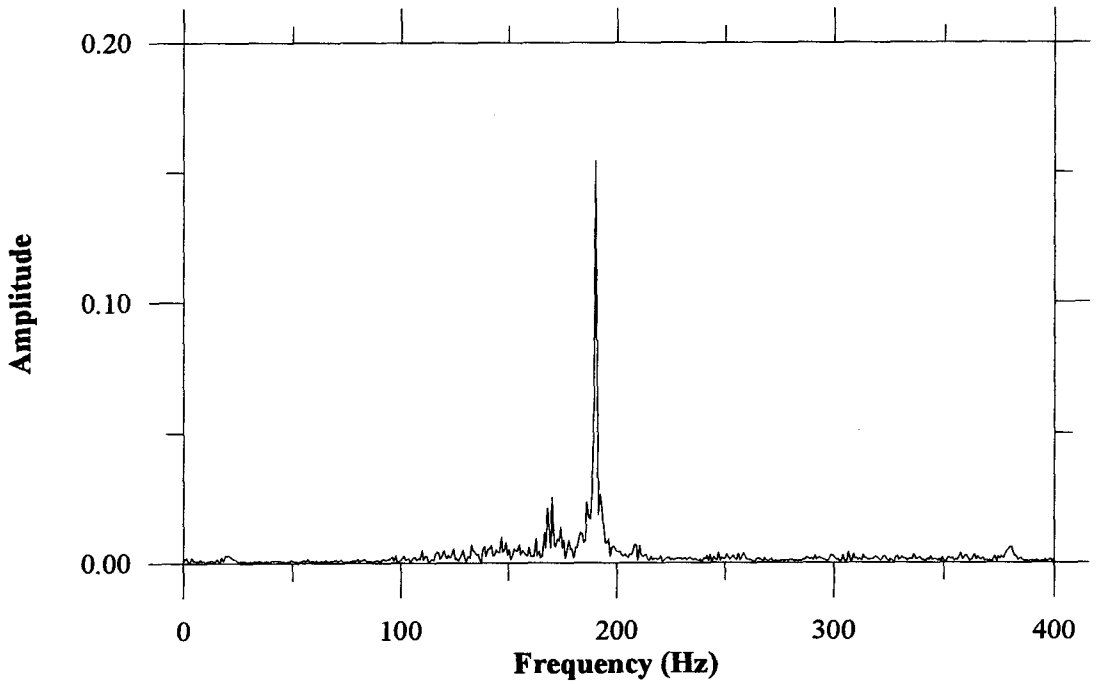

b) Experimental pressure FFT.

Figure 4.22: Comparison of numerical and experimental, 188 Hz pressure FFTs for a $V_{dump} = 30 m/s$ (b=0.0063); Type I.

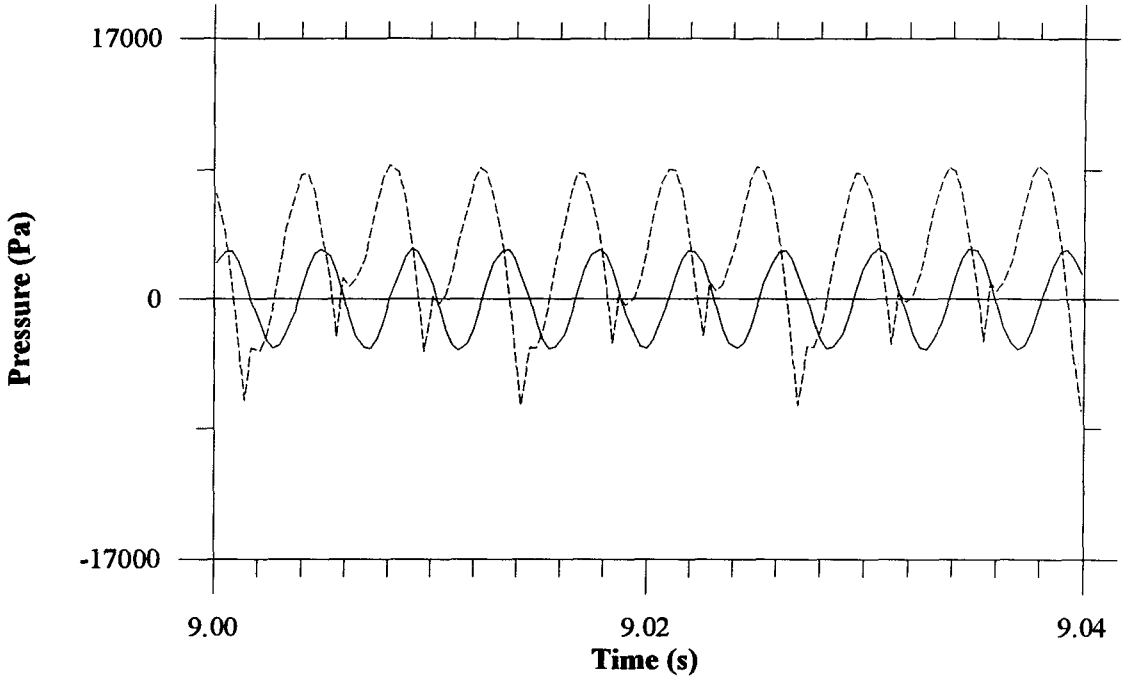

i) Sample pressure and heat release traces (solid = p', dashed = q').

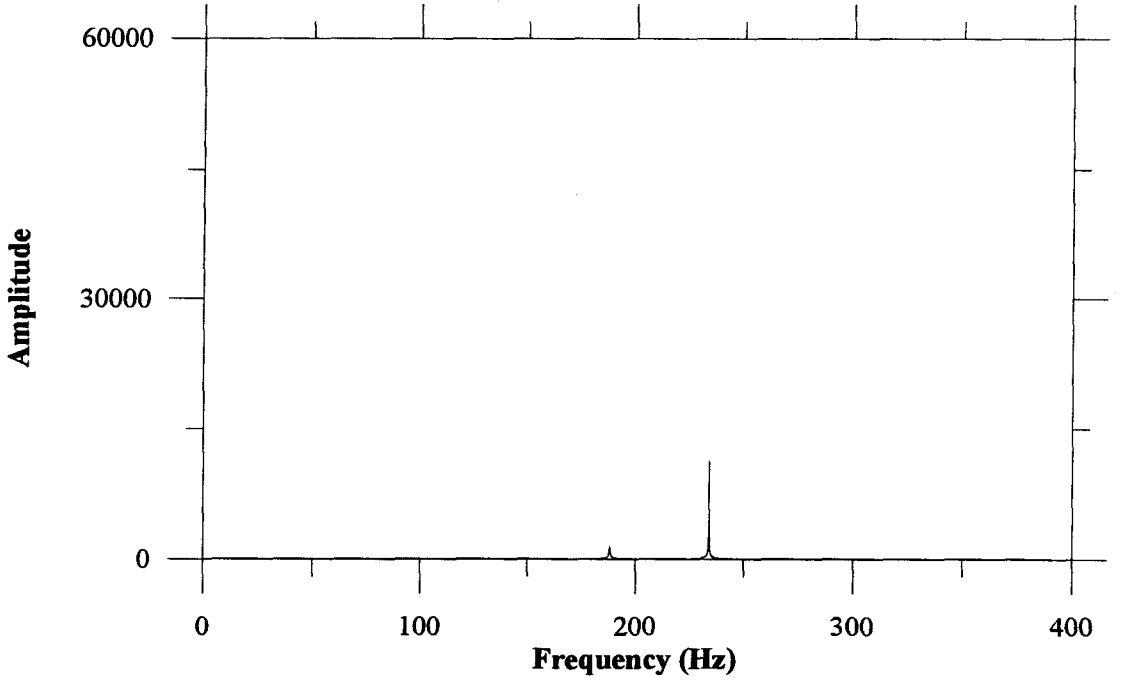

ii) Pressure FFT.

Figure 4.23a: 234 Hz mode: b=0.003, σ_a=0.05.

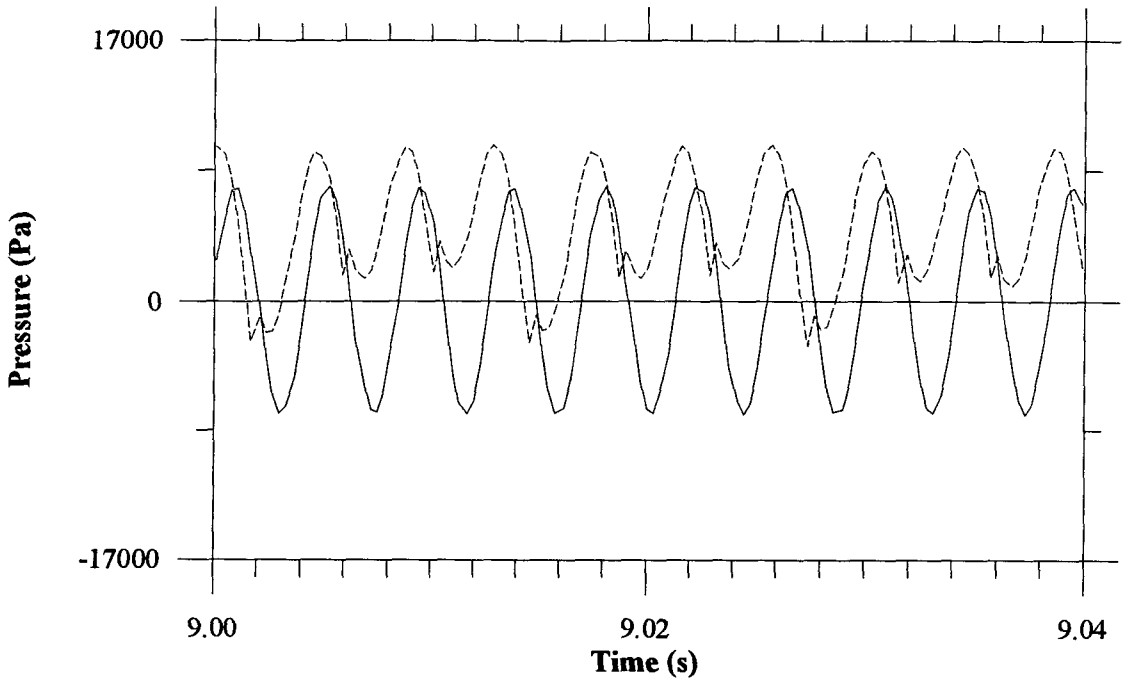

i) Sample pressure and heat release traces (solid = p', dashed = q').

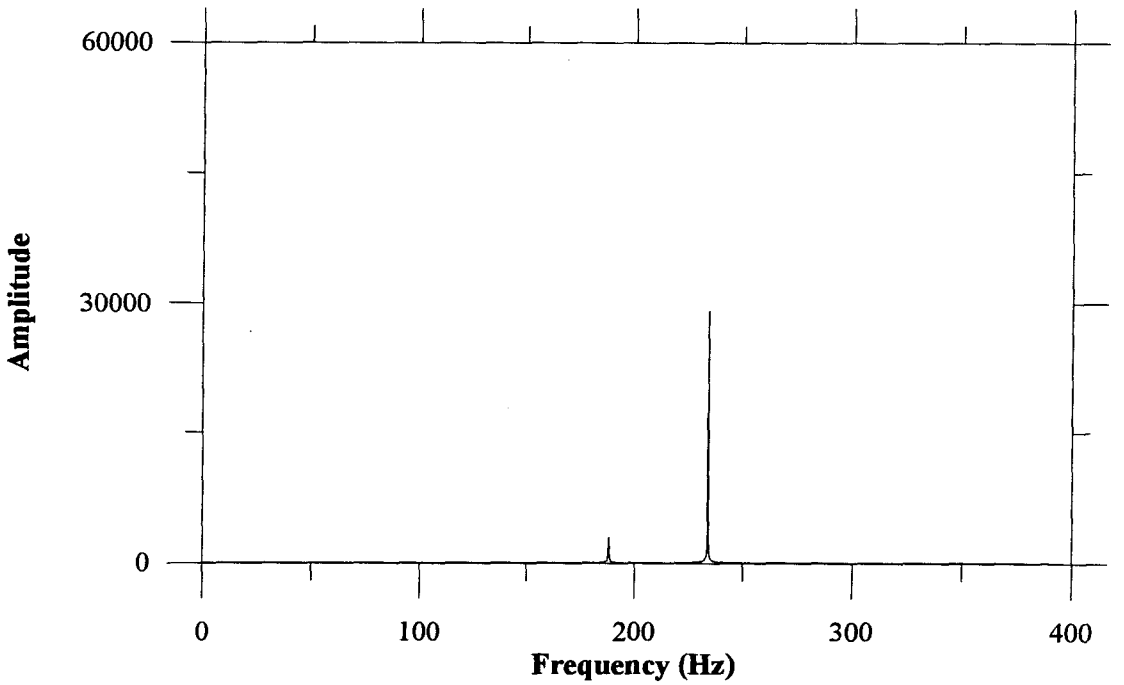

ii) Pressure FFT.

Figure 4.23b: 234 Hz mode: b=0.004, σ_a=0.05.

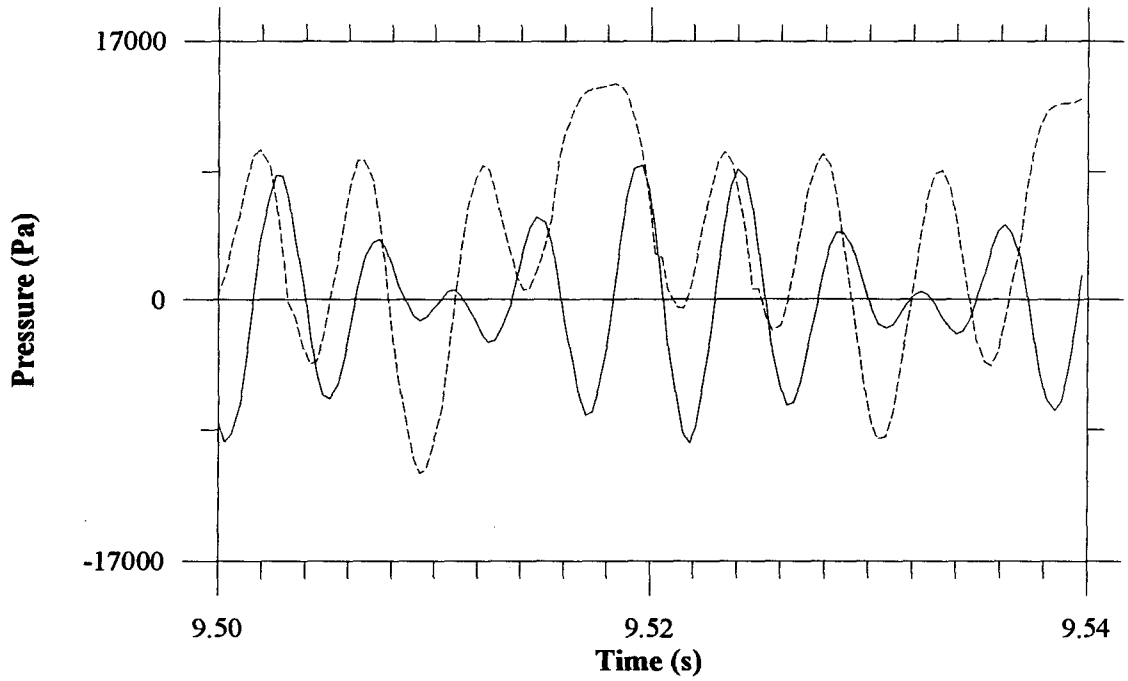

i) Sample pressure and heat release traces (solid = p', dashed = q').

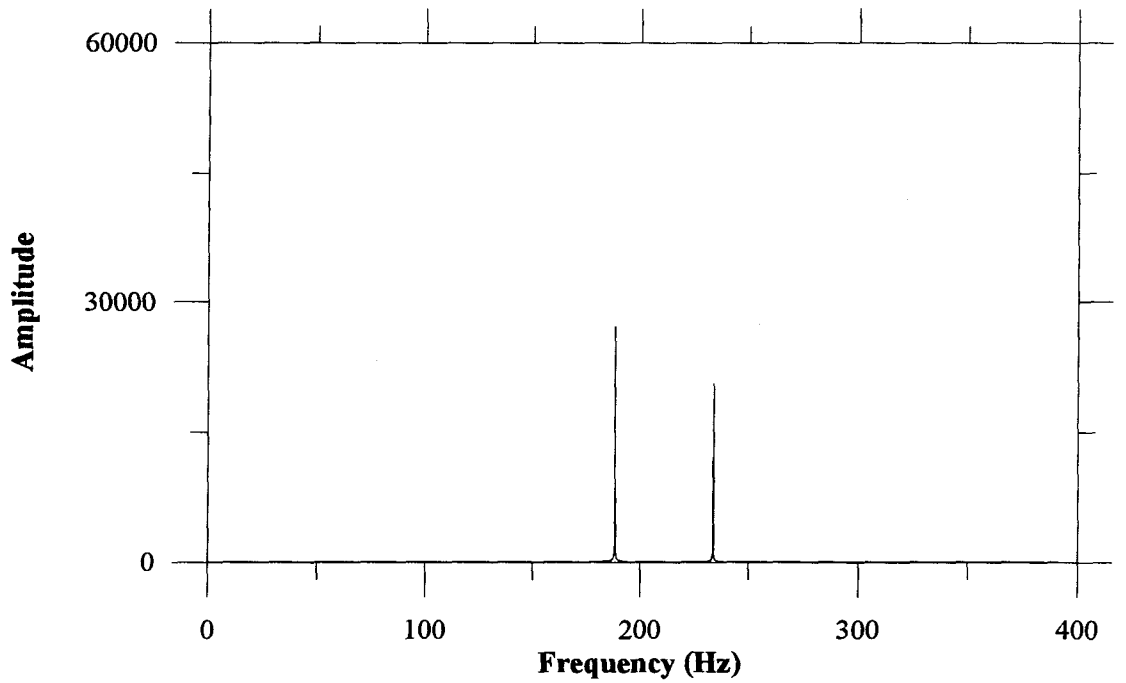

ii) Pressure FFT.

Figure 4.23c: Mode transition: b=0.0045, σ_a=0.05.

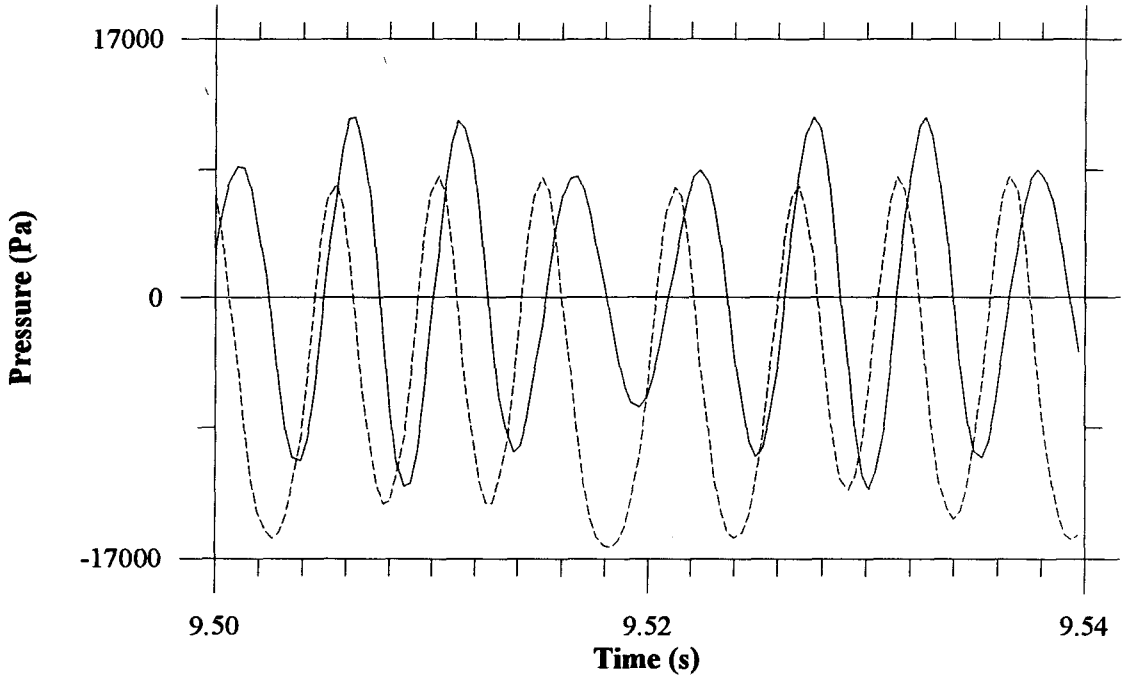

i) Sample pressure and heat release traces (solid = p', dashed = q').

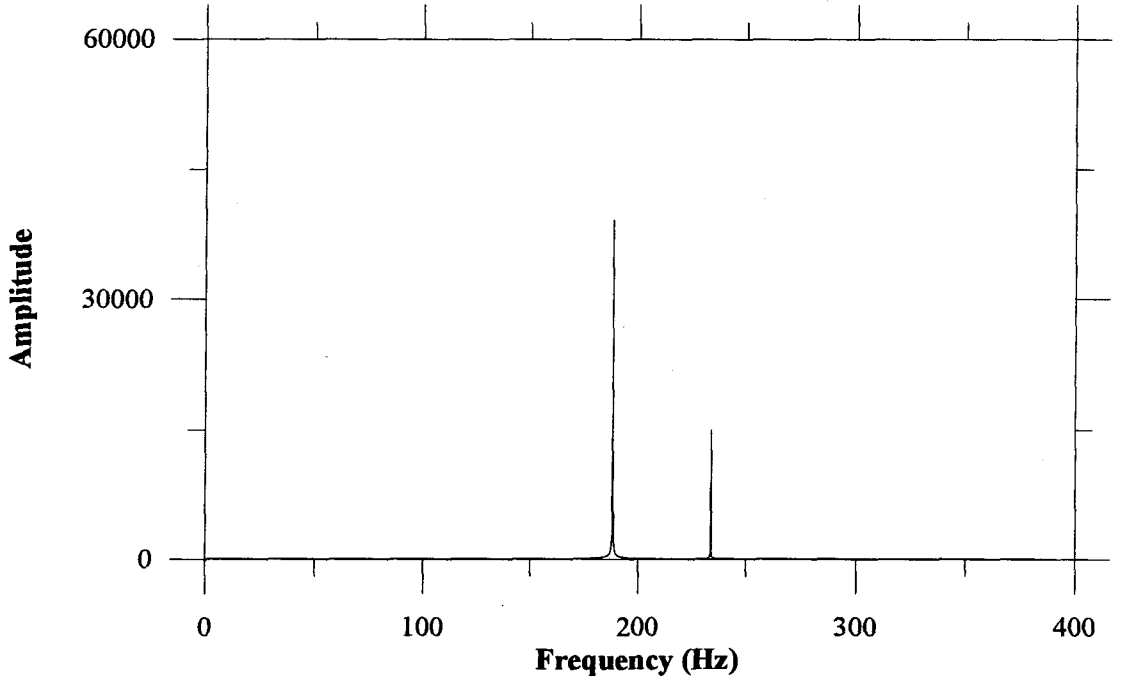

ii) Pressure FFT.

Figure 4.23d: 188 Hz mode: b=0.005, σ_a=0.05.

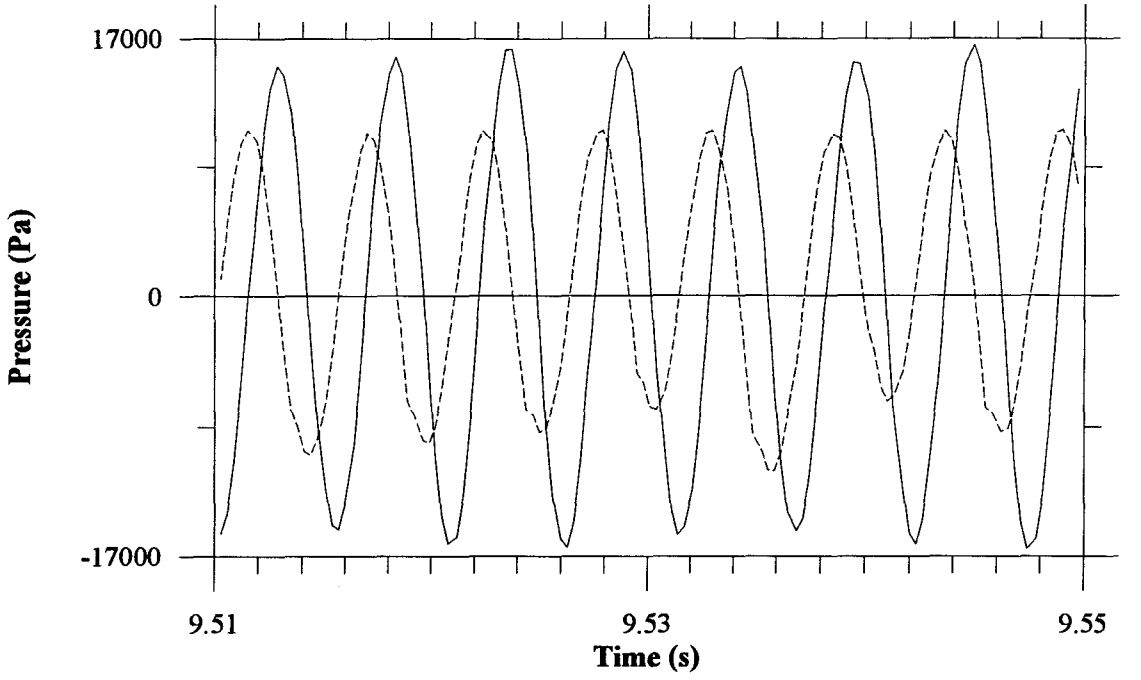

i) Sample pressure and heat release traces (solid = p', dashed = q').

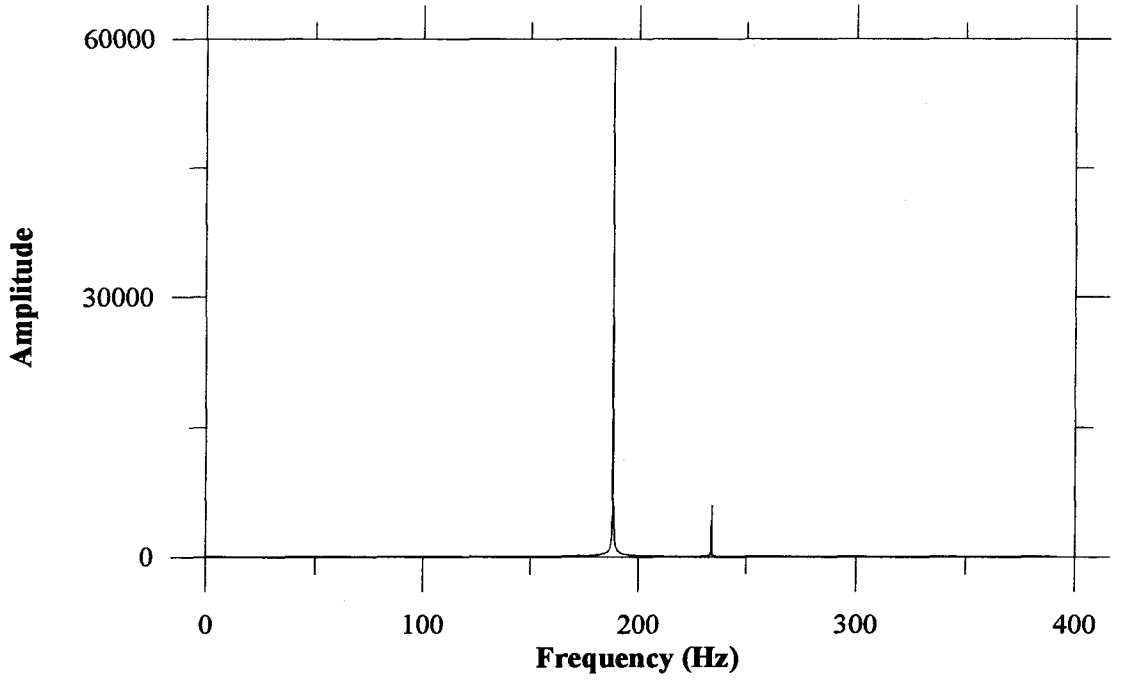

ii) Pressure FFT.

Figure 4.23e: 188 Hz mode: b=0.006, σ_a=0.05.

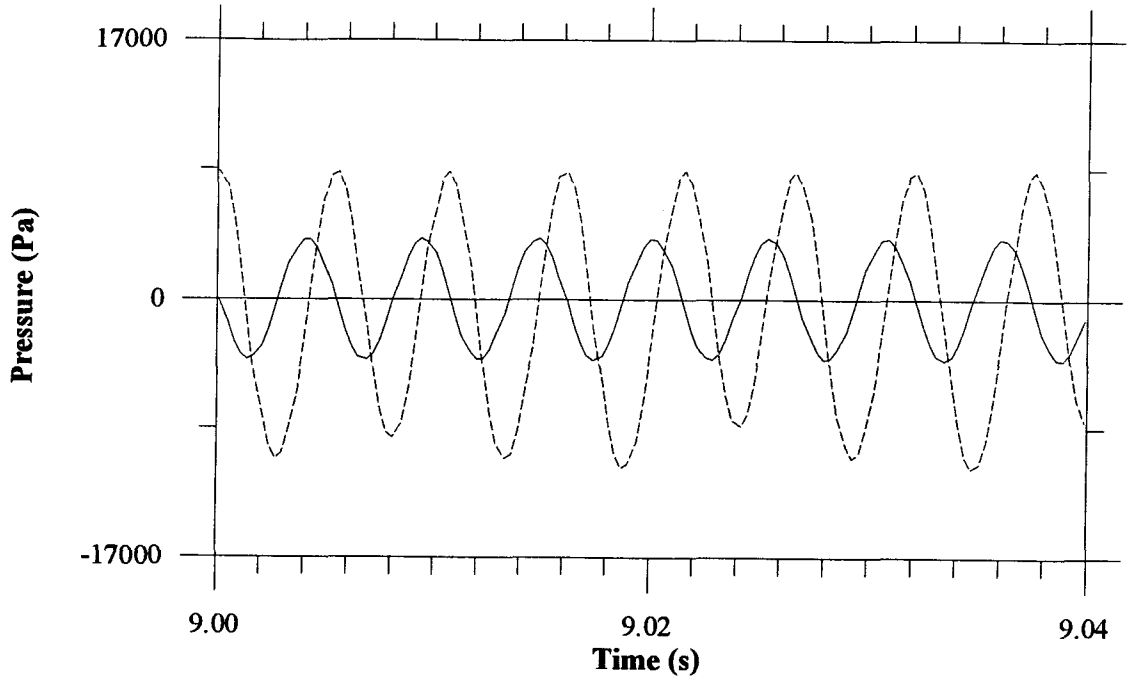

i) Sample pressure and heat release traces (solid = p', dashed = q').

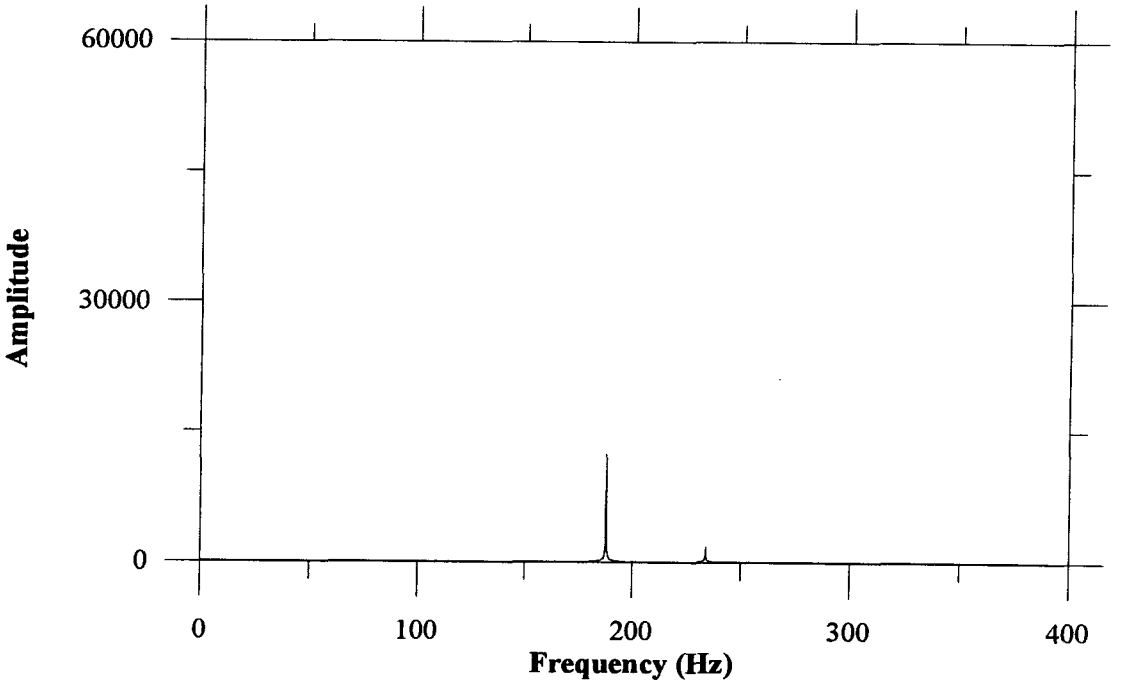

ii) Pressure FFT.

Figure 4.23f: 188 Hz mode: b=0.0057, m=0, σ_a=0.05.

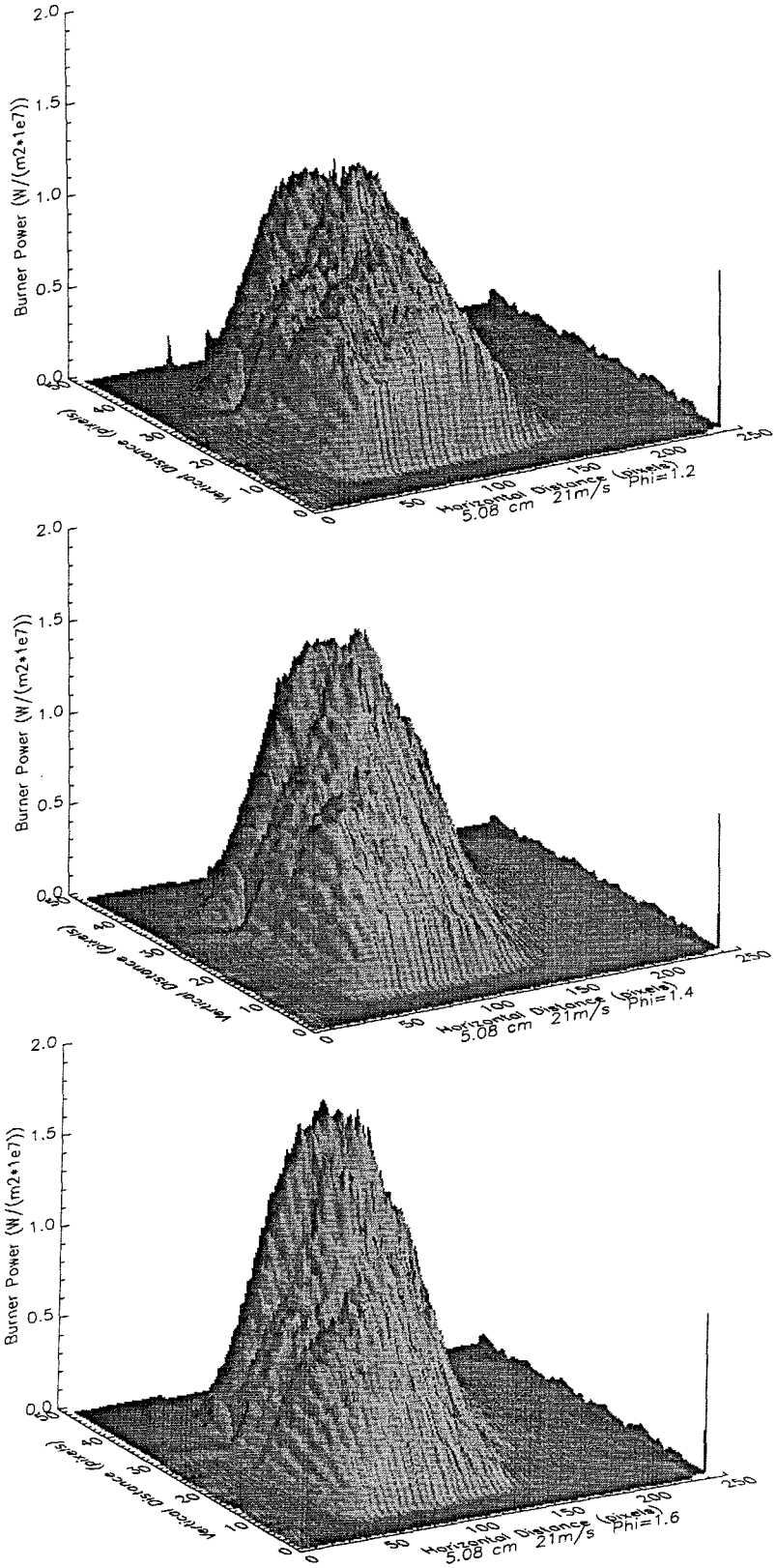

(a) $\phi = 1.2$

(b) $\phi = 1.4$

(c) $\phi = 1.6$

Figure 4.24: Average burner distribution shapes for mode transition: 5.08 cm duct, 21 m/s.

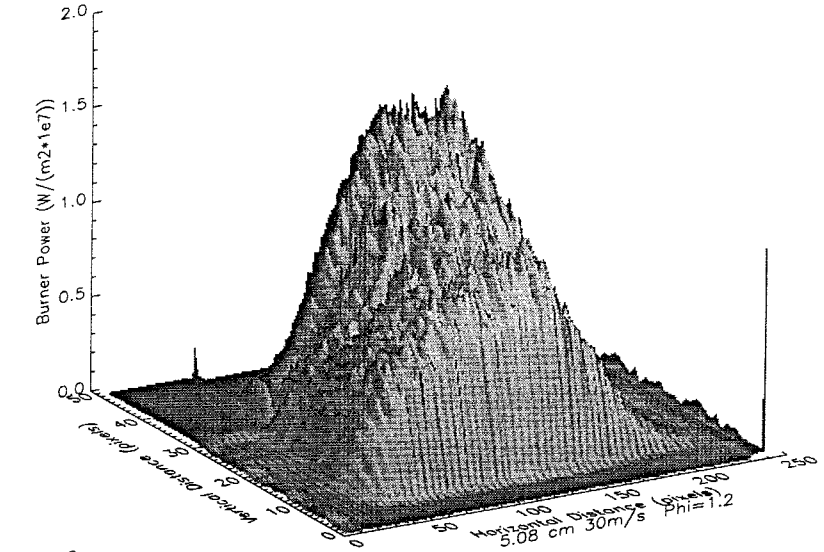

(a) $\phi = 1.2$

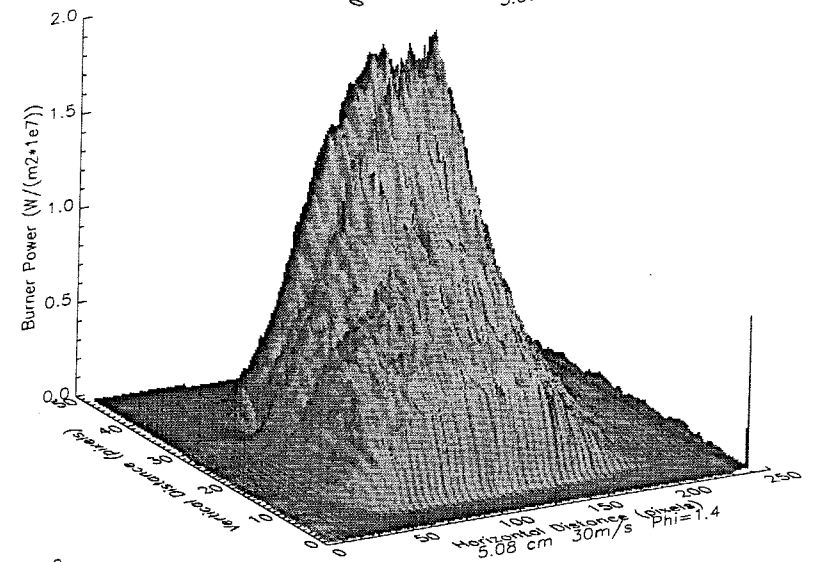

(b) $\phi = 1.4$

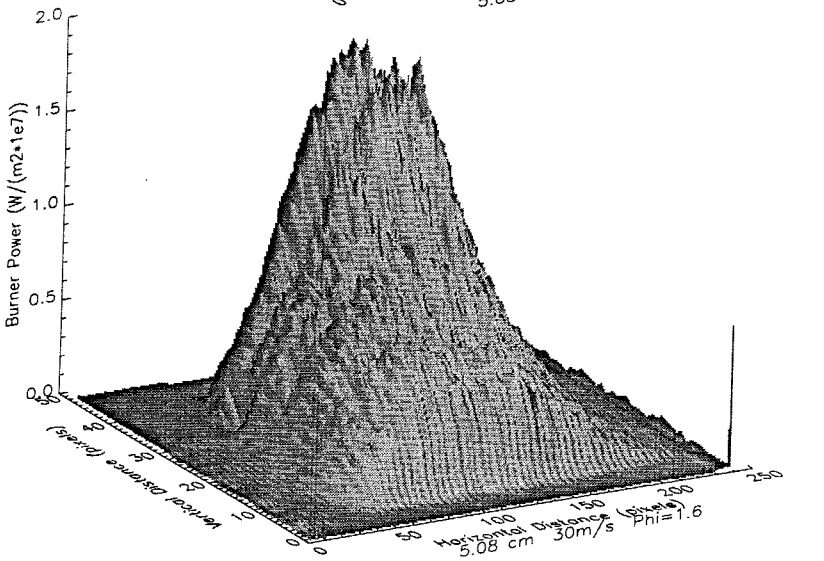

(c) $\phi = 1.6$

Figure 4.25: Average burner distribution shapes for mode transition: 5.08 cm duct, 30 m/s.

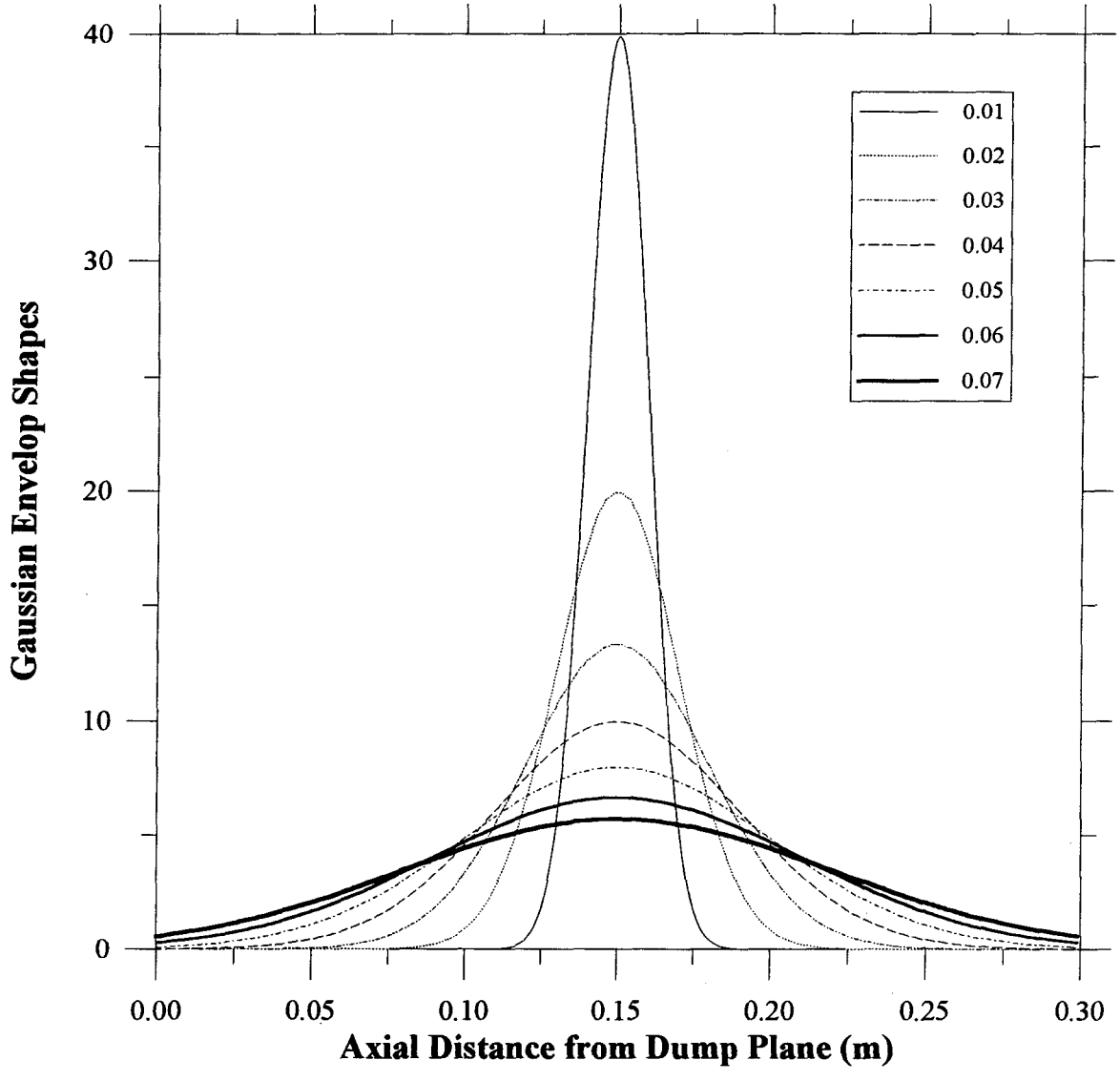

Figure 4.26: Gaussian envelops used in numerical simulations. Each curve denotes a unique σ_{a_i} as indicated in the legend.

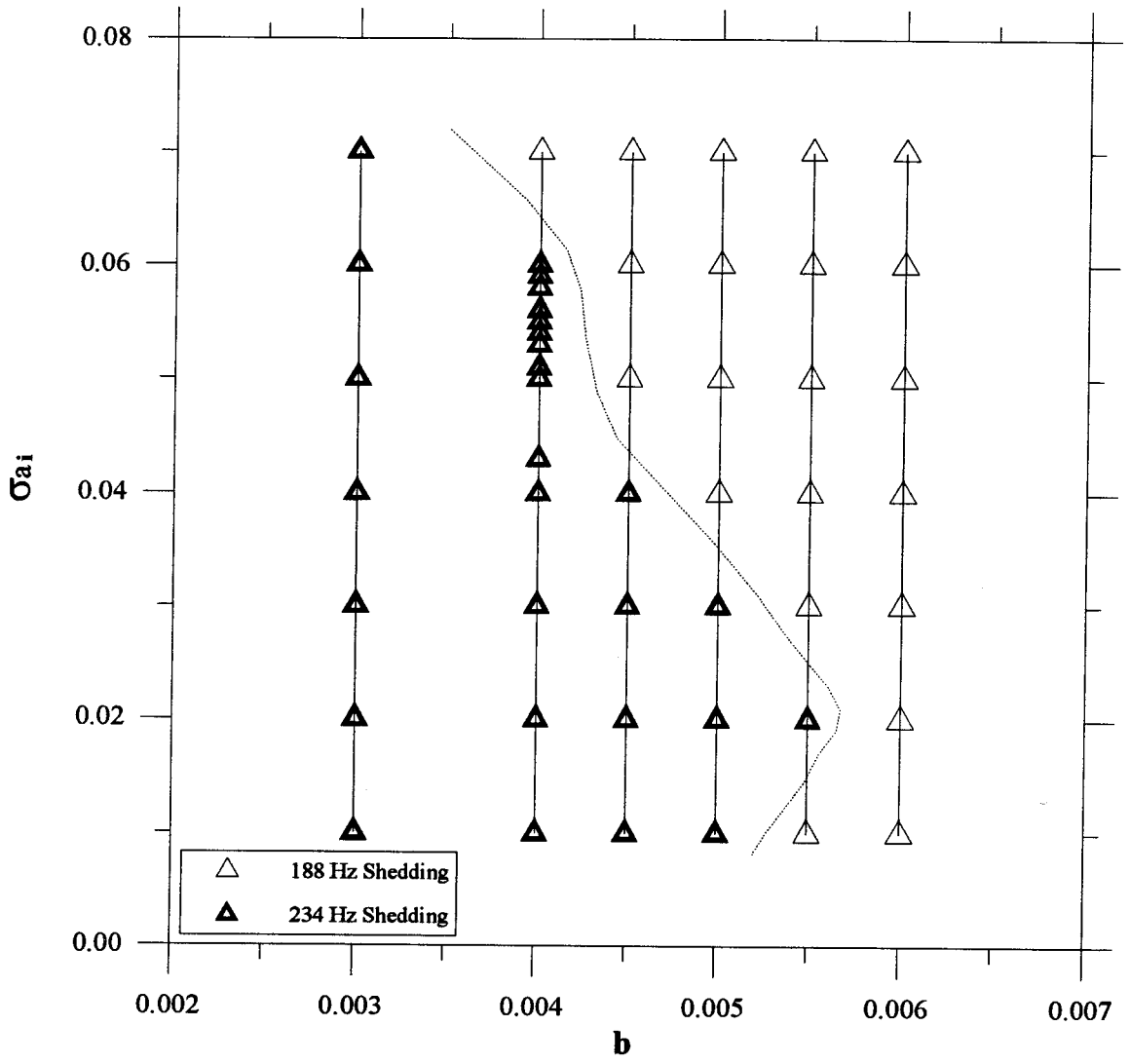

Figure 4.27: Numerical cases showing stability of 234/188 Hz modes (30 m/s).

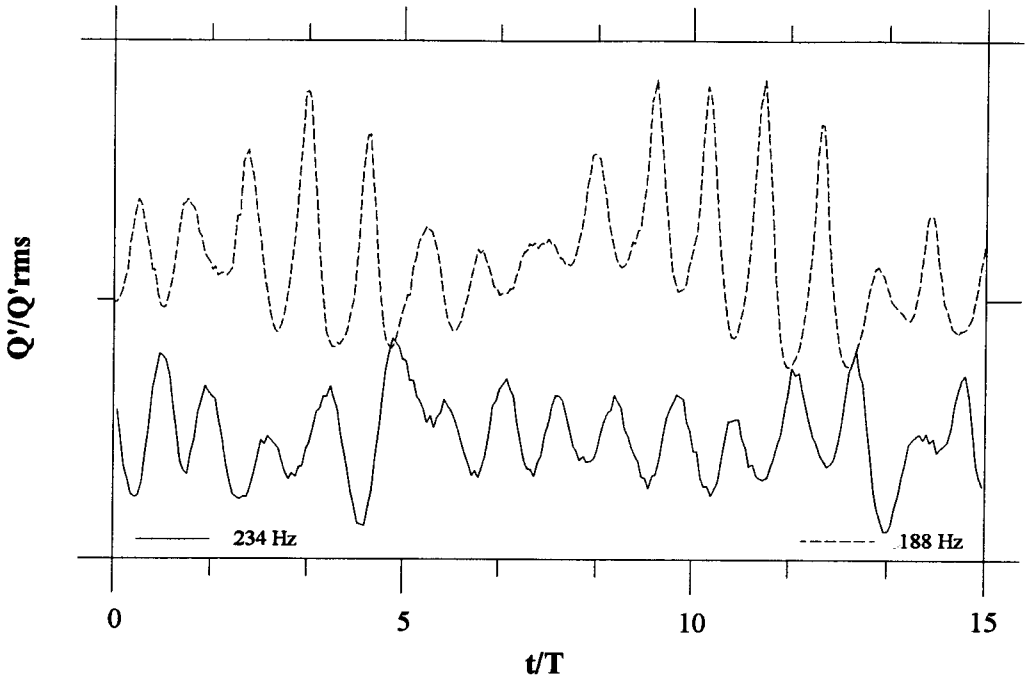

Figure 4.28: Heat release traces for 234 and 188 Hz instabilities (35 m/s) showing narrowing of temporal trace for 188 Hz mode.

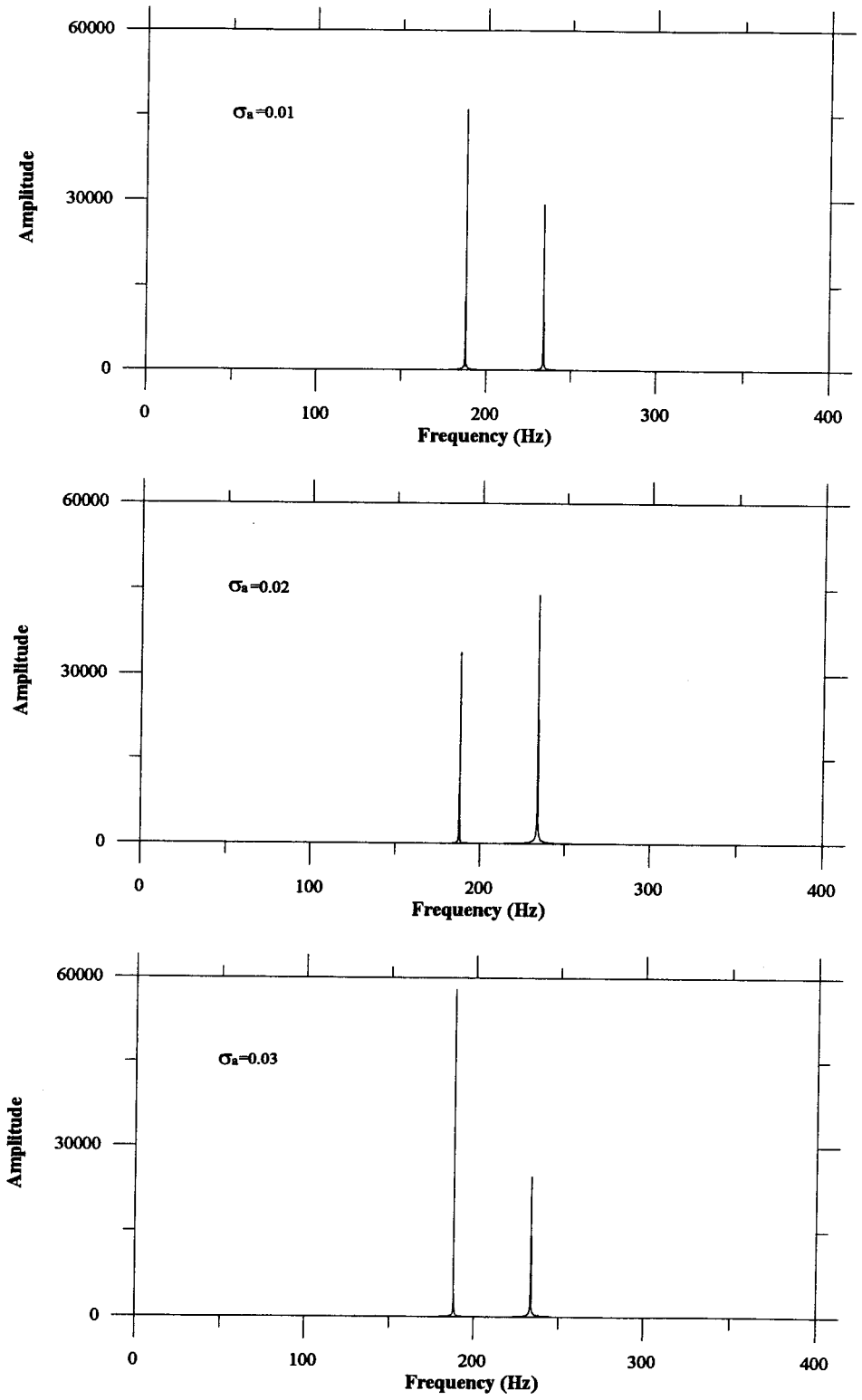

Figure 4.29: "Saddle Instability" near σ_a=0.05, b=0.0055.

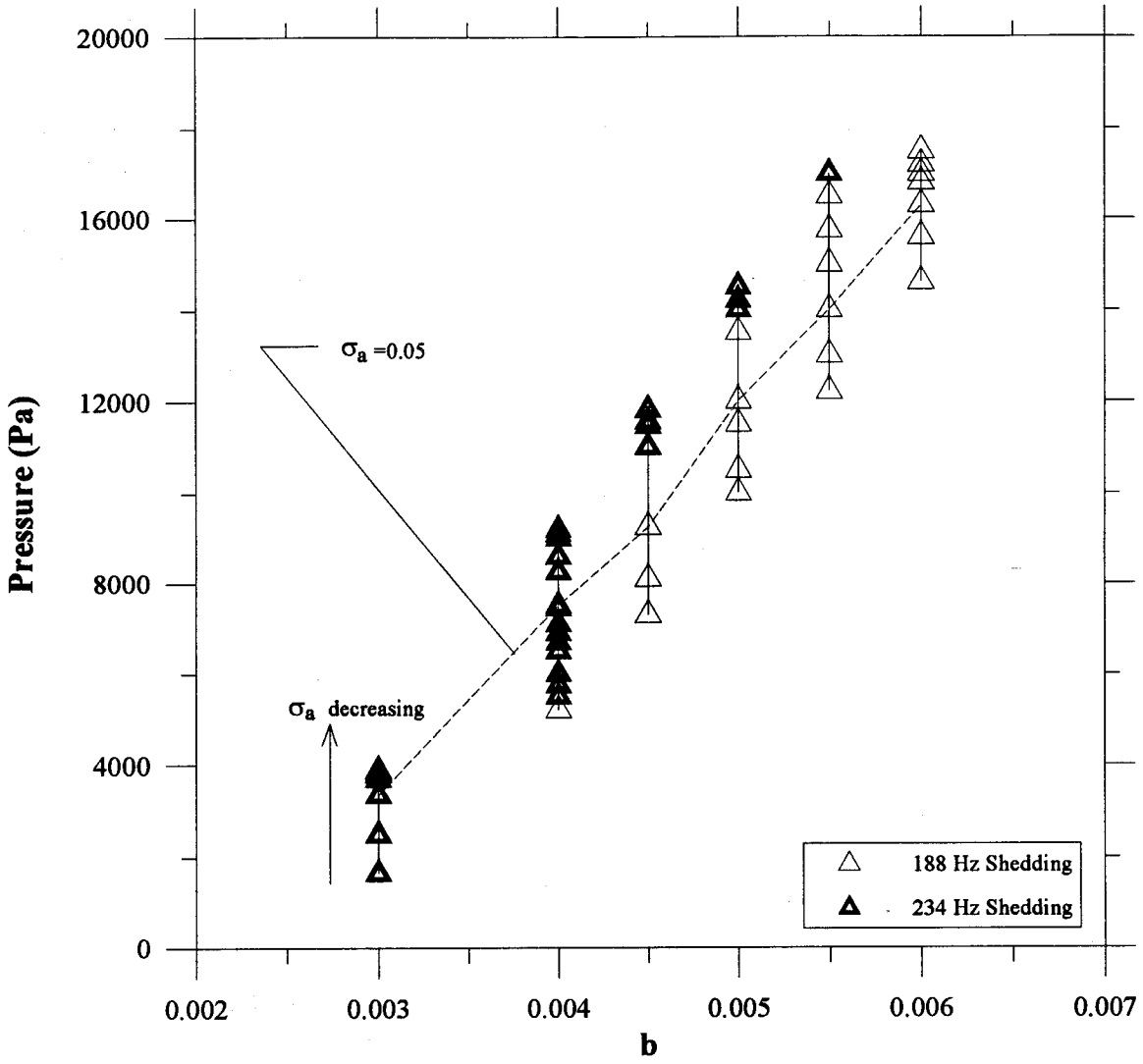

Figure 4.30: Summary of corresponding pressure magnitudes for numerical cases.

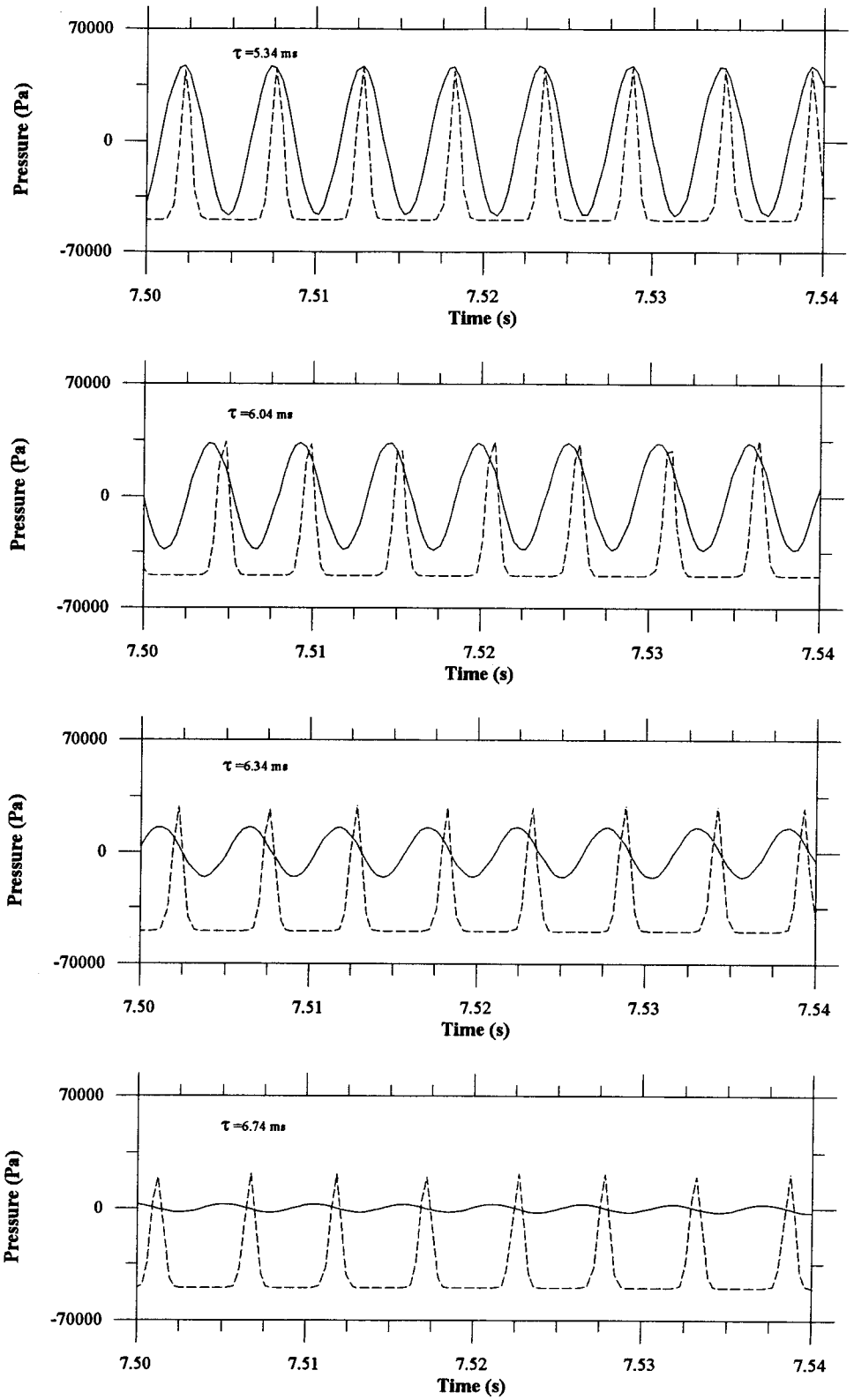

Figure 4.31a: Pressure dependence with heat pulse location (solid = p', dashed = q').

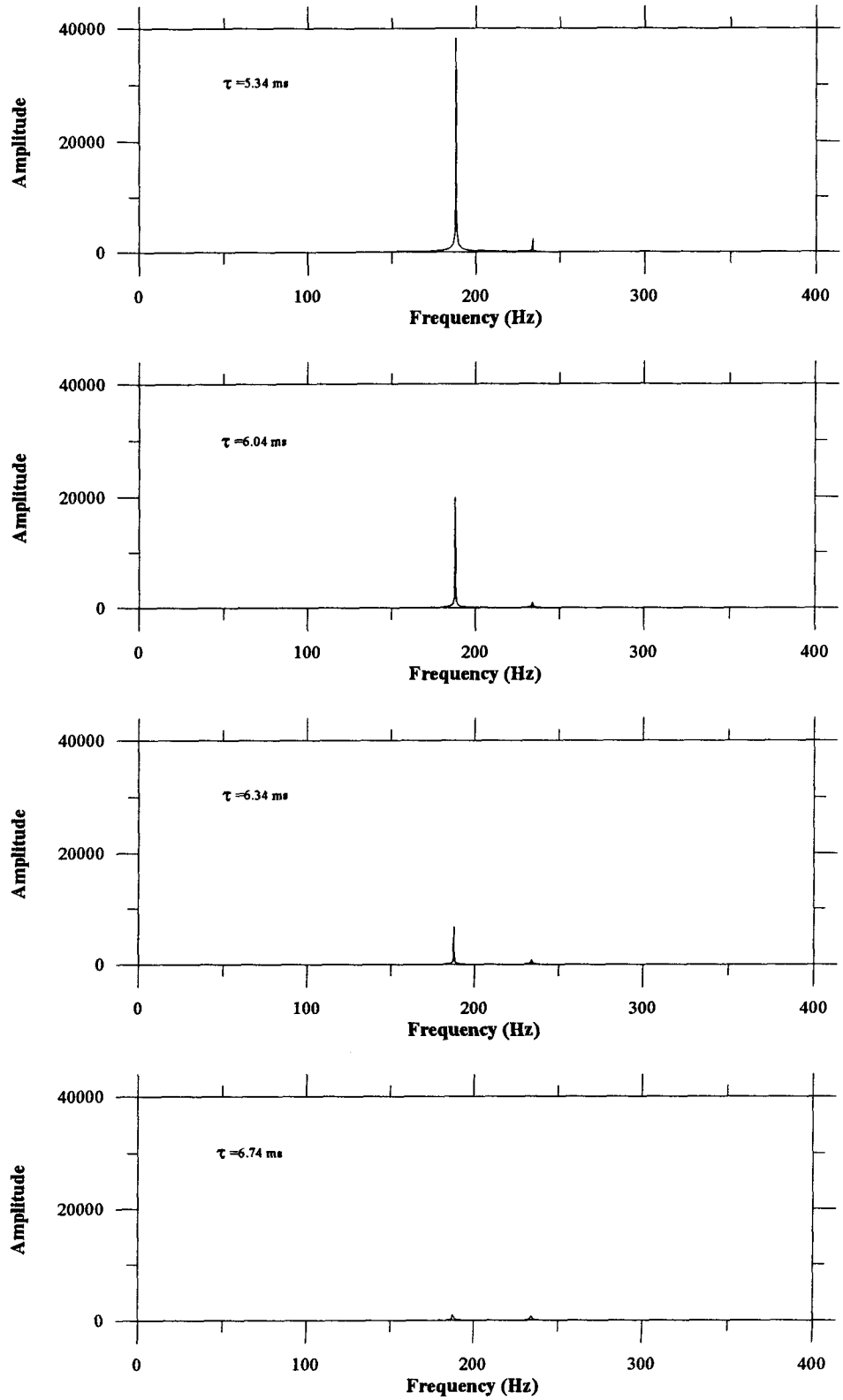

Figure 4.31b: Corresponding pressure FFTs.

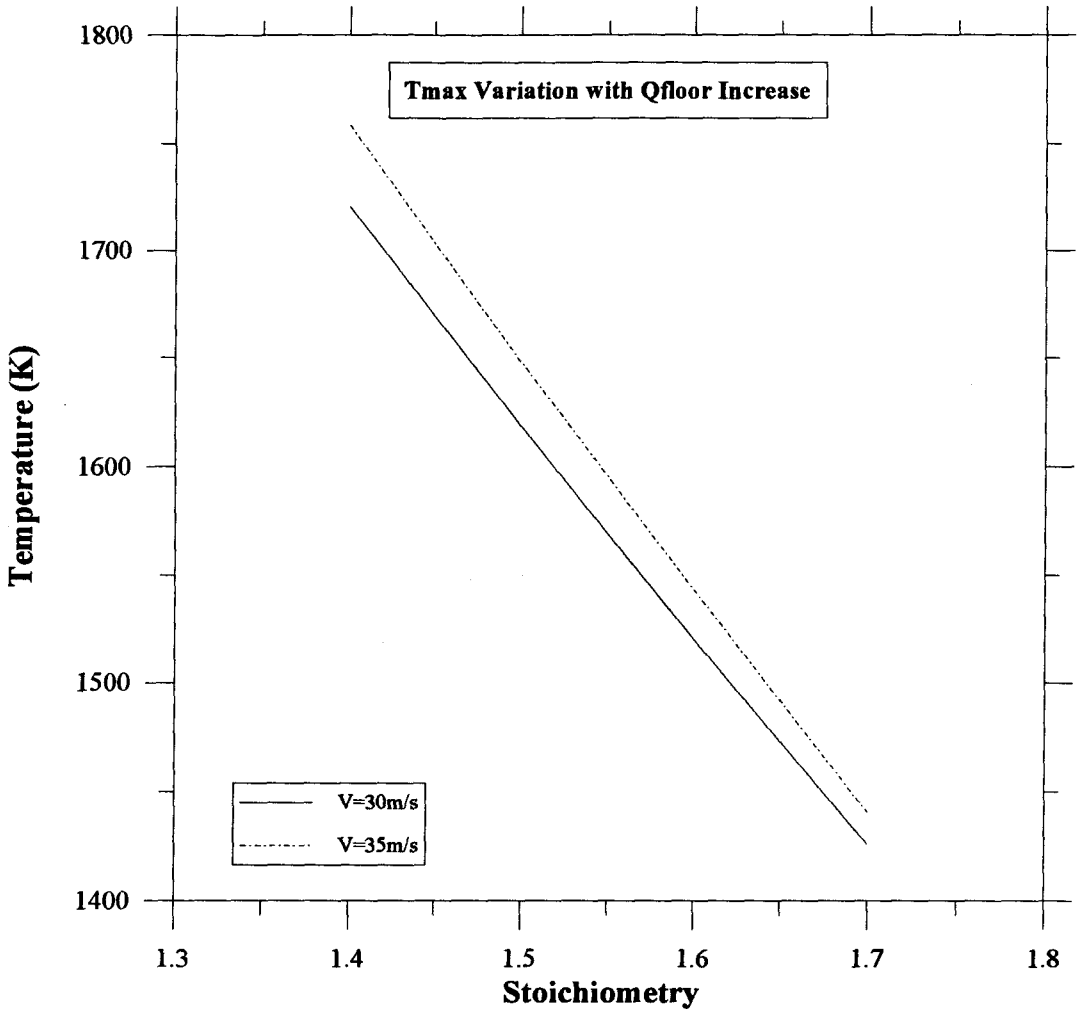

Figure 4.32: Temperature drops due to $\dot{Q}_{floor}$.

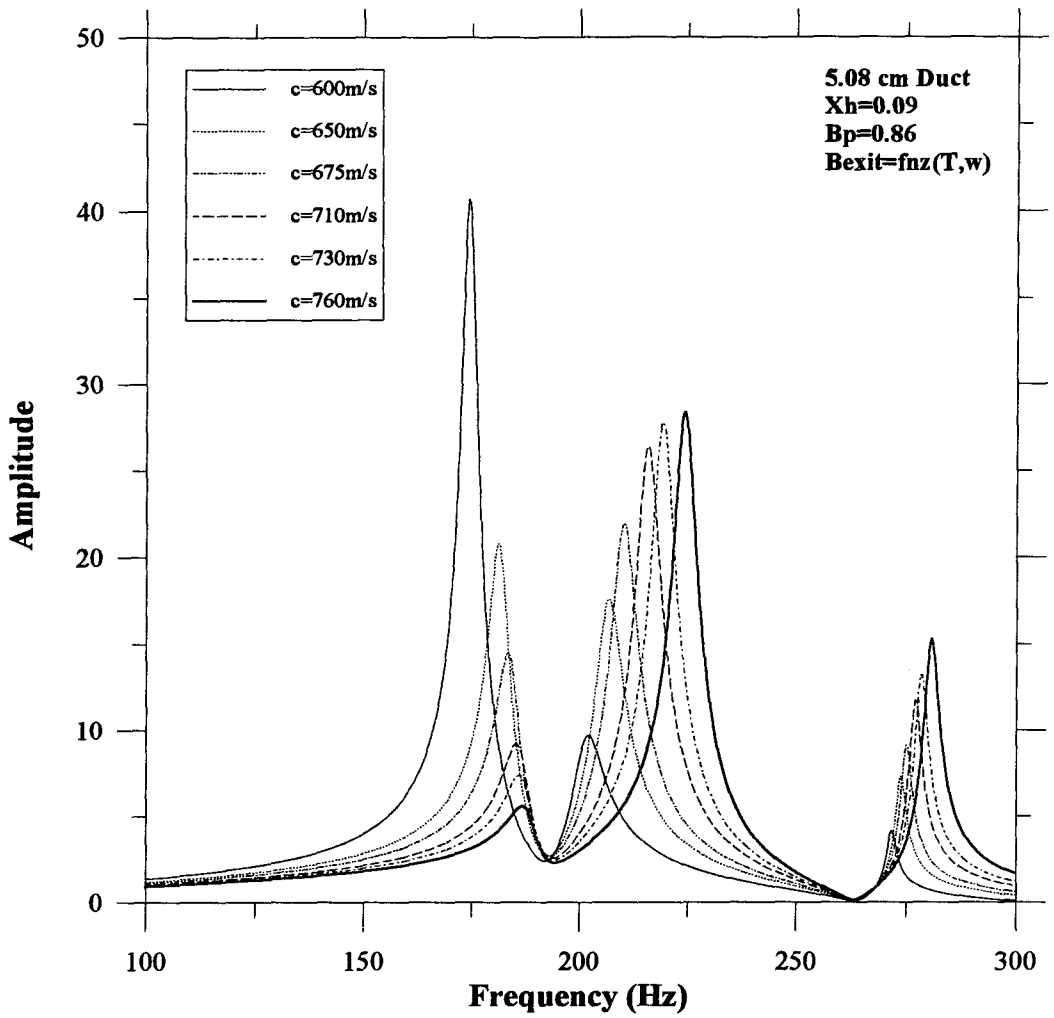

Figure 4.33: Pressure spectrum variation with sound speed changes.

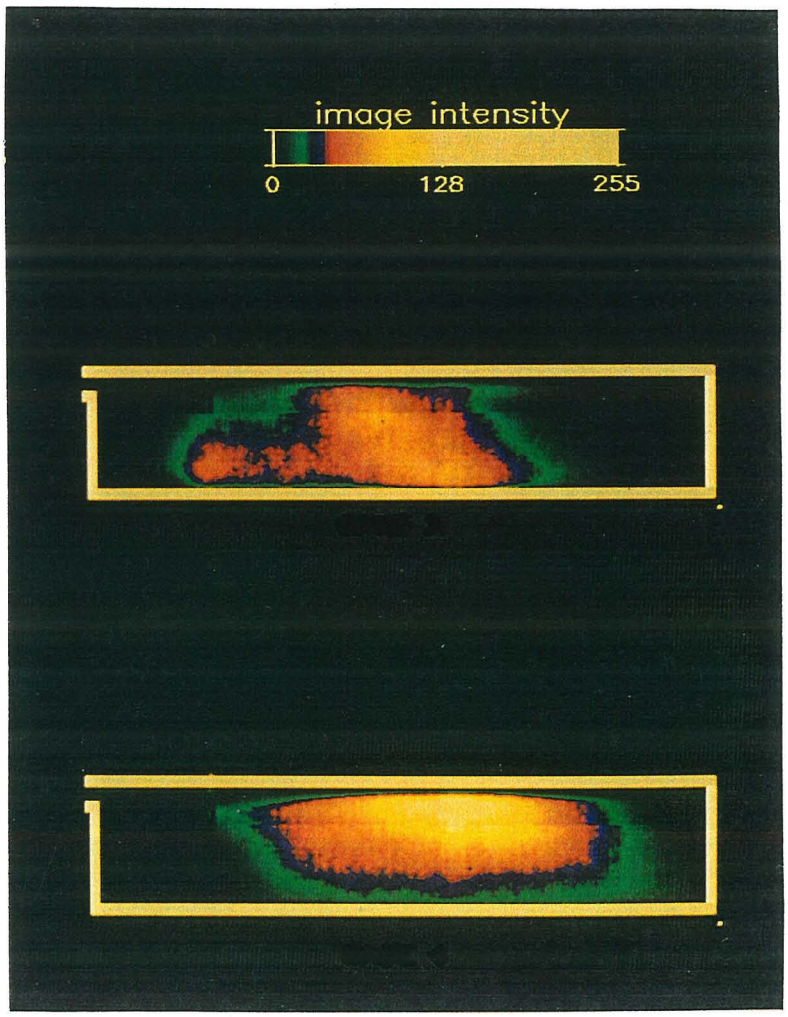

Figure 4.34: Downstream shift in peak burning location: (a) $\phi = 1.2$ and (b) $\phi = 1.4$; 5.08 cm duct, 35 m/s.

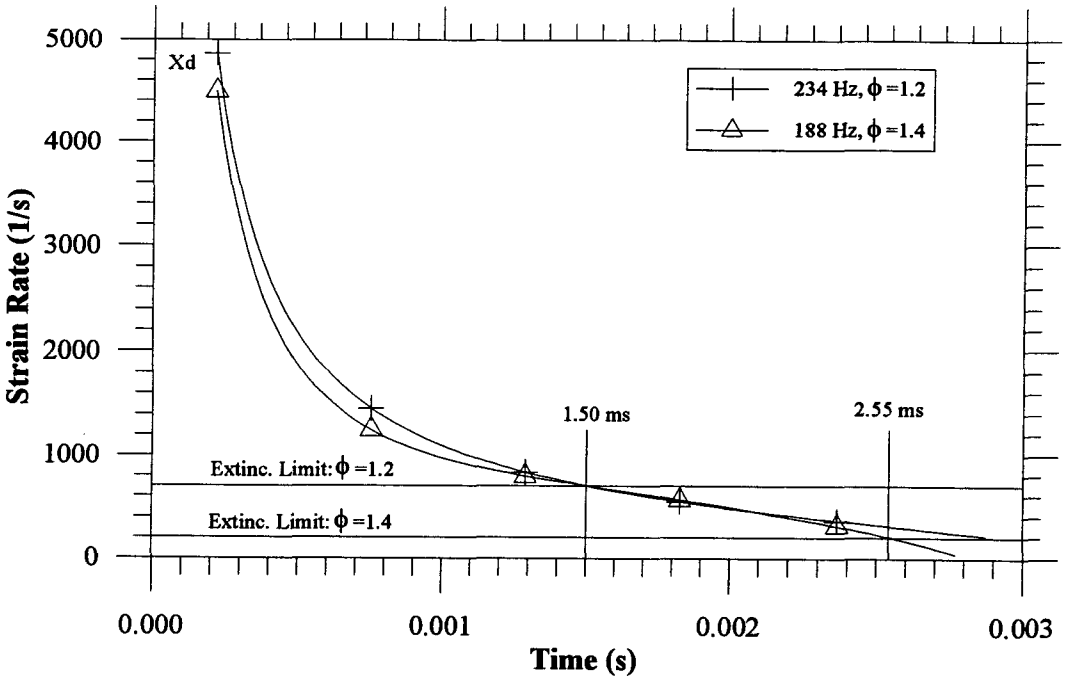

Figure 4.35: Straining curve based on X_d: 5.08 cm duct, 35 m/s.

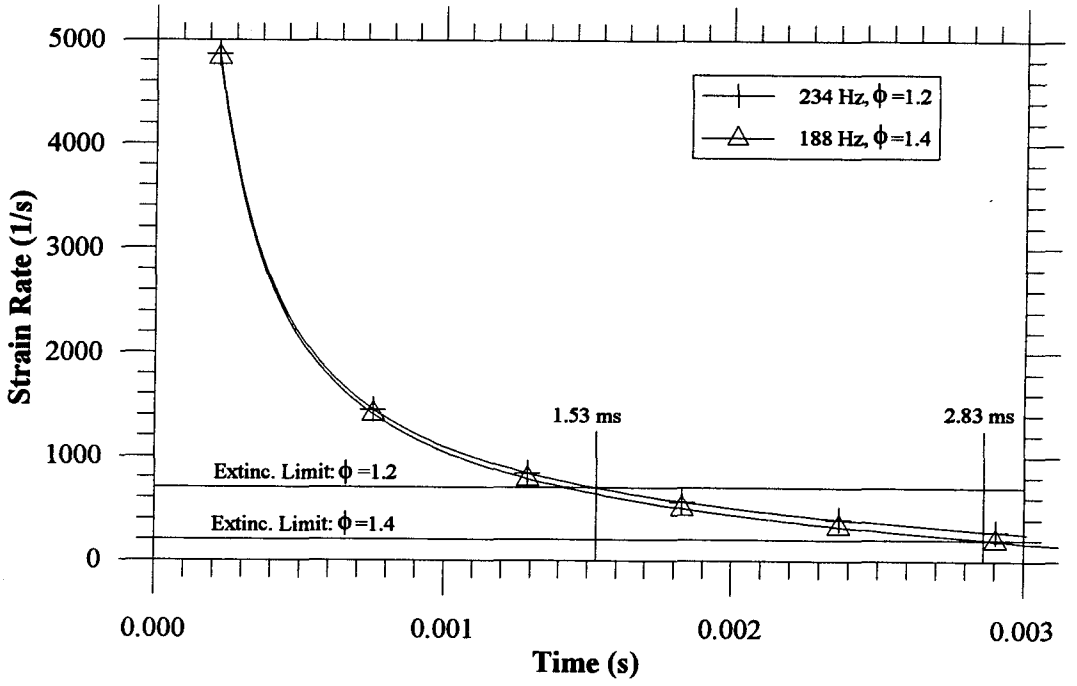

Figure 4.36: Straining curve based on $\left(L-\frac{1}{2}V_{dump}t\right)$: 5.08 cm duct, 35 m/s.

CHAPTER FIVE
CONCLUSIONS

5.1 CONCLUSIONS

An experimental and numerical investigation into the reacting vortex structures shed from the lip of a rearward facing step flameholder was performed to gain insight into the mode selection process. A premixed $CH_4 - air$ mixture was employed in all runs, ranging in stoichiometry from 1.2 to 1.7, duct heights from 2.54 to 7.62 *cm* and speeds of 21, 30 and 35 *m/s*. New diagnostic techniques have been added from previous Jet Propulsion Center work (Zsak, 1993; Sterling, 1987; Smith, 1985) which included high-speed CCD imagery, temporally resolved vortex and floor temperature measurements and floor heat flux measurements. The combined usage of high-speed shadowgraphy and chemiluminescence measurements provided a complete description of the typically nonuniform development of the reacting structures. In addition, a numerical technique adopted from Culick's representation of the acoustic field as an expansion of orthogonal modes (Culick, 1976) was employed to show how the flowfield variables effect mode selection. The model was used in conjunction with other linear acoustic modeling (Zsak, 1993) which, unfortunately, was unable to output the excited mode(s) for a given set of inputs. The main conclusions of the present investigation can be stated as follows:

(1) The unsteady combustion process was sustained from periodic vortex shedding due to acoustic velocity fluctuations at the step. The subsequent combustion of these structures was the necessary feedback mechanism to maintain the instability.

(2) The generic "188" and "234" *Hz* longitudinal acoustic modes were the only excited modes for the above geometric, speed and stoichiometric ranges.

(3) Comparison of high-speed shadowgraphs and CCD images revealed a distinct delay from injection of the fresh charge into the chamber till ignition. This ignition delay was found to depend most importantly on geometry and prior combustor pressures and was relatively invariant to stoichiometric variations (a slight decrease in ignition delay with stoichiometry was actually found). It is postulated that this delay could be due to low recirculation zone temperatures, insufficient time for the cold charge to mix with residual hot products to attain ignition temperatures and high initial strain rates. Ignition also caused noticeable enlargement of the structures as evidenced from plots of X_w versus time.

(4) Decreasing the duct height caused a noticeable lengthening in the burning zone due to the retarding of the vortex's growth through impingement with the floor and the subsequent forcing of hot products upstream and downstream. High-speed CCD cinematography revealed that decreasing the duct height caused sizeable increases in combustion intensity due to more intense and accelerated mixing and burning mechanisms facilitated by the close proximity of the floor. Structures shed in the largest duct, however, had to rely on their own vorticity and diffusional capabilities to initiate combustion as the floor's influence was much weaker. As such, they spent almost one more complete cycle of pressure in the duct relative to their 2.54 *cm* counterparts. Time-averaged duct and floor temperatures and floor heat flux values concurred with average CCD images in the broadening of the combustion zone with decreasing duct height.

(5) The Rayleigh Mechanism of energy transfer to the acoustic field dominated other energy transfer mechanisms. Two-dimensional Rayleigh plots revealed regions of driving and damping are unique to the excited mode with the 188 *Hz* mode exhibiting a single driving region extending from the dump plane to the middle of the duct and a damping region thereafter. The 234 *Hz* instability is, conversely, marked by a central driving region (centered further downstream than its 188 *Hz* counterpart) saddled between two damping regions. Time-varying, two-dimensional Rayleigh Indexes revealed that these driving/damping zones reverse their roles as energy addition or dissipation regions, respectively, throughout the vortex's cycle.

(6) Floor temperature and heat flux measurements revealed "hot spots" near the vortex impingement zone due to the increases in turbulent shear stresses and fluctuations there. Heat flux profiles for the 7.62 and 5.08 *cm* ducts closely reassembled their steady, separated flow counterparts in that they were characterized by low magnitudes in the recirculation zone, high values at impingement and values approaching their steady, turbulent counterparts further downstream. Pulsed values, as expected, exceed steady values and are poorly depicted by Quasi-Steady Theory. A more thorough heat transfer model was proposed and showed that the present flowfield incorporates turbulent pipe flow, flow pulsation and separated flow heat transfer mechanisms. Heat flux increases were also noted with the introduction of the 188 *Hz* mode and were postulated to be due to increased fluid dynamics associated with the 188 *Hz* mode as evidenced by the subsequent pressure increases. Calculations of Rayleigh Efficiency revealed 188 *Hz* instabilities had more energy transfer to the acoustic field, thereby strengthening the pulsations.

(7) Time-resolved vortex temperatures revealed a fairly linear temperature growth rate for structures undergoing a 234 *Hz* mode while their 188 *Hz* counterparts exhibited an initially delayed growth rate, probably due to lower duct temperatures associated with the increase in stoichiometry. By the third measurement station, however, 188 *Hz* structures exhibited temperatures exceeding their 234 *Hz* counterparts and such trends were most likely due to greater turbulent exchange processes (from greater combustor pressures) accompanying the richer run.

(8) It is proposed that turbulent exchange processes dominated their chemical counterparts for this flowfield. Evaluation of Rayleigh Efficiencies showed more energy was added to the 188 *Hz* instabilities, thus driving up pressures and hence turbulent effects, thereby quelling opposing chemical trends which would have slowed vortex temperature growth rates (see Item 7). Further evidence of this fluid dynamical dominance was in calculations of ignition delay and in τ_{max} which both showed decreases with increasing stoichiometry. As such, the mechanical delay τ_{mech} must be much larger than τ_{chem} ($\tau_{mech} >> \tau_{chem}$).

(9) Mode shifts occur due to initial chemical effects which lengthen acoustic periods (as far as the 188 *Hz* mode is concerned) and in changes in τ_{max} resulting from increased turbulent effects and alterations in the pressure-velocity phase angle, $\theta_{p'-v'}$, which changes from 47° to 127° as the excited mode shifts from 234 to 188 *Hz*. Stoichiometric effects were shown to have no effect on increasing ignition delays and consequently τ_{max}. Mode strengthening, as evidenced from increased Rayleigh Efficiencies and combustor pressures, is most likely due to decreases in τ_{max} incurred from the continued increases in turbulent exchange mechanisms which shifts the heat pulse closer to pressure maxima.

(10) Numerical results showed the importance of the phasing between the heat pulse and ensuing pressure trace, *temporal* shape of the heat pulse (which may or may not be related to the average heat release distribution shape[7]) and there exists preferred directions the heat pulse most likely takes during a mode transition.

(11) Straining and floor heat flux effects may provide additional, less dominate mechanisms to encourage shifts in the excited modes.

5.2 GENERAL REMARKS

As typically found by most pulsed combustion researchers, the phasing between the heat pulse and pressure trace is paramount in characterizing if and to what extent a pulsation may occur. What must be addressed, however, is why most all 7.62 *cm* ducts revealed 234 *Hz* instabilities while 2.54 *cm* ducts exhibited only 188 *Hz* instabilities, irrespective of stoichiometric changes which were the most influential parameter in the mode selection process for the 5.08 *cm* configuration. As expected, it is a question of how long the vortex takes to burn since the structure's combustion is the necessary feedback mechanism to sustain the instabilities.

With the largest duct height, the vortex must rely on its own vorticity and diffusional capabilities to entrain hot combustion products to initiate ignition and full combustion since the floor is much further away and recirculation zone temperatures are several hundred of degrees lower than their 2.54 *cm* counterparts. This would

[7] If the duct height is made smaller, the heat release distribution will automatically broaden as previously shown.

consequently encourage longer τ_{max} values which favour 234 *Hz* instabilities due to the unique pressure-velocity phasing for this mode. In fact, the Rayleigh Efficiency values showed one passes through a maximum in pulsation strength (Barr and Dwyer, 1991) as the stoichiometry increases from 1.2 to 1.6 (see Table 3.3): the heat pulse moved *leftward* due to shorter τ_{max} values. The same argument holds for the smallest duct height. The accelerated and more intense combustion due to the more influential effects of the floor necessitates shorter τ_{max} values, thereby favouring 188 *Hz* instabilities, irrespective of any stoichiometric change. Furthermore, once either a *strong* 234 or 188 *Hz* instability is engaged (as evidenced from its larger pressures or Rayleigh Efficiencies), it becomes more resistant to any external changes such as stoichiometry. Compare all 7.62 *cm*, 234 *Hz* instabilities to their much weaker 5.08 *cm* counterparts (Table 3.3). Such resistance was also shown numerically whereby some strong limit cycles were more resistant to changes in the parameter *b*.

Hence the duct geometry has the most influential effect in the mode selection process as it typically dictates impingement and eventual combustion locations. The 5.08 *cm* configuration, therefore, provides an intermediate geometry where the researcher can study more intricate effects as temperature changes on acoustic frequencies or turbulent mixing processes. The material presented herein should prove beneficial to the ongoing computational effort on unstable combustion as it has shown the intricacies of cycle-to-cycle nonuniformities, geometries and the dominance of fluid dynamic effects which are typically ignored.

REFERENCES

Aaron, K. (1985) "Edgetones and Acoustic Resonance's in a Duct," *Ph.D. Thesis*, California Institute of Technology, Pasadena, CA.

Alhaddad, A. and Coulman, G. (1982) "Experimental and Theoretical Study of Heat Transfer in Pulse-Combustion Heaters," *Proceedings Vol 1: Symp. on Pulse Combustion Applications*, GRI-82/0009.2, Atlanta, GA.

Aragaki, T., Iwata, S. Tange, H., Hiraoka, S., Yamada, I. and Kawaizumi, F. (1991) "Theoretical Analysis of Turbulent Flow and Heat Transfer around a Surface-Mounted Obstacle," *J. Chem. Engng. Japan*, **24**(2), 171-177.

Arpaci, V., Dec, J. and Keller, J. (1993) "Heat Transfer in Pulse Combustor Tailpipes," *Combust. Sci. and Tech.*, **94**, 131-146.

Bai, T., Cheng, X., Daniel, B., Jagoda, J. and Zinn, B. (1993) "Vortex Shedding and Periodic Combustion Processes in a Rijke Type Pulse Combustor," *Combust. Sci. and Tech.*, **94**, 245-258.

Barr, P., Keller, J., Bramlette, T., Westbrook, C. and Dec, J. (1990) "Pulse Combustor Modeling Demonstration of the Importance of Characteristic Times," *Combust. Flame*, **82**, 252-269.

Barr, P. and Dwyer, H. (1991) "Pulse Combustor Dynamics: A Numerical Study," *Prog. Astro. and Aero.*, **135**, 673-710.

Barr, P. and Keller, J. (1991) "Pulse Combustion: The Importance of Flame Extinction by Fluid Dynamic Strain," *Proceedings of the International Symp. on Pulsating Combustion*, **1**, Paper D-5, Monterey, CA.

Bauwens, L. and Daily, J. (1992) "Flame Sheet Algorithm for use in Numerical Modeling of Ramjet Combustion Instability," *J. Prop. Pwr.*, **8**(2), 264-270.

Bhatia, R. and Sirignano, W. (1991) "One-Dimensional Analysis of Liquid-Fueled Combustion Instability," *J. Propul.*, **7**(6), 953-961.

Boris, J. and Book, D. (1976) "*Methods of Computational Physics*," Academic, New York, **16**.

Bowditch, F. (1953) "Some Effects of Turbulence on Combustion," *Fourth Symp. (Intl.) on Combustion*, The Combustion Institute, 674-682.

Bradley, D. and Entwistle, A. (1966) "The Total Hemispherical Emittance of Coated Wires," *Brit. J. Appl. Phys.*, **17**, 1155-1164.

Bradley, D. and Mathews, K. (1968) "Measurement of High Gas Temperatures with Fine Wire Thermocouples," *J. of Mech. Engnrg. Sci.*, **10**, 299-305.

Bray, K. (1980) "*Turbulent Reacting Flows*," (P. A. Libby and F. A. Williams, Eds.), Springer-Verlag, New York.

Bray, K., Libby, P., Masuya, G. and Moss, J. (1981) "Turbulence Production in Premixed Turbulent Flames," *Combust. Sci. and Tech.*, **25**, 127-.

Bulewicz, E. (1967) "Some Observations on Chemiluminescence and Chemiionization in Flames," *Combust. Flame*, **11**, 297-308.

Cambry, P. (1986) "Measuring Thermocouple Time Constants: A New Method," *Combust. Sci. and Tech.*, **45**, 221-224.

Carslaw, H. and Jaeger, J. (1959) "*Conduction of Heat in Solids*," 2nd Ed., Oxford University Press, Oxford.

Chandran, S., Komerath, N. and Strahle, W. (1984) "Scalar Velocity Correlations in a Turbulent Premixed Flame," *Twentieth Symp. (Intl.) on Combust.*, The Combustion Institute, 429-435.

Cho, H. and Hyun, J. (1990) "Numerical Solutions of Pulsating Flow and Heat Transfer Characteristics in a Pipe," *Int. J. Heat and Fluid Flow*, **11**(4), 321-330.

Cho, H. and Goldstein, R. (1994) "An Improved Low-Reynold's-Number κ–ε Turbulence Model for Recirculating Flows," *Int. J. Heat Mass Transfer*, **37**(10), 1495-1508.

Chu, B. (1956) "On the Energy Transfer to Small Disturbances in a Viscous Compressible Heat Conductive Medium," *AFOSR Contract Rep.*, John Hopkins University.

Chu, B. (1965) *Acta Mech.*, **I**, 215-.

Clark T. and Bittker, D. (1954) "A Study of the Radiation from Laminar and Turbulent Open Propane-Air Flames as a Function of Flame Area, Equivalence Ratio, and Fuel Flow Rate," *NACA RM*, Lewis Flight Propulsion Laboratory, Cleveland, Ohio.

Corliss, J., Putnam, A., Murphy, M. and Lockin, D. (1984) *Proceedings of the 105th ASME Winter Annual Meeting*, Paper No. 84-JPGC-APC-2, New Orleans, LA.

Crauford, N., Liew, S. and Moss, J. (1985) "Experimental and Numerical Simulation of a Buoyant Fire," *Combust. Flame*, **61**, 63-77.

Crocco, L. and Cheng, S. (1956) "*Theory of Combustion Instabilities in Liquid Propellant Rocket Motors*," AGARDOGRAPH, **8**, Butterworth Scientific Publications, London.

Crump, J., Schadow, K., Yang, V. and Culick, F. (1986) "Longitudinal Combustion Instabilities in Ramjet Engines: Identification of Acoustic Modes," *J. Prop. Pwr.*, **2**, 105-109.

Culick, F. (1975) "Stability of Three-dimensional Motions in a Combustion Chamber," *Combust. Sci. and Tech.*, **10**, 109-.

Culick, F. (1976) "Nonlinear Behavior of Acoustic Waves in Combustion Chambers, Parts I and II," *Acta Astronautica*, **47**(13), 714-.

Culick, F. (1987) "A Note on Rayleigh's Criterion," *Combust. Sci. and Tech.*, **56**, 159-166.

Culick, F. (1988) "Combustion Instabilities in Liquid-Fueled Propulsion Systems," *AGARD Conference Proceedings*, No. 450, 1-73.

Culick, F. (1990) "Some Recent Results for Nonlinear Acoustics in Combustion Chambers," AIAA 90-3927; also published (1994) *AIAA Journal*, **32**(1), 146-170.

Culick, F., Paparizos, L., Sterling, J. and Burnley, V. (1991) "Combustion Noise and Combustion Instabilities in Propulsion Systems," *AGARD Conference Proceedings*, No. 512, 1-26.

Culick, F. (1992) "*Combustion Instabilities and Rayleigh's Criterion*," Modern Research Topics in Aerospace Propulsion, Eds. G. Angelino, L. De Luca and W. Sirignano, Springer-Verlag, New York, 135-191.

Culick, F. (1994) *Private Communication.*

Davis, D. (1981) "Coaxial Dump Combustor Instabilities, Part I - Parametric Test Data," *Interim Report*, Aero Propulsion Laboratory, Air Force Wright Aeronautical Laboratories, Wright-Patterson AFB, Ohio.

Davisson, C. and Weeks, J. (1924) "The Relations Between the Total Thermal Emissive Power of a Metal and its Electrical Resistivity," *J. Opt. Soc. Amer.*, **8**, 581-.

Dec, J. and Keller, J. (1989) "Pulse Combustor Tail-Pipe Heat Transfer Dependence on Frequency, Amplitude, and Mean Flow Rate," *Combust. Flame*, **77**, 359-374.

Dec. J. and Keller, J. (1990) "Time-Resolved Gas Temperatures in the Oscillating Turbulent Flow of a Pulse Combustor Tail Pipe," *Combust. Flame*, **80**, 358-370.

Dec, J., Keller, J. and Arpaci, V. (1992) " Heat Transfer Enhancement in the Oscillating Turbulent Flow of a Pulse Combustor Tail Pipe," *Int. J. Heat Mass Transfer.*, **33**(9), 2311-2324.

Diederichsen, J. and Gould, R. (1965) "Combustion Instability: Radiation from Premixed Flames of Variable Burning Velocity," *Combust. Flame*, **9**, 25-31.

Drewry, J. (1978) "Fluid Dynamic Characterization of Sudden-Expansion Ramjet Combustor Flowfields," *AIAA Journal*, **16**, 313-319.

Driscoll, J., Sutkus, D., Roberts, WM., Post, M. and Goss, L. (1994) "The Strain Exerted by a Vortex on a Flame-Determined from Velocity Field Images," *Combust. Sci. and Tech.*, **96**, 213-229.

Edelman, R., Turan, A. and France, D. (1979) *Proceedings: Symp. on Pulse Combustion.*

Eibeck, P., Keller, J., Bramlette, T. and Sailor, D. (1993) "Pulse Combustion: Impinging Jet Heat Transfer Enhancement", *Combust. Sci. and Tech.*, **94**, 147-165.

Fristrom, R. and Westenberg, A. (1965) "*Flame Structure*," McGraw-Hill, New York.

Fung, Y. (1991) "Active Control of Linear and Nonlinear Pressure Oscillations in Combustion Chambers," *Ph.D. Thesis*, Pennsylvania State University, Pennsylvania.

Gabruk, R. and Roe, L. (1994) "Velocity Characteristics of Reacting and Nonreacting Flows in a Dump Combustor," *J. Propul. Pwr.*, **10**(2), 149-154.

Gaydon, A. and Wolfhard, H. (1970) "*Flames: Their Structure, Radiation and Temperature*," 3rd Ed., Chapman and Hall, London.

Ghoniem, A. (1991) "Vortex Simulation of Reacting Shear Flow," *Prog. in Astro. Aero.*, **135**, 305-348.

Grillo, A. and Slack, M. (1976) "Shock Tube Study of Ignition Delay Times in Methane-Oxygen-Nitrogen-Argon Mixtures," *Combust. Flame*, **27**, 377-381.

HA, J., Proctor, D., Pearson, I. and Brumale, S. (1992) "Numerical and Experimental Studies of a Pulse Combustor," *Proceedings of the Eleventh Australian Fluid Mechanics Conference*, Hobart, Australia.

Habib, M. and McEligot, D. (1982) "Turbulent Heat Transfer In A Swirl Flow Downstream Of An Abrupt Pipe Expansion," *Proceedings of The Seventh Intl. Heat Transfer Conference*, Munich, Germany.

Hammer, J. (1993) "Lifted Turbulent Jet Flames," *Ph.D. Thesis*, California Institute of Technology, Pasadena, CA.

Hanby, V. (1969) "Convective Heat Transfer in a Gas-Fired Pulsating Combustor," *ASME J. Engng. Pwr.*, **91**, 48-52.

Hedge, U., Reuter, D., Daniel, B. and Zinn, B. (1986) "Flame Driving of Longitudinal Instabilities in Dump Type Ramjet Combustors," AIAA 86-0371.

Hedge, U., Reuter, D., Zinn, B. and Daniel, B. (1987) "Fluid Mechanically Coupled Combustion-Instabilities in Ramjet Combustors," AIAA 87-0216.

Heitor, M., Taylor, A. M. and Whitelaw, J. (1984) "Influence of Confinement on Combustion Instabilities of Premixed Flames Stabilized on Axisymmetric Baffles," *Combust. Flame.*, **57**, 109-121.

Hopkins, K., LaRue, J. and Samuelson, G. (1989) "Effect of Mean and Variable Time Constant on Compensated Thermocouple Measurements," In Durao, D. F. G. et al., (Eds.), *Instrumentation for Combustion and Flow in Engines*, Kluwer Academic, Boston, 55-68.

Hurle, I., Price, R., Sugden, T. and Thomas, A. (1968) "Sound from Open Turbulent Premixed Flames," *Proc. Roy. Soc.*, **303**, 409-427.

Kailasanath, J., Gardner, J., Oran, E. and Boris, J. (1991) "Numerical Simulations of Unsteady Reactive Flows in a Combustion Chamber," *Combust. Flame*, **86**, 115-134.

Keller, J., Vaneveld, L., Korschelt, D., Hubbard, G., Ghoniem, A., Daily, J. and Oppenheim, A. (1981) "Mechanism of Instabilities in Turbulent Combustion Leading to Flashback," AIAA 81-0107R.

Keller, J. and Westbrook, C. (1986) "Response of a Pulse Combustor to Changes in Fuel Composition," *Twenty-First Symp (Intl.) on Combust.*, The Combustion Institute, 547-555.

Keller, J., Barr, P., Bramlette, T., Evens, L. and Marchant, R. (1989) "Pulse Combustion: Demonstration of the Characteristic Mixing Time in a Commercial Burner," *Combust. Sci. and Tech.*, **66**, 127-137.

Keller J., Bramlette, T., Dec, J. and Westbrook, C. (1989) "Pulse Combustion: The Importance of Characteristic Times," *Combust. Flame*, **75**, 33-44.

Keller, J., Bramlette, T., Westbrook, C. and Dec, J. (1990) "Pulse Combustion: The Quantification of Characteristic Times," *Combust. Flame*, **79**, 151-161.

Keller, J. and Hongo, I. (1990) "Pulse Combustion: The Mechanism of NO_x Production," *Combust. Flame*, **80**, 219-237.

Kendrick, D., Zsak, W. and Zukoski, E. (1993) "An Experimental and Numerical Investigation of Premixed Combustion in a Vortex in a Laboratory Dump Combustor," in print, Kluwer Academic Press.

Kim, S., Kang, B. and Hyun, J. (1993) "Heat Transfer in the Thermally Developing Region of a Pulsating Channel Flow," *Int. J. Heat Mass Transfer*, **36**(17), 4257-4266.

Kobayashi, H. and Kitano, M. (1993) "Effects of Equivalence Ratio on the Extinction Stretch Rate of Cylindrical Premixed Flames," *Combust. Sci. and Tech.*, **89**, 253-263.

Koram, K. and Sparrow, E. (1978) "Turbulent Heat Transfer Downstream of a Unsymmetric Blockage in a Tube," *Trans. ASME*, **100**(4), 588-594.

Kostiuk, L. and Bray, K. (1994) "Mean Effects of Stretch on Laminar Flamelets in a Premixed Turbulent Flame," *Combust. Flame*, **95**, 193-212.

Kreith, F. and Bohn., M. (1986) "*Principles of Heat Transfer*," Fourth Ed., Harper & Row, New York.

Kuo, K. (1986) "*Principles of Combustion*," John Wiley & Sons, New York.

Lalwani, P., Das, K., Bhattacharyya, T. and Bhaduri, D. (1979) "Heat Transfer Characteristics of a Pulsating Combustion System," *Mech. Engng. Bull.*, **10**, 7-10.

Laverdant, A., Poinsot, T. and Candel, S. (1986) "Mean Temperature Field Effect on Acoustic Mode Structure in Dump Combustors," *J. Propul. Pwr.*, **2**(4), 311-316.

Law, C., Zhu, D. and Yu, G. (1986) "Propagation and Extinction of Stretched Premixed Flames," *Twenty-First Symp. (Intl.) on Combustion*, The Combustion Institute, 1419-1426.

Law, C. (1988) "Dynamics of Stretched Flames," *Twenty-Second Symp. (Intl.) on Combust.*, The Combustion Institute, 1381-1402.

Libby, P. and Bray, K. (1981) "Countergradient Diffusion in Premixed Turbulent Flames," *AIAA Journal*, **19**, 205-.

Liepmann, H. and Roshko, A. (1957) "*Elements of Gasdynamics*," John Wiley and Sons, New York.

Liou, T., Hwang, J. and Chen, S. (1993) "Simulations and Measurement of Enhanced Turbulent Heat Transfer in a Channel with Periodic Ribs on One Principal Wall," *Int. J. Heat Mass Transfer*, **36**(2), 507-517.

Lund, C. (1978) *University of California Lawrence Livermore National Laboratory Report*, UCRL-52504.

Masuya, G. and Libby, P. (1981) "Nongradient Theory for Oblique Turbulent Flames with Premixed Reaction," *AIAA Journal*, **19**, 1590-1599.

Menon, S. and Jou, W. (1987) "Simulations of Ramjet Combustor Flow Fields: Part I. Numerical Model, Large-scale and Mean Motions," AIAA 87-1421.

Menon, S. and Jou, W. (1991) "Large-Eddy Simulations of Combustion Instability in an Axisymmetric Ramjet Combustor," *Combust. Sci. and Tech.*, **75**, 53-72.

Menon, S. (1992) "Active Combustion Control in a Ramjet Using Large-Eddy Simulations," *Combust. Sci. and Tech.*, **84**, 51-79.

Mi, J. and Antonia, R. (1993) "Temperature Distributions within Vortices in the Wake of a Cylinder," *Int. J. Heat Mass Transfer*, **37**(6), 1048-1050.

Miles, P. and Gouldin, F. (1993) "Determination of the Time Constant of Fine-Wire Thermocouples for Compensated Temperature Measurements in Premixed Turbulent Flames," *Comb. Sci. and Tech.*, **89**, 181-199.

Miyashita, H., Takayanagi, A., and Wakabayashi, K. (1980) *Kagaku Kogaku Ronbunshu*, **6**, 152-.

Najm, H. and Ghoniem, A. (1991) "Numerical Simulations of the Convective Instability in a Dump Combustor," *AIAA Journal*, **29**(6), 911-919.

Najm, H. and Ghoniem, A. (1993) "Modeling Pulsating Combustion due to Flow-Flame Interactions in Vortex-Stabilized Pre-Mixed Flames," *Combust. Sci. and Tech.*, **94**(1-6), 259-278.

Nina, M. and Pita, G. (1985) "Measurements of Fluctuating Gas Temperatures Using Compensating Fine Wire Thermocouples," *AGARD Conference Proceedings on Heat Transfer and Cooling in Gas Turbines* (No. 390), Neuilly Sur Seine, France.

Odidi, A. (1974) "The Influence of Turbulence on the Time-mean Rate of Chemical Reactions," *Ph. D. Thesis*, University of London, U.K.

Oran, E. and Gardner, J. (1985) "Chemical-Acoustic Interactions in Combustion Systems," *Prog. Energy Combust. Sci.*, **11**, 253-276.

Park, J., Taylor, M. and McEligot, D. (1982) "Heat Transfer to Pulsating, Turbulent Gas Flow," *Proceedings of the Seventh Intl. Heat Transfer Conference*, Munich, Germany.

Perry, E. and Culick, F. (1974) "Measurements of Wall Heat Transfer in the Presence of Large-Amplitude Combustion-Driven Oscillations," *Combust. Sci. and Tech.*, **9**, 49-53.

Petit, C., Gajan, P., Lecordier, J. and Parathoen, P. (1982) "Frequency Response of Fine-Wire Thermocouple," *J. Phys. E: Sci. Instrum.*, **15**, 760-.

Poinsot, T., Trouvé, A., Veynante, D., Candel, S. and Espitito, E. (1987) "Vortex-Driven Acoustically Coupled Combustion Instabilities," *J. Fluid Mech.*, **117**, 265.

Poinsot, T., Veynante, D. and Candel, S. (1991) "Quenching Processes and Premixed Turbulent Combustion Diagrams," *J. Fluid Mech.*, **228**, 561-606.

Ponizy B. and Wojcicki, S. (1984) "On Modeling Pulse Combustors," *Twentieth Symp (Intl.) on Combust.*, The Combustion Institute, 2019-2024.

Putnam, A. and Faulkner, L. (1982) "An Overview of Combustion Noise," *J. Energy*, **7**, 458-469.

Rayleigh, Lord J. W. S. (1878) "*Nature*", **18**, 319; also (1945) "*The Theory of Sound*," Dover Publications, New York, **2**.

Roberts, WM., Driscoll, J., Drake, M. and Ratcliffe, J. (1992) "*OH* Fluorescence Images of the Quenching of a Premixed Flame during an Interaction with a Vortex," *Twenty-Fourth Symp (Intl.) on Combust.*, The Combustion Institute, 169-176.

Roberts, WM., Driscoll, J., Drake, M. and Goss, L. (1993) "Images of the Quenching of a Flame by a Vortex-To Quantify Regimes of Turbulent Combustion," *Combust. Flame*, 94, 58-69.

Rogers, D. and Marble, F. (1956) "A Mechanism for High-Frequency Oscillations in Ramjet Combustors and Afterburners," *Jet Propul.*, June, 456-462.

Rutland, C. and Ferziger, J. (1991) "Simulations of Flame-Vortex Interactions," *Combust. Flame*, **84**, 343-360.

Samaniego, J. M., Yip, B., Poinsot, T. and Candel, S. (1991) "Combustion Instabilities in a Side-Dump Model Ramjet Combustor," *Proceedings of the International Symposium on Pulsating Combustion*, **1**, August 1991, Paper D-8, Monterey, CA.

Samaniego, J. M., Yip, B., Poinsot, T. and Candel, S. (1993) "Low-Frequency Combustion Instability Mechanisms in a Side-Dump Combustor," *Combust. Flame*, **94**, 363-180.

Samuelson, G., LaRue, J. and Seiler, E. (1984) "Instantaneous Two-Component Laser Anemometry and Temperature Measurements in a Complex Reacting Flow," *Proceedings of the Second Intl. Symp. on the Appl. of Laser Anemon. to Fluid Mech.*, Paper 11.3, Lisbon, Portugal.

Schadow, K., Gutmark, T., Parr, T., Parr, K., Wilson, K. and Crump, J. (1989) "Large-Scale Coherent Structures as Drivers of Combustion Instability," *Combust. Sci. and Tech.*, **64**, 167-186.

Schadow, K., Gutmark, T. and Wilson, K. (1992) "Active Combustion Control in a Coaxial Dump Combustor," *Combust. Sci. and Tech.*, **81**, 285-300.

Scherer, V. and Wittig, S. (1991) "The Influence of the Recirculation Region: A Comparison of the Convective Heat Transfer Downstream of a Backward-Facing Step and Behind a Jet in a Crossflow," *J. Engng. for Gas Turb. Pwr.*, **113**, 126-134.

Scherer, V., Wittig, S., Bittlinger, G. and Pfeiffer, A. (1993) "Thermographic Heat Transfer Measurements in Separated Flows," *Exper. in Fluids*, **14**, 17-24.

Seider, E. and Tate, C. (1936) "Heat Transfer and Pressure Drop of Liquids in Tubes," *Ind. Eng. Chem.*, **28**, 1429-.

Shyy, W. and Udaykumar, H. (1990) "Numerical Simulation of Thermo-Acoustic Effect on Longitudinal Combustion Instabilities," AIAA 90-2065.

Smith, D. A. (1985) "An Experimental Study of Acoustically Excited, Vortex Driven, Combustion Instability within a Rearward Facing Facing Step Combustor," *Ph.D. Thesis*, Daniel and Florence Guggenheim Jet Propulsion Center, California Institute of Technology, Pasadena, CA.

Sobota, T. A. (1987) "An Experimental and Numerical Investigation of Swirling Flows in a Rectangular Nozzle," *Ph.D. Thesis*, Daniel and Florence Guggenheim Jet Propulsion Center, California Institute of Technology, Pasadena, CA.

Spalding, D. (1982) "The 'Shadow' Method of Particle-Size Calculation in Two-Phase Combustion," *Nineteen Symp. (Intl.) on Combust.*, The Combustion Institute, 941-951.

Sparrow, E., Kang, S. and Chuck, W. (1987) "Relation Between the Points of Flow Reattachment and Maximum Heat Transfer for Regions of Flow Separation," *Int. J. Heat Mass Transfer*, **30**(7), 1237-1245.

STANJAN (1985) *Chemical Equilibrium Solver.*

Sterling, J. D. (1987) "Longitudinal Mode Instabilities in Air Breathing Engines," *Ph.D. Thesis*, Daniel and Florence Guggenheim Jet Propulsion Center, California Institute of Technology, Pasadena, CA.

Sterling, J. (1991) "Characterization and Modeling of Aperiodic Pressure Oscillations in Combustion Chambers," AIAA 91-2082, Sacramento, CA.

Sterling, J. and Zukoski, E. (1991) "Nonlinear Dynamics of Laboratory Combustor Pressure Oscillations," *Combus. Sci. and Tech.*, **77**, 225-238.

Swift, G. (1988) "Thermoacoustic Engines," *J. Acoust. Soc. Am.*, **84**(4), 1145-1180.

Talby, R. Anselmet, F. and Fulachier, L. (1990) "Temperature Fluctuation Measurements with Fine Thermocouples," *Exp. in Fluids*, **9**, 115-.

Tanaka, H. and Yanagi, T. (1983) "Cross-Correlation of Velocity and Temperature in a Premixed Turbulent Flame," *Combust. Flame*, **51**, 183-.

Tang, J., Daniel, B., Jagoda, J. and Zinn, B. (1991) "Interaction Between Flow Field and Flame Spread in a Helmholtz Type Pulse Combustor," *Proceedings of the Intl. Symp. on Pulsating Combust.*, **1**, August, 1991, Paper D-8.

Touloukian, Y. (1967) "*Thermophysical Properties of High Temperature Solid Materials*," **1**, Macmillan, New York.

Tsuji, H. and Yamaoka, I. (1981) *First Specialist Meeting (Intl.) of the Combust. Institute*, The Combustion Institute, 111-.

Tsujimoto, Y. and Machii, N. (1986) "Numerical Analysis of a Pulse Combustor," *Twenty-First Symp. (Intl.) on Combust.*, The Combustion Institute, 539-.

Vogel, J. and Eaton, J. (1985) "Combined Heat Transfer and Fluid Dynamic Measurements Downstream of a Backward-Facing Step," *J. Heat Transfer (Transactions of the ASME)*, **107**, 922-929.

Westbrook, C., Pitz, W., Thorton, M. and Malte, P. (1988) "A Kinetic Modeling Study of n-Pentane Oxidation in a Well-Stirred Reactor," *Combust. Flame*, **72**, 45-.

Wiggins, S. (1990) "*Introduction to Applied Nonlinear Dynamical Systems and Chaos*," Springer-Verlag, New York.

Wohl, K., Shore, L., Rosenberg, H. and Weil, C. (1953) "The Burning Velocity of Turbulent Flames," *Fourth Symp. (Intl.) on Combustion*, The Combustion Institute, 620-635.

Wu, C. and Law, C. (1985) "On the Determination of Laminar Flame Speeds from Stretched Flames," *Twentieth Symp. (Intl.) on Combustion*, The Combustion Institute, 1941-1949.

Yang, V. (1984) "Pressure Oscillations in Liquid-Fueled Ramjet Engines," *Ph.D. Thesis*, California Institute of Technology, Pasadena, CA.

Yoshida, A. and Tsuji, H. (1982) "Characteristic Scale of Wrinkles in Turbulent Premixed Flames," *Nineteenth Symp. (Intl.) on Combust.*, The Combustion Institute, 403-411.

Yoshida, A. and Tsuji, H. (1984) "Mechanisms of Flame Wrinkling in Turbulent Premixed Flames," *Twelfth Symp. (Intl.) on Combust.*, The Combustion Institute, 445-451.

Yoshida, A. (1986) "Characteristic Time-Scale Distributions and Mean and Most Probable Length Scales of Flamelets in Turbulent Premixed Flames," *Twenty-First Symp. (Intl.) on Combust.*, The Combustion Institute, 1393-1401.

Yu, G., Law, C. and Wu, C. (1986) "Laminar Flame Speeds of Hydrocarbon + Air Mixtures with Hydrogen Addition," *Combust. Flame*, **63**, 339-.

Yu, K., Trouve, A. and Daily, J. (1991) "Low-Frequency Pressure Oscillations in a Model Ramjet Combustor," *J. Fluid Mech.*, **232**, 47-72.

Yule, A., Taylor, D. and Chigier, N. (1978) "Thermocouple Signal Processing and On-line Digital Compensation," *J. Energy*, **2**, 223-.

Zsak, W., Kendrick, D., Sterling, J. and Zukoski, E. (1991) "An Investigation of Reacting Vortex Structures Associated with Pulse Combustion," *Proceedings of the Intl. Symp. on Pulsating Combustion*, **1**, Paper D-7, Monterey, CA.

Zsak, T. W. (1993) "An Investigation of the Reacting Vortex Structures Associated with Pulsed Combustion," *Ph.D. Thesis*, Daniel and Florence Guggenheim Jet Propulsion Center, California Institute of Technology, Pasadena, CA.

Žukauskas, A., Šlančiauskas, A. and Pedišius, A. (1982) "Heat Transfer in a Turbulent Boundary Layer Behind a Two-dimensional Bluff Body at Different *Pr* numbers," *Proceedings of The Seventh Intl. Heat Transfer Conference*, Munich, Germany.

Zukoski, E. and Marble, F. (1956) "Experiments Concerning the Mechanism of Flame Blowoff from Bluff Bodies," in *Proceedings of Gas Dynamics Symp. on Aerothermochemistry*, 205-210, Northwest University Press.